EVALUATION AND APPLICATION OF MAX-DOAS METHODS FOR MONITORING AEROSOLS, NO_2, AND SO_2 IN URBAN AND INDUSTRIAL ENVIRONMENTS

ZOË YUN-WAN DAVIS

A DISSERTATION SUBMITTED TO THE FACULTY OF GRADUATE STUDIES IN PARTIAL FUFILLMENT OF THE REQUIREMENTS FOR THE DEGREE OF

DOCTOR OF PHILOSOPHY

GRADUATE PROGRAM IN EARTH & SPACE SCIENCE

LASSONDE SCHOOL OF ENGINEERING

YORK UNIVERSITY

TORONTO, ONTARIO

DECEMBER 2019

ABSTRACT

The ideal measurement technique to effectively address an air quality problem depends on the chemical and physical properties of the species and its environment. Multi-Axis Differential Optical Absorption Spectroscopy (MAX-DOAS) techniques allow a diversity of applications for studying atmospheric species, including the determination of emissions, vertical profiles, and the tropospheric column loading of trace gases. Deployment of the MAX-DOAS instrument during the comprehensive air quality campaign in the Athabasca Oil Sands Region in 2013 provided a rare opportunity to evaluate the performance of multiple aspects of the MAX-DOAS retrievals. Retrievals of aerosol extinction, NO_2, and SO_2 were compared to data from lidar, sun photometer, Active-DOAS, and airborne in-situ measurements of trace gases. The MAX-DOAS retrievals performed well except under conditions of rapidly changing vertical profiles of pollution. Important elements required to achieve useful inter-comparisons of MAX-DOAS with other instruments (e.g., the lidar S-ratio) and advantages of the MAX-DOAS technique were identified. MAX-DOAS measurements of SO_2 gas calibration cells were conducted to determine the optimal settings for fitting SO_2 differential slant column densitities (dSCDs), currently absent in the literature. Fitting dSCDs of SO_2 from solar measurements is challenging due to the effects of stray light, potential interference by O_3 absorption, and low solar intensity in wavelength regions where SO_2 absorption features are strong. Based on the experiments, the use of a short-pass filter and a fitting window of $307.5 < \lambda < 319$ nm are recommended. MAX-DOAS measurements in Toronto, Ontario, during 2015 quantified the impact of lake-breeze circulations on the tropospheric loading of NO_2 and aerosol extinction. These first measurements of the total tropospheric loading of pollutants behind a lake breeze front on multiple days using MAX-DOAS confirms previously theorized 3-D structures of lake breezes. Finally, the mobile-MAX-DOAS technique of estimating NO_x and SO_2 emissions was improved by conducting simultaneous Mobile-MAX-DOAS and in-situ NO-NO_2-NO_x measurements and deploying a modular meteorological station while observing urban plumes in the industrial city of Sarnia, Ontario. These studies demonstrated the utility of MAX-DOAS techniques for monitoring tropospheric air quality in industrial and urban settings when in-situ and other remote sensing techniques are limited.

ACKNOWLEDGEMENTS

It takes a community to help a student not only complete a Ph.D. but also enjoy and grow from the experience. I have been very fortunate in and am grateful to the diverse community that supported me during my graduate experience.

To my supervisor, Dr. Robert McLaren, thank you for being the best of supervisors, a gentleman and a scholar. Your humour, mentorship, support, and enthusiasm for science allowed me to grow as a scientist and person. Memorable field work experiences in your group significantly increased my love for outdoor adventuring! Thank you also to my committee members, Dr. Tom McElroy and Dr. Donald Hastie for your guidance and for providing your formidable expertise.

Thanks also to the wonderful people at the Institute for Environmental Physics in Heidelberg, Germany, especially Martin Horbanski and Udo Frieß. I could not have asked for a more welcoming group to spend a research exchange with and to teach me how to become a DOAS nerd.

Members of the Centre for Atmospheric Chemistry formed invaluable members of my community, increasing my success and enjoyment of graduate school. I would particularly like to thank Carol Weldon for being an inspiring woman and keeping the CAC members ticking along in the right direction for many years. Thank you also to Marcia Gaynor for your kindness and helping me navigate the complex terrain of the graduate system.

All of my projects benefitted greatly from the fantastic assistance and support from my group members, Aida Khanbabkhani, Sabour Baray, Csilla Csukat, and William Fujs, as well as our undergraduate research assistants. I couldn't have asked for a more intelligent, supportive, or hilarious group of people. Thanks for all the problem-solving sessions, uncontrollable laughter, and field work adventures.

Thank you to all my coauthors for your invaluable data contributions, scientific discussions and editorial feedback that shaped the publications. Particularly, thank you to the researchers and managers at Environment and Climate Change Canada as well as the Ontario Ministry of the Environment for the invaluable research opportunities and support. Thank you to Mr. Barry Duffey for helping me get my last and favourite project off the ground.

Much gratitude is felt towards my partner, Andrew Lohmann, for the unwavering scientific and emotional support. You help keep me balanced when I waver on my own. Also, thanks for saving me countless hours of work by persuading me to embrace the joys of MATLAB.

Finally, thank you to my wonderful and unconventional parents for all the love, advice (both solicited and unsolicited), editing wizardry, and even assistance in the field. You both went above and beyond. If possible, I would bestow multiple honorary degrees for all your involvement. I attribute a large portion of my success to your unwavering support and enthusiasm and will be forever grateful.

TABLE OF CONTENTS

LIST OF TABLES

LIST OF FIGURES

LIST OF SYMBOLS AND ABBREVIATIONS

Acronym or Symbol	Expansion
α	Viewing Elevation Angle
λ_{cutoff}	Cutoff wavelength of Short-pass Filter
λ_{high}	Upper Limit Wavelength of Fitting Window
λ_{low}	Lower Limit Wavelength of Fitting Window
(B)	Base Case Measurement (No Filter and Offset Function Disabled)
(B+F)	Measurement with Short-Pass Filter
(B+F+O)	Measurement with Short-Pass Filter Fit using Offset Function
(B+O)	Measurement with Fit using Offset Function
A.g.l.	Above ground level
AERONET	Aerosol Robotic Network
AOD	Aerosol Optical Depth
AOSR	Athabasca Oil Sands Region
APS	Aerodynamic Particle Sizer
BrO	Bromine Oxide
CCD	Charge-Coupled Device
ClO	Chlorine Oxide
DOAS	Differential Optical Absorption Spectroscopy
dSCD	Differential Slant Column Density
ECCC	Environment and Climate Change Canada
FRS	Fraunhofer Reference Spectrum
HCHO	Formaldehyde
LBC	Lake-breeze Circulation
LBF	Lake-breeze Front
Lidar	Light Detection and Ranging
MAX-DOAS	Multi-Axis Differential Optical Absorption Spectroscopy
MOECC	Ontario Ministry of the Environment and Climate Change

molec cm^{-2}	Molecules per square centimeter
NH_3	Ammonia
nm	nanometers
NO_2	Nitrogen Dioxide
NO_3	Nitrate Radical
NO_x	Nitrogen Oxides (NO_2 + NO)
O_3	Ozone
O_4	Tetraoxygen
OH	Hydroxyl Radical
$PM_{2.5}$	Particulate Matter with a Diameter < 2.5 Micrometres
ppbv	Parts Per Billion Volume
ppt	Parts Per Trillion Volume
RI	Refractive Index
SMPS	Scanning Mobility Particle Sizer
SO_2	Sulphur Dioxide
SP-AMS	Soot-Particle Aerosol Mass Spectrometer
UV	Ultraviolet
VCD	Vertical Column Density
WBEA	Wood Buffalo Environmental Association

Chapter 1

Important Tropospheric Species and Selected Atmospheric Measurement Techniques.

Nothing in life is to be feared, it is only to be understood.

Now is the time to understand more, so that we may fear less.

-Marie Curie

1 Tropospheric species relevant to this research are discussed in Section 1.1. Description of techniques for measurement of atmospheric species, including MAX-DOAS, follows in Section 1.2. The final section (1.3) describes the author's contribution to the field of monitoring atmospheric species.

1.1 Tropospheric Species: Aerosols, NO_2, SO_2, and O_4

1.1.1 Aerosols

Aerosols are tiny particles in the atmosphere composed of a suspension of liquid or solid particles in a gas (Seinfeld and Pandis, 2006). Aerosols impact visibility, air quality, the formation of clouds, the Earth's radiative budget and hydrological cycle, and result in acid deposition (Ramanathan et al., 2001; Seinfeld and Pandis, 2006; Strawbridge et al., 2018). These particles play an important role in atmospheric chemistry by serving as surfaces for heterogeneous chemical reactions. Aerosols contribute to atmospheric particulate matter (PM) with diameters <2.5 μm ($PM_{2.5}$) that intensify cardiovascular and respiratory conditions and are estimated to have caused ~4.2 million deaths in 2015 (Cohen et al., 2017). Removal mechanisms of aerosols from the atmosphere are dry and wet deposition, to the Earth's surface and incorporation into precipitation droplets (Seinfeld and Pandis, 2006). Aerosols can be transported across large distances globally, having tropospheric lifetimes of a few hours to a few weeks, depending on their size and the meteorological conditions (Uno et al., 2009).

The diameter of aerosols ranges from ~0.002 to ~100 μm and are broadly characterized as "fine" if <2.5 μm and "coarse" if >2.5 μm (Figure 1-1). While fine and coarse particles are often emitted by the same sources, they differ in chemical composition, optical properties, and mechanisms for transformation and removal from the atmosphere. In the fine mode, nucleation and Aiken mode particles have diameters of up to ~0.01 μm and ~0.01-0.1 μm, respectively. Nuclei mode particles are produced by the condensation of hot vapours during combustion or nucleation of atmospheric species and are lost via coagulation with larger particles. The accumulation mode consists of particles with diameters between ~0.1 and 2.5 μm that typically contribute to much of the total aerosol mass and surface area. These particles are formed from condensation onto existing particles and coagulation of nuclei mode particles. Removal mechanisms are least effective for the accumulation mode, allowing these particles to have generally longer lifetimes compared to the other modes. Coarse mode particles are formed via mechanical processes and form anthropogenic and biogenic dust. These particles are removed from the atmospheric relatively quickly because of large sedimentation velocities. Once emitted or formed, the size and composition of aerosols can change due to coalescence or aggregation with other aerosols, or condensation of other gases on to the aerosol (Seinfeld and Pandis, 2006).

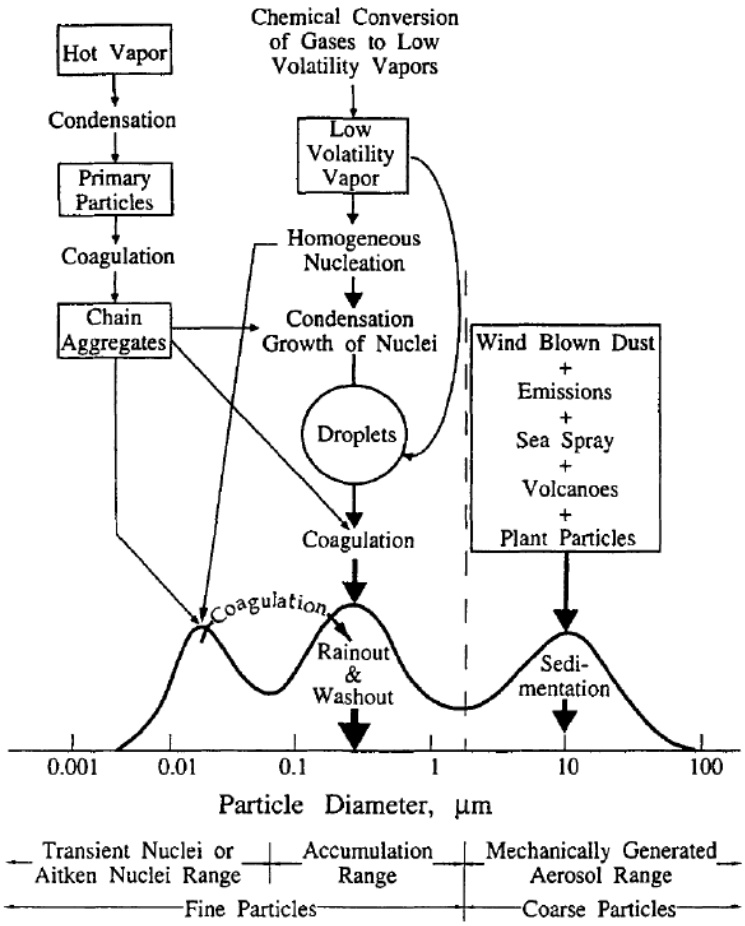

Figure 1-1 Idealized diagram of aerosol surface area distribution showing the three size modes with their sources, formation and removal processes. Adapted from Seinfeld and Pandis (2006).

Primary aerosols are particles that are directly emitted while secondary aerosols are formed by the conversion of gases or via chemical transformation within the particle phase. In the troposphere, a large fraction of the aerosols is anthropogenic and can contain nitrate, sulphate, sodium, chloride, and trace metals, among others. The major sources of anthropogenic aerosol emissions are industrial processes, fossil fuel combustion and vehicular traffic. Natural sources of aerosols include terrestrial dust, volcanic activity, biomass burning, sea spray, and conversion from biogenic gas emissions (Seinfeld and Pandis, 2006). Given aerosols' diversity of sources and potential for transformation and transportation, the vertical profile of aerosols in the atmosphere varies spatially and temporally. Knowledge of the vertical profiles of tropospheric aerosols can be critical for understanding air quality and climate (Strawbridge, 2013) but, due to the profiles' variability, accurately modelling the profiles is typically challenging without large temporal averaging (Guibert et al., 2005; Wu et al., 2017b).

Aerosols have direct and indirect radiative forcing effects, resulting in a deviation in the net radiative flux at the tropopause (Ramanathan et al., 2001). In the direct forcing effect, aerosols scatter and absorb solar and thermal

infrared radiation, impacting the Earth's albedo and radiative budget. In the indirect effect, aerosols alter the radiative properties of clouds, impacting cloud lifetime and radiative properties. Aerosols can increase the concentration of cloud droplets while decreasing droplet size. The decreased droplet size typically increases cloud lifetime, thickness and water content (Haywood and Boucher, 2000). Thus, aerosols can impact both the radiative budget and hydrological cycles.

1.1.2 Nitrogen Dioxide (NO_2)

Nitrogen oxides are some of the most important trace gases for atmospheric chemistry (Seinfeld and Pandis, 2006). Nitrogen dioxide (NO_2) is a key component in the production of tropospheric ozone (O_3), forms atmospheric oxidants (e.g., nitrate radical, NO_3), influences the abundance of hydroxyl (OH) and peroxy radicals, and contributes to acid deposition (Finlayson-Pitts and Pitts, 2000). High concentrations of NO_2 can irritate the human respiratory system and exacerbate respiratory diseases (US EPA, 2016). Nitrate aerosols (NO_3^-), a major component of $PM_{2.5}$ (Jung et al., 2016), are formed from NO_2 through homogeneous reactions producing nitric acid (HNO_3) that can react with NH_3 to produce NH_4NO_3. Heterogeneous reactions on aerosol surfaces also allow formation of nitrate aerosols (Bauer et al., 2007). Anthropogenic emissions of NO_x ($NO+NO_2$) in 2000 were estimated to be ~57 Tg N by Lamarque et al. (2010) and ~40 Tg N by Jaeglé et al. (2005). As shown in Table 1-1, the largest source of NO_x is fossil fuel combustion (Ehhalt et al., 2018), and other important sources include natural and anthropogenic biomass burning, soil emissions, and lightning (Lamarque et al., 2010). Vertical column densities (VCDs) of NO_2 are highest over large cities or industrial regions due to anthropogenic emissions (Figure 1-2).

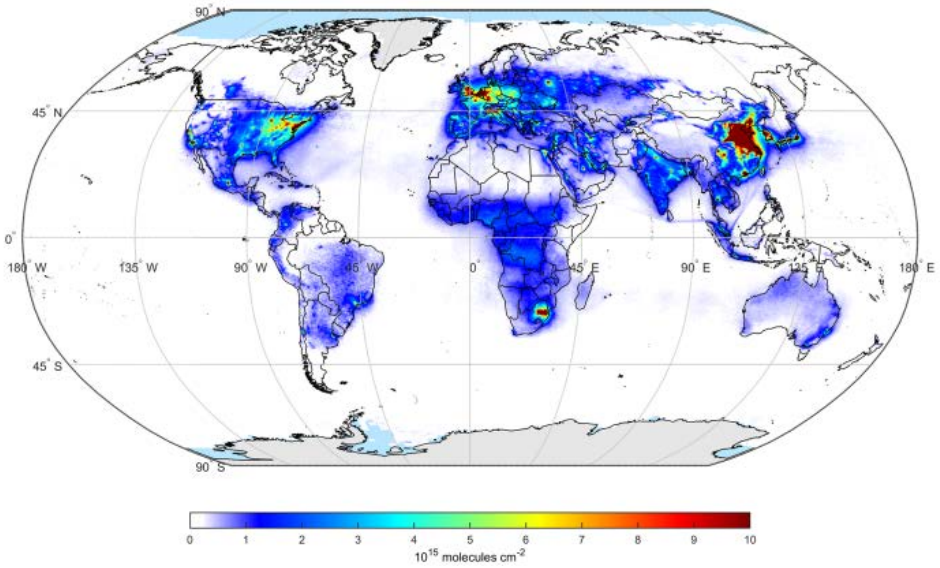

Figure 1-2 Map of global NO_2 VCDs from SCIAMACHY satellite data averaged from 2002-2012 adapted from Schneider et al. (2015).

Table 1-1 Global NO_x Emissions for the year 2000 (Jaeglé et al., 2005).

Source	Emissions (Tg N y^{-1})
Fossil Fuel Combustion	26 ± 1.4
Biomass Burning	6 ± 2
Soil emissions	9 ± 2

NO_x is primarily emitted as nitrogen oxide (NO) from fossil fuel combustion, but NO and NO_2 inter-convert rapidly during the day through reaction with O_3.

$$NO + O_3 \rightarrow NO_2 + O_2 \quad (1)$$

NO_2 can also react with O_3 to form the nitrate radical (NO_3), which photolyzes rapidly during the day but is an important oxidant in the nighttime troposphere.

$$NO_2 + O_3 \rightarrow NO_3 + O_2 \quad (2)$$

During the daytime troposphere, NO_2 is photolyzed to form NO and an $O(^3P)$ atom by ultra-violet (UV) radiation $\lambda<420$ nm.

$$NO_2 \xrightarrow{h\nu} NO + O(^3P) \quad (3)$$

Ozone is formed through the three-body reaction between the $O(^3P)$ atom and molecular oxygen.

$$O(^3P) + O_2(+M) \rightarrow O_3(+M) \quad (4)$$

The O_3 can then re-form NO_2 from NO via reaction (1).

When $O(^3P)$ is steady state, the mixing ratio of O_3 depends on the NO and NO_2 concentrations via the following equation:

$$[O_3] = (J[NO_2])/(k_1[NO]) \quad (5)$$

Where J_{NO2} and k_1 are the photolysis rate of NO_2 and the rate constant for reaction (1), respectively.

The Leighton ratio (ϕ) is produced by dividing both sides of equation (5) by $[O_3]$

$$\phi = \frac{J_{NO2}[NO_2]}{k_8[NO][O_3]} \quad (6)$$

If the Leighton ratio is unity, the ratio of NO_2 to NO is controlled by the concentration of O_3. The value of ϕ tends to be unity in regions with high NO_x levels but can deviate when loss processes for O_3 other than Eq. (1) become

significant. Deviations also occur at large solar zenith angles (SZAs) because the photolysis rate of NO_2 is smaller (Finlayson-Pitts and Pitts, 2000).

Reactions 1 and 3-4 in photochemical equilibrium represent net-zero production of O_3. However, in the presence of peroxy radicals, RO_2 and HO_2, and sufficient NO_x, net photochemical production of O_3 occurs because NO_2 is regenerated without the destruction of O_3 via Eq. (1).

$$NO + HO_2 \rightarrow NO_2 + HO \quad (7)$$

$$NO + RO_2 \rightarrow NO_2 + RO \quad (8)$$

Daytime removal of NO_x is primarily via formation of HNO_3 by the reaction of NO_2 with OH but can also form nitrous acid (HONO) through the heterogeneous reaction of NO_2 with water (H_2O) on surfaces.

$$NO_2 + OH + M \rightarrow HNO_3 + M \quad (9)$$

$$NO_2 + NO_2 + H_2O \rightarrow HNO_{3\,(aq.surface)} + HONO_{(g)} \quad (10)$$

$$HONO + h\nu \rightarrow NO + OH \quad (11)$$

The loss to HNO_3 is the major NO_x sink because the majority of HNO_3 is removed from the atmosphere through wet deposition (i.e., acid rain) and dry deposition while HONO may release NO through photolysis at slow rates. In the troposphere, the lifetime of NO_x is relatively short, on the order of a few hours near the surface and up to weeks in the free troposphere (Valin et al., 2013). NO_x lifetime is determined by multiple factors, including season (e.g., insolation, humidity) (Liu et al., 2016), initial concentration of the emissions (Nunnermacker et al., 2000), and the presence of other chemical species (e.g., VOCs) that oxidize NO_x or compete with NO_x oxidizing reactions (Seinfeld and Pandis, 2006). Therefore, NO_x lifetimes can significantly vary both spatially and temporally in the lower troposphere (Liu et al., 2016). This variability can increase the difficulty of accurately estimating emissions of NO_x using remote sensing measurements of NO_2 VCDs (e.g., from satellite) downwind of sources, especially from point sources that emit highly concentrated and localized plumes.

1.1.3 Sulphur Dioxide (SO_2)

Sulphur dioxide (SO_2) is a toxic substance regulated by the government of Canada (ECCC, 2009) and is a criteria air pollutant in the U.S.A. (US EPA, 2017). High concentrations of SO_2 can cause changes to pulmonary and respiratory function following exposure periods as small as 10 minutes (Health Canada, 2016; WHO, 2006). Studies in the literature suggest a causal relationship between short-term exposure to ambient levels of SO_2 and morbidity due to respiratory conditions in adults and children (Health Canada, 2016). SO_2 is emitted from anthropogenic activities, predominantly burning of fossil fuels with global anthropogenic emissions estimated to be 50-55 Tg S yr^{-1} (Lee et al., 2011). Natural sources also emit SO_2, with volcanoes being the largest source (Seinfeld and Pandis, 2006) and oceanic emissions of dimethyl sulfide (DMS), with subsequent conversion to SO_2 also being high. The global

distribution of SO_2 VCDs and the location of major anthropogenic and biogenic point sources are shown in Figure 1-3 Figure 1-4, respectively, obtained from Fioletov et al. (2011).

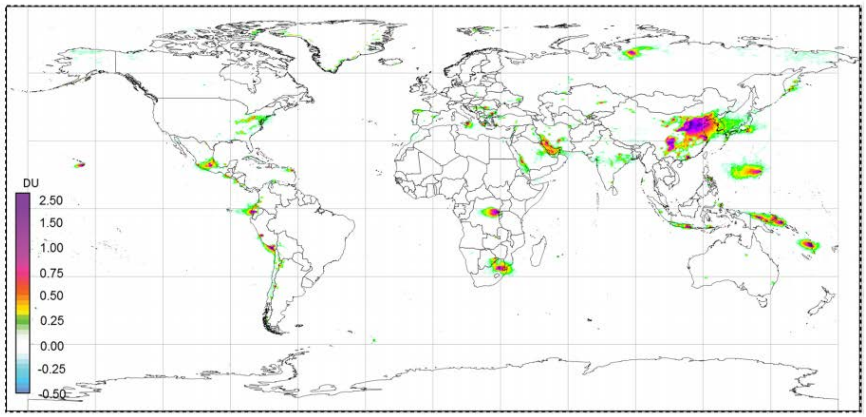

Figure 1-3 Map of the global distribution of SO_2 (in DU) measured by OMI averaged from 2005-2007 from Fioletov et al. (2011).

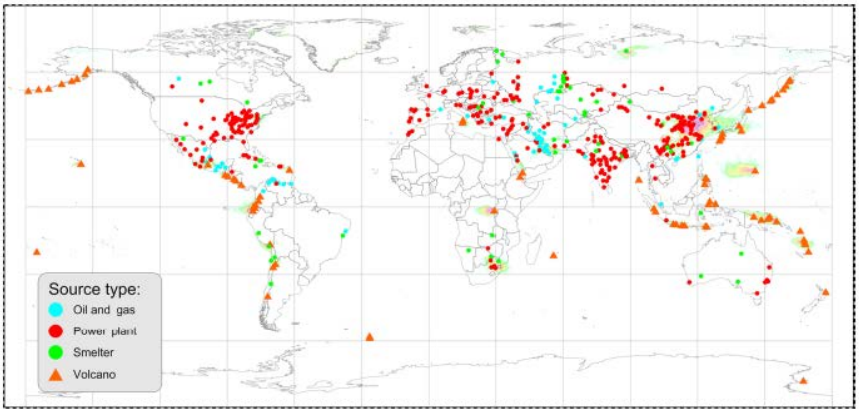

Figure 1-4 Locations of point sources of SO_2 emitting >30 kt SO2 yr^{-1} from 2005-2007 OMI satellite data Fioletov et al. (2011).

Atmospheric removal of SO_2 occurs through wet and dry deposition, and oxidation chemical reactions (Seinfeld and Pandis, 2006). In the troposphere, nearly all SO_2 is oxidized quickly to sulphate aerosol through gas and aqueous phase reactions. The OH radical dominates the oxidation route of SO_2 in the gas-phase, forming bisulphate ($HOSO_2$) (Holloway and Wayne, 2010). The lifetime of SO_2 with respect to reaction with OH is typically on the order of one week (Seinfeld and Pandis, 2006). Further oxidation of $HOSO_2$ forms sulfuric acid (H_2SO_4), which condenses onto pre-existing aerosols or can nucleate with water vapour (H_2O) and gaseous ammonia (NH_3) to form sulphate aerosol (Kulmala et al., 2004).

$$SO_2 + OH + M \rightarrow HOSO_2 + M \quad (12)$$

$$HOSO_2 + O_2 \rightarrow SO_3 + HO_2 \quad (13)$$

$$SO_3 + H_2O + M \rightarrow H_2SO_4 + M \quad (14)$$

SO_2 has high solubility in liquid water, leading to an equilibrium between gas-phase SO_2 and liquid phase SO_3^{2-}.

$$SO_{2(g)} + H_2O_{(l)} \leftrightarrow H_2SO_{3(l)} \quad (15)$$

$$H_2SO_{3(l)} \leftrightarrow HSO_{3(l)}^- + H_{(l)}^+ \quad (16)$$

$$HSO_{3(l)}^- \leftrightarrow SO_{3(l)}^{2-} + H_{(l)}^+ \quad (17)$$

Aqueous phase reactions form sulphate aerosol efficiently with H_2O_2 and O_3, further oxidizing $HSO_{3(l)}^-$ to $H_2SO_{4(l)}$ and $SO_{4(l)}^{2-}$ (Seinfeld and Pandis, 2006). Oxidation by transition metal ions and NO_2 in clouds can also contribute to the heterogeneous formation of sulphate aerosols (Shao et al., 2019).

Sulphate aerosols act as cloud condensation nuclei (CCN), impacting climate, precipitation and cloud formation (Stocker et al., 2013). Direct and indirect radiative forcing of sulphate aerosols is -0.26 to -0.82 Wm^{-2} and -0.3 to -1.8 Wm^{-2}, respectively (Ramaswamy et al., 2018). Sulphate aerosols reduce visibility (Cass, 1979) and are another key component of $PM_{2.5}$ in addition to nitrate aerosols (Wang et al., 2016). Wet deposition dominates the removal of sulphate aerosol and results in acid rain that can lead to freshwater and soil acidification (Psenner, 1994; Zhao et al., 2009).

1.1.4 The O_4 Collisional Dimer

The oxygen collisional complex $(O_2)_2$ is a useful species for deriving aerosol information from remote sensing measurements of the atmosphere due to its well-known atmospheric vertical profile and broad, unstructured absorption bands in the UV-Visible wavelength range (Greenblatt et al., 1990; Wagner et al., 2002, 2004). The vertical profile can be modelled as follows,

$$(O_2)_2(z) = k_{eq} * \left(0.21 * c_{air}(z)\right)^2 \quad (18)$$

Where z is altitude, c_{air} is the concentration of air, and k_{eq} is the equilibrium constant. k_{eq} is included in the literature cross-section of $(O_2)_2$ and, thus, does not need to be quantified to retrieve the optical densities. The vertical profile of $(O_2)_2$ depends on temperature and pressure but is relatively constant in time. This profile allows information on changes in radiative transfer due to aerosols along the measured light path to be derived from observations of changes in the $(O_2)_2$ absorption. Aerosol information can be retrieved from scattered sunlight measurements of the absorption of $(O_2)_2$ using radiative transfer simulations and inversion methods (Wagner et al., 2002). An advantage of this method over other aerosol remote sensing instruments (discussed in Section 2) is that absolute calibration is not required because the method analyzes the differential absorption (Wagner et al., 2004). $(O_2)_2$ will be hereon referred to as O_4.

1.2 Atmospheric Techniques for Measurement of Aerosols and Trace-gases

1.2.1 In-Situ Techniques

In-situ techniques at ground level provide highly localized measurements that are critical for applications such as health exposure studies. Advantages of in-situ instruments include typically high temporal resolution and low limits of detection. However, in-situ techniques may require a network of many instruments when the spatial distribution of a species is horizontally inhomogeneous and may deliver insufficient information on the total burden of pollution within the boundary layer. For example, these techniques under-sample elevated plumes that may mix down to the surface down-wind. The utility of in-situ techniques can be expanded to larger spatial scales using mobile platforms such as motor vehicles and aircraft, although the latter is costly.

1.2.1.1 Chemiluminescence

Chemiluminescence is a chemistry and phyics technique that is commonly utilized for in-situ monitoring deployed at, for example, long-term air quality monitoring stations. The spectroscopic chemiluminescence method was developed in response to the desire for highly sensitive measurements of pollutants such as O_3, NO_x, and compounds of sulphur (Skoog et al., 2007). The method determines NO by measuring the luminescence radiation from the de-excitation of NO_2^* to NO_2 using a photomultiplier tube (PMT), following the reaction of NO with an excess of O_3 produced by an electrogenerator within the instrument.

$$NO + O_3 \rightarrow NO_2^* + O_2 \quad (19)$$

$$NO_2^* \rightarrow NO_2 + h\nu \ (\lambda = 600 - 2800 \text{ nm}) \quad (20)$$

This method quantifies NO_x ($NO + NO_2$) by converting the NO_2 in the sample air to NO using a Molybdenum converter. Subtracting the NO measurement from the subsequent NO_x measurement gives an indirect determination of the NO_2. A disadvantage of this method is that non-NO_x reactive nitrogen oxides (NO_z) other than NO_2 present in the sample (e.g., HNO_3) can also be reduced to NO by the Molybdenum converter, leading to an overestimation of the mixing ratios of NO_x and NO_2. This overestimation can be important for field measurements in low NO_x regions. The chemiluminescence method can also be used to quantify concentrations of atmospheric O_3 and SO_2 (Skoog et al., 2007).

1.2.1.2 Pulse Fluorescence

Pulsed fluorescence is the most commonly used in-situ technique to measure SO_2 (Medina et al., 2011). This technique uses UV radiation in the 190-230 nm range to excite SO_2 and measures the resulting fluorescence between 240 and 420 nm. The UV radiation is pulsed from a light source such as a xenon flash lamp (Luke, 1997). Transmission or reflective bandpass filters allow only the signal from the fluorescence of the excited SO_2 molecules to reach the PMT. The light signal received by the PMT is converted to SO_2 concentration based on the direct proportionality of the signal to the SO_2 concentration. Detection limits of pulsed fluorescence analyzers can be as

low as 0.05 ppbv SO_2 over a 300 second averaging time (Medina et al., 2011). However, if the sample air contains small concentrations of SO_2 in a complex mixture of gases, accurate SO_2 measurement must address potential interferences from other species. Fluorescence of other species present in the sample, such as NO and aromatic hydrocarbon compounds, can positively bias the SO_2 measurements. Interference by NO can be accounted for by measuring the NO concentration and calculating the expected fluorescence. A semipermeable hydrocarbon "kicker" membrane can be installed to reduce the hydrocarbon interferences (Luke, 1997). Oxygen and water can quench the fluorescence of the excited SO_2, leading to a negative bias (Medina et al., 2011). Water can be removed from the sample using a dryer, and oxygen quenching can be reduced by diluting the sample and calibrating the SO_2 analyzer with a synthetic SO_2 standard (Mohn and Emmenegger, 2014).

1.2.2 Selected Spectroscopic Remote Sensing Techniques

Spectroscopic remote sensing techniques allow quantification of atmospheric species on a variety of spatial scales (vertically or horizontally) without requiring a mobile platform. These techniques typically do not affect the species they observe, which is important for highly reactive trace gases, and allow observations of locations difficult to measure with in-situ techniques alone.

1.2.2.1 Sun Photometers for Aerosol Studies

Sun photometers have been used since the 1950s to quantify aerosols (Volz, 1959). These instruments view the entire atmosphere by measuring direct solar radiance at multiple wavelengths (Twitty, 1975). Observations from ground-based sun photometers can directly yield very precise values of aerosol optical depth (AOD), a measure of the total aerosol extinction along the light path. The AOD at each wavelength is determined based on the use of the Beer-Lambert-Bouguer law (AERONET, 2002).

$$V = V_o(r/r_o)^2 e^{-m[AOD + a_R(p/p_o)]} \quad (21)$$

Where V is the voltage measured by the instrument, V_o is the calibration constant of the instrument, r/r_o is Earth-sun distance, m is the relative air mass estimated from the solar elevation angle, a_R is the estimated optical depth due to Rayleigh scattering, and p/p_o is the ratio of the ambient atmospheric pressure to standard atmospheric pressure. Other aerosol characteristics can be derived from sun photometer measurements using Mie scattering theory and inversion retrieval methods, including aerosol refractive index, size distribution, and single scattering albedo (Devaux et al., 1998; King et al., 1978; Li et al., 2006; Romanov et al., 1999; Shaw, 1979; Twitty, 1975). The aerosol robotic network (AERONET) of sun photometers currently provides aerosol information at over 500 stations worldwide (Holben et al., 1998). A disadvantage of the sun photometer is that only properties from the total atmospheric column can be derived. Sun photometers are, therefore, often not ideal for monitoring aerosol levels in the lower troposphere.

1.2.2.2 Lidar

Lidar (light detection and ranging) instruments measure the intensity of backscattered light emitted from a pulsed laser to quantify vertical profiles of aerosol extinction. These instruments typically operate in a zenith pointing mode, emitting a pulsed laser beam into the atmosphere and measuring the return signal from elastic backscattering (Rayleigh and aerosol scattering) using a telescope and detector system (Figure 1-5). The power of the return signal as a function of time provides range-dependent information that can be combined to determine vertical profiles of the backscatter coefficient. These profiles can yield the vertical profile of aerosols using Mie backscatter lidar as well as O_3 and water vapour using the differential absorption lidar (DIAL) and Raman lidar techniques, respectively (Strawbridge et al., 2018).

The aerosol volume extinction coefficient is often determined from the measurements by assuming a linear relationship between the backscatter and extinction coefficients based on the S-ratio. The S-ratio is the ratio of the volume extinction coefficient to the backscatter coefficient and dictates the signal strength of the return laser radiation (Strawbridge, 2013). Extinction profiles are often retrieved using a fixed S-ratio value chosen based on the type of particles expected in the studied environment (Irie et al., 2015). A fixed S-ratio adds a source of uncertainty in lidar measurements of aerosol extinction since lidar S-ratios are variable, depending on relative humidity and the shape, size distribution and chemical composition of the aerosol particles (Weitkamp, 2005). Another limitation of the zenith-pointing lidar technique is that detection close to the surface is not possible due to challenges with signal overlap (Zieger et al., 2011). Lidar can also only be operated at a limited number of wavelengths and can have additional uncertainties due to calibration issues (Klett, 1981). Advantages of lidar over sun photometer instruments for aerosol retrievals include the ability to operate at night and resolve the vertical profile of aerosol extinction with high temporal and spatial resolution.

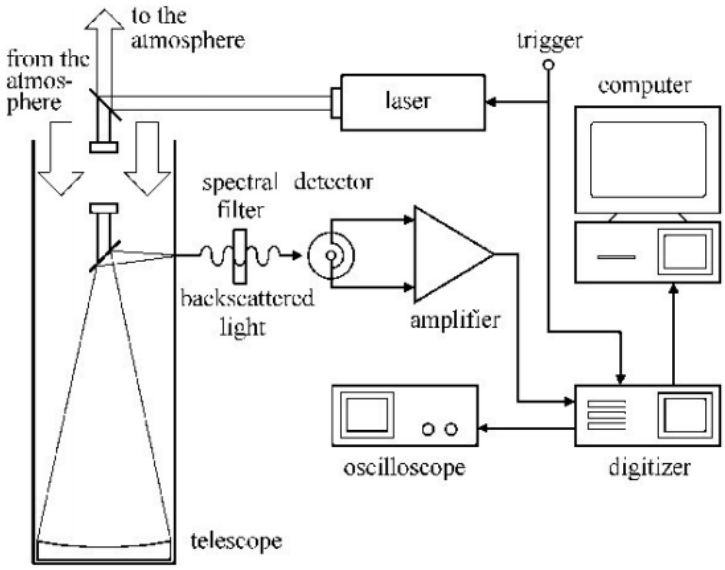

Figure 1-5 Schematic of a lidar system. Adapted from Castrejon-Garcia et al. (2002).

1.2.2.3 Satellite Remote Sensing

Satellites are increasingly being used as a platform for monitoring air quality of not only regional areas but also localized sources. Measurements of air quality from space have advanced since the 1990s to include SO_2, NO_2, O_3, methane (CH_4), formaldehyde (HCHO), carbon monoxide (CO), AOD, and others (McLinden et al., 2014). The combination of modelling and satellite data allows retrieval of surface concentrations of trace gases and particles (Lamsal et al., 2014; Lin et al., 2015) and emission rates of species such as NO_x and SO_2 (Beirle et al., 2011, 2014; Fioletov et al., 2011; Streets et al., 2013). Current air quality monitoring instruments include OMI (Ozone Monitoring Instrument, 2004-present) on the AURA satellite and GOME-2 (Global Ozone Monitoring Experiment-2, 2006-present, 2012-present) on the ERS-2 satellite (McLinden et al., 2014). A new satellite, Sentinel-5P, was launched in 2017 with the aim of measuring air quality with a resolution as fine as 7 km x 3.5 km, up to six times greater spatial resolution than previously available (European Space Agency, 2019; McKinnon, 2017). Sentinel-5P will measure species including O_3, SO_2, and NO_2, HCHO, and CH_4 as well as aerosols and clouds (European Space Agency, 2019). Satellite retrievals are useful for estimating "top-down" emissions on regional and global scales over long periods of time (Huang et al., 2014; Kim et al., 2014; Liu et al., 2016; McLinden et al., 2012). However, disadvantages include that accuracy over small regions can be limited by insufficient pixel resolution due to horizontal averaging and retrieval reliance on modelled a-priori vertical profiles that may not resolve small regions (Heckel et al., 2011). Satellite measurements are also typically limited to up to a few overpasses per day, providing no information on diurnal trends.

1.2.2.4 DOAS Technique, Molecular Absorption Spectra, and DOAS Instruments

The Differential Optical Absorption Spectroscopy (DOAS) technique quantifies trace-gases by analyzing the spectral signal of light after attenuation from passing through a gaseous medium with unique spectral absorption structures (Figure 1-6). DOAS has been used since its introduction by Brewer et al. (1973), Noxon (1975), Perner et al. (1976), and Platt et al. (1979) to measure atmospheric species with narrow-band structures of absorption in the visible and near UV wavelength region. These species include NO_2, SO_2, OH, bromine monoxide (BrO), NO_3, ammonia (NH_3), chlorine monoxide (ClO), and others.

Molecular Absorption Spectra

Molecular absorption spectra originate from transitions of a molecule between quantum states due to the absorption of a photon. Absorption of a photon with energy in the sub-mm to microwave, infrared, and UV-visible wavelength range results in transitions between rotational, vibrational and electronic levels, respectively. Rotational transitions are related to the rotation (angular momentum) of the entire molecule (Schmidt, 2005). Vibrational transitions are related to the vibration of atoms relative to each other within the molecule (Platt and Stutz, 2008). Electronic transitions lead to electronic excitation, reconfiguration of the electrons in the outer shell of atoms or molecules. These transitions correspond to wavelengths for transitions between an electronically excited state and ground state and depend on electrons in the outer shell of atoms or molecules (the valence electrons).

While atoms exhibit only electronic transitions, molecules exhibit rotational and vibration excitation schemes simultaneous with electronic transitions (Platt and Stutz, 2008). Simultaneous transitions occur because, for each electronic energy level, molecules can exist in several distinct configurations of the electronic shell and each configuration has its own set of vibrational and rotational levels (Platt and Stutz, 2008). Consequently, molecular electronic spectra in the UV-vis spectra are made up of a set of electronic-vibrational (vibronic) "bands" with fine rotational structure "lines." These rotational lines are extremely narrow and only apparent in spectroscopic measurements with very high spectral resolutions (Khristenko et al., 1998). At lower resolutions, the rotational lines appear as quasi-continuous absorption within a vibrational band. The variability in the strengths of vibrational bands within an electronic spectrum is explained by the Franck-Condon principle. This principle states that since the speed of electronic transition is faster than the time need for one vibration, the most likely vibrational state of the excited state is the one that has the same inter-nuclei distance as the ground state and the highest greatest overlap of the two vibrational wave functions. Transitions to lower or higher vibrational states are of lower probability and, therefore, lead to a weaker absorption cross-section (Platt and Stutz, 2008).

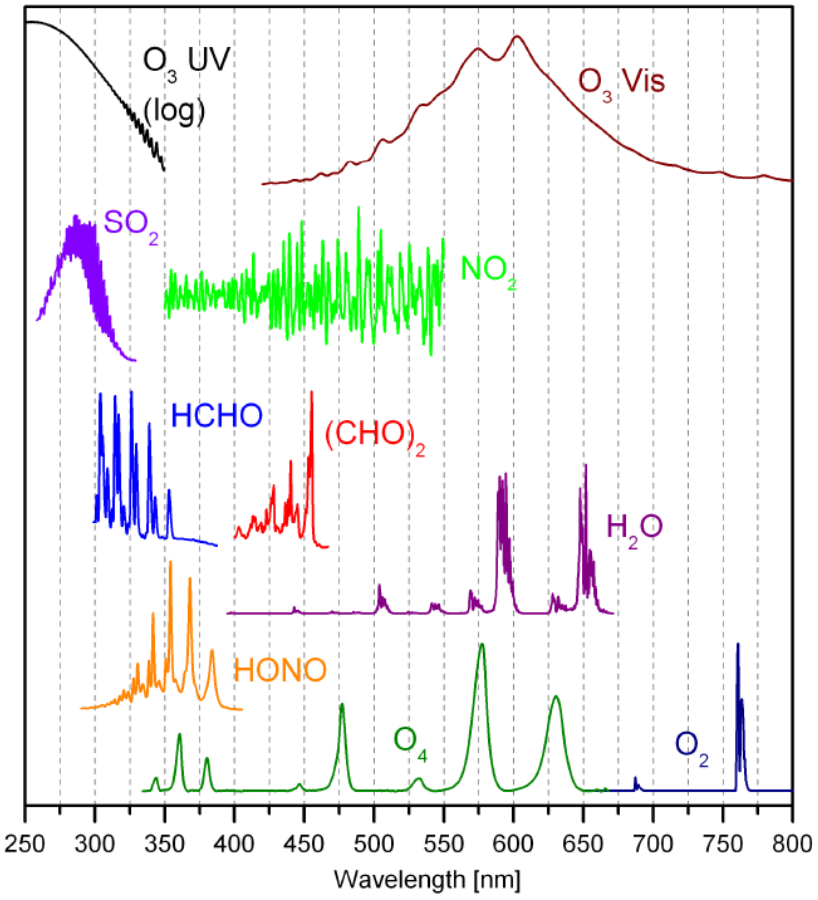

Figure 1-6 Absorption cross-sections of trace-gases in the atmosphere in the 250-800 nm range adapted from Yilmaz (2012).

The absorption spectrum of a molecule depends on multiple factors. These factors include the configuration of the valence electrons and the structure of the molecule (e.g., the molecular symmetry and types of chemical bonds). For example, the presence of hydrogen bonding in a molecule inhibits vibrations and rotations, impacting the molecule's vibrational and rotational spectrum. Rotational transitions depend on the rotational degrees of freedom around the molecule's centre mass. For example, large polyatomic molecules will have more rotational energy states than diatomic molecules (Schmidt, 2005). Absorption spectra can also exhibit changes due to temperature and pressure variation (Orphal and Chance, 2003).

The origins of the absorption structures in the UV-visible spectra of the three molecules focused on in this thesis, SO_2, NO_2, and O_4, are shown in Figure 1-6 and will be briefly discussed. The NO_2 UV-vis spectral features used in DOAS applications are due to electronic transitions within the NO_2 molecule with an $A^2B_1 \leftarrow X^2A_1$ band system between ~330 and ~500 nm with a maximum at ~400 nm. States before and after transition are designated using the notation $[State]^{2S+1}[AM]_{\Lambda+\Sigma}$ where [State] is the electronic state of the molecule (X is the ground state), S is the electronic spin, [AM] is angular momentum, and $\Lambda+\Sigma$ indicates the projection of the total angular momentum of the electrons on the nuclei-molecule axis. The SO_2 absorption spectrum exhibits three band systems with narrow vibrational bands. The medium strength "B" band system from 340 to 390 nm used in UV-Vis applications is due to the $A^1B_1 \leftarrow X^1A_1$ transition. The absorption structures in the O_4 absorption spectrum between 300 and 700 nm are due to the simultaneous electronic transition of the two O_2 molecules from the ground state, which contain rotational-vibrational bands, and electronically excited states of both O_2 molecules (Platt and Stutz, 2008). For more detailed information on molecular absorption spectra, see Chapter 3 and Appendix B in Platt and Stutz (2008).

The DOAS Technique

The DOAS technique modifies the Beer-Lambert-Bouguer law, which describes the attenuation of light with wavelength λ emitted by a radiation source $I_o(\lambda)$ as it passes through the atmosphere along the path length L by an absorber with an absorption cross-section $\sigma(\lambda)$ and number concentration c (Honninger et al., 2004a).

$$I(\lambda, L) = I_o(\lambda) e^{-\sigma(\lambda) c L} \quad (22)$$

Since multiple trace gases (i) are present simultaneously in the atmosphere and their cross-sections are temperature (T) and pressure (p) dependent,

$$I(\lambda, L) = I_o(\lambda) e^{\int [\sum_{i=i}^{n} -\sigma_i(\lambda, T, p) c_i(s)] dl} \quad (23)$$

Determination of trace gas concentration using Eq. (23) would require quantification of all factors affecting the light intensity, including the effect of scattering of light (Mie and Rayleigh), turbulence, variation in the light source, and changes in spectral sensitivity of the detector (Platt and Stutz, 2008). Expanding upon Eq. (25) to include Mie and Rayleigh scattering,

$$I(\lambda, L) = I_o(\lambda) e^{-\int [\sum_{i=i}^{n} \sigma_i(\lambda, T, p) c_i(l) + \epsilon_R(\lambda, l) + \epsilon_M(\lambda, l)] dl} \quad (24)$$

The DOAS technique eliminates the problem of having to quantify all these factors (above) by separating the broadband absorption structures ($\sigma^{B}(\lambda)$) from the differential structures ($\sigma'(\lambda)$).

$$\sigma_i(\lambda) = \sigma_i'(\lambda) + \sigma_i^{B}(\lambda) \tag{25}$$

Differential structures vary rapidly with wavelength while the broadband features vary relatively slowly (Figure 1-7). The spectral structures unique to each trace-gas are differential while the unknown factors that influence light intensity are broadband in structure and can be modelled using a polynomial function (see below) (Honninger et al., 2004a).

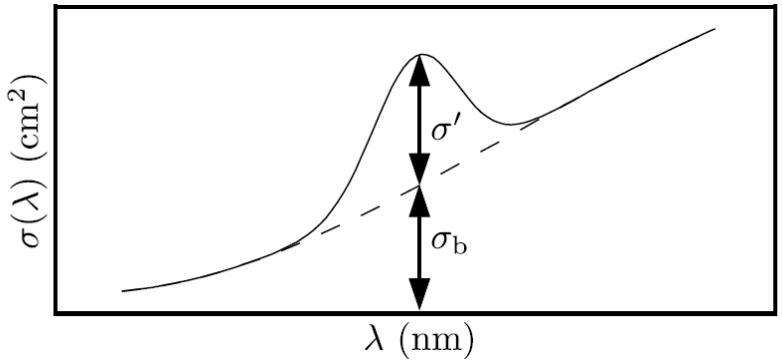

Figure 1-7 The differential **σ'** and broadband $\boldsymbol{\sigma}_b$ components of absorption **σ** adapted from Platt et al. (2008).

The absorption cross-sections are separated into their differential $\sigma_i'(\lambda)$ and broadband $\sigma_i^{B}(\lambda)$ components.

$$I(\lambda, L) = I_o(\lambda) e^{-\int [\sum_{i=i}^{n} [\sigma'_i(\lambda,T,p) + \sigma_{B,i}(\lambda,T,p)] c_i(l) + \epsilon_R(\lambda,l) + \epsilon_M(\lambda,l)] dl} \tag{26}$$

Separating the differential and broadband components leads to Eq. (27)

$$I(\lambda, L) = I'_o(\lambda) e^{-\int [\sum_{i=i}^{n} \sigma'_i(\lambda,T,p) c_i(l)] dl} \tag{27}$$

$I'_o(\lambda)$ contains all the broadband structures, including $I_o(\lambda)$, the Mie and Rayleigh extinction and broadband absorption.

The differential optical density, $\tau'(\lambda, L)$ can then be defined as,

$$\tau'(\lambda, L) = \ln \frac{I'_o(\lambda)}{I(\lambda, L)} \tag{29}$$

DOAS measurements of $\tau'(\lambda, L)$ yield the Slant Column Density (SCD), which is a trace gas number concentration integrated over the slant light path through the atmosphere.

$$SCD = \int_0^L c(l) dl \tag{30}$$

$$SCD = \frac{\tau'(\lambda, \mathrm{L})}{\sigma'(\lambda, \mathrm{T}, \mathrm{p})} \tag{31}$$

This method has the advantages of inherent calibration of the measurements and the potential for simultaneous quantification of multiple trace-gases with absorption structures in the same spectral region (Platt and Stutz, 2008).

DOAS systems consist of a broadband source of light, and a telescope, spectrograph and detector set-up to receive and record absorption spectra (Figure 1-8). High resolution cross-sections of the absorbing trace gases are obtained from literature and convoluted with the instrument's slit function, which is typically determined from measurements of the emission lines of a mercury lamp. DOAS instruments are divided into two categories: Active DOAS techniques that use artificial light sources and passive DOAS techniques that measure direct or scattered natural light.

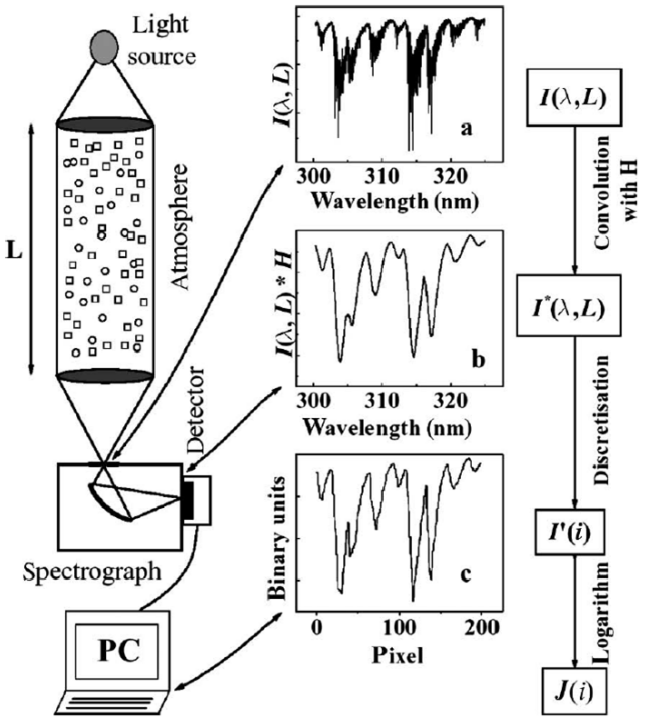

Figure 1-8 Schematic of basic DOAS instrument. Light passing through the atmosphere is attenuated by absorption and reaches the detector. The absorption spectrum is convoluted (degraded resolution) by the instrumental slit function and converted to discrete pixels to be stored in the computer for numerical analysis. Adapted from Stutz and Platt (1996).

1.2.2.4.1 Active-DOAS

Long-path (LP-DOAS) is a commonly used active DOAS method that uses an artificial light source, typically Xe-Arc Lamps or LEDs, and a retroreflector array to produce a light path length of several hundreds of meters to kilometres (Figure 1-9). Modern LP-DOAS instruments use fibre bundles to couple light from the light source into the telescope and receive light into the spectrograph (Merten, 2008). The measured spectrum is generally evaluated

against a “lamp” measurement obtained by positioning a reference plate in front of the fibre bundle, sending the light directly into the spectrograph without passing through the path length in the atmosphere. The use of an artificial light source allows measurements in a wide spectral region during both the day and night. An advantage of active compared to passive DOAS methods is that the known light path length allows trace-gas concentrations to be derived directly from the fitted SCD without the need for radiative transfer modelling (see passive section below). Limitations of LP-DOAS include that a lack of instrument portability and only spatially averaged measurements since the method requires long light paths.

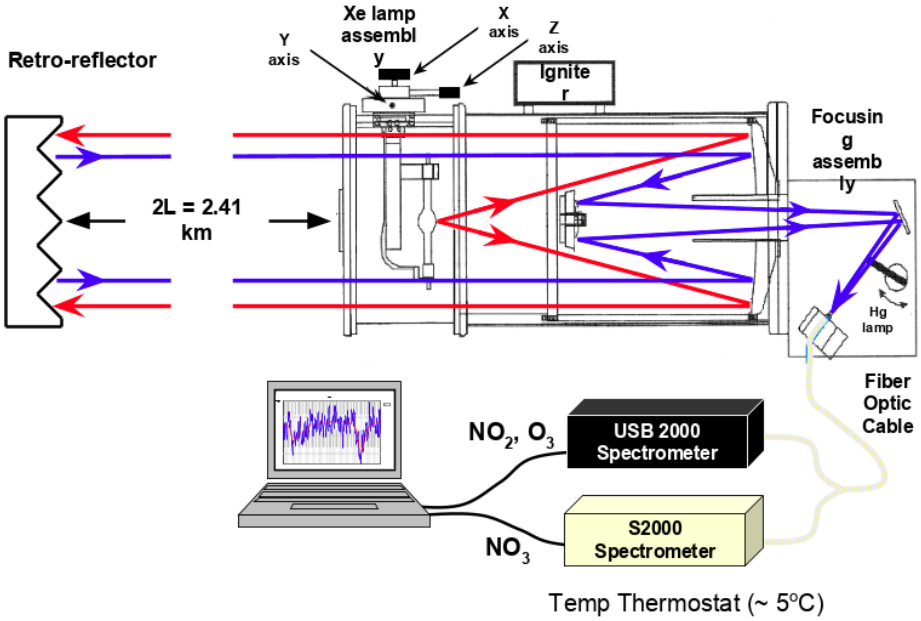

Figure 1-9 Schematic of LP-DOAS system, including light source, fibre bundle, telescope, retro-reflector array, and a spectrometer.

A relatively new active-DOAS technique, cavity-enhanced DOAS (CE-DOAS) allows in-situ measurements by propagating light inside an optical resonator to achieve long absorption light paths (Figure 1-10) (Langridge et al., 2006; Platt et al., 2009). CE-DOAS instruments typically use two or three highly reflective mirrors and LED light sources with an open or closed path resonator set-up (Ball et al., 2004). Since only a small portion of the light is transmitted upon each reflection, the photons travel a long distance within the cavity before reaching the detector (Horbanski et al., 2019), achieving path lengths of 10’s of kilometres. This technique has the advantage of high sensitivity from a compact optical system of 10 cm to a few metres in length, compared to the much longer path lengths of other DOAS methods. Disadvantages include that traditional CE-DOAS instruments are heavy, sensitive to fluctuations in the absolute light intensity, and require high technical maintenance. These characteristics limit the unattended, long-term operation of CE-DOAS instruments, especially outside of the laboratory or large platforms. The newly developed iterative method (ICAD) for CE-DOAS reduces the sensitivity to fluctuations in the light intensity and results in a compact and lightweight instrument appropriate for stationary and ground-based studies

(Horbanski et al., 2019). These instruments, therefore, combine all the advantages of the DOAS technique with an in-situ measurement system.

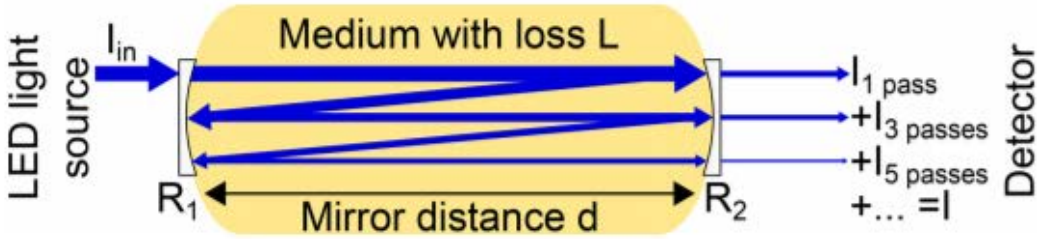

Figure 1-10 Principle of cavity-enhanced absorption spectroscopy from Horbanski et al. (2019).

1.2.2.4.2 Passive DOAS

1.2.2.4.2.1 Lunar DOAS

Lunar DOAS uses moonlight to determine VCDs of important nighttime species such as NO_3. There are relatively few publications on lunar DOAS compared to other DOAS techniques (Chen et al., 2011; Otten et al., 1998; Smith and Solomon, 1990; Wagner et al., 2000; Weaver et al., 1996). The measured slant column densities (SCDs) are converted to VCDs using a geometric approximation, radiative transfer modelling or simultaneous measurements from LP-DOAS (Chen et al., 2011; Nikelski, 2016). The lunar DOAS method is the only passive DOAS method that can quantify nighttime chemical species. However, the most sensitive lunar DOAS measurements require strong moonlight (full moon) in addition to cloud-free conditions, limiting the technique to a maximum of a few days a month.

1.2.2.4.2.2 Pandora spectral sun photometer

Pandora spectral sun photometers quantify column amounts of gases using measurements of sunlight in the UV-visible spectrum and the DOAS technique (Herman et al., 2009). Pandora instruments have been used to measure total columns of O_3, NO_2, and SO_2 in the atmosphere with high temporal resolution (Fioletov et al., 2016a; Herman et al., 2009; Tzortziou et al., 2012). Pandora measurements can be conducted in direct sun (sun tracking), zenith sky, or multi-axis modes (Fioletov et al., 2016a). The direct-sun mode has the advantages over other passive DOAS techniques of not requiring radiative transfer modelling, accommodation for the Ring effect, assumptions about horizontal inhomogeneity, or prior knowledge of the trace-gas vertical profile to determine the VCD (Herman et al., 2009). Limitations include that the technique does not provide information on the vertical profile of the trace-gas and derivation of tropospheric columns (e.g., of NO_2) can require modelling of the stratospheric column (McLinden, 2000).

1.2.2.4.2.3 MAX-DOAS

MAX-DOAS instruments quantify atmospheric species by measuring scattered sunlight at multiple viewing elevation angles, α, above the horizon. Spectra measured at elevation angles close to horizon-pointing have high sensitivity to ground-level gases since the light paths are longer near the surface and are, therefore, well suited to probing the troposphere (Honninger et al., 2004a). An idealized schematic of the viewing geometry of a MAX-DOAS measurement assuming only one scattering event for each photon along the total light path is shown in Figure 1-11. The MAX-DOAS spectral measurements are fitted against a Fraunhofer reference spectrum (FRS), a Ring spectrum, differential cross-sections of trace gases absorbing in the fitting window, and a low order polynomial that models the broadband features (Wagner et al., 2010). See Appendix B for details of the MAX-DOAS fitting algorithm. The FRS is typically measured in a zenith-pointing direction and is essential because evaluation of the relatively weak absorption structures of trace gases require removal of the strong absorption lines in the solar spectrum, Fraunhofer lines. The Fraunhofer lines are due to absorbtion by gases (e.g., calcium) in the photosphere, the outer region of the Sun. A FRS measured by the instrument is used for fitting, as opposed to using a calculated solar spectrum, because the measured FRS will exhibit the same instrument effects as the measured spectrum (e.g., does not require convolution to match the instrument's lower spectral resolution). Also, if the measurement spectrum to be fit and the FRS are collected close in time, the stratospheric component in the two spectra can be assumed to be same so that the fit yields a tropospheric columm measurement (Platt and Stutz, 2008). See equations 34 and 35, below for further explanation. The inclusion of the Ring spectrum accounts for the Ring effect, the "filling-in" of the optical densities of the Fraunhofer lines. The Ring effect is due to air molecules causing ineleastic Raman scattering of the photons, changing the scattered photon's wavelength (Brinkmann 1968). Measured intensity is reduced in the wavelength regions of the Frauhofer regions compared to adjacent regions such that the probability of photos scattering inelastacially into the lines is greater than out of the lines. The Ring spectrum must be included in the fit because the optical densities of the Ring effect can be up to two magnitudes greater than the trace gas optical densities. The Ring effect increases with increasing length of light paths and with greater solar zenith angles (Institute of Environmental Physics, Heidelberg University, 2009). A numerical approach (used in this work) to determine the Ring spectrum is to apply a modelled cross-section of inelastic Raman scattering based on the known rotational states of the two major atmospheric constituents, nitrogen (N_2) and oxygen (O_2) to the FRS (Chance and Spurr, 1997). This approach yields a Ring spectrum with the same spectral characteristics of the instrument that measured the FRS (Platt and Stutz, 2008).

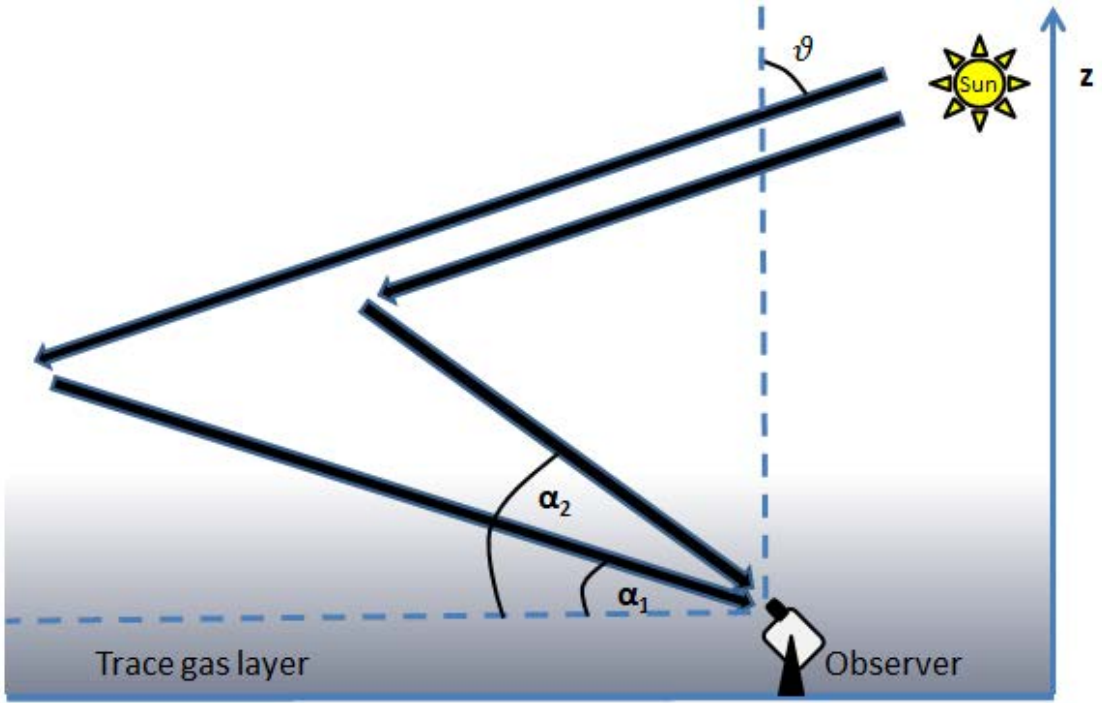

Figure 1-11 Geometries of observation of scattered sunlight by MAX-DOAS. Photons enter the atmosphere at solar zenith angle ϑ and are scattered into the telescope viewing directions with observation elevation angles α, passing through a layer of trace gas near the surface. Adapted from Honninger et al. (2004).

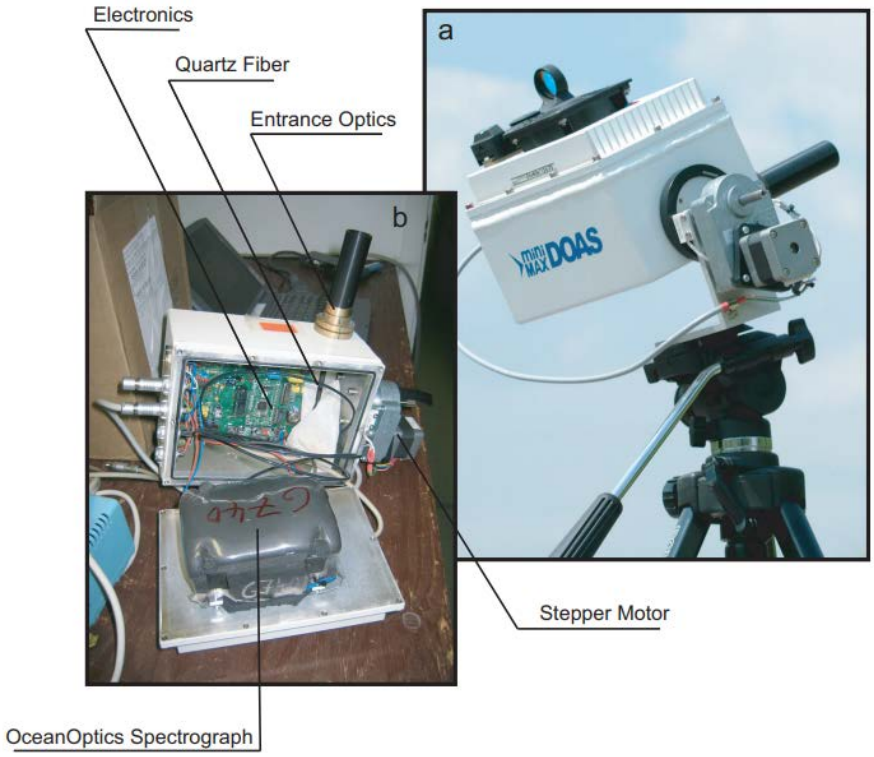

Figure 1-12 Photos of mini-MAX-DOAS instruments during measurements (a), and major components (b) adapted from Bobrowski and Filsinger (2005).

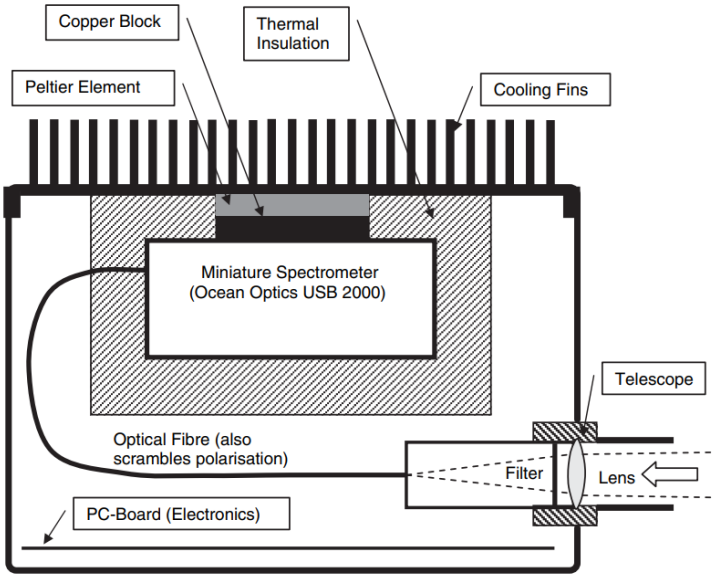

Figure 1-13 Cross-section schematic of a mini-MAX-DOAS system (excludes stepper motor). Adapted from Bobrowski (2005).

Since the FRS also contains absorptions by trace gases in the atmosphere, the MAX-DOAS analysis yields a differential SCD (DSCD), the difference between SCD of the measurement (SCD_{meas}) and the SCD of the FRS (SCD_{ref}).

$$DSCD_{meas}(\alpha) = SCD_{meas}(\alpha) - SCD_{ref}(\alpha) \tag{32}$$

Note that the SCD from solar measurements is the sum of the contributions of the tropospheric and stratospheric SCDs.

$$SCD_{meas} = SCD_{trop} + SCD_{strat} \tag{33}$$

Measured spectra may be fit against a single FRS obtained near solar noon that contains a minimum absorption of the trace gases. This method results in DSCDs with a distinct diurnal signal of stratospheric absorption and a constant offset from the FRS (Sinreich et al., 2005). Spectra fit can alternatively be fit against a FRS that is a zenith-pointing measurement obtained in the same series of angles (i.e., close in time; <20 minutes). In this case, the SCD_{strat} can be assumed to be equal in both spectra for trace-gases where the stratospheric component is similar or less than the tropospheric component (with the exception of O_3) because changes in the SZA are small (Wagner et al., 2010). The resulting DSCD yields the tropospheric DSCD that contain only tropospheric absorption. The assumption about the stratospheric components is valid for measurements except those obtained near sunrise and sunset when the SZA changes rapidly.

$$DSCD_{meas}(\alpha) = SCD_{trop}(\alpha) + SCD_{strat}(\alpha) - SCD_{trop}(90^o) + SCD_{strat}(90^o) \tag{34}$$

$$DSCD_{meas}(\alpha) = SCD_{trop}(\alpha) - SCD_{trop}(90^o) = DSCD_{trop}(\alpha) \quad (35)$$

The MAX-DOAS light path and resulting SCD depends on several factors: clouds, ground albedo, pressure, temperature, wavelength, aerosols, trace gas concentrations, viewing geometry and solar geometry (Honninger et al., 2004a). Therefore, SCDs are typically converted to a more useful value, the vertical column density (VCD). The VCD is the trace gas concentration integrated along the entire vertical path through the atmosphere and is, in principle, independent of the viewing geometry and the meteorological conditions (e.g., boundary layer height). VCDs are well suited to the measurement of total emissions into an air mass and validation of satellite VCDs. The VCD is determined from SCDs using an air mass factor AMF, which is the ratio of the SCD and VCD.

$$VCD = \frac{SCD}{AMF} \quad (36)$$

The AMF depends on the radiative transfer in the atmosphere and is influenced by the same parameters that influence the SCD. The determination of AMFs and VCDs from MAX-DOAS measurements is complicated by the lack of knowledge of the path length (Platt and Stutz, 2008). Unlike passive DOAS that has a well-defined light path, the MAX-DOAS measured intensity is the sum of the intensities of the different light beams. The "light path" is the most probable path determined by the average of a large number of registered photons (Sinreich et al., 2005).

The geometric approximation is the simplest method to estimate the VCDs from the SCD and assumes a single scattering event (Honninger and Platt, 2002).

$$AMF_{trop} \approx \frac{1}{sin(\alpha)} \; and \; AMF_{strat} \approx \frac{1}{cos(\vartheta)} \quad (37)$$

When the measured spectrum is fit against the FRS from the angle sequence, combining Eqs. (35) to (37) leads to Eq. (38), the tropospheric geometric approximation (Wagner et al., 2010).

$$VCD_{trop} \approx \frac{DSCD_{trop}(\alpha)}{\frac{1}{sin(\alpha)} - 1} \quad (38)$$

However, this approximation is only accurate for elevation angles >10° under conditions of low to moderate aerosol loading (Wagner et al., 2010). Geometric VCDs have been shown to deviate by up to ±20% from the more accurate VCDs from radiative transfer modelling (Shaiganfar et al., 2011). Under high aerosol conditions, multiple scattering events can occur, and the geometric approximation becomes invalid. The dependency of the AMF on elevation angle at lower elevation angles is weak under high aerosol loading because the aerosols decrease the mean free path of photons and the height of the last scattering event of the photon. The path lengths in the lowest atmospheric layers become shorter, and a more vertical path in the higher layers is more likely. Other factors that influence the AMF include ground albedo and non-uniform trace gas distributions. More accurate AMFs that account for all of these factors can be determined using radiative transfer modelling (RTM) (Honninger et al., 2004a).

Ground-based MAX-DOAS can retrieve vertical profiles of aerosol extinction and trace-gases by combining MAX-DOAS data with radiative transfer modelling (Frieß et al., 2006; Heckel et al., 2005; Honninger et al., 2004; Honninger and Platt, 2002; Irie et al., 2008; Wagner et al., 2004, 2011). The MAX-DOAS measures at a series of angles ranging from near-horizon pointing to zenith (e.g., α=2°, 4°, 8°, 15°, 30°, and 90°) to determine information on the vertical profile of trace gases and aerosol extinction through measurements of O_4 (Frieß et al., 2019). The MAX-DOAS technique has been used to retrieve vertical profiles of NO_2 (Tan et al., 2018; Wagner et al., 2011), SO_2 (Tan et al., 2018), BrO (Frieß et al., 2011; Honninger and Platt, 2002), HCHO (Heckel et al., 2005; Wagner et al., 2011), and aerosol extinction (Clemer et al., 2010; Frieß et al., 2011; Irie et al., 2008, 2015; Li et al., 2010; Zieger et al., 2011). Aerosol extinction profiles retrieved from MAX-DOAS measurements of O_4 are sensitive to the lower troposphere, especially close to the ground, and do not require absolute calibration of the instrument. Additional information on retrievals of vertical profiles from MAX-DOAS measurements is described in Appendix A. Advantages of this MAX-DOAS method includes the ability to simultaneously derive tropospheric vertical profiles and total column measurements of aerosol extinction and trace-gases without the need for knowledge of additional parameters (e.g., the lidar S-ratio). A limitation of MAX-DOAS methods include that measurements require daytime, cloud-free conditions.

A recently developed Mobile-MAX-DOAS technique allows determination of trace-gas by driving the instrument around the region of interest. This method can estimate emissions with a high spatial resolution (~1 km) on a nearly hourly basis. Emissions are estimated from tropospheric VCDs determined from MAX-DAOS measurements at higher elevation angles (>15°). Only higher angles are used so that the geometric approximation for estimating tropospheric VCDs from DSCDs in Eq. (36) is valid. The DSCDs are determined by fitting the measured spectra against a single FRS since the trace gas field observed by the non-zenith and zenith spectra in the same series can be significantly different due to the movement of the vehicle. However, these DSCDs contain contributions of the SCD due to the difference in SZA between the measurement and the FRS (SCD_{SZA}), and the tropospheric SCD observed by the FRS (SCD_{trop}). The tropospheric VCD can be derived by estimating these SCD contributions using the offset method (Wagner et al., 2010). More details on this method are detailed in Chapter 5. Mobile-MAX-DOAS has been used to estimate NO_x emissions from power-plants (Wu et al., 2017a) and cities (Ibrahim et al., 2010; Shaiganfar et al., 2011, 2017), validate satellite and air quality modelled VCDs (Dragomir et al., 2015; Shaiganfar et al., 2015), estimate surface NO_2 mixing ratios from NO_2 VCDs (Shaiganfar et al., 2011), and determine the horizontal variability of trace-gas VCDs within satellite pixels (Wagner et al., 2010). Mobile-MAX-DOAS is a low-cost, "top-down" approach for quantifying real-world emissions that can be used to validate "bottom-up" emission inventories (Shaiganfar et al., 2011). The method is ideal in regions where the small horizontal spatial scale of emission sources limits the use of other techniques (e.g., satellite).

1.3 Dissertation's Contribution to the Field of Monitoring Atmospheric Species

The ideal measurement technique to effectively address an air quality problem depends on the chemical and physical properties of the species and its environment. Practical constraints include instrumental cost and ease of operation. Addressing a problem involves a series of decisions, including what methodology to use and how to interpret the

data, meaning that while science aims for objectivity, it is not a value-free process (Douglas, 2005). Since the federal government of Canada has set "evidence-based" policymaking as a top priority (Government of Canada, 2016), choosing an ineffective measurement technique may have negative repercussions beyond the academic realm. Scientific evidence from non-ideal sampling techniques could hinder the development of environmental policies needed to protect communities and sensitive ecosystems. The simultaneous use of multiple measurement techniques may be required to adequately address complex environmental problems since each technique has unique advantages and limitations, depending on the application.

MAX-DOAS techniques allow a diversity of applications for studying atmospheric species, complementary to in-situ and remote sensing techniques. MAX-DOAS applications can determine emissions, vertical profiles, and tropospheric column loading of trace-gases. This dissertation contributes to the field of remote sensing of atmospheric species by evaluating the performance of MAX-DOAS retrievals of aerosol extinction, NO_2, and SO_2, and demonstrating the advantages of stationary and mobile MAX-DOAS techniques over traditional techniques (e.g., satellite, aircraft, or in-situ) for monitoring tropospheric air quality in industrial and urban settings. This research addresses four questions: How do the MAX-DOAS retrievals perform at measuring aerosol extinction and trace-gases in comparison with other commonly used air quality monitoring techniques? How can MAX-DOAS measurements of an important pollutant, SO_2, be optimized? For which air quality problems do MAX-DOAS techniques have advantages over other techniques? How can these MAX-DOAS technique(s) be advanced?

1.4 Dissertation Outline

The dissertation consists of four chapters, each comprising a manuscript that is currently either published or under review by a journal. The first two publications focus on characterizing the performance of MAX-DOAS retrievals of aerosol extinction and trace-gases under different atmospheric conditions and provide technical recommendations. Deployment during the comprehensive air quality campaign in the Athabasca Oil Sands Region (AOSR) in 2013 provided a rare opportunity to evaluate the performance of multiple aspects of the MAX-DOAS retrievals. The results are presented in Chapter 2. Retrievals of aerosol extinction, NO_2, and SO_2 from MAX-DOAS measurements were compared to data from lidar, AERONET sun photometer, Pandora sun photometer, Active-DOAS, and airborne in-situ measurements of trace-gases. Important factors that must be considered to achieve useful inter-comparisons of MAX-DOAS with other instruments (e.g., lidar) were determined.

Several MAX-DOAS studies have measured SO_2, but there is an absence of standardized guidelines for measuring and retrieving SO_2 dSCDs based on quantitative experiments using MAX-DOAS. Fitting SO_2 from solar measurements is challenging due to low solar intensity in the wavelength region where SO_2 absorption features are strong, the effect of stray light, and potential interference by O_3 absorption features. Chapter 3 discusses the determination of the optimal settings for fitting SO_2 from MAX-DOAS measurements using SO_2 gas calibration cells.

Building on the work of the first two chapters, chapters 4 and 5 identify air quality problems where MAX-DOAS techniques are advantageous and other common techniques are limited. Chapter 4 discusses the utility of MAX-

DOAS for observing the impact of mesoscale meteorology on pollutants in the tropospheric column. This study quantifies the impact of lake-breeze circulations on the tropospheric loading of NO_2 and aerosol extinction in Toronto, Ontario, using MAX-DOAS measurements. Lake-breeze fronts were identified using co-located in-situ measurements of pollutants NO_x, O_3, and $PM_{2.5}$, and meteorological variables. This research contributes the first measurements of the total tropospheric loading of pollutants behind a lake breeze front on multiple days using MAX-DOAS measurements and is consistent with previously theorized 2-D structures of lake breezes. Chapter 5 presents a methodological improvement on the mobile-MAX-DOAS technique of estimating top-down NO_x emissions and demonstrates the technique's potential for low-cost emission estimates of pollutants in small industrial regions where other top-down emission estimate techniques are limited. Mobile-MAX-DOAS and in-situ NO-NO_2-NO_x measurements were simultaneously conducted while observing urban plumes at multiple times per day in the small industrial city of Sarnia, Ontario, Canada. SO_2 emissions were also quantified from the MAX-DOAS measurements. Finally, Chapter 6 discusses the key findings of the four manuscripts and the future research potential of MAX-DOAS. Note that Zoë Davis (the author) performed all MAX-DOAS experimental design and data analysis and wrote the associated manuscripts. The contribution of manuscript co-authors will be clarified on the title page of each chapter. Note also that each chapter ends with a reference list that contains only the references used in the respective chapter.

1.5 References

AERONET: Calculating Aerosol Optical Thickness, [online] Available from: https://aeronet.gsfc.nasa.gov/Operational/BSSN/aerosol2-GLOBE.pdf (Accessed 5 September 2019), 2002.

Ball, S. M., Langridge, J. M. and Jones, R. L.: Broadband cavity enhanced absorption spectroscopy using light emitting diodes, Chem. Phys. Lett., 398(1–3), 68–74, doi:10.1016/j.cplett.2004.08.144, 2004.

Bauer, S. E., Koch, D., Unger, N., Metzger, S. M., Shindell, D. T. and Streets, D. G.: Nitrate aerosols today and in 2030: a global simulation including aerosols and tropospheric ozone, Atmospheric Chem. Phys., 7(19), 5043–5059, doi:10.5194/acp-7-5043-2007, 2007.

Beirle, S., Boersma, K. F., Platt, U., Lawrence, M. G. and Wagner, T.: Megacity Emissions and Lifetimes of Nitrogen Oxides Probed from Space, Science, 333(6050), 1737–1739, doi:10.1126/science.1207824, 2011.

Beirle, S., Hörmann, C., Penning de Vries, M., Dörner, S., Kern, C. and Wagner, T.: Estimating the volcanic emission rate and atmospheric lifetime of SO2 from space: a case study for Kīlauea volcano, Hawai`i, Atmos Chem Phys, 14(16), 8309–8322, doi:10.5194/acp-14-8309-2014, 2014.

Bobrowski, N.: Volcanic Gas Studies by Multi Axis Differential Optical Absorption Spectroscopy, PhD, Ruperto Carola University of Heidelberg, Germany. [online] Available from: http://archiv.ub.uni-heidelberg.de/volltextserver/6052/1/dissnicole.pdf, 2005.

Bobrowski, N. and Filsinger, F.: Mini-MAX-DOAS Manual, 2005.

Brewer, A. W., Mcelroy, C. T. and Kerr, J. B.: Nitrogen Dioxide Concentrations in the Atmosphere, Nature, 246(5429), 129–133, doi:10.1038/246129a0, 1973.

Brinkmann, R.: Rotational Raman Scattering in Planetary Atmospheres, Astrophys. J., 154(3P1), 1087-+, doi:10.1086/149827, 1968.

Cass, G. R.: On the relationship between sulfate air quality and visibility with examples in los angeles, Atmospheric Environ. 1967, 13(8), 1069–1084, doi:10.1016/0004-6981(79)90031-3, 1979.

Castrejon-Garcia, R., Varela, J. R., Castrejon-Pita, J. R. and Morales, A.: The laser-backscattering equations and their application to the study of the atmospheric structure, Rev. Mex. Fis., 48(6), 513–518, 2002.

Chance, K. V. and Spurr, R. J. D.: Ring effect studies: Rayleigh scattering, including molecular parameters for rotational Raman scattering, and the Fraunhofer spectrum, Appl. Opt., 36(21), 5224–5230, doi:10.1364/AO.36.005224, 1997.

Chen, C. M., Cageao, R. P., Lawrence, L., Stutz, J., Salawitch, R. J., Jourdain, L., Li, Q. and Sander, S. P.: Diurnal variation of midlatitudinal NO3 column abundance over table mountain facility, California, Atmospheric Chem. Phys., 11(3), 963–978, doi:10.5194/acp-11-963-2011, 2011.

Clemer, K., Van Roozendael, M., Fayt, C., Hendrick, F., Hermans, C., Pinardi, G., Spurr, R., Wang, P. and De Maziere, M.: Multiple wavelength retrieval of tropospheric aerosol optical properties from MAXDOAS measurements in Beijing, Atmospheric Meas. Tech., 3(4), 863–878, doi:10.5194/amt-3-863-2010, 2010.

Cohen, A. J., Brauer, M., Burnett, R., Anderson, H. R., Frostad, J., Estep, K., Balakrishnan, K., Brunekreef, B., Dandona, L., Dandona, R., Feigin, V., Freedman, G., Hubbell, B., Jobling, A., Kan, H., Knibbs, L., Liu, Y., Martin, R., Morawska, L., Pope, C. A., Shin, H., Straif, K., Shaddick, G., Thomas, M., van Dingenen, R., van Donkelaar, A., Vos, T., Murray, C. J. L. and Forouzanfar, M. H.: Estimates and 25-year trends of the global burden of disease attributable to ambient air pollution: an analysis of data from the Global Burden of Diseases Study 2015, Lancet, 389(10082), 1907–1918, doi:10.1016/S0140-6736(17)30505-6, 2017.

Devaux, C., Vermeulen, A., Deuzé, J. L., Dubuisson, P., Herman, M., Santer, R. and Verbrugghe, M.: Retrieval of aerosol single-scattering albedo from ground-based measurements: Application to observational data, J. Geophys. Res. Atmospheres, 103(D8), 8753–8761, doi:10.1029/98JD00276, 1998.

Douglas, H.: Inserting the Public Into Science, in Democratization of Expertise?, vol. 24, edited by S. Maasen and P. Weingart, pp. 153–169, Springer-Verlag, Berlin/Heidelberg., 2005.

Dragomir, C. M., Constantin, D.-E., Voiculescu, M., Georgescu, L. P., Merlaud, A. and Van Roozendael, M.: Modeling results of atmospheric dispersion of NO2 in an urban area using METI-LIS and comparison with

coincident mobile DOAS measurements, ATMOSPHERIC Pollut. Res., 6(3), 503–510, doi:10.5094/APR.2015.056, 2015.

ECCC: List of toxic substances managed under Canadian Environmental Protection Act, [online] Available from: https://www.canada.ca/en/environment-climate-change/services/management-toxic-substances/list-canadian-environmental-protection-act.html (Accessed 28 August 2019), 2009.

Ehhalt, D., Prather, M., Dentener, F., Derwent, R., Dlugokencky, E., Holland, E., Isaksen, I., Katima, J., Kirchhoff, V., Matson, P., Midgley, P., Wang, M., Berntsen, T., Bey, I., Brasseur, G., Buja, L., Collins, W. J., Daniel, J., DeMore, W. B., Derek, N., Dickerson, R., Etheridge, D., Feichter, J., Fraser, P., Friedl, R., Fuglestvedt, J., Gauss, M., Grenfell, L., Grübler, A., Harris, N., Hauglustaine, D., Horowitz, L., Jackman, C., Jacob, D., Jaeglé, L., Jain, A., Kanakidou, M., Karlsdottir, S., Ko, M., Kurylo, M., Lawrence, M., Logan, J. A., Manning, M., Mauzerall, D., McConnell, J., Mickley, L., Montzka, S., Müller, J. F., Olivier, J., Pickering, K., Pitari, G., Roelofs, G. J., Rogers, H., Rognerud, B., Smith, S., Solomon, S., Staehelin, J., Steele, P., Stevenson, D., Sundet, J., Thompson, A., van Weele, M., Joos, F. and McFarland, M.: Atmospheric Chemistry and Greenhouse Gases, Intergov. Panel Clim. Change, 50, 2018.

European Space Agency: Sentinel-5P - ESA EO Missions - Earth Online - ESA, [online] Available from: https://earth.esa.int/web/guest/missions/esa-eo-missions/sentinel-5p (Accessed 27 August 2019), 2019.

Finlayson-Pitts, B. J. and Pitts, J. N. (James N.: Chemistry of the upper and lower atmosphere: theory, experiments and applications, Academic Press, San Diego, Calif., 2000.

Fioletov, V. E., McLinden, C. A., Krotkov, N., Moran, M. D. and Yang, K.: Estimation of SO2 emissions using OMI retrievals, Geophys. Res. Lett., 38, L21811, doi:10.1029/2011GL049402, 2011.

Fioletov, V. E., McLinden, C. A., Cede, A., Davies, J., Mihele, C., Netcheva, S., Li, S.-M. and O'Brien, J.: Sulfur dioxide (SO2) vertical column density measurements by Pandora spectrometer over the Canadian oil sands, Atmos Meas Tech, 9(7), 2961–2976, doi:10.5194/amt-9-2961-2016, 2016.

Frieß, U., Monks, P. S., Remedios, J. J., Rozanov, A., Sinreich, R., Wagner, T. and Platt, U.: MAX-DOAS O4 measurements: A new technique to derive information on atmospheric aerosols: 2. Modeling studies, J. Geophys. Res.-Atmospheres, 111(D14), D14203, doi:10.1029/2005JD006618, 2006.

Frieß, U., Sihler, H., Sander, R., Poehler, D., Yilmaz, S. and Platt, U.: The vertical distribution of BrO and aerosols in the Arctic: Measurements by active and passive differential optical absorption spectroscopy, J. Geophys. Res.-Atmospheres, 116, D00R04, doi:10.1029/2011JD015938, 2011.

Frieß, U., Beirle, S., Alvarado Bonilla, L., Bösch, T., Friedrich, M. M., Hendrick, F., Piters, A., Richter, A., Roozendael, M. van, Rozanov, V. V., Spinei, E., Tirpitz, J.-L., Vlemmix, T., Wagner, T. and Wang, Y.:

Intercomparison of MAX-DOAS vertical profile retrieval algorithms: studies using synthetic data, Atmospheric Meas. Tech., 12(4), 2155–2181, doi:https://doi.org/10.5194/amt-12-2155-2019, 2019.

Government of Canada: New Science Advisor will be the key to evidence-based policy, Innov. Sci. Econ. Dev. Can. [online] Available from: https://www.ic.gc.ca/eic/site/064.nsf/eng/08043.html (Accessed 23 September 2019), 2016.

Greenblatt, G. D., Orlando, J. J., Burkholder, J. B. and Ravishankara, A. R.: Absorption measurements of oxygen between 330 and 1140 nm, J. Geophys. Res., 95(D11), 18577, doi:10.1029/JD095iD11p18577, 1990.

Guibert, S., Matthias, V., Schulz, M., Bosenberg, J., Eixmann, R., Mattis, I., Pappalardo, G., Ritaperrone, M., Spinelli, N. and Vaughan, G.: The vertical distribution of aerosol over Europe—synthesis of one year of EARLINET aerosol lidar measurements and aerosol transport modeling with LMDzT-INCA, Atmos. Environ., 39(16), 2933–2943, doi:10.1016/j.atmosenv.2004.12.046, 2005.

Haywood, J. and Boucher, O.: Estimates of the direct and indirect radiative forcing due to tropospheric aerosols: A review, Rev. Geophys., doi:10.1029/1999RG000078, 2000.

Health Canada: Human Health Risk Assessment for Sulphur Dioxide, [online] Available from: http://publications.gc.ca/collections/collection_2016/sc-hc/H144-29-2016-eng.pdf (Accessed 1 January 2019), 2016.

Heckel, A., Richter, A., Tarsu, T., Wittrock, F., Hak, C., Pundt, I., Junkermann, W. and Burrows, J. P.: MAX-DOAS measurements of formaldehyde in the Po-Valley, Atmospheric Chem. Phys., 5, 909–918, doi:10.5194/acp-5-909-2005, 2005.

Heckel, A., Kim, S.-W., Frost, G. J., Richter, A., Trainer, M. and Burrows, J. P.: Influence of low spatial resolution a priori data on tropospheric NO2 satellite retrievals, Atmos Meas Tech, 4(9), 1805–1820, doi:10.5194/amt-4-1805-2011, 2011.

Herman, J., Cede, A., Spinei, E., Mount, G., Tzortziou, M. and Abuhassan, N.: NO2 column amounts from ground-based Pandora and MFDOAS spectrometers using the direct-sun DOAS technique: Intercomparisons and application to OMI validation, J. Geophys. Res.-Atmospheres, 114, D13307, doi:10.1029/2009JD011848, 2009.

Holben, B. N., Eck, T. F., Slutsker, I., Tanre, D., Buis, J. P., Setzer, A., Vermote, E., Reagan, J. A., Kaufman, Y. J., Nakajima, T., Lavenu, F., Jankowiak, I. and Smirnov, A.: AERONET - A federated instrument network and data archive for aerosol characterization, Remote Sens. Environ., 66(1), 1–16, doi:10.1016/S0034-4257(98)00031-5, 1998.

Holloway, A. M. and Wayne, R.: Atmospheric Chemistry, RSC Publishing, Cambridge, UK., 2010.

Honninger, G. and Platt, U.: Observations of BrO and its vertical distribution during surface ozone depletion at Alert, Atmos. Environ., 36(15–16), 2481–2489, doi:10.1016/S1352-2310(02)00104-8, 2002.

Honninger, G., von Friedeburg, C. and Platt, U.: Multi axis differential optical absorption spectroscopy (MAX-DOAS), Atmospheric Chem. Phys., 4, 231–254, 2004.

Horbanski, M., Pöhler, D., Lampel, J. and Platt, U.: The ICAD (iterative cavity-enhanced DOAS) method, Atmospheric Meas. Tech., 12(6), 3365–3381, doi:10.5194/amt-12-3365-2019, 2019.

Huang, M., Bowman, K. W., Carmichael, G. R., Chai, T., Pierce, R. B., Worden, J. R., Luo, M., Pollack, I. B., Ryerson, T. B., Nowak, J. B., Neuman, J. A., Roberts, J. M., Atlas, E. L. and Blake, D. R.: Changes in nitrogen oxides emissions in California during 2005-2010 indicated from top-down and bottom-up emission estimates, J. Geophys. Res.-ATMOSPHERES, 119(22), 12928–12952, doi:10.1002/2014JD022268, 2014.

Ibrahim, O., Shaiganfar, R., Sinreich, R., Stein, T., Platt, U. and Wagner, T.: Car MAX-DOAS measurements around entire cities: quantification of NOx emissions from the cities of Mannheim and Ludwigshafen (Germany), ATMOSPHERIC Meas. Tech., 3(3), 709–721, doi:10.5194/amt-3-709-2010, 2010.

Irie, H., Kanaya, Y., Akimoto, H., Iwabuchi, H., Shimizu, A. and Aoki, K.: First retrieval of tropospheric aerosol profiles using MAX-DOAS and comparison with lidar and sky radiometer measurements, Atmospheric Chem. Phys., 8(2), 341–350, doi:10.5194/acp-8-341-2008, 2008.

Irie, H., Nakayama, T., Shimizu, A., Yamazaki, A., Nagai, T., Uchiyama, A., Zaizen, Y., Kagamitani, S. and Matsumi, Y.: Evaluation of MAX-DOAS aerosol retrievals by coincident observations using CRDS, lidar, and sky radiometer in Tsukuba, Japan, Atmospheric Meas. Tech., 8(7), 2775–2788, doi:10.5194/amt-8-2775-2015, 2015.

Jaeglé, L., Steinberger, L., Martin, R. V. and Chance, K.: Global partitioning of NOx sources using satellite observations: Relative roles of fossil fuel combustion, biomass burning and soil emissions, Faraday Discuss., 130, 407–423, doi:10.1039/b502128f, 2005.

Jung, C. H., Shin, H. J., Lee, J. Y. and Kim, Y. P.: Sensitivity and Contribution of Organic Aerosols to Aerosol Optical Properties Based on Their Refractive Index and Hygroscopicity, Atmosphere, 7(5), 65, doi:10.3390/atmos7050065, 2016.

Kim, N. K., Kim, Y. P., Morino, Y., Kurokawa, J. and Ohara, T.: Verification of NOx emission inventories over North Korea, Environ. Pollut., 195, 236–244, doi:10.1016/j.envpol.2014.06.034, 2014.

King, M. D., Byrne, D. M., Herman, B. M. and Reagan, J. A.: Aerosol Size Distributions Obtained by Inversions of Spectral Optical Depth Measurements, J. Atmospheric Sci., 35(11), 2153–2167, doi:10.1175/1520-0469(1978)035<2153:ASDOBI>2.0.CO;2, 1978.

Klett, J. D.: Stable analytical inversion solution for processing lidar returns, Appl. Opt., 20(2), 211–220, doi:10.1364/AO.20.000211, 1981.

Kulmala, M., Vehkamäki, H., Petäjä, T., Dal Maso, M., Lauri, A., Kerminen, V.-M., Birmili, W. and McMurry, P. H.: Formation and growth rates of ultrafine atmospheric particles: a review of observations, J. Aerosol Sci., 35(2), 143–176, doi:10.1016/j.jaerosci.2003.10.003, 2004.

Lamarque, J.-F., Bond, T. C., Eyring, V., Granier, C., Heil, A., Klimont, Z., Lee, D., Liousse, C., Mieville, A., Owen, B., Schultz, M. G., Shindell, D., Smith, S. J., Stehfest, E., Van Aardenne, J., Cooper, O. R., Kainuma, M., Mahowald, N., McConnell, J. R., Naik, V., Riahi, K. and van Vuuren, D. P.: Historical (1850–2000) gridded anthropogenic and biomass burning emissions of reactive gases and aerosols: methodology and application, Atmospheric Chem. Phys., 10(15), 7017–7039, doi:10.5194/acp-10-7017-2010, 2010.

Lamsal, L. N., Krotkov, N. A., Celarier, E. A., Swartz, W. H., Pickering, K. E., Bucsela, E. J., Gleason, J. F., Martin, R. V., Philip, S., Irie, H., Cede, A., Herman, J., Weinheimer, A., Szykman, J. J. and Knepp, T. N.: Evaluation of OMI operational standard NO2 column retrievals using in situ and surface-based NO2 observations, Atmospheric Chem. Phys., 14(21), 11587–11609, doi:10.5194/acp-14-11587-2014, 2014.

Langridge, J. M., Ball, S. M. and Jones, R. L.: A compact broadband cavity enhanced absorption spectrometer for detection of atmospheric NO2 using light emitting diodes, Analyst, 131(8), 916–922, doi:10.1039/b605636a, 2006.

Lee, C., Martin, R. V., van Donkelaar, A., Lee, H., Dickerson, R. R., Hains, J. C., Krotkov, N., Richter, A., Vinnikov, K. and Schwab, J. J.: SO2 emissions and lifetimes: Estimates from inverse modeling using in situ and global, space-based (SCIAMACHY and OMI) observations, J. Geophys. Res.-Atmospheres, 116, D06304, doi:10.1029/2010JD014758, 2011.

Li, X., Brauers, T., Shao, M., Garland, R. M., Wagner, T., Deutschmann, T. and Wahner, A.: MAX-DOAS measurements in southern China: retrieval of aerosol extinctions and validation using ground-based in-situ data, Atmospheric Chem. Phys., 10(5), 2079–2089, doi:10.5194/acp-10-2079-2010, 2010.

Li, Z. Q., Goloub, P., Devaux, C., Gu, X. F., Deuze, J. L., Qiao, Y. L. and Zhao, F. S.: Retrieval of aerosol optical and physical properties from ground-based spectral, multi-angular, and polarized sun-photometer measurements, Remote Sens. Environ., 101(4), 519–533, doi:10.1016/j.rse.2006.01.012, 2006.

Lin, C., Li, Y., Yuan, Z., Lau, A. K. H., Li, C. and Fung, J. C. H.: Using satellite remote sensing data to estimate the high-resolution distribution of ground-level PM2.5, Remote Sens. Environ., 156, 117–128, doi:10.1016/j.rse.2014.09.015, 2015.

Liu, F., Beirle, S., Zhang, Q., Doerner, S., He, K. and Wagner, T.: NOx lifetimes and emissions of cities and power plants in polluted background estimated by satellite observations, Atmospheric Chem. Phys., 16(8), 5283–5298, doi:10.5194/acp-16-5283-2016, 2016.

Luke, W. T.: Evaluation of a commercial pulsed fluorescence detector for the measurement of low-level SO2 concentrations during the Gas-Phase Sulfur Intercomparison Experiment, J. Geophys. Res. Atmospheres, 102(D13), 16255–16265, doi:10.1029/96JD03347, 1997.

McKinnon, M.: Advanced Satellite Tracks Air Pollution in Extraordinary Detail - Eos, Earth Space Sci. News [online] Available from: https://eos.org/articles/advanced-satellite-tracks-air-pollution-in-extraordinary-detail (Accessed 27 August 2019), 2017.

McLinden, C. A.: Stratospheric ozone in 3-D models: A simple chemistry and the cross-tropopause flux., J. Geophys. Res., 105(D11), 14653–14665, doi:10.1029/2000JD900124, 2000.

McLinden, C. A., Fioletov, V., Boersma, K. F., Krotkov, N., Sioris, C. E., Veefkind, J. P. and Yang, K.: Air quality over the Canadian oil sands: A first assessment using satellite observations, Geophys. Res. Lett., 39, L04804, doi:10.1029/2011GL050273, 2012.

McLinden, C. A., Fioletov, V., Boersma, K. F., Kharol, S. K., Krotkov, N., Lamsal, L., Makar, P. A., Martin, R. V., Veefkind, J. P. and Yang, K.: Improved satellite retrievals of NO2 and SO2 over the Canadian oil sands and comparisons with surface measurements, Atmospheric Chem. Phys., 14(7), 3637–3656, doi:10.5194/acp-14-3637-2014, 2014.

Medina, D. S., Liu, Y., Wang, L. and Zhang, J.: Detection of Sulfur Dioxide by Cavity Ring-Down Spectroscopy, Environ. Sci. Technol., 45(5), 1926–1931, doi:10.1021/es103739r, 2011.

Merten, A.: Neues Design von Langpfad-DOAS-Instrumenten basierend auf Faseroptiken und Anwendung der Untersuchung der urbanen Atmosphäre, Dissertation., 2008.

Mohn, J. and Emmenegger, L.: Determination of Sulphur Dioxide in Pulsed UV-Fluorescence, White Paper, Swiss Federal Laboratories for Materials Testing and Research, Dubendorf, Switzerland. [online] Available from: https://www.envirotech-online.com/white-paper/air-monitoring/6/cem/determination-of-sulphur-dioxide-by-pulsed-uv-fluorescence/76, 2014.

Nasse, J.-M., Eger, P. G., Pöhler, D., Schmitt, S., Frieß, U. and Platt, U.: Recent improvements of long-path DOAS measurements: impact on accuracy and stability of short-term and automated long-term observations, Atmospheric Meas. Tech., 12(8), 4149–4169, doi:10.5194/amt-12-4149-2019, 2019.

Nikelski, K. M.: Measurement of Atmospheric NOy Species Using Active and Lunar DOAS in an Urban and Forested Region, York University, Toronto, Canada., 2016.

Noxon, J. F.: Nitrogen Dioxide in the Stratosphere and Troposphere Measured by Ground-Based Absorption Spectroscopy, Science, 189(4202), 547–549, doi:10.1126/science.189.4202.547, 1975.

Nunnermacker, L. J., Kleinman, L. I., Imre, D., Daum, P. H., Lee, Y.-N., Lee, J. H., Springston, S. R., Newman, L. and Gillani, N.: NO y lifetimes and O3 production efficiencies in urban and power plant plumes: Analysis of field data, J. Geophys. Res. Atmospheres, 105(D7), 9165–9176, doi:10.1029/1999JD900753, 2000.

Otten, C., Ferlemann, F., Platt, U., Wagner, T. and Pfeilsticker, K.: Groundbased Doas UV/visible measurements at Kiruna (Sweden) during the sesame winters 1993/94 and 1994/95., J. Atmospheric Chem., 30(1), 141–162, doi:10.1023/A:1005810732347, 1998.

Perner, D., Ehhalt, D., Pätz, H., Platt, U., Röth, E.-P. and Volz-Thomas, A.: OH - Radicals in the lower troposphere, Geophys. Res. Lett. - GEOPHYS RES LETT, 3, 466–468, doi:10.1029/GL003i008p00466, 1976.

Platt, U., Perner, D. and Patz, H.: Simultaneous Measurement of Atmospheric CH2O, O3, and NO2 by Differential Optical-Absorption, J. Geophys. Res.-Oceans Atmospheres, 84(NC10), 6329–6335, doi:10.1029/JC084iC10p06329, 1979.

Platt, U., Stutz, J., Springer E-books - York University and SpringerLink (Online service): Differential optical absorption spectroscopy: principles and applications, Springer Verlag, Berlin. [online] Available from: http://www.library.yorku.ca/eresolver/?id=1261530, 2008.

Platt, U., Meinen, J., Poehler, D. and Leisner, T.: Broadband Cavity Enhanced Differential Optical Absorption Spectroscopy (CE-DOAS) - applicability and corrections, Atmospheric Meas. Tech., 2(2), 713–723, doi:10.5194/amt-2-713-2009, 2009.

Psenner, R.: Environmental impacts on freshwaters: acidifaction as a global problem., Sci. Total Environ., 143(1), 53–61, doi:10.1016/0048-9697(94)90532-0, 1994.

Ramanathan, V., Crutzen, P. J., Kiehl, J. T. and Rosenfeld, D.: Aerosols, Climate, and the Hydrological Cycle, Science, 294(5549), 2119–2124, doi:10.1126/science.1064034, 2001.

Ramaswamy, V., Boucher, O., Haigh, J., Hauglustaine, D., Haywood, J., Myhre, G., Nakajima, T., Shi, G. Y., Solomon, S., Betts, R., Charlson, R., Chuang, C., Daniel, J. S., Joos, F. and Srinivasan, J.: Radiative Forcing of Climate Change, Intergov. Panel Clim. Change, 68, 2018.

Romanov, P., O'Neill, N. T., Royer, A. and McArthur, B. L. J.: Simultaneous retrieval of aerosol refractive index and particle size distribution from ground-based measurements of direct and scattered solar radiation, Appl. Opt., 38(36), 7305–7320, doi:10.1364/AO.38.007305, 1999.

Schneider, P., Lahoz, W. A. and van der A, R.: Recent satellite-based trends of tropospheric nitrogen dioxide over large urban agglomerations worldwide, Atmospheric Chem. Phys., 15(3), 1205–1220, doi:10.5194/acp-15-1205-2015, 2015.

Seinfeld, J. H. and Pandis, S. N.: Atmospheric Chemistry and Physics: From Air Pollution to Climate Change, John Wiley & Sons., 2006.

Shaiganfar, R., Beirle, S., Sharma, M., Chauhan, A., Singh, R. P. and Wagner, T.: Estimation of NOx emissions from Delhi using Car MAX-DOAS observations and comparison with OMI satellite data, ATMOSPHERIC Chem. Phys., 11(21), 10871–10887, doi:10.5194/acp-11-10871-2011, 2011.

Shaiganfar, R., Beirle, S., Petetin, H., Zhang, Q., Beekmann, M. and Wagner, T.: New concepts for the comparison of tropospheric NO2 column densities derived from car-MAX-DOAS observations, OMI satellite observations and the regional model CHIMERE during two MEGAPOLI campaigns in Paris 2009/10, ATMOSPHERIC Meas. Tech., 8(7), 2827–2852, doi:10.5194/amt-8-2827-2015, 2015.

Shaiganfar, R., Beirle, S., van der Gon, H. D., Jonkers, S., Kuenen, J., Petetin, H., Zhang, Q., Beekmann, M. and Wagner, T.: Estimation of the Paris NOx emissions from mobile MAX-DOAS observations and CHIMERE model simulations during the MEGAPOLI campaign using the closed integral method, Atmospheric Chem. Phys., 17(12), 7853–7890, doi:10.5194/acp-17-7853-2017, 2017.

Shao, J., Chen, Q., Wang, Y., Lu, X., He, P., Sun, Y., Shah, V., Martin, R. V., Philip, S., Song, S., Zhao, Y., Xie, Z., Zhang, L. and Alexander, B.: Heterogeneous sulfate aerosol formation mechanisms during wintertime Chinese haze events: air quality model assessment using observations of sulfate oxygen isotopes in Beijing, Atmospheric Chem. Phys., 19(9), 6107–6123, doi:10.5194/acp-19-6107-2019, 2019.

Shaw, G. E.: Inversion of optical scattering and spectral extinction measurements to recover aerosol size spectra, Appl. Opt., 18(7), 988–993, doi:10.1364/AO.18.000988, 1979.

Sinreich, R., Frieß, U., Wagner, T. and Platt, U.: Multi axis differential optical absorption spectroscopy (MAX-DOAS) of gas and aerosol distributions, Faraday Discuss., 130, 153–164, doi:10.1039/B419274P, 2005.

Skoog, D. A., Holler, J. F. and Crouch, S. R.: Principles of Instrumental Analysis, 6th ed., Thomson, Blemont, CA., 2007.

Smith, J. P. and Solomon, S.: Atmospheric NO3 3. Sunrise disappearance and the stratospheric profile, J. Geophys. Res. Atmospheres, 95(D9), 13819–13827, doi:10.1029/JD095iD09p13819, 1990.

Stocker, T. F., Qin, D., Plattner, G.-K., Tignor, M., Allen, S. K., Boschung, J., Nauels, A., Bex, V. and Midgley, P. M.: Intergovernmental Panel on Climate Change. Climate Change 2013: The Physical Science Basis. Contribution of Working Group I to the Fifth Assessment Report of the Intergovernmental Panel on Climate Change., Cambridge University Press, New York., 2013.

Strawbridge, K. B.: Developing a portable, autonomous aerosol backscatter lidar for network or remote operations, Atmos Meas Tech, 6(3), 801–816, doi:10.5194/amt-6-801-2013, 2013.

Strawbridge, K. B., Travis, M. S., Firanski, B. J., Brook, J. R., Staebler, R. and Leblanc, T.: A fully autonomous ozone, aerosol and nighttime water vapor lidar: a synergistic approach to profiling the atmosphere in the Canadian oil sands region, Atmospheric Meas. Tech., 11(12), 6735–6759, doi:10.5194/amt-11-6735-2018, 2018.

Streets, D. G., Canty, T., Carmichael, G. R., de Foy, B., Dickerson, R. R., Duncan, B. N., Edwards, D. P., Haynes, J. A., Henze, D. K., Houyoux, M. R., Jacob, D. J., Krotkov, N. A., Lamsal, L. N., Liu, Y., Lu, Z., Martin, R. V., Pfister, G. G., Pinder, R. W., Salawitch, R. J. and Wecht, K. J.: Emissions estimation from satellite retrievals: A review of current capability, Atmos. Environ., 77, 1011–1042, doi:10.1016/j.atmosenv.2013.05.051, 2013.

Stutz, J. and Platt, U.: Numerical analysis and estimation of the statistical error of differential optical absorption spectroscopy measurements with least-squares methods, Appl. Opt., 35(30), 6041, doi:10.1364/AO.35.006041, 1996.

Tan, W., Liu, C., Wang, S., Xing, C., Su, W., Zhang, C., Xia, C., Liu, H., Cai, Z. and Liu, J.: Tropospheric NO2, SO2, and HCHO over the East China Sea, using ship-based MAX-DOAS observations and comparison with OMI and OMPS satellite data, Atmospheric Chem. Phys., 18(20), 15387–15402, doi:10.5194/acp-18-15387-2018, 2018.

Twitty, J. T.: The Inversion of Aureole Measurements to Derive Aerosol Size Distributions, J. Atmospheric Sci., 32(3), 584–591, doi:10.1175/1520-0469(1975)032<0584:TIOAMT>2.0.CO;2, 1975.

Tzortziou, M., Herman, J. R., Cede, A. and Abuhassan, N.: High precision, absolute total column ozone measurements from the Pandora spectrometer system: Comparisons with data from a Brewer double monochromator and Aura OMI: PANDORA TOTAL COLUMN OZONE RETRIEVAL, J. Geophys. Res. Atmospheres, 117(D16), n/a-n/a, doi:10.1029/2012JD017814, 2012.

Uno, I., Eguchi, K., Yumimoto, K., Takemura, T., Shimizu, A., Uematsu, M., Liu, Z., Wang, Z., Hara, Y. and Sugimoto, N.: Asian dust transported one full circuit around the globe, Nat. Geosci., 2(8), 557–560, doi:10.1038/NGEO583, 2009.

US EPA, O.: Basic Information about NO2, US EPA [online] Available from: https://www.epa.gov/no2-pollution/basic-information-about-no2 (Accessed 29 August 2019), 2016.

US EPA, O.: Criteria Air Pollutants, [online] Available from: https://www.epa.gov/criteria-air-pollutants (Accessed 28 August 2019), 2017.

Valin, L. C., Russell, A. R. and Cohen, R. C.: Variations of OH radical in an urban plume inferred from NO2 column measurements, Geophys. Res. Lett., 40(9), 1856–1860, doi:10.1002/grl.50267, 2013.

Volz, F.: Photometer mit Selen-Photoelement zur spektralen Messung der Sonnenstrahlung und zur Bestimmung der Wellenlängenabhängigkeit der Dunsttrübung, Arch. Für Meteorol. Geophys. Bioklimatol. Ser. B, 10(1), 100–131, doi:10.1007/BF02243122, 1959.

Wagner, T., Otten, C., Pfeilsticker, K., Pundt, I. and Platt, U.: DOAS moonlight observation of atmospheric NO3 in the Arctic winter, Geophys. Res. Lett., 27(21), 3441–3444, doi:10.1029/1999GL011153, 2000.

Wagner, T., von Friedeburg, C., Wenig, M. O., Otten, C. and Platt, U.: UV-visible observations of atmospheric O-4 absorptions using direct moonlight and zenith-scattered sunlight for clear-sky and cloudy sky conditions., J. Geophys. Res.-ATMOSPHERES, 107(D20), doi:10.1029/2001JD001026, 2002.

Wagner, T., Dix, B., von Friedeburg, C., Frieß, U., Sanghavi, S., Sinreich, R. and Platt, U.: MAX-DOAS O-4 measurements: A new technique to derive information on atmospheric aerosols - Principles and information content, J. Geophys. Res.-Atmospheres, 109(D22), D22205, doi:10.1029/2004JD004904, 2004.

Wagner, T., Ibrahim, O., Shaiganfar, R. and Platt, U.: Mobile MAX-DOAS observations of tropospheric trace gases, ATMOSPHERIC Meas. Tech., 3(1), 129–140, 2010.

Wagner, T., Beirle, S., Brauers, T., Deutschmann, T., Frieß, U., Hak, C., Halla, J. D., Heue, K. P., Junkermann, W., Li, X., Platt, U. and Pundt-Gruber, I.: Inversion of tropospheric profiles of aerosol extinction and HCHO and NO2 mixing ratios from MAX-DOAS observations in Milano during the summer of 2003 and comparison with independent data sets, Atmospheric Meas. Tech., 4(12), 2685–2715, doi:10.5194/amt-4-2685-2011, 2011.

Wang, G., Zhang, R., Gomez, M. E., Yang, L., Levy Zamora, M., Hu, M., Lin, Y., Peng, J., Guo, S., Meng, J., Li, J., Cheng, C., Hu, T., Ren, Y., Wang, Y., Gao, J., Cao, J., An, Z., Zhou, W., Li, G., Wang, J., Tian, P., Marrero-Ortiz, W., Secrest, J., Du, Z., Zheng, J., Shang, D., Zeng, L., Shao, M., Wang, W., Huang, Y., Wang, Y., Zhu, Y., Li, Y., Hu, J., Pan, B., Cai, L., Cheng, Y., Ji, Y., Zhang, F., Rosenfeld, D., Liss, P. S., Duce, R. A., Kolb, C. E. and Molina, M. J.: Persistent sulfate formation from London Fog to Chinese haze, Proc. Natl. Acad. Sci., 113(48), 13630–13635, doi:10.1073/pnas.1616540113, 2016.

Weaver, A., Solomon, S., Sanders, R. W., Arpag, K. and Miller, H. L.: Atmospheric NO3 .5. Off-axis measurements at sunrise: Estimates of tropospheric NO3 at 40 degrees N, J. Geophys. Res.-Atmospheres, 101(D13), 18605–18612, doi:10.1029/96JD01537, 1996.

Weitkamp, C.: Lidar: range-resolved optical remote sensing of the atmosphere., Springer Science+Business Media, New York., 2005.

WHO: WHO Air quality guidelines for particulate matter, ozone, nitrogen dioxide and sulfur dioxide. Global update 2005. Summary of Risk Assessment. [online] Available from: https://apps.who.int/iris/bitstream/handle/10665/69477/WHO_SDE_PHE_OEH_06.02_eng.pdf?sequence=1 (Accessed 18 April 2019), 2006.

Wu, F., Li, A., Xie, P., Chen, H., Hu, Z., Zhang, Q., Liu, J. and Liu, W.: Emission Flux Measurement Error with a Mobile DOAS System and Application to NOx Flux Observations, Sensors, 17(2), doi:10.3390/s17020231, 2017a.

Wu, Y., de Graaf, M. and Menenti, M.: The impact of aerosol vertical distribution on aerosol optical depth retrieval using CALIPSO and MODIS data: Case study over dust and smoke regions: THE IMPACT OF AEROSOL VERTICAL PROFILE, J. Geophys. Res. Atmospheres, 122(16), 8801–8815, doi:10.1002/2016JD026355, 2017b.

Yilmaz, S.: Retrieval of Atmospheric Aerosol and Trace Gas Vertical Profiles using Multi-Axis Differential Optical Absorption Spectroscopy, Dissertation, University of Heidelberg, Heidelberg, Germany. [online] Available from: http://archiv.ub.uni-heidelberg.de/volltextserver/13128/1/Dissertation_Yilmaz_Selami.pdf (Accessed 17 September 2019), 2012.

Zhao, Y., Duan, L., Xing, J., Larssen, T., Nielsen, C. P. and Hao, J.: Soil Acidification in China: Is Controlling SO 2 Emissions Enough?, Environ. Sci. Technol., 43(21), 8021–8026, doi:10.1021/es901430n, 2009.

Zieger, P., Weingartner, E., Henzing, J., Moerman, M., de Leeuw, G., Mikkila, J., Ehn, M., Petaja, T., Clemer, K., van Roozendael, M., Yilmaz, S., Frieß, U., Irie, H., Wagner, T., Shaiganfar, R., Beirle, S., Apituley, A., Wilson, K. and Baltensperger, U.: Comparison of ambient aerosol extinction coefficients obtained from in-situ, MAX-DOAS and LIDAR measurements at Cabauw, Atmospheric Chem. Phys., 11(6), 2603–2624, doi:10.5194/acp-11-2603-2011, 2011.

Chapter 2

Validation of MAX-DOAS retrievals of aerosol extinction, SO_2 and NO_2 through comparison with lidar, sun photometer, active-DOAS and aircraft measurements in the Athabasca Oil Sands Region.

Zoë Y. W. Davis[1], Udo Frieβ[2], Kevin B. Strawbridge[3], Monika Aggarwaal[1], Sabour Baray[4], Elijah G. Schnitzler[5], Akshay Lobo4[4,6], Vitali E. Fioletov[3], Ihab Abboud[3], Chris A. McLinden[3], Jim Whiteway[1], Megan D. Willis[5,7], Alex K. Y. Lee[8], Jeff Brook[3,9], Jason Olfert[10], Jason O'Brien[3], Ralf Staebler[3], Hans D. Osthoff[11], Cristian Mihele[3], and Robert McLaren[4].

[1] Department of Earth and Space Science, York University, Toronto, M3J 1P3, Canada
[2] Institute of Environmental Physics, Heidelberg, 69120, Germany
[3] Environment and Climate Change Canada, Toronto, M3H 5T4, Canada
[4] Department of Chemistry, York University, Toronto, M3J 1P3, Canada
[5] Department of Chemistry, University of Toronto, M5S 3H6, Canada
[6] *now at* Department of Orthopaedics, University of British Columbia, Vancouver, V5Z 1M9, Canada
[7] *now at* Chemical Sciences Division, Lawrence Berkeley National Lab, Berkeley, California, 94720, USA
[8] Department of Civil and Environmental Engineering, National University of Singapore, 117576, Singapore
[9] *now at* Dalla Lana School of Public Health, University of Toronto, M5S 3H6, Canada
[10] Department of Mechanical Engineering, University of Alberta, Edmonton, Alberta, T6G 1H9
[11] Department of Chemistry, University of Calgary, Calgary, T2N 1N4, Canada

In Discussion: Atmospheric Measurement Techniques (2019), https://doi.org/10.5194/amt-2019-296

Author Contributions. ZYWD: MAX-DOAS study concept, design, investigation and data analysis, data visualization, and writing of manuscript and modifications of the same with contribution from all co-authors. UF: supervision and validation of MAX-DOAS data analysis. KBS: ground-based lidar study concept, design, investigation, and data analysis. MA: airborne lidar study concept, design, investigation, and analysis and S-ratio modelling. SB: analysis and visualization of SO_2 flight data. EGS: SMPS design, investigation, and data analysis. AL: active-DOAS investigation and data analysis. VEF: Pandora study concept, design, investigation, and data analysis. IA: AERONET AOD study concept, design, investigation, and data analysis. CAM: PRATMO modelling for Pandora data analysis and provision of Pandora data. JW: supervision of airborne lidar study. MDW and AKYL: SP-AMS study concept, design, and investigation. JB: Project administration and supervision for all studies in the field. JO: SMPS supervision and APS data analysis. JO'B: SO_2 flight data study concept, design, and investigation. RS: windRASS study concept, design, investigation, and data analysis. HDO: APS supervision. CM: APS investigation. RM: Active-DOAS study concept, design, and supervision and MAX-DOAS supervision.

Abstract. Vertical profiles of aerosols, NO_2, and SO_2 were retrieved from Multi-Axis Differential Optical Absorption Spectroscopy (MAX-DOAS) measurements at a field site in northern Alberta, Canada, during August and September 2013. The site is approximately 16 km north of two mining operations that are major sources of industrial pollution in the Athabasca Oil Sands Region. Pollution conditions during the study ranged from atmospheric background conditions to heavily polluted with elevated plumes, according to the meteorology. This study aimed to evaluate the performance of the aerosol and trace gas retrievals through comparison with data from a suite of other instruments. Comparisons of AODs from MAX-DOAS aerosol retrievals, lidar vertical profiles of aerosol extinction, and AERONET sun photometer indicate good performance by the MAX-DOAS retrievals. These comparisons and modelling of the lidar S-ratio highlight the need for accurate knowledge of the temporal variation in the S-ratio when comparing MAX-DOAS and lidar data. Comparisons of MAX-DOAS NO_2 and SO_2 retrievals to Pandora spectral sun photometer VCDs and Active-DOAS mixing ratios indicate good performance of the retrievals except when vertical profiles of pollutants within the boundary layer varied rapidly, temporally and spatially. Near-surface retrievals tended to overestimate Active-DOAS mixing ratios. The MAX-DOAS observed elevated pollution plumes not observed by the Active-DOAS, highlighting one of the instrument's main advantages. Aircraft measurements of SO_2 were used to validate retrieved vertical profiles of SO_2. Advantages of the MAX-DOAS instrument include increasing sensitivity towards the surface and the ability to simultaneously retrieve vertical profiles of aerosols and trace gases without requiring additional parameters such as the S-ratio. This complex dataset provided a rare opportunity to evaluate the performance of the MAX-DOAS retrievals under varying atmospheric conditions.

2.1 Introduction

The Athabasca Oil sands operations in Alberta contain significant sources of industrial atmospheric pollutants such as sulphur dioxide (SO_2) and nitrogen dioxide (NO_2) (ECCC, 2018b, 2018c). Oil extraction and upgrading activities such as surface mining, acid gas flaring, and transporting materials in heavy hauler trucks emit aerosols and trace gas pollutants (Liggio et al., 2016). Pollutant emissions from the industrial smokestacks result in uplifted profiles with the potential to be transported farther downwind compared to emission released at the surface, particularly for stacks with high volume flow rates and temperatures that can rise high in the atmosphere (Zhang et al., 2018). While the Athabasca Oil Sands Region (AOSR) experiences moderate annual average concentrations of SO_2 relative to all Canadian in-situ stations, the short-term concentrations can be significantly higher than in most Canadian cities (Government of Canada, 2018). The AOSR contains some of the few monitoring sites in Canada that experience peak 1-hour average concentrations of SO_2 of greater than 70 ppbv (Government of Canada, 2018), which is the new 2020 Canadian Ambient Air Quality Standard for SO_2 (Canadian Council of Ministers of the Environment, 2014). SO_2 concentrations of up to 131 ppbv were also observed by aircraft measurements downwind of an AOSR industrial facility in 2013, approximately midway between Syncrude Mildred Lake Plant and Fort McKay (Baray et al., 2018). High concentrations of SO_2 over short durations are a health concern because negative pulmonary and respiratory effects of inhalation can occur after exposure periods as small as 10 minutes (Health Canada, 2016; WHO, 2006). Exposure to NO_2 at high concentrations over short-term is also associated with significant health

impacts (WHO, 2006) and NO_x ($NO + NO_2$) is a precursor to tropospheric ozone (O_3), acid rain and fine particulate matter (Seinfeld and Pandis, 2006).

Emissions of NO_x and SO_2 lead to the formation of nitrate and sulphate aerosols, which constitute a significant fraction of the $PM_{2.5}$ air mass in urban and industrially-impacted regions (Pui et al., 2014). The highest peak and annual average $PM_{2.5}$ concentrations in Canada in 2016 were observed at two monitoring stations within Fort McMurray with annual averages of over 18 μg m^{-3} compared to 8 μg m^{-3} in an industrial area of Toronto, Ontario (Government of Canada, 2018). Exposure to $PM_{2.5}$ leads to adverse effects on respiratory and cardiovascular systems (WHO, 2006).

In the troposphere, nearly all SO_2 is oxidized to H_2SO_4 aerosol through reactions in the gas and aqueous phases. The hydroxyl (OH) radical initiates the oxidation route of SO_2 in the gas phase, forming $HOSO_2$ (Holloway and Wayne, 2010). Sulfuric acid (H_2SO_4) is formed through further oxidation of $HOSO_2$ to SO_3, which can condense onto already present aerosols or can nucleate with water vapour (H_2O) and gaseous ammonia (NH_3), forming sulphate aerosol (Kulmala et al., 2004). Aqueous phase reactions form sulphate aerosol efficiently with H_2O_2 and O_3 acting as oxidants (Seinfeld and Pandis, 2006). Wet deposition dominates the removal of sulphate aerosol. Therefore, elevated levels of SO_2 and NO_2 observed over the AOSR region are an environmental concern since atmospheric depositions of sulphur oxides (SO_x) and nitrogen oxides (NO_x) can lead to freshwater and soil acidification (Psenner, 1994; Zhao et al., 2009). Deposition of nitrogen compound can harm sensitive ecosystems through eutrophication (excessive nutrient richness) of water bodies (Fenn et al., 2015).

High concentrations of SO_2 and other pollutants over the AOSR have prompted measurements using aircraft studies (Baray et al., 2018; Gordon et al., 2015; Liggio et al., 2016, 2019; Simpson et al., 2010), in-situ measurements (Amiri et al., 2018; Hsu, 2013; Tokarek et al., 2018b), sun photometer (Fioletov et al., 2016a), and satellite (McLinden et al., 2012, 2014, 2016). Long-term monitoring through satellite measurements is an attractive choice due to the large scale of the operations. However, surface concentrations are difficult to determine accurately from satellite measurements (Fioletov et al., 2016a), and data acquisition is limited to the satellite overpass times. Satellite retrievals in the AOSR region are also complicated by multiple factors: landscapes are complex, emissions can change relatively rapidly, and the winds within the higher boundary layer can quickly disperse pollution emissions. Rapid industrial expansion can also require updating retrieval algorithms (McLinden et al., 2014). Apparent peak concentrations are reduced, and small-scale variability cannot be resolved, due to spatial averaging within the footprint of a pixel that can be large relative to the scale of point-source plumes.

SO_2, NO_2 and aerosol levels in the total column and near-surface can be simultaneously monitored using the Multi-Axis Differential Optical Absorption Spectroscopy (MAX-DOAS) technique (Honninger et al., 2004b). The elevated levels of SO_2 observed in the AOSR increase the ease of MAX-DOAS measurements compared to within most Canadian cities, where SO_2 levels are significantly lower. Differential Optical Absorption Spectroscopy (DOAS) is a remote sensing technique that quantifies tropospheric trace gases using light spectra and the unique spectral absorption cross-sections of trace gases. Since its introduction by Platt et al. (1979) DOAS has been used to

quantify trace gases in the troposphere, including NO_2, SO_2, OH, BrO, NO_3, NH_3, ClO and others. The technique has the advantage of allowing the simultaneous quantification of multiple trace gases Platt and Stutz (2008). The MAX-DOAS method measures scattered sunlight spectra at multiple viewing directions and/or elevation angles to allow sensitive quantification of tropospheric pollutants. Spectra measured at elevation angles close to horizon-pointing have a higher sensitivity to ground-level pollutants since the light paths are longer near the surface (Honninger et al., 2004b). Ground-based MAX-DOAS measurements determine tropospheric vertical column densities (VCDs) of trace gases, quantifying total boundary layer pollution loading. VCDs have the advantage of being independent of boundary layer height and are spatially averaged (horizontally) on the order of a few kilometres along the light path.

Ground-based MAX-DOAS data combined with radiative transfer modelling allows retrieval of vertical profiles of aerosol extinction and trace gases (Frieß et al., 2006; Honninger et al., 2004; Honninger and Platt, 2002; Irie et al., 2008; Wagner et al., 2004). The MAX-DOAS technique has been used to retrieve vertical profiles of aerosol extinction (Clemer et al., 2010; Frieß et al., 2011; Irie et al., 2008, 2015; Li et al., 2010; Zieger et al., 2011), BrO (Frieß et al., 2011; Honninger and Platt, 2002), HCHO (Heckel et al., 2005; Wagner et al., 2011), SO_2 (Tan et al., 2018) and NO_2 (Tan et al., 2018; Wagner et al., 2011).

There are few comparisons of vertical profiles of aerosol extinction from MAX-DOAS to vertical profiles from other instruments in the literature. MAX-DOAS aerosol extinction profiles have been compared to smoothed extinction profiles from a sun photometer (Frieß et al., 2011) and aircraft aerosol profiles (Wagner et al., 2011). Near-surface MAX-DOAS retrievals of aerosol extinction have been compared with in-situ measurements of aerosols (Zieger et al., 2011). There are also relatively few published comparisons of MAX-DOAS AODs with lidar AODs (Irie et al., 2008, 2015). Relatively few studies have focused on MAX-DOAS measurements of anthropogenic SO_2 (Irie et al., 2011; Jin et al., 2016; Wang et al., 2014, 2017; Wu et al., 2018, 2013). Most studies that present MAX-DOAS vertical profile retrievals compare them to trace gas VCDs or near-surface measurements from in-situ or LP-DOAS instruments. Tan et al. (2018) and Wang et al. (2017) compared MAX-DOAS SO_2 VCDs to satellite VCDs of trace gases. Tan et al. (2018) and Wagner et al. (2011) compared MAX-DOAS retrievals of vertical profiles of NO_2 to satellite VCDs and near-surface NO_2 mixing ratios from LP-DOAS, respectively.

In this study, a MAX-DOAS instrument was deployed during a comprehensive air quality campaign conducted during August and September 2013. Pollution conditions ranged from background to heavily polluted with a well-mixed boundary layer to distinctly elevated pollution plumes. Vertical profiles of aerosols, NO_2, and SO_2 in the troposphere were retrieved using optimal estimation inverse modelling from the MAX-DOAS measurements. These retrievals allowed characterization of the vertical structure of the boundary layer. The retrieval used a two-step approach: 1) aerosol extinction profiles are retrieved from measured MAX-DOAS O_4 Differential Slant Column Densities (dSCDs), and 2) the aerosol extinction profiles are used as forward model parameters for retrieval of trace gas profiles from measured trace gas dSCDs.

Our study adds to the current literature by comparing MAX-DOAS aerosol and trace gas retrievals with data from numerous other instruments deployed during the campaign. The aerosol retrievals were compared to aerosol extinction data from a co-located lidar instrument and a nearby sun photometer. Validation of the aerosol retrievals is essential because these profiles are used as model parameters for the trace gas retrievals. MAX-DOAS NO_2 and SO_2 retrievals were compared to mixing ratios from a co-located active-DOAS instrument and tropospheric VCDs of trace gas from a Pandora sun photometer. In-situ measurements of SO_2 from an aircraft allowed comparison of MAX-DOAS vertical profiles of SO_2. Evaluation of the retrievals was aided by co-located, near-surface measurements of particle size distribution and composition, and nearby, high-resolution measurements of vertical profiles of wind speed and -direction.

The objectives of our study were to 1) determine the factors required to validate MAX-DOAS aerosol retrievals through comparison with lidar and sun photometer data, 2) evaluate the performance of the aerosol and trace gas retrievals through comparison to other datasets, 3) identify conditions that limit the use of the MAX-DOAS technique, and 4) identify conditions under which the MAX-DOAS method was advantageous over other instruments.

This complex dataset from comprehensive measurements in the vicinity of oil sand operations provided a unique opportunity to test the performance of the MAX-DOAS aerosol and trace gas retrievals.

2.2 Experimental

2.2.1 Field Sites

The MAX-DOAS instrument (Hoffmann Messtechnik GmbH) measured scattered sunlight at an elevation of ~10 m above the surface from Aug. 14 – Sept. 9, 2013 at the Fort McKay South field site (57.149N, 111.642W) north of Fort McMurray, Alberta concurrent with an Environment and Climate Change Canada (ECCC) intensive measurement campaign (Figure 2-1 & A1). A second site was located 4km north of Fort McKay South (Oski-Ôtin; 57.184N, 111.640W) in the Fort MacKay community. Two major sources of aerosols, NO_2, SO_2 and other pollutants are located south of Fort McKay South: the Syncrude Mildred Lake Plant and the Suncor Millennium Plant, 12 km South and 20 km South-South-East, respectively (Figure 2-1). The 2013 NPRI reported emissions of SO_2 and NO_x from these facilities were 63 and 14 kilotonnes (kt) and 14 and 8 kt, respectively (ECCC, 2018a). Relatively smaller sources of pollutants are located north of Fort McKay South: Shell Jackpine and Muskeg River Mines, CNRL Horizon, and Imperial Oil Kearl Mine (Figure 2-1). Tables A1 and A2 show the 2013 NPRI emissions of SO_2 and NO_x from these five facilities. A recent study suggests that total industrial emissions of NO_x were underestimated in the NPRI report, particularly for ground sources (Zhang et al., 2018). Since there are NO_x sources that are not included in the NPRI emissions data, also included in Tables A1 and A2 are the 2010 vehicular emissions associated with each facility and 2012-2013 annual stack and area source emissions from Zhang et al. (2018).

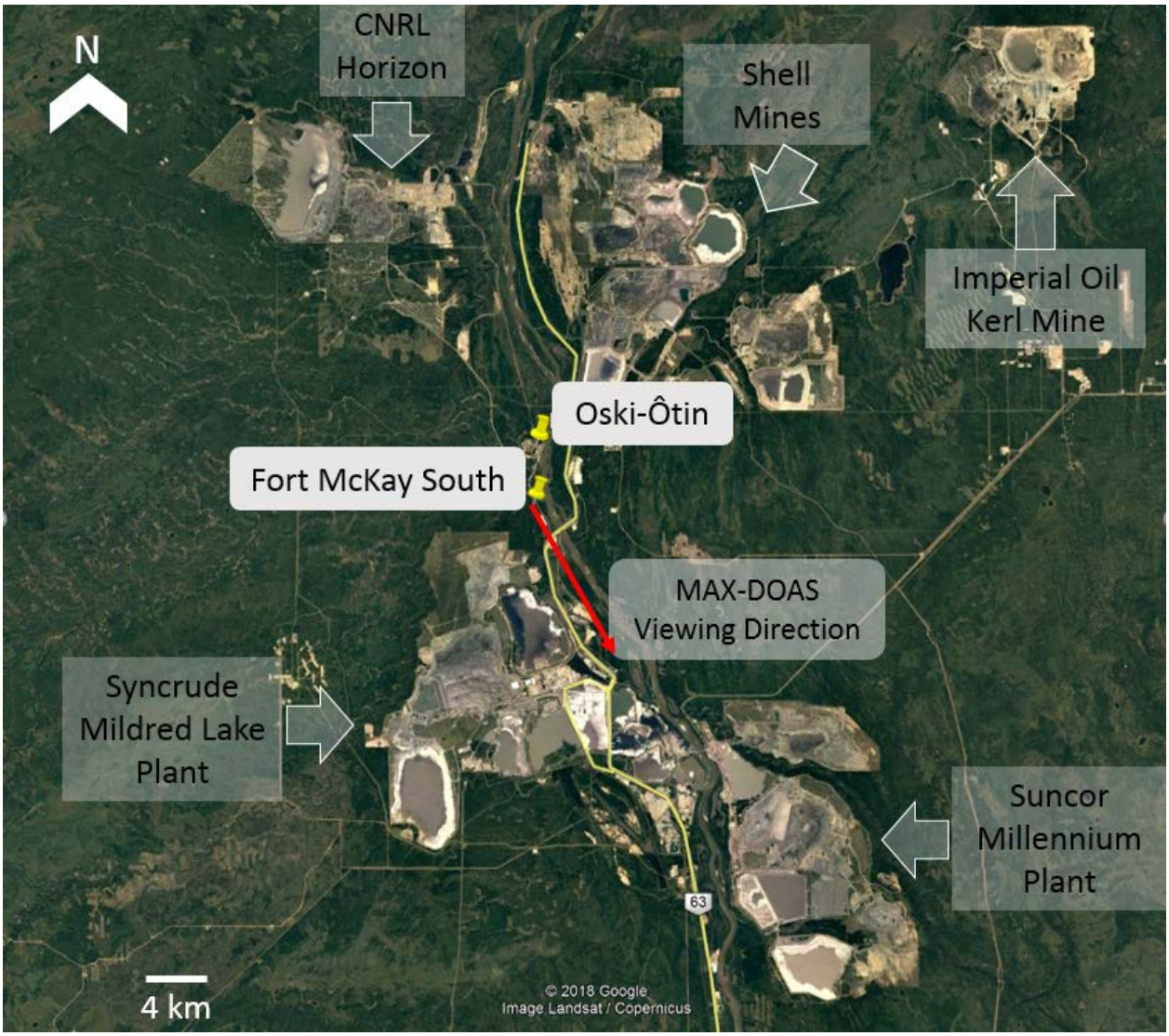

Figure 2-1 Location of field sites Fort McKay South and Oski-Ôtin and major industry sources.

2.2.2 Instrumentation

A mini-MAX-DOAS instrument measured scattered sunlight with a viewing azimuth angle of 155° South-South-East (SSE) at sequential viewing elevation angles 2°, 4°, 8°, 15°, 30° and 90° (zenith) above the horizon. The instrument consisted of a sealed metal box containing entrance optics, UV fibre-coupled spectrograph and all electronics. The instrument field of view was approximately 0.6°. Incident light was focused on a cylindrical quartz lens (focal length = 40 mm) into a quartz fibre that transmitted the light into the OceanOptics USB2000 spectrograph. The spectrograph detector was a Sony ILX511 linear silicon Charge-Coupled Device (CCD) array (2048 pixels, pixel size 14x200 microns, signal-to-noise ratio at full signal 250:1). The spectrograph had a spectral range of 290-433 nm, a 50 µm wide entrance slit and a spectral resolution of ~0.6 nm FWHM. The spectrograph was cooled by a Peltier stage to maintain the selected temperature (5°C). Spectrometer data was transferred to a laptop computer via USB cable. The instrument was controlled using the software package DOASIS, which allowed

automated measurements by JScript programs. The instrument was mounted on an elevated scaffold approximately 10 m above ground level (a.g.l.), approximately at the height of the surrounding forest canopy. Each recorded measurement spectrum was an average of 2000 measured spectra with an exposure time that varied between 50 and 200 milliseconds, depending on the ambient light levels.

MAX-DOAS aerosol and trace gas retrieved data were inter-compared with data from various other instruments deployed during the campaign.

Table 2-1 provides information on these instruments and papers that describe their operation.

An Active-DOAS instrument located at the same site was used to retrieve mixing ratios of NO_2 and SO_2 at 3.5 m a.g.l. Measurements of trace gases with the active-DOAS system have been described previously (McLaren et al., 2010, 2012; Wojtal et al., 2011) although details changed in the current study. DOAS measurements were made using a modified DOAS 2000 Instrument (TEI Inc.) utilizing a 150W high-pressure Xe-arc lamp and a coaxial Cassegrain telescope. The outgoing beam traversed the atmosphere for 1.15 km (pathlength =2.3 km) at an average height of 3.5 m a.g.l. where it impacted a retroreflector array composed of 30×2" hollow corner cubes mounted on a raiseable tower. The beam traversed through an exploration line cut (5-10 m wide × 2 km) in a mature coniferous forest. Return light was collected with a 2 m × 600 μm UV transparent fibre optic cable and spectrometer (Ocean Optics USB2000, Grating #10, λ=288-492 nm, 1800 lines mm^{-1}, 2048 element CCD, 25 μm slit, UV2 upgrade, L2 lens). Integration times of 30-40 ms and 4000 averages gave ≈ 2 min resolution with detection limits (3σ) of 120 pptv and 170 pptv for NO_2 and SO_2, respectively. Xenon lamp, Hg calibration, offset and dark noise spectra were collected for spectral fitting with DOASIS software. A small diffuser was installed in the entrance of the fibre to lower atmospheric turbulence noise (Stutz and Platt, 1993) in addition to using an optical fibre bending mode mixer.

A Pandora spectral sun photometer at Oski-Ôtin measured in direct-sun and zenith-sun viewing modes to retrieve total atmospheric column VCDs of SO_2 and NO_2 with precisions (1σ) of 4.6×10^{15} and 0.3×10^{15} molecules cm^{-2}, respectively (Fioletov et al., 2016a). Tropospheric VCDs of NO_2 were determined from the Pandora total column VCDs by subtracting stratospheric VCDs modelled using the PRATMO stratospheric photochemical box model (McLinden, 2000). PRATMO was used as described in Adams et al. (2016) except monthly-mean OSIRIS ozone profiles (Degenstein et al., 2009) and MODIS surface reflectivities (McLinden et al., 2014) were employed. The Pandora SO_2 VCDs presented are assumed to be representative of tropospheric SO_2 VCDs since stratospheric SO_2 was assumed to be negligible. Pandora trace gas and MAX-DOAS data were both available for inter-comparison for 4 days during the study. SO_2 and NO_2 mixing ratios were also measured from the air on board a Convair 580 research aircraft (Baray et al., 2018) using Thermo Scientific 43iTLE and 42i-TL analyzers, respectively, between 12 August and 7 September 2013, including a spiral ascent near Fort McKay South (Sept. 03).

Aerosol optical depths (AOD) at 380 nm and 340 nm were obtained from Level 2.0 AERONET data, measured by second sun photometer at Oski-Ôtin. Aerosol extinction profiles at 532 nm from 0.1-12 km a.g.l. were retrieved using a ground-based, zenith-pointing lidar operated at Fort McKay South (Strawbridge, 2013). In this study, the lidar profiles from 0.1-4 km were considered in order to match the vertical observation extent of the MAX-DOAS.

The lidar has the advantage over sun photometer instruments because it can determine the vertical profile of optical extinction rather than just a column-averaged value but has higher uncertainty when the S-ratio is variable (Strawbridge, 2013). Aerosol extinction profiles are retrieved from the measurements of the laser return signal using a chosen S-ratio value. The S-ratio is the ratio of the volume extinction coefficient to the backscatter coefficient and dictates the signal strength of the received return of the lidar's pulsed laser source (Strawbridge, 2013). Lidar S-ratios are known to be variable but are often estimated given the type of particles expected in an environment (Irie et al., 2015). The S-ratio depends on the shape, size distribution and chemical composition of the aerosol particles, as well as the relative humidity (Weitkamp, 2005). A constant lidar ratio ("S-ratio") of 25 was used for the lidar retrievals unless otherwise specified. S-ratios were modelled using Mie scattering theory and measurements of surface-level particle composition and size distribution at Fort McKay South for various times during Aug. 23 to determine temporal variability in the S-ratio. Source code for the Mie scatting calculations can be found in (Aggarwal et al., 2018).

Ground-level particle composition was measured using an Aerodyne high resolution soot-particle aerosol mass spectrometer (SP-AMS) (Lee et al., 2019). Particle size distributions were measured using Scanning Mobility Particle Sizer (SMPS) ("dry" line mode) and Aerodynamic Particle Sizer (APS) instruments (see supplementary information in (Tokarek et al., 2018b) for more details). Particle diameters measured by the SMPS and by the APS were 0.014-0.74 μm and 0.5-19.81 μm, respectively. Data from these instruments were combined to determine particle size distributions from 0.014 to 19.81 μm, assuming the particles were unit density. Use of "dry" line mode SMPS increased uncertainties in the size distributions because ambient aerosols have more volume than dry aerosols. However, even in the highest relative humidity range, the ambient aerosol had only 30% more volume compared to the dry aerosol which, assuming spherical particles, only results in a maximum increase in particle diameter of 9%. The resulting error is expected to be much smaller than other errors such as converting mobility and aerodynamic diameters to optical diameters.

A radio acoustic meteorological profiler (windRASS, model MFAS, Scintec, Germany) at Oski-Ôtin measured temperature, wind speed and -direction at 10 m intervals from 40 m to up to a maximum altitude of 800 m (Gordon et al., 2017).

Table 2-1 Description and locations of the study instruments.

Instrument	Variables Measured	Institution	Temporal Resolution	Viewing Direction	Field Site	Reference
Mini-MAX-DOAS	Vertical profiles of SO_2, NO_2, aerosol extinction	York University	20-30 minutes	SSE at multiple elevation angles	Fort McKay South	Current Paper
Active-DOAS	Mixing ratios of SO_2, NO_2	York University	~2 minutes	SE, horizontal	Fort McKay South	(McLaren et al., 2010)
Pandora Sun Photometer	VCDs of SO_2, NO_2	ECCC	~1 minute	Direct sun viewing	Oski-Ôtin	(Fioletov et al., 2016a)
Sun Photometer	AOD, Angstrom Exponent	ECCC	~3 minutes	Direct sun viewing	Oski-Ôtin	(Sioris et al., 2017)
Ground-based lidar	Vertical Profile of Aerosol Extinction	ECCC	1 minute	Zenith Viewing	Fort McKay South	(Strawbridge, 2013)
TSI APS 3321	PM_{10-1} Size Distribution	University of Calgary	6 minutes	N/A	Fort McKay South	(Tokarek et al., 2018b)
TSI SMPS (3081 DMA, 3776 CPC)	PM_1 size distribution	University of Alberta	6 minutes	N/A	Fort McKay South	(Tokarek et al., 2018b)
Aerodyne SP-AMS	rBC, $NH4^+_{(p)}$, $SO_4^{2-}{}_{(p)}$, $NO_3^-{}_{(p)}$, $Cl^-_{(p)}$, organics	University of Toronto and ECCC	~1 minute	N/A	Fort McKay South	(Lee et al., 2019)
Scintec model MFAS windRASS	Vertical profile of wind and temperature	ECCC	15 minutes	Zenith Viewing	Oski-Ôtin	(Gordon et al., 2017)
Airborne Thermo Scientific 43iTLE	Mixing ratios of SO_2	ECCC	1 second	N/A	N/A	(Baray et al., 2018)

2.2.3 MAX-DOAS Data Analysis

2.2.3.1 MAX-DOAS Fitting

Trace gas Differential Slant Column Densities (dSCDs) were obtained using the DOAS technique (Platt and Stutz, 2008) with DOASIS software (Institute of Environmental Physics, Heidelberg, Germany). All spectra were corrected for dark current and electronic offset and wavelength calibrated using a measurement of a Hg lamp. Table 2-2 shows the wavelength windows and fit components used to retrieve dSCDs of NO_2, SO_2 and O_4. Cross-sections

were obtained from the MPI-MAINZ UV/VIS Spectral Atlas of Gaseous Molecules of Atmospheric Interest (Keller-Rudek et al., 2013). Examples of spectral retrievals of the gases are shown in Figure A2. Each non-zenith measured spectrum was fit against the closest zenith spectrum in time, also known as the Fraunhofer Reference Spectrum (FRS). The statistical error of the O_4 dSCDs was $<1.1x10^{42}$ molecules cm^{-2}. The O_4 error for off-axis measurements relative to the FRS are <6% for angles below 30° and <10% for the 30° measurements. The statistical fit errors of the SO_2 and NO_2 dSCDs were $0.4\text{-}1.2x10^{16}$ and $0.4\text{-}1.6x10^{15}$ molecules cm^{-2}, respectively. Uncertainties in the absorption cross-sections result in systematic errors in the retrieved dSCDs. The reported uncertainty in the SO_2 and NO_2 absorption cross-sections used is approximately 3% (Bogumil et al., 2003a). The absolute value of the O_4 cross-section and its dependence on temperature is uncertain. Some studies suggest that the absolute value of the cross-section may be overestimated by up to 25%, requiring the use of a scaling factor (Clemer et al., 2010; Wagner et al., 2002, 2009). However, Frieß et al. (2011) found that the best results for measured O_4 dSCDs and the retrieved vertical profiles of aerosol extinction retrieved from them were achieved without a scaling factor. Irie et al. (2015) found that a scaling factor of 1.25 resulted in an overestimation of near-surface aerosol extinction coefficients (AECs) but also reduced residuals at high viewing elevation angles. Wagner et al. (2019) found that measured and radiative transfer modelled O_4 absorptions showed good agreement on one study day but poor agreement on the second. An O_4 scaling factor was not used for the O_4 fitting in this study because of 1) a lack of conclusive need based on the literature and 2) the good agreement between the lidar and MAX-DOAS AODs when the modelled S-ratios were applied to the lidar data (see discussion in Section 3.1.2).

The SO_2 fitting range was determined based on an experiment using an SO_2 calibration cell from Resonance Ltd. with a slant column density (SCD) of $2.2x10^{17}$ (± 10%) molecules cm^{-2} placed inside the MAX-DOAS telescope. Scattered solar light spectra were recorded around solar noon at multiple viewing elevation angles above the horizon, followed by a 90° measurement without the cell (the FRS). For each of the measured spectra, dSCDs of SO_2 were fit in DOASIS by varying the fitting windows in ~0.3 nm increments with a range of lower and upper limits of 303-318 nm 309-340 nm, respectively. The fit components are the same as in Table 2-2. See Appendix A, Section 2 for details. The NO_2 and O_4 fitting ranges were from McLaren et al. (2010) and Frieß et al. (2011), respectively.

Table 2-2 Information on MAX-DOAS spectral fitting.

Gas	Fitting Window	Included in the Fit
NO_2	410-435nm	FRS, Ring, Bogumil 2003 NO_2 (293K) and Bogumil 2003 (293K and 243K) O_3, 3rd order polynomial
SO_2	310.5-324nm	FRS, Ring, Bogumil 2003 SO_2 (293K) and Bogumil 2003 (293K and 223K) O_3, 3rd order polynomial, Offset Function
O_4	350-375nm	FRS, Ring, Hermans 2011 O_4 Bogumil 2003 (293K) NO_2, Bogumil 2003 (293K and 223K) O_3, 3rd order polynomial

2.2.3.2 Retrieval of Vertical Profiles from MAX-DOAS dSCDs using Optimal Estimation

Aerosol and trace gas profiles were retrieved using a two-step approach: 1) aerosol extinction profiles were retrieved from measured MAX-DOAS O_4 dSCDs and 2) aerosol extinction profiles were used as forward model parameters for retrieval of NO_2 and SO_2 profiles from dSCDs of NO_2 and SO_2, respectively. Vertical profiles were determined from dSCDs using retrieval algorithms based on the (Rodgers, 2000) optimal estimation technique (Frieß et al., 2011, 2016, 2019). Generally, the desired state of the atmosphere (**x**) can be estimated from remote sensing measurements (**y**) using a forward model **F**.

$$\mathbf{y} = \mathbf{F}(\mathbf{x}, \mathbf{b}) + \boldsymbol{\varepsilon} \quad (1)$$

Where $\boldsymbol{\varepsilon}$ is the measurement error and **b** is the vector of model parameters that are assumed to be known and not determined by the modelling, such as aerosol microphysical properties. In this study, the SCIATRAN radiative transfer model was used as the forward model (Rozanov et al., 2005).

The optimal estimation method determined the most probable atmospheric state, $\hat{\mathbf{x}}$, based on a set of measurements, **y**, and an a-priori state vector $\mathbf{x_a}$. The $\mathbf{x_a}$ was the best guess of the vertical profile to be retrieved. The $\hat{\mathbf{x}}$ was the aerosol extinctions or the trace gas mixing ratios at a series of altitude intervals, for the aerosol retrieval and trace gas retrievals, respectively. The **y** was the O_4 dSCDs and the trace gas dSCDs measured at different angles, for the aerosol and trace gas retrievals, respectively. Note that in our retrievals, **y** was the dSCDs measured at sequential elevation angles during 20-minute periods before 17:00 local time and during 30-minute periods after 17:00. The wavelengths for the optimal estimation retrievals of O_4, NO_2 and SO_2 were 360.8, 422.5, and 318.0 nm, respectively.

The optimal estimation solution $\hat{\mathbf{x}}$ is the maximum a posteriori (MAP) solution, which selects the most probable state from the set of possible states described by maximizing the probability of **x** occurring given the observations **y** (Rodgers, 2000). The MAP solution is found by minimizing the cost function (χ^2).

$$\chi^2 = (\mathbf{y} - \mathbf{F}(\mathbf{x}, \mathbf{b}))^T \boldsymbol{S_E^{-1}} (\mathbf{y} - \mathbf{F}(\mathbf{x}, \mathbf{b})) + (\mathbf{x} - \mathbf{x}_a)^T \boldsymbol{S_a^{-1}} (\mathbf{x} - \mathbf{x}_a) \quad (2)$$

where $\mathbf{S_a}$ and $\mathbf{S_E}$ are the error covariance matrices associated with the a-priori and measurement vectors, respectively (Rodgers, 2000). The retrieval yields important quantities that allow the characterization of the retrieval. These include the weighting function, $\boldsymbol{K} = \frac{\partial \mathbf{F}}{\partial \mathbf{x}}$, which quantifies the sensitivity of the measurement towards the atmospheric state, and the averaging kernel matrix, $\mathbf{A} = \frac{\partial \hat{\mathbf{x}}}{\partial \mathbf{x}}$, which quantifies the vertical resolution of the retrieval. **A** describes the sensitivity of the retrieved profile to changes in the true atmospheric profile. Rows of **A** are averaging kernels for each altitude interval in the retrieved profile. The full width half maximum (FWHM) of each kernel gives an estimate of the retrieval's vertical resolution at height z. Each averaging kernel ideally peaks at a magnitude of 1.0 at the height of the kernel. However, the peak value of a kernel is generally less than 1.0 due to finite vertical resolution and may peak at a slightly different height, resulting in the smoothing of the true atmospheric profile into the retrieved profile.

Aerosol Extinction Retrievals

Retrieval of aerosol extinction profiles was non-linear since the aerosol extinction affects the radiative transfer in the forward model. The input for the aerosol retrieval was the measurement vector of the O_4 dSCDs at different elevation angles and an a-priori state vector that decreased exponentially with altitude with a scale height of 0.6 km and a surface magnitude of $0.1 km^{-1}$. A single a-priori profile choice is preferable for a set of consecutive measurements where information content is potentially limited since the a-priori will always have some impact on the retrieved profile (Rodgers, 2000). Otherwise, diurnal and day-to-day trends in the retrieved profiles due to real atmospheric changes could be indistinguishable from changes due to a variable a-priori profile.

Our aerosol retrieval used an iterative algorithm based on the Levenberg-Marquart method (Levenberg, 1944; Marquardt, 1963). For aerosol retrievals, the weighting function **K** is calculated using the a-priori $\mathbf{x_a}$ and the measurement vector **y**. The **K** of each retrieval depended on the state vector and changed depending on the determined aerosol extinction profile. The height resolution of the aerosol extinction vertical profile grid was 100 m with a maximum height of 4 km. A detailed description of the aerosol retrieval algorithm can be found in (Frieß et al., 2006).

Trace gas Retrievals

The retrievals of NO_2 and SO_2 vertical profiles were linear because these weak absorbers do not significantly impact the radiative transfer. The inputs for the NO_2 and SO_2 retrievals were the measurement vectors of the NO_2 and SO_2 dSCDs at different elevation angles, respectively, and an a-priori state vector that decreased exponentially (scale height = 0.6 km and surface magnitude = 30 ppbv and 10 ppbv for SO_2 and NO_2, respectively).

In this linear case, the forward model is independent of the atmospheric state **x**, and the weighting function matrix represents the forward model.

$$\mathbf{y} = \mathbf{F}(\mathbf{x}, \mathbf{b}) + \boldsymbol{\varepsilon} = \mathbf{K}\mathbf{x} + \boldsymbol{\varepsilon} \qquad (3)$$

In our retrieval, the box-air mass factors (AMF) that are components of **K** were modelled using the Monte Carlo radiative transfer model in SCIATRAN (Deutschmann et al., 2011; Frieß et al., 2010). The aerosol profiles retrieved in step 1 were used to recalculate the Box-AMFs for each trace gas retrieval since the extinction profiles varied. The height resolution of the trace gas vertical profile grid was 100 m with a maximum height of 4 km a.g.l.

Determination of Retrieval Errors

The retrieval covariance matrix $\widehat{\boldsymbol{S}}$ quantifies the error of the state vector and is the sum of the independent sources of error: smoothing error $\boldsymbol{S_s}$, representing the retrieval's limited vertical resolution, and the retrieval noise $\boldsymbol{S_M}$, representing the uncertainty due to errors in the measurement. $\widehat{\boldsymbol{S}} = \boldsymbol{S_M} + \boldsymbol{S_s}$. The error covariance matrix produced by the retrieval does not include model parameter errors or forward model errors (Frieß et al., 2006). The error covariance matrix is calculated following Eq. (4):

$$\widehat{\boldsymbol{S}} = \left(\boldsymbol{K}^{\boldsymbol{T}}\boldsymbol{S}_{\boldsymbol{\varepsilon}}^{-\mathbf{1}}\boldsymbol{K} + \boldsymbol{S}_{\boldsymbol{a}}{}^{-\mathbf{1}}\right)^{-\mathbf{1}} \quad (4)$$

$\mathbf{S_E}$ and $\boldsymbol{S_a}$ are the measurement and a-priori covariance matrices, respectively. In our retrievals, $\boldsymbol{S_a}$ was determined by setting the relative error of the a-priori to 100%. The $\mathbf{S_E}$ was the diagonal matrix of errors of the retrieved dSCDs as determined by the DOASIS retrievals.

2.3.3 Conversion of Other Instruments' Data for Comparison to MAX-DOAS Data

Lidar and AERONET extinction data were converted to the MAX-DOAS aerosol retrieval wavelength of 361 nm following Eq. (5):

$$E(361nm) = E(\lambda_1) * \left(\frac{361nm}{\lambda_1}\right)^{-\propto} \quad (5)$$

Equation (5) accounts for the dependence of aerosol extinction on wavelength based on the Angstrom exponent, $\propto$. AERONET 300-500nm and 340-440nm Angstrom exponents were used to convert the 532 nm lidar aerosol extinctions and the 380 nm and 340 nm AERONET AODs, respectively. The two resulting AERONET AODs at 361 nm were then averaged. The Angstrom exponent was assumed to be constant with altitude and representative of both field sites. The similarity in trends in AODs and trace gas VCDs between the two sites can indicate when the Angstrom exponent determined from Oski-Ôtin was valid for both sites.

Due to the limited vertical resolution of the MAX-DOAS measurements, MAX-DOAS vertical profiles of aerosol extinction and AODs can only be directly compared to lidar profiles and AODs after smoothing the 361 nm lidar profiles using the MAX-DOAS averaging kernel matrix, **A** (Rodgers and Connor, 2003). The lidar AODs referred to in the paper below and shown in plots are the smoothed AODs determined by vertically integrating the smoothed lidar vertical profiles of extinction at 361 nm unless otherwise stated.

The lidar profiles were averaged into the same altitude and temporal intervals as the MAX-DOAS retrievals and then smoothed using the respective matrix **A** following Eq. (6):

$$\boldsymbol{x}_s = \boldsymbol{x}_a + \boldsymbol{A}(\boldsymbol{x}_L - \boldsymbol{x}_a) \quad (6)$$

Where $\boldsymbol{x}_s$ is the smoothed lidar profile, $\boldsymbol{x}_a$ is the MAX-DOAS retrieval a-priori profile and $\boldsymbol{x}_L$ is averaged lidar profile. $\boldsymbol{x}_s$ represents the (noise-free) vertical profile that the MAX-DOAS retrieval would produce if $\boldsymbol{x}_L$ was the true atmospheric profile given the variable sensitivity of the MAX-DOAS retrieval with altitude. The deviation of $\boldsymbol{x}_s$ from $\boldsymbol{x}_L$ at each altitude depends on $\boldsymbol{x}_a$ and the sensitivity of the MAX-DOAS to the atmosphere at that altitude. MAX-DOAS sensitivity to the true atmospheric state decreases with increasing altitude (Frieß et al., 2006) with typical height resolutions of ~200 m at lower altitudes, increasing to ~700 m at higher altitudes. Therefore, the smoothing is generally expected to smooth the true profiles towards lower altitudes. Also, even if the two instruments viewed the same air mass, the retrieved and smoothed profiles are expected to differ at least slightly due to two factors. The first factor is the retrieval noise $\boldsymbol{G\varepsilon}$, which is unknown since the true measurement error $\boldsymbol{\varepsilon}$ is

unknown. $\boldsymbol{G}$ is the gain matrix, which describes the retrieval's sensitivity to the measurements. The true smoothed profiles would be described using the following Eq. (7):

$$\boldsymbol{x_{retrieved}} = \mathbf{x}_a + \mathbf{A}(\mathbf{x}_{true} - \mathbf{x}_a) + \boldsymbol{G\varepsilon} \quad (7)$$

The second factor is that lidar vertical profiles observed straight up, measured only above 100 m a.g.l. and are the least sensitive close to the surface. The 0-100 m a.g.l. extinction in the lidar profiles was assumed to be equal to the average extinction measured between 100-200 m a.g.l. but the vertical profiles may have been variable below 150 m a.g.l. Uncertainty in the lidar vertical profiles is greatest in the lowest 150 m a.g.l., introducing uncertainty into the smoothed lidar profiles.

Error bars on the MAX-DOAS AODs, VCDs and mixing ratios shown in figures were obtained from the optimal estimation retrieval. Error bars on the lidar and AERONET AODs are the standard error of the temporally averaged values since these instruments have a finer time resolution than the MAX-DOAS retrievals. Error bars on the active-DOAS mixing ratios are the root sum square errors of the standard error of the averaged values and the average error reported by the respective DOASIS retrievals. Error bars on the Pandora VCDs are root sum square errors of the standard error of the average values and the reported instrumental precision. Deming fit linear regressions were performed using the Monte Carlo method, which included the errors on the *x* and *y* data, with the "linfitxy" function in MATLAB (Browaeys, 2017). The Aug. 23 and Sept. 03 AERONET and Pandora data were also correlated with MAX-DOAS and lidar data by subtracting 30 minutes from the Oski-Ôtin data to account for the time of air mass transport between the Fort McKay South and Oski-Ôtin given the wind-speeds.

2.3 Results and Discussion

This paper discusses results from largely cloud-free days when industrial plumes were observed (Aug. 23, Sept. 03, Sept. 04, Sept. 06, Sept. 07) and one day with clean conditions (Sept. 05). Nine days are not discussed due to the presence of clouds most of the day.Vertical profiles of wind speed and -direction measured by the windRASS are shown in Figure 2-2 and Figure 2-3, respectively. A summary of wind conditions and pollution levels for each day is shown in Table 2-3.

Aug. 23 exhibited the greatest enhancements in aerosol and trace gas pollution during the study. Wind-directions in the morning were North to East-North-East and South-East to South-South-West in the afternoon. Winds were relatively low-speed with minimal wind shear. The pollution enhancement periods were associated with Southerly (S) winds, suggesting that air-masses rich in industrial emissions originated from the Syncrude and Suncor mining areas south of the sites (Figure 2-1). The pollution enhancements impacted both sites (AMS 13 and Oski-Ôtin).

Sept. 03 exhibited moderate pollution levels. Pollution data is only presented from 11:00 onwards due to the presence of clouds before this time. Wind-directions varied from South-East to South-South-West with occasional South-West to North-West winds. Significant wind-shear was observed in the vertical profiles of wind. The pollution enhancements impacted both sites.

Table 2-3 Daytime wind and pollution conditions during the study days.

Date	Wind-Directions	Wind-Speeds	Wind-Shear	Pollution Levels
Aug. 23	Morning: N to ENE Afternoon: SE to SSW	Low	Minimal	Low to very high
Sept. 03	Variable; mostly SE to SSW	Low to Moderate	Significant	Moderate to High
Sept. 04	Mostly S to SE	Low to Moderate	Significant	Low to moderate
Sept. 05	WSW to W	High	Moderate	Very Low
Sept. 06	N to NE	Low near the surface, high aloft	Significant	Low to moderate
Sept. 07	Morning: SSE Afternoon: SW to SSW	Morning: low Afternoon: moderate to high	Significant	Low to moderate

Sept. 04 exhibited moderate pollution levels. Wind-directions were frequently South to South-Easterly with intermittent periods of South-West and North-West winds. Significant wind shear was observed: wind-directions tended to rotate clockwise from South-South-East near the surface to North-East as altitude increased. The limited afternoon wind data suggest North-West winds. Wind speeds were low to moderate, tending to increase with altitude. The pollution enhancements impacted both sites.

Sept. 05 exhibited the cleanest conditions and greatest wind-speeds during the study. Winds were West-South-West to Westerly. Both sites were impacted by air-masses that passed over boreal forests.

Sept. 06 exhibited low to moderate pollution enhancements in the morning with low pollution conditions in the afternoon. Winds were North to North-Easterly but varied over time and with altitude. Wind-speeds tended to be low at the surface but moderate to large at higher altitudes; significant wind-shear was present. Fort McKay South was impacted by emissions from facilities north of the sites: Shell Jackpine and Muskeg River Mines, CNRL Horizon, and Imperial Oil.

Sept. 07 exhibited moderate to low pollution. Winds-directions were South-South-East during the morning and South-West to South-South-West during the afternoon. Significant wind shear was observed in the lowest 400 m a.g.l. between 9:00 and 11:00 and during the afternoon around 16:00. Different air-masses may have impacted the two sites.

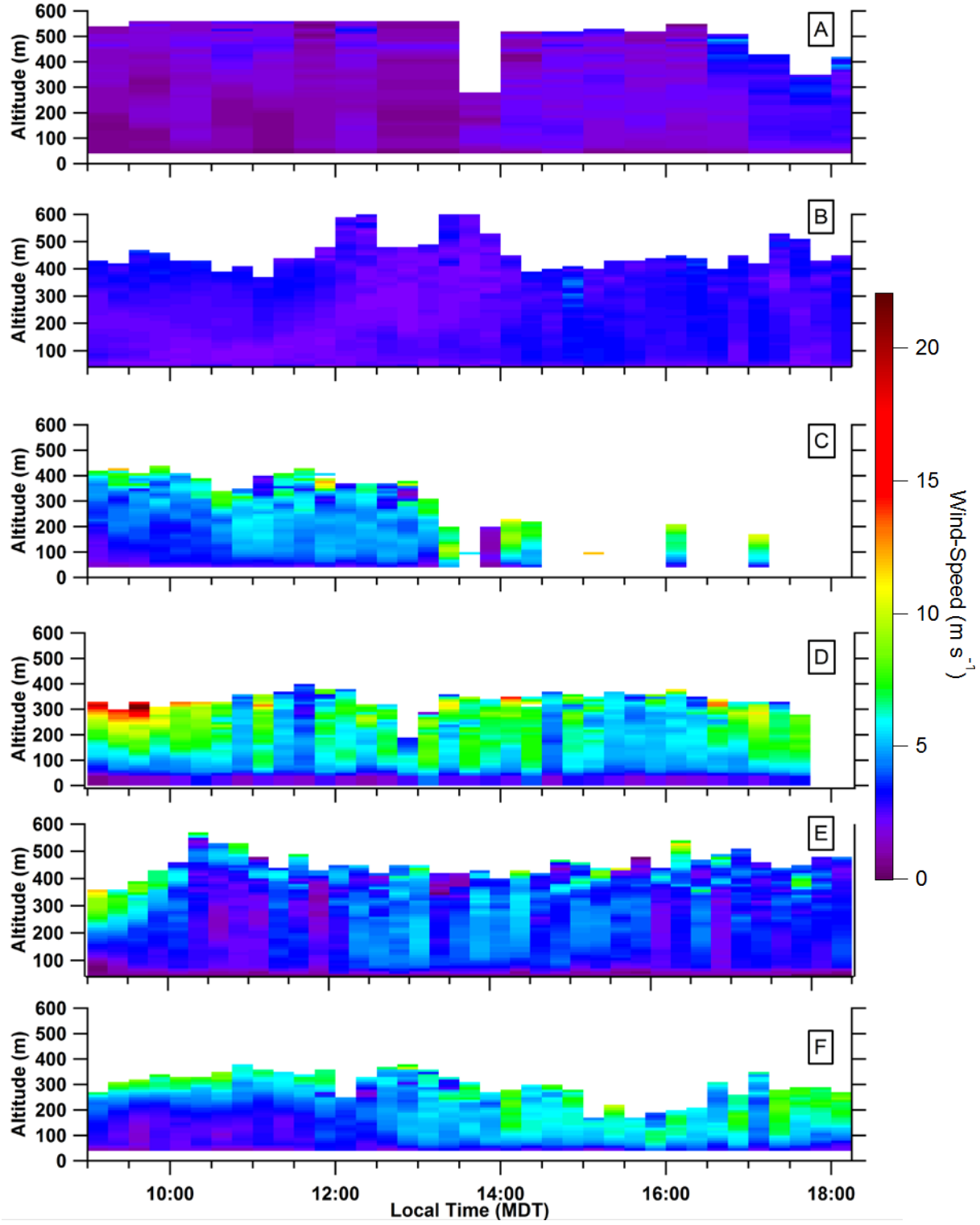

Figure 2-2 Vertical profiles of wind speed: Aug. 23 (A), Sept. 03 (B), Sept. 04 (C), Sept. 05 (D), Sept. 06 (E), and Sept. 07 (F).

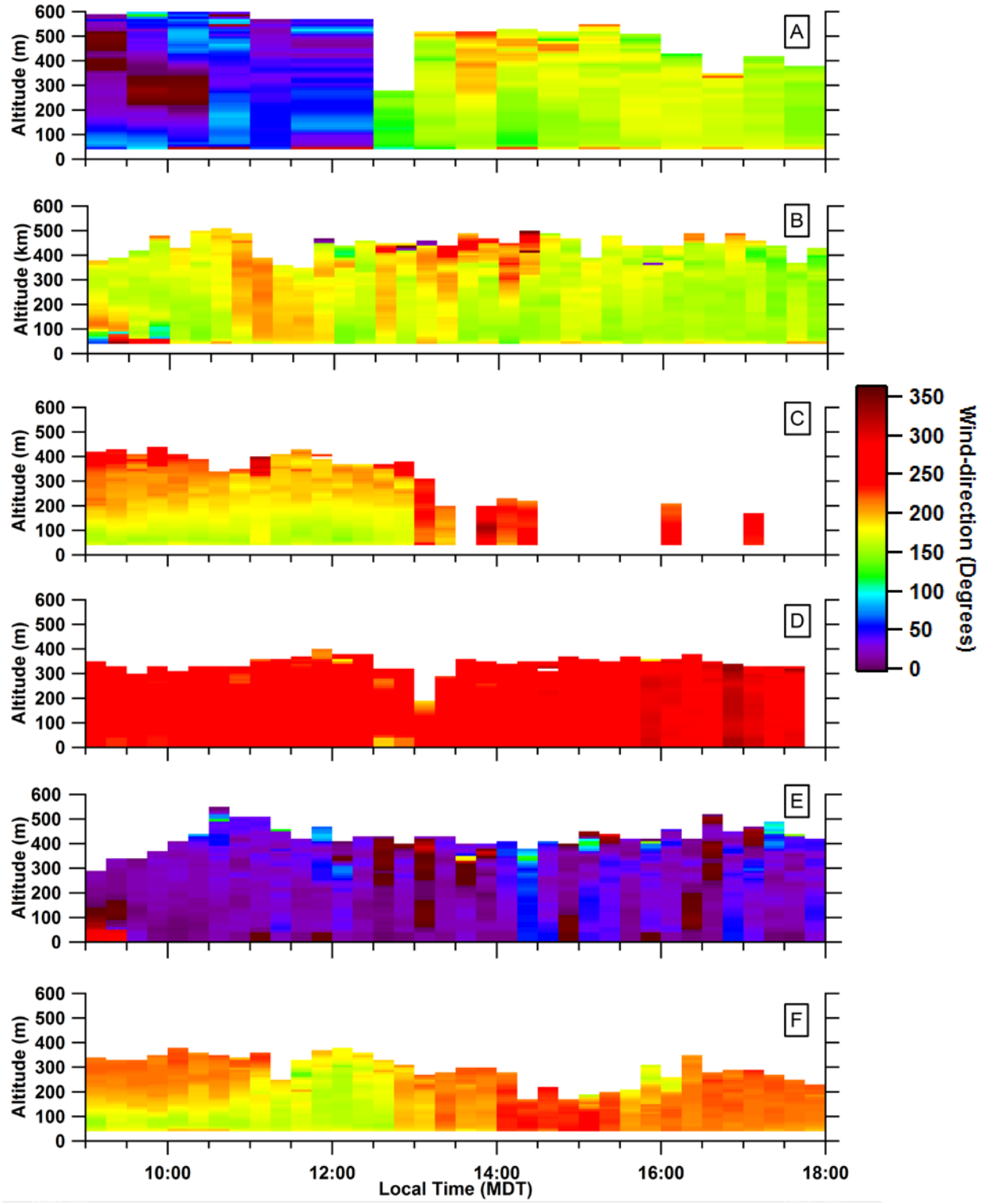

Figure 2-3 Vertical profiles of wind direction: Aug. 23 (A), Sept. 03 (B), Sept. 04 (C), Sept. 05 (D), Sept. 06 (E), and Sept. 07 (F).

2.3.1 Inter-comparisons of MAX-DOAS aerosol retrievals with lidar and AERONET data

The AODs from the MAX-DOAS, lidar and AERONET sun photometer instruments exhibited similar temporal trends on Aug. 23, Sept. 03, Sept. 04, Sept. 05 and Sept. 07 (Figure 2-4 to Figure 2-9(a)). The MAX-DOAS AODs were statistically different from the lidar and AERONET AODs for approximately half the data, even when the two sites experienced the same air-masses. This result is expected based on three factors: 1) the different vertical extents of the atmosphere observed by the instruments, 2) temporal variability in the lidar S-ratio, and 3) the limited sensitivity of the MAX-DOAS measurements at higher altitudes. These factors will be discussed below to evaluate the performance of the MAX-DOAS AOD retrievals under various atmospheric conditions.

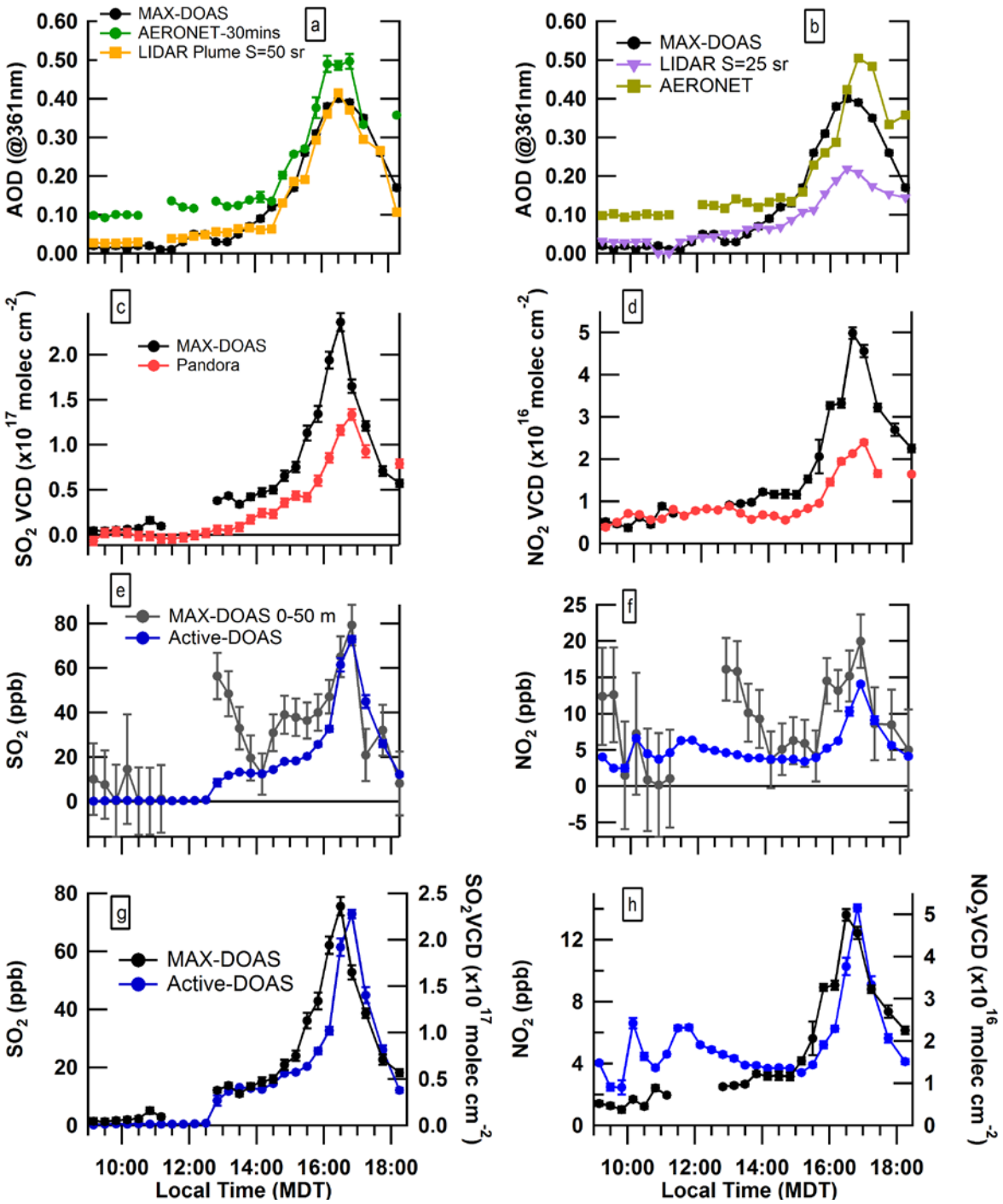

Figure 2-4 Aug. 23 AODs from MAX-DOAS, lidar (S-ratio=44 sr >14:30), and AERONET (-30 mins.) (a); AODS from MAX-DOAS, lidar (S-ratio = 25 sr), and AERONET (b); MAX-DOAS and Pandora SO_2 VCDs (c); MAX-DOAS and Pandora NO_2 VCDs (d); MAX-DOAS 0-100 m and Active-DOAS SO_2 mixing ratios (e); MAX-DOAS 0-100 m and Active-DOAS NO_2 mixing ratios (f); MAX-DOAS VCDs and Active-DOAS mixing ratios of SO_2 (g); and MAX-DOAS VCDs and Active-DOAS mixing ratios of NO_2 (h).

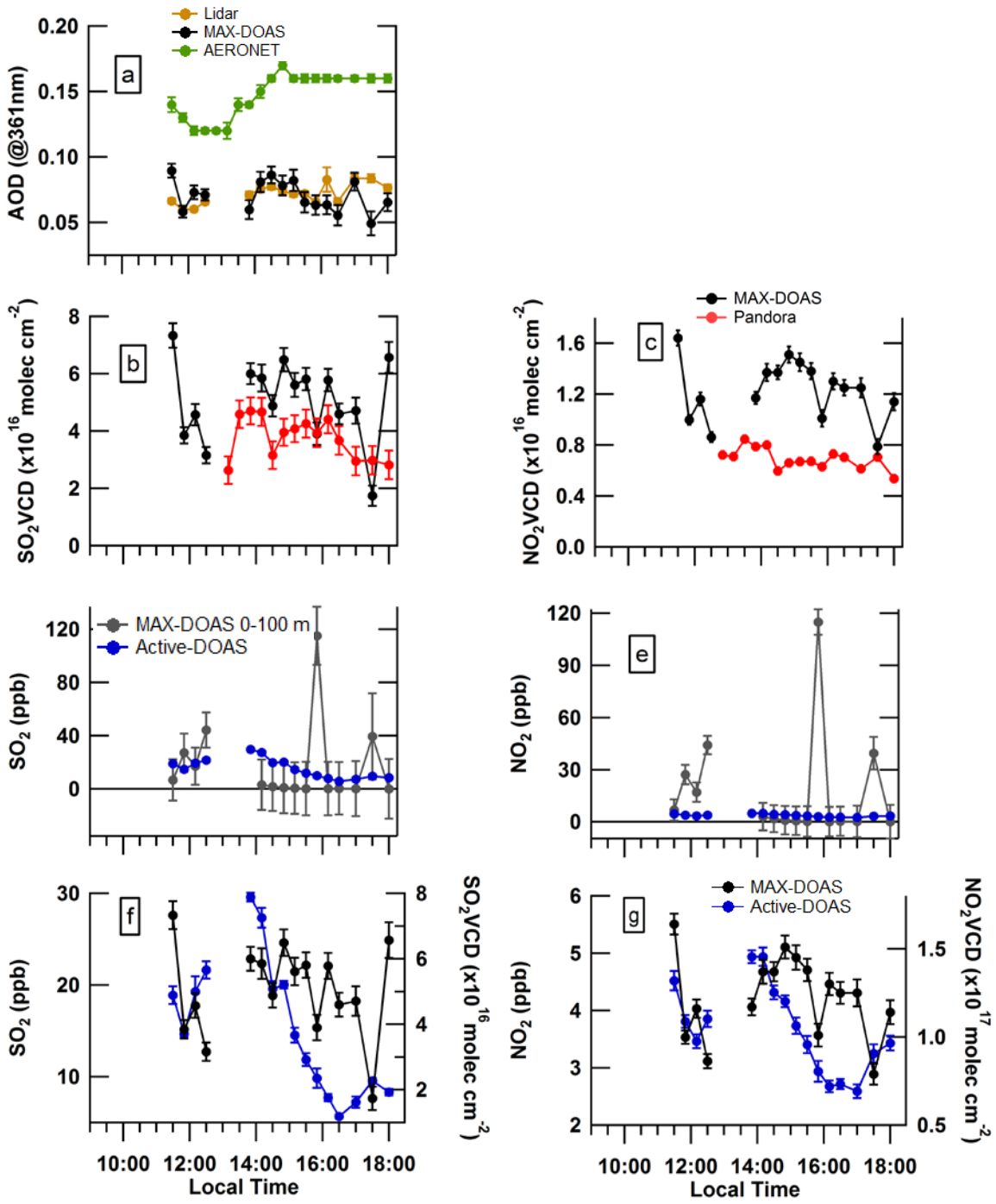

Figure 2-5 Sept. 03 AODs from MAX-DOAS, lidar, and AERONET (a); MAX-DOAS and Pandora SO_2 VCDs (b); MAX-DOAS and Pandora NO_2 VCDs (c); MAX-DOAS 0-100 m and Active-DOAS SO_2 mixing ratios (d); MAX-DOAS 0-100 m and Active-DOAS NO_2 mixing ratios (e); MAX-DOAS VCDs and Active-DOAS mixing ratios of SO_2 (f); and MAX-DOAS VCDs and Active-DOAS mixing ratios of NO_2 (g).

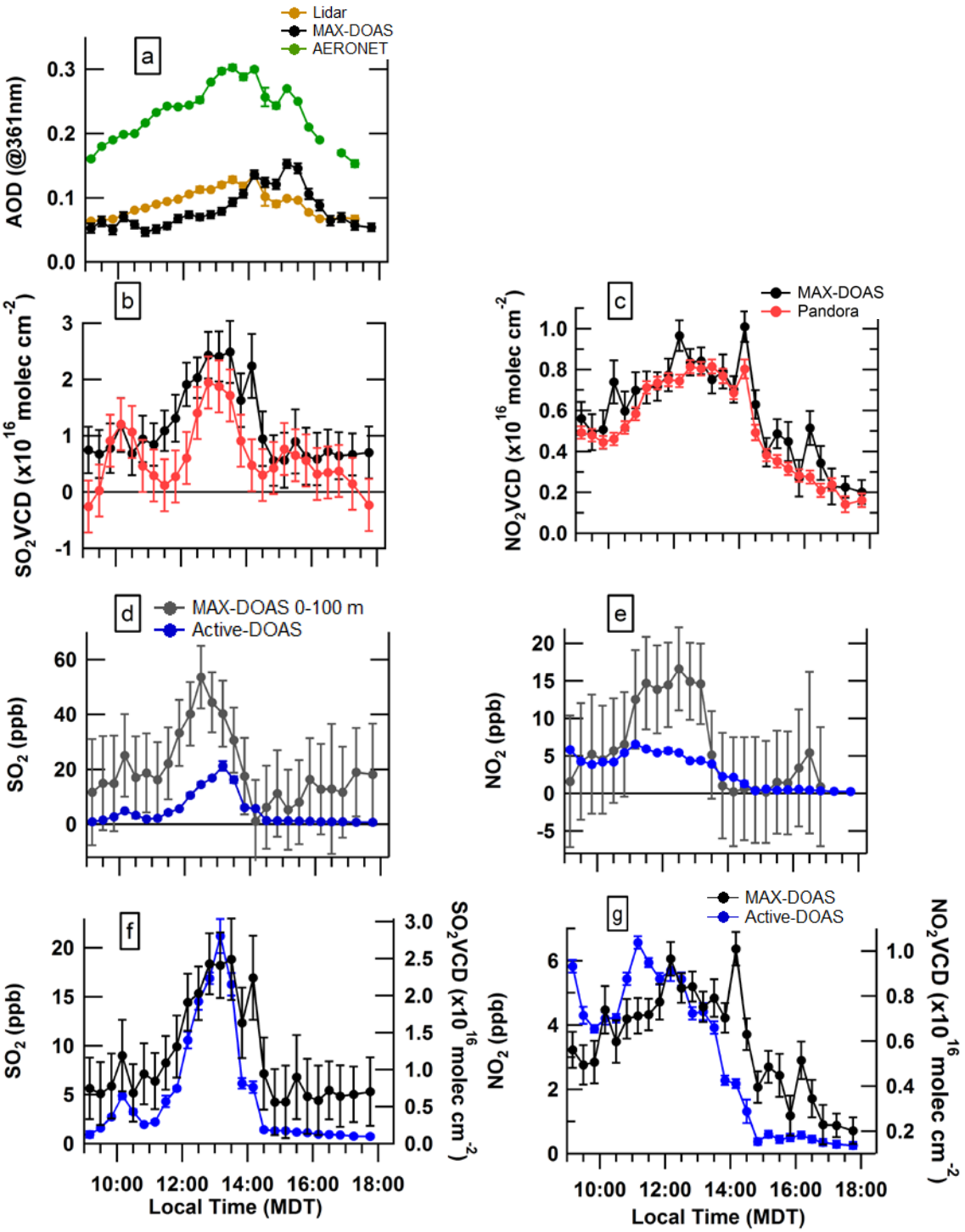

Figure 2-6 Sept. 04 AODs from MAX-DOAS, lidar, and AERONET (a); MAX-DOAS and Pandora SO_2 VCDs (b); MAX-DOAS and Pandora NO_2 VCDs (c); MAX-DOAS 0-100 m and Active-DOAS SO_2 mixing ratios (d); MAX-DOAS 0-100 m and Active-DOAS NO_2 mixing ratios (e); MAX-DOAS VCDs and Active-DOAS mixing ratios of SO_2 (f); and MAX-DOAS VCDs and Active-DOAS mixing ratios of NO_2 (g).

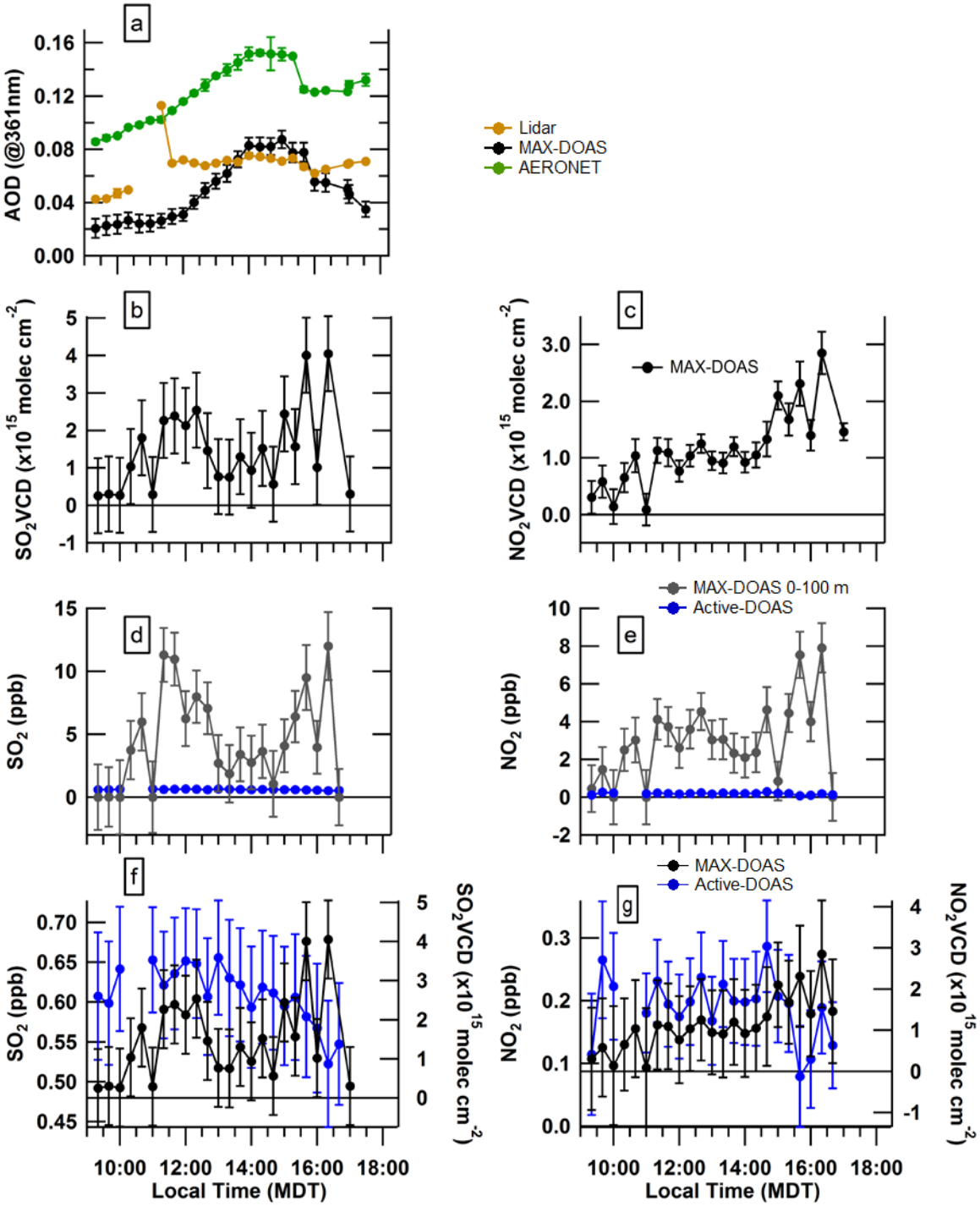

Figure 2-7 Sept. 05 AODs from MAX-DOAS, lidar, and AERONET (a); MAX-DOAS SO_2 VCDs (b); MAX-DOAS NO_2 VCDs (c); MAX-DOAS 0-100 m and Active-DOAS SO_2 mixing ratios (d); MAX-DOAS 0-100 m and Active-DOAS NO_2 mixing ratios (e); MAX-DOAS VCDs and Active-DOAS mixing ratios of SO_2 (f); and MAX-DOAS VCDs and Active-DOAS mixing ratios of NO_2 (g).

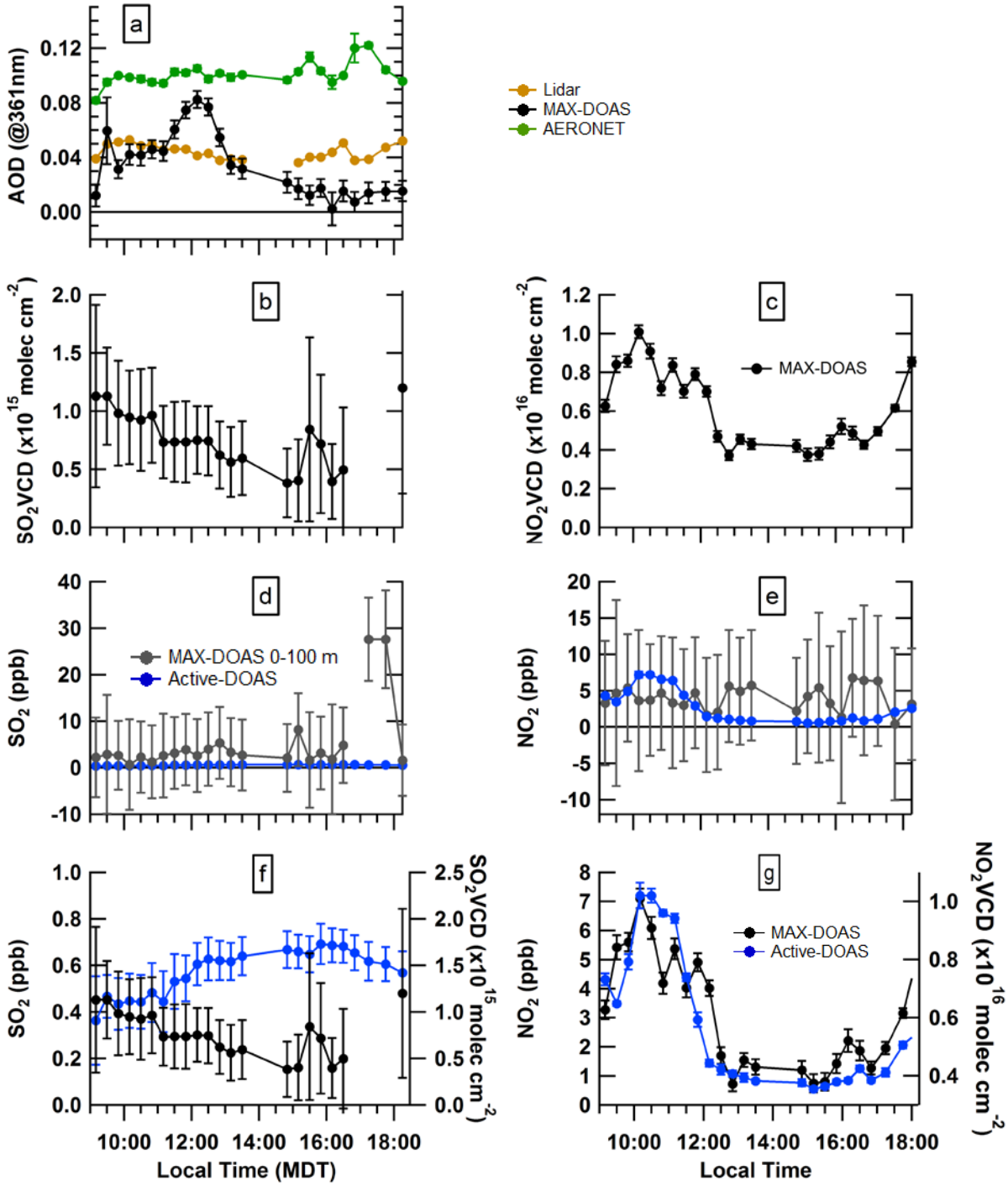

Figure 2-8 Sept. 06 AODs from MAX-DOAS, lidar, and AERONET (a); MAX-DOAS SO_2 VCDs (b); MAX-DOAS NO_2 VCDs (c); MAX-DOAS 0-100 m and Active-DOAS SO_2 mixing ratios (d); MAX-DOAS 0-100 m and Active-DOAS NO_2 mixing ratios (e); MAX-DOAS VCDs and Active-DOAS mixing ratios of SO_2 (f); and MAX-DOAS VCDs and Active-DOAS mixing ratios of NO_2 (g).

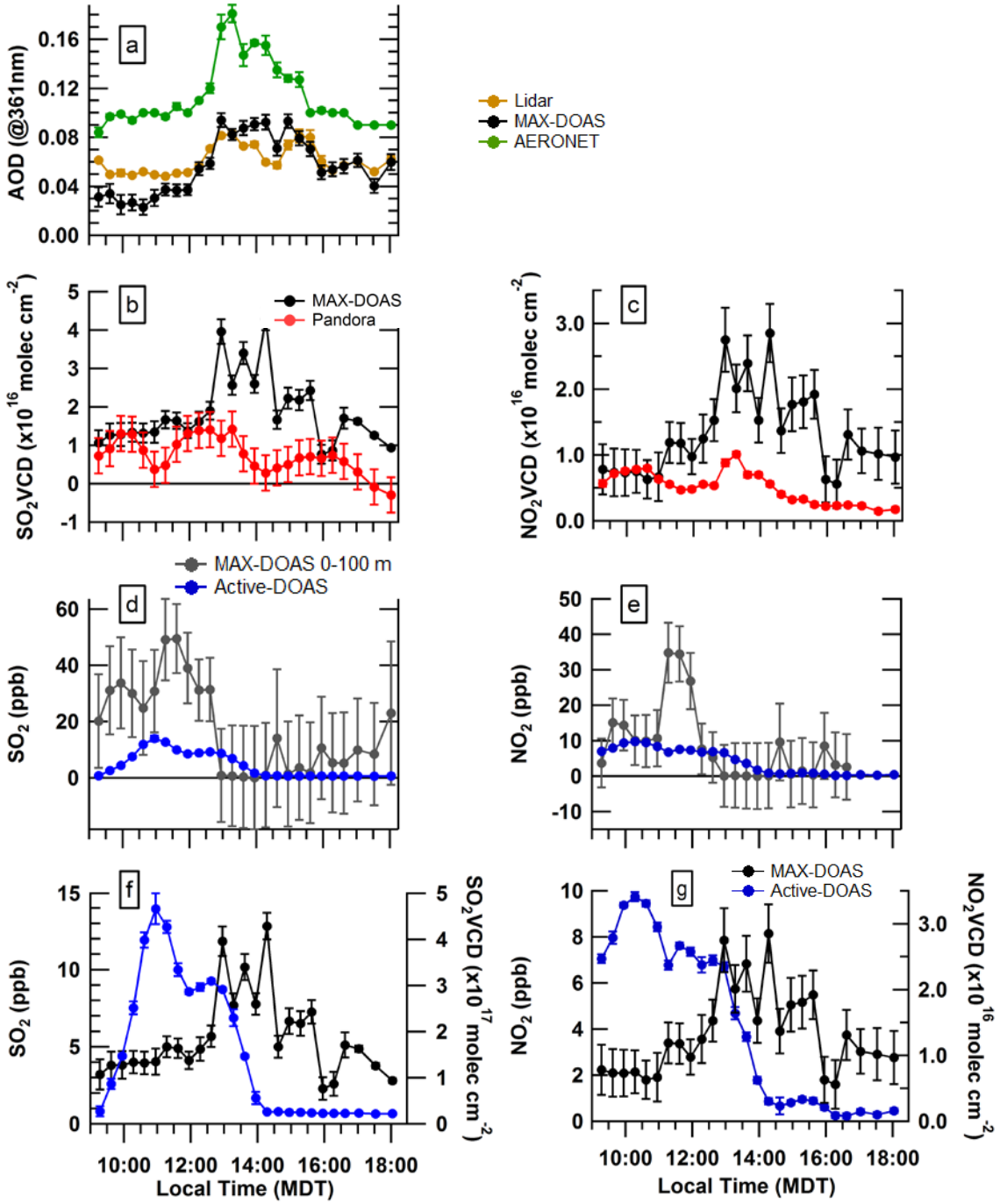

Figure 2-9 Sept. 07 AODs from MAX-DOAS, lidar, and AERONET (a); MAX-DOAS and Pandora SO_2 VCDs (b); MAX-DOAS and Pandora NO_2 VCDs (c); MAX-DOAS 0-100 m and Active-DOAS SO_2 mixing ratios (d); MAX-DOAS 0-100 m and Active-DOAS NO_2 mixing ratios (e); MAX-DOAS VCDs and Active-DOAS mixing ratios of SO_2 (f); and MAX-DOAS VCDs and Active-DOAS mixing ratios of NO_2 (g).

2.3.1.1 Impact of Instrumental Vertical Sensitivity on AOD

AERONET AODs were generally significantly greater than MAX-DOAS and lidar AODs, except during the greatest pollution events (Figure 2-4 to Figure 2-9 (a)). During the low-pollution day of Sept. 05, AERONET AODs reached a maximum of 0.15±0.00 while maximum MAX-DOAS AODs were 0.08±0.01 (Figure 2-4 (b)). On Sept. 05 the MAX-DOAS and AERONET AODs had a slope of linear correlation of 1.04±0.08 (R^2=0.77) but had a linear intercept of -0.08±0.01 km^{-1}. This negative intercept can be attributed to aerosol loading above the boundary layer that was observed by the sun photometer but not by the MAX-DOAS. This result is expected because the AERONET sun photometer observed aerosol extinction throughout the entire column (tropospheric and stratospheric) while the MAX-DOAS and smoothed lidar profiles observed up to 4 km. Further, the MAX-DOAS retrieved and smoothed lidar profiles likely only captured enhancements below 2 km because of the exponentially decreasing a-priori profiles used and the decreasing sensitivity of the MAX-DOAS retrieval with increasing altitude. The MAX-DOAS and smoothed lidar AODs are, therefore, expected to be significantly smaller than the AERONET AODs when the aerosol extinction in the boundary layer was "clean" and contributed a small fraction to the total tropospheric extinction (e.g., Figure 2-10; Aug. 23_9:10). MAX-DOAS AODs were also significantly smaller than AERONET AODs even under moderately polluted conditions when the magnitudes of the aerosol extinction remained enhanced above the boundary layer. On Sept. 04 the extinctions above the boundary layer could be relatively large, ~1/3 the near-surface extinctions (Figure 2-10 & Figure 2-15 (a)), leading to much smaller MAX-DOAS AODs than AERONET AODs (Figure 2-6 (a)). Aerosols can be non-trivial in the free troposphere since fine mode particles can remain in the atmosphere for days (Zhong and Zaveri, 2017). These results indicate that the ratio of the MAX-DOAS AODs to AERONET AODs depends on the location of the aerosol extinction within the tropospheric profile. The use of simple linear regressions to evaluate the performance of MAX-DOAS AOD retrievals using sun photometer AODs may be appropriate only when the aerosol extinction in the boundary layer dominates the total tropospheric AOD.

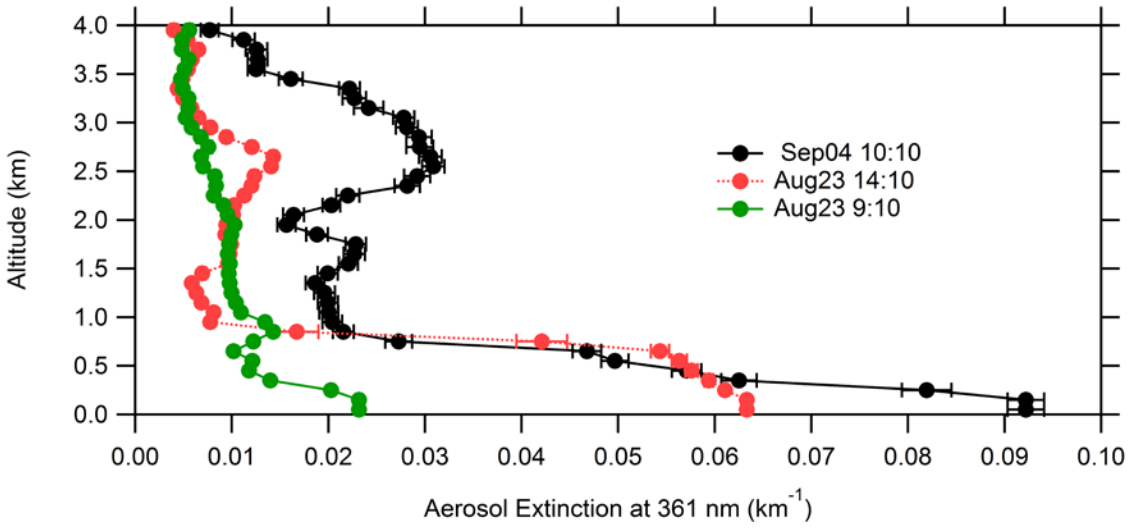

Figure 2-10 Examples lidar vertical profiles of aerosol extinction (averaged into MAX-DOAS retrieval height intervals and times) on Aug. 23 and Sept. 04.

2.3.1.2 Impact of S-ratio Variability on Lidar AODs

MAX-DOAS AODs significantly exceeded the smoothed lidar AODs during the most polluted periods (Figure 2-4 (b)). This result is unexpected, given that the instruments' AODs should ideally be equal when the instruments observed the same airmasses. However, the deviation can be explained by variation in the lidar S-ratio. The S-ratio of 25 steradians (sr) appears accurate during relatively clean periods (e.g., Sept. 05, Aug. 23 morning) but an underestimation under the industrially polluted conditions of the afternoon of Aug. 23 (Figure 2-4 (b) & Figure 2-12). Modeled S-ratios for Aug. 23 were 21-28 sr during the low pollution morning and 36-44 sr during the peak pollution enhancement at ~16:50 (Table 2-4). The morning S-ratios were calculated using the refractive indices of toluene or kaolinite, based on the dominance of organic particles and dust in the region during background atmospheric conditions (Figure 2-11 (a)). The afternoon S-ratios were modelled using the refractive index of sulphate particles based on the significant enhancement in sulphate particle loading (Figure 2-11 (a)). Increased loading of sulphate particles tends to increase the S-ratio. Note that the 16:50 S-ratios were greater than the morning S-ratios for all refractive indices because the particle size distribution of the industrial plume (fine-mode dominated) increased the S-ratio. The modelled variability in the S-ratio is supported by lidar measurements in the AOSR in 2018 that allowed determination of temporal and vertical variability in the S-ratio (Strawbridge et al., 2018). Measured S-ratios ranged from 20 to 60 sr within the boundary layer at Oski-Ôtin in 2018 (Figure A6).

Table 2-4 Modelled lidar S-ratios (sr) for selected periods on Aug. 23 using refractive indices (RI) of different particles.

Local Time	RI of Toluene	RI of Kaolinite	RI of Sulphate Aerosol
9:10	21	25	30
9:30	25	28	34
14:10	17	33	38
14:30	18	33	37
16:30	31	32	38
16:50	36	40	44
17:15	36	40	44

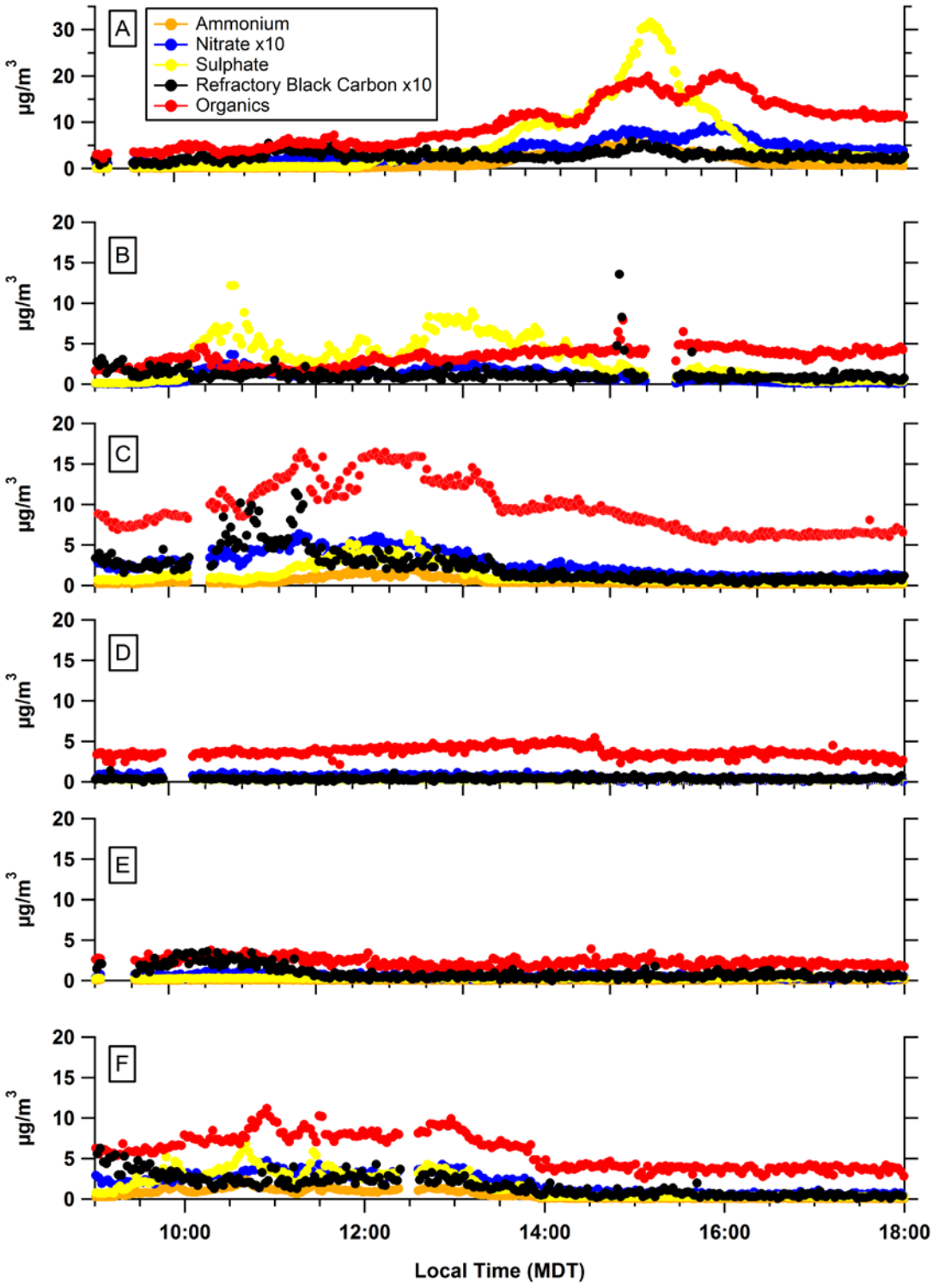

Figure 2-11 Near-surface particle compositions on Aug. 23 (A), Sept. 03 (B), Sept. 04 (C), Sept. 05 (D), Sept. 06 (E), and Sept. 07 (F). Note different y-axis scale for Aug. 23 and that Nitrate and Refractory Black Carbon are shown multiplied by 10.

Based on these results, lidar vertical profiles of aerosol extinction were retrieved using an S-ratio of 44 sr for the extinction below the free troposphere after 14:30 on Aug. 23. As shown in Figure 4 (a), the updated lidar AODs are in more reasonable agreement with the MAX-DOAS and AERONET AODs compared to the original lidar AODs shown in 4(b). The linear regression of the MAX-DOAS and updated lidar AODs has a slope of 1.15±0.02 with an intercept of -0.01±0.02 (R^2 = 0.97) instead of 2.18±0.03 for the original lidar AODs (R^2 = 0.97) (Table A3). Modelling S-ratios using particle data measured at the near-surface appears to be valid during Aug. 23 because the vertical profile was relatively well mixed. A well-mixed boundary layer was indicated by the similarity in temporal trends between the Active-DOAS mixing ratios and MAX-DOAS VCDs and between the AODs and the surface particle loading (Figure 2-4 (g, h) & Figure 2-11 (a)). However, if the distribution of particles in space is inhomogeneous, this method cannot be used to determine the S-ratio of the total boundary layer.

Results from Sept. 03 and Sept. 06 illustrate that near-surface measurements of particles properties can be invalid for modelling the total column S-ratio due to complex vertical profiles of particles. Despite near-surface enhancements in sulphate particles (Figure 2-11) and SO_2 mixing ratios observed by Active-DOAS (Figure 2-5 (f)), the MAX-DOAS and lidar AODs were very similar after 11:30-17:00 on Sept. 03 (Figure 2-5 (a)). The MAX-DOAS and Pandora SO_2 VCDs were moderate compared to the enhancements on Aug. 23, suggesting that the sulphate enhancements were confined mainly near the surface after 11:30. Due to wind-shear, the near-surface air (<200 m a.g.l.) was often impacted by industrial pollution from the south while the air at higher altitudes was impacted by less polluted regions (North-West and Northerly winds), particularly around 14:00 (Figure 2-3 (b)). Thus, the S-ratio of 25 sr was representative of the total boundary layer after 11:30 despite sulphate enhancements at the surface, leading to similar magnitudes of MAX-DOAS and lidar AODs. S-ratios modelled using the near-surface measurements of particles during the afternoon of Sept. 03 would have overestimated the S-ratio within the total boundary layer.

Similarly, near-surface measurements of particles would not represent the total boundary layer on Sept. 06 due to an elevated industrial plume. The MAX-DOAS NO_2 VCDs remained enhanced while the Active-DOAS mixing ratios rapidly decreased from ~7 ppbv to ~1 ppbv (Figure 2-8 (g)). The MAX-DOAS AODs approached the AERONET AODs around noon (Figure 2-8 (a)), maximizing around the time that the lidar observed elevated vertical profiles of aerosol extinction. These results suggest that elevated plumes from the industrial facilities to the north of Fort McKay South (Figure 1) increased the S-ratios at higher altitudes. S-ratios modelled using the surface data during this time, therefore, would have underestimated the average S-ratio within the boundary layer.

These results suggest that the MAX-DOAS retrievals of AODs performed well when the vertical extent of instrumental viewing and S-ratio variability are considered.

2.3.1.3 Comparison of MAX-DOAS Vertical Profiles of Aerosol Extinction with Averaged and Smoothed Lidar Vertical Profiles

MAX-DOAS vertical profiles of aerosol extinction are compared to averaged and smoothed lidar vertical profiles in Figures 12 to 18.

Smoothing alters the shape and magnitude of the averaged lidar profiles in several ways. Smoothing the averaged lidar profiles generally "compresses" the profiles by vertically attributing extinction at higher altitudes to lower altitudes (compare panels (a) and (b) in Figure 2-12to Figure 2-18). This result is expected due to the decreasing sensitivity of the MAX-DOAS retrieval with increasing altitude apparent in the averaging kernels (Figure A7). The smoothing also replaces lidar aerosol extinction above ~1.5 km a.g.l. with the (small) a-priori extinction values because the MAX-DOAS measurements have little information content at high altitudes (Figure A7). This effect is apparent when comparing the Sept. 03 averaged and smoothed lidar profiles above 1.5 km a.g.l. (Figure 2-14). Profiles that were relatively uniform within a few hundred meters of the surface can sometimes be smoothed into apparently elevated profiles because the averaging kernel attributes much of the extinction from altitudes aloft to one altitude bin closer to the surface. For example, the averaging kernels for the Sept. 04 14:10 retrieval for altitudes 0.55 to 1.25 km peak at 0.45 km rather than at their respective height (Figures A7 & A8). Conversely, the smoothing can transform vertically narrow and distinctly elevated profiles near the surface into exponentially decreasing profiles due to the limited vertical resolution of the retrieval (see the 9:30 profile in Figure 2-17). Therefore, interpretation of the retrieved MAX-DOAS profiles must account for the effects of smoothing on the true atmospheric profiles.

On Aug. 23, the MAX-DOAS and smoothed lidar vertical profiles (S-ratio = 25 sr) exhibited similar temporal trends and vertical enhancements within the boundary layer (Figure 2-12). The magnitudes of aerosol extinctions were consistent between the smoothed lidar and MAX-DOAS vertical profiles in the morning, supporting the hypothesis that the S-ratio of 25 sr was appropriate for "clean" periods. In contrast, the MAX-DOAS extinctions exceeded the smoothed lidar extinctions in the afternoon (Figure 2-12). Using an S-ratio of 44 sr within the afternoon plume (discussed in 3.1.2) resulted in smoothed lidar profiles consistent with the MAX-DOAS profiles (Figure 2-13). While temporal trends and overall magnitudes were similar, MAX-DOAS retrievals tended to exhibit more distinctly elevated profiles than the smoothed lidar profiles. The use of a constant S-ratio within the plume may have caused the lidar profiles to appear more vertically uniform than the true profiles since S-ratios can maximize where extinction peaks (Figure A6). Also, the MAX-DOAS viewing geometry observed air masses south of the field site, closer to industrial sources, where the vertical profiles may have been less well-mixed. Finally, MAX-DOAS measurement errors can be mapped into the retrieved profile, leading to uncertainties, but are probably only important at higher altitudes where the measurements contain little information content. Deviations in the MAX-DOAS profiles from the smoothed lidar profiles after 17:00 can be attributed to reduced light levels and the longer retrieval time, reducing signal-to-noise ratio and the probability of the viewed airmasses changing significantly within the time required to capture the measurements for the retrieval, respectively.

For the Sept. 03, Sept. 04 and Sept. 07 (morning) comparisons, the MAX-DOAS retrieved profiles generally captured the same temporal and vertical trends in extinction enhancements as the smoothed lidar profiles, but the lidar extinctions were smaller than the MAX-DOAS extinctions (Figure 2-14, Figure 2-15, & Figure 2-18). The S-ratio of 25 sr probably underestimated the true values given the presence of sulphate particles (Figure 2-11 (b, c, f)) and enhanced SO_2 VCDs (Figure 2-5Figure 2-6Figure 2-9 5(b)). On Sept. 05 the S-ratio of 25 sr is expected to be appropriate due to the clean conditions. The magnitudes of the MAX-DOAS extinctions were unexpectedly greater than the smoothed lidar extinctions but were generally equal within error (Figure 2-16). The Sept. 06 MAX-DOAS aerosol retrievals appear noisier than the smoothed lidar profiles (Figure 2-17). The elevated plumes present in the MAX-DOAS retrievals but not in the lidar profiles may be related to an increased S-ratio due to the impact of plumes from north (Figure 2-8 (g)). On Sept. 07 the MAX-DOAS aerosol extinction profiles were of greater magnitude and different in vertical profile shape compared to the smoothed lidar profiles after 12:00. The deviation can be attributed to significant wind-shear and rapid temporal variation in the wind profiles after 12:00 (Figure 2-2(f) & Figure 2-3(f)). Aerosol extinction magnitudes varied by up to a factor of five within 10 minutes in the afternoon (Figure A9). These conditions violate two assumptions of the MAX-DOAS retrievals: low horizontal inhomogeneity and that the spectra measured during the retrieval time observed the same airmass. Although the MAX-DOAS retrievals of AOD were consistent with the smoothed lidar AODs, the temporal and vertical resolutions of the MAX-DOAS retrievals were insufficient to retrieve accurate vertical profile shapes. The afternoon MAX-DOAS vertical profile retrievals are, therefore, not expected to represent the true atmospheric state.

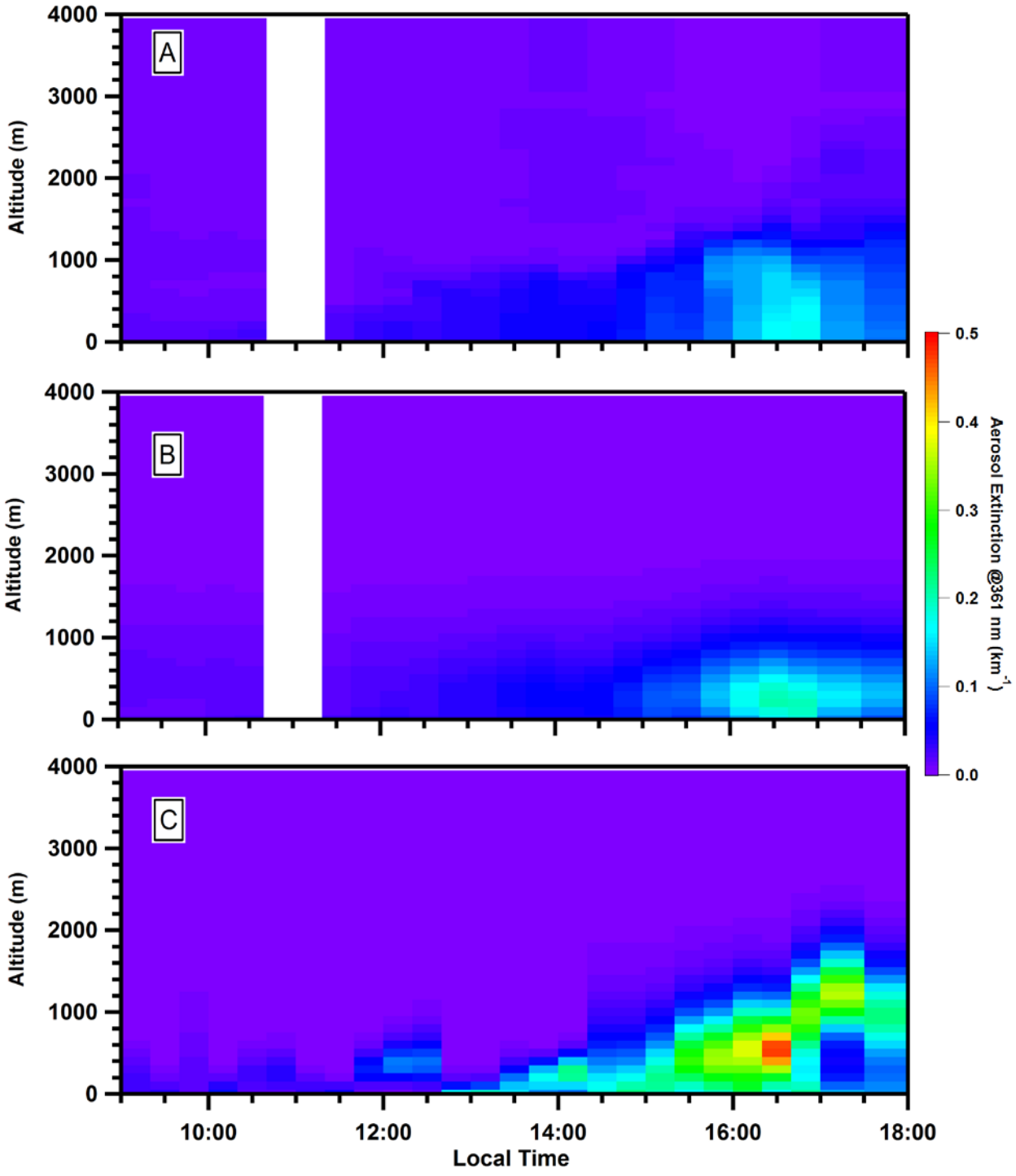

Figure 2-12 Aug. 23 vertical profiles of aerosol extinction (361 nm) from S-ratio=25 sr: averaged lidar (a), smoothed lidar (b), and MAX-DOAS retrieved (c).

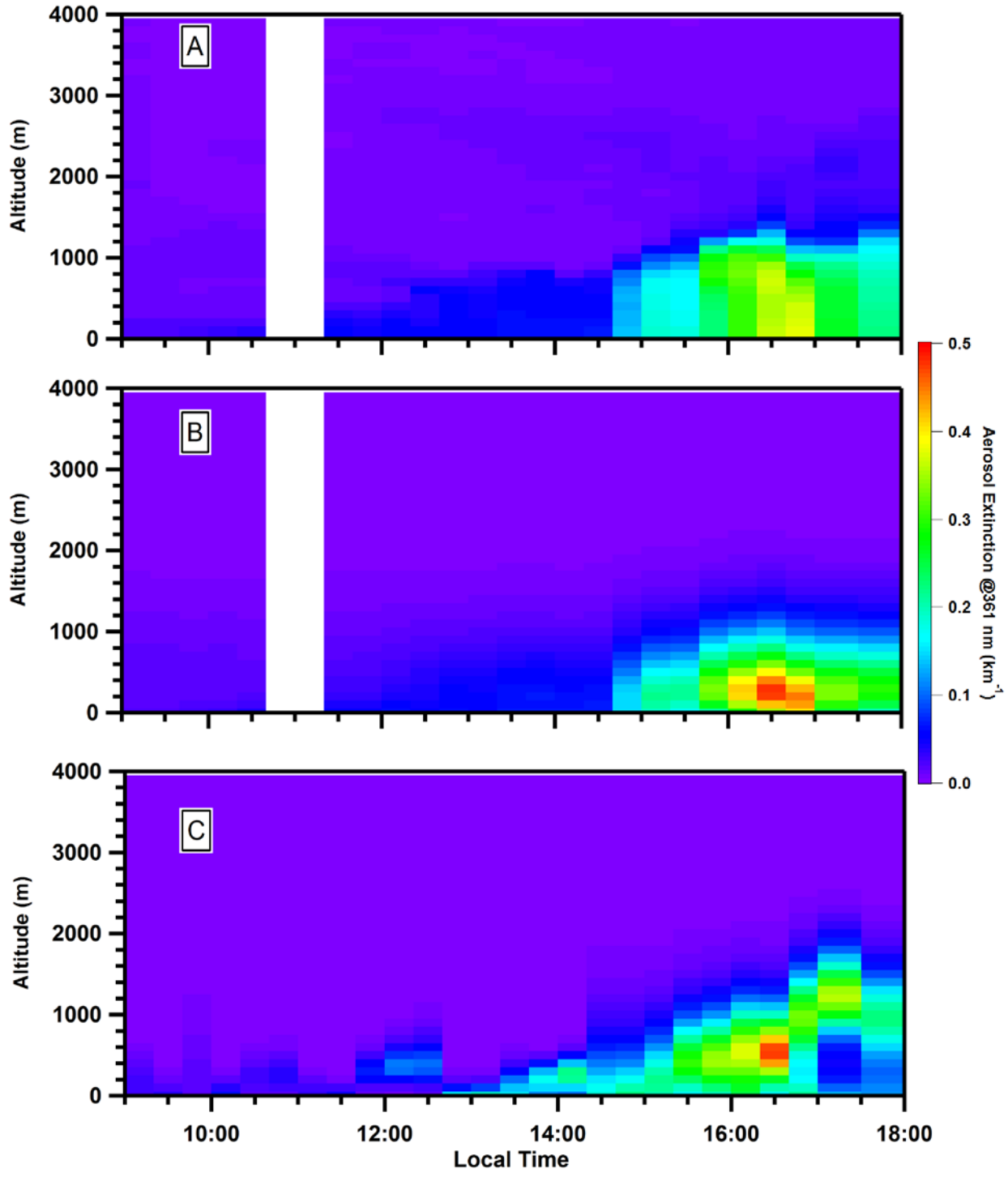

Figure 2-13 Aug. 23 vertical profiles of aerosol extinction (361 nm) from S-ratio=44 sr within the plume >14:30 local time: averaged lidar (a), smoothed lidar (b), and MAX-DOAS retrieved (c).

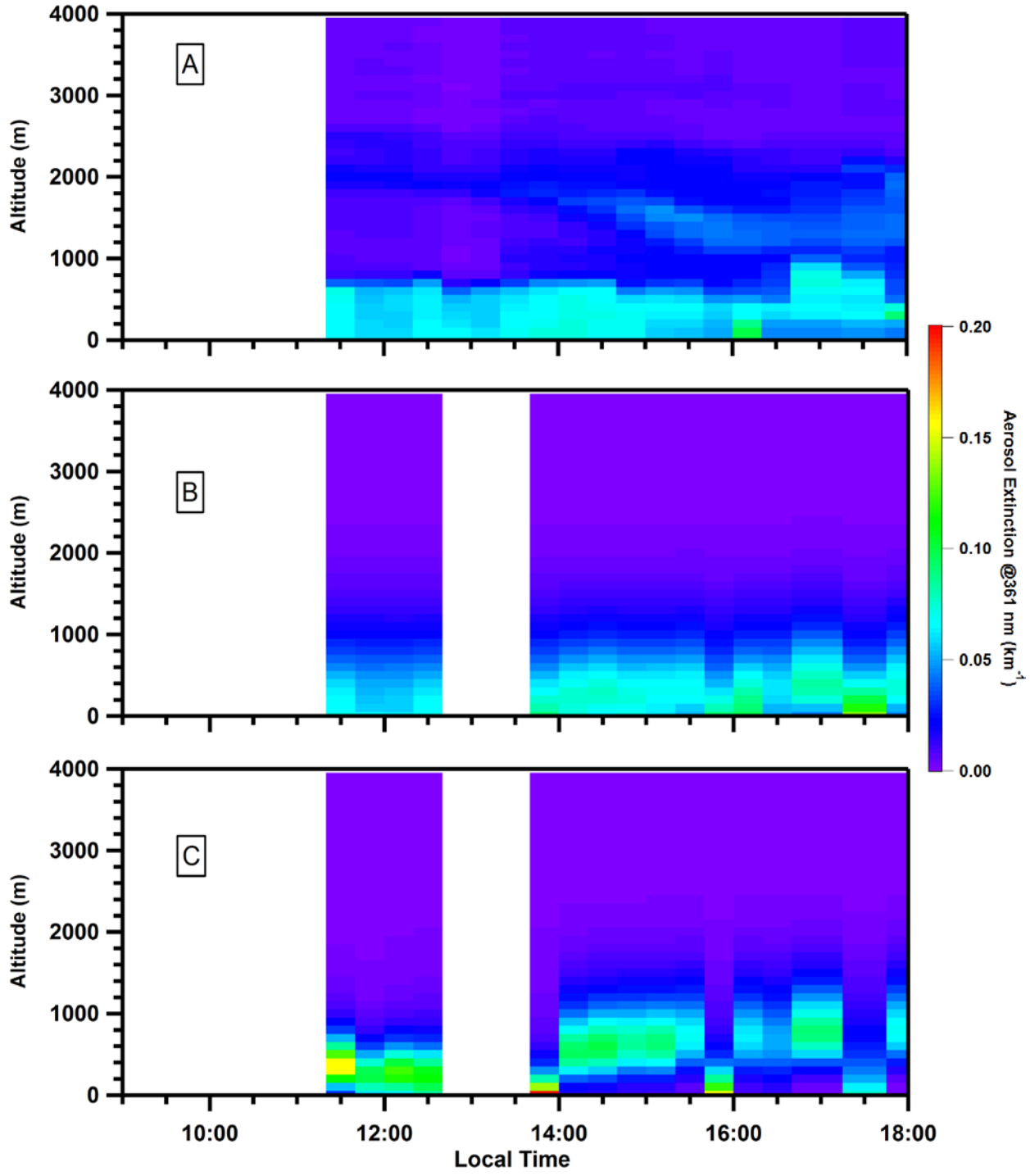

Figure 2-14 Sept. 03 vertical profiles of aerosol extinction (361 nm) from averaged lidar (a), smoothed lidar (b), and MAX-DOAS retrieved (c).

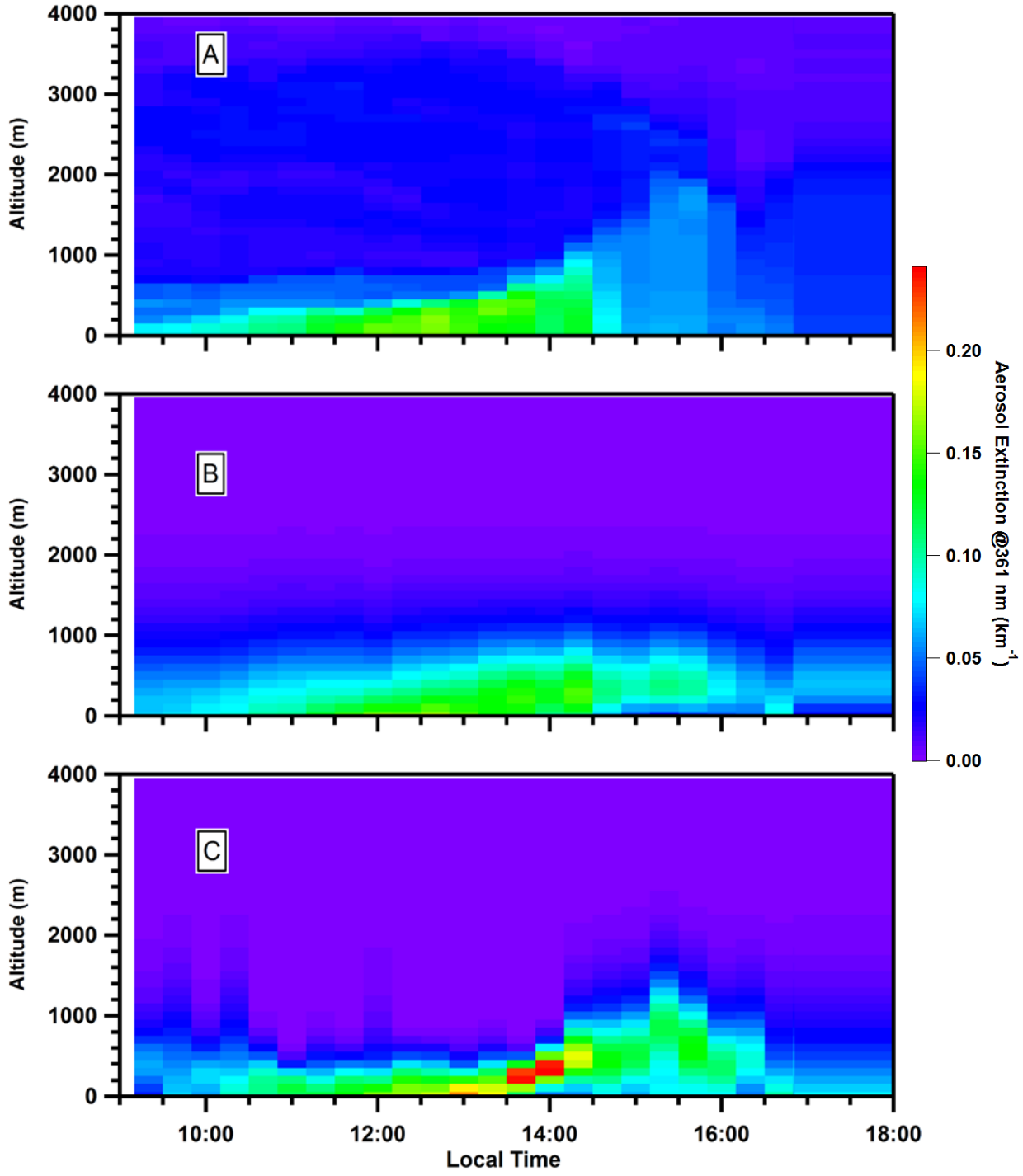

Figure 2-15 Sept. 04 vertical profiles of aerosol extinction (361 nm) from averaged lidar (a), smoothed lidar (b), and MAX-DOAS retrieved (c).

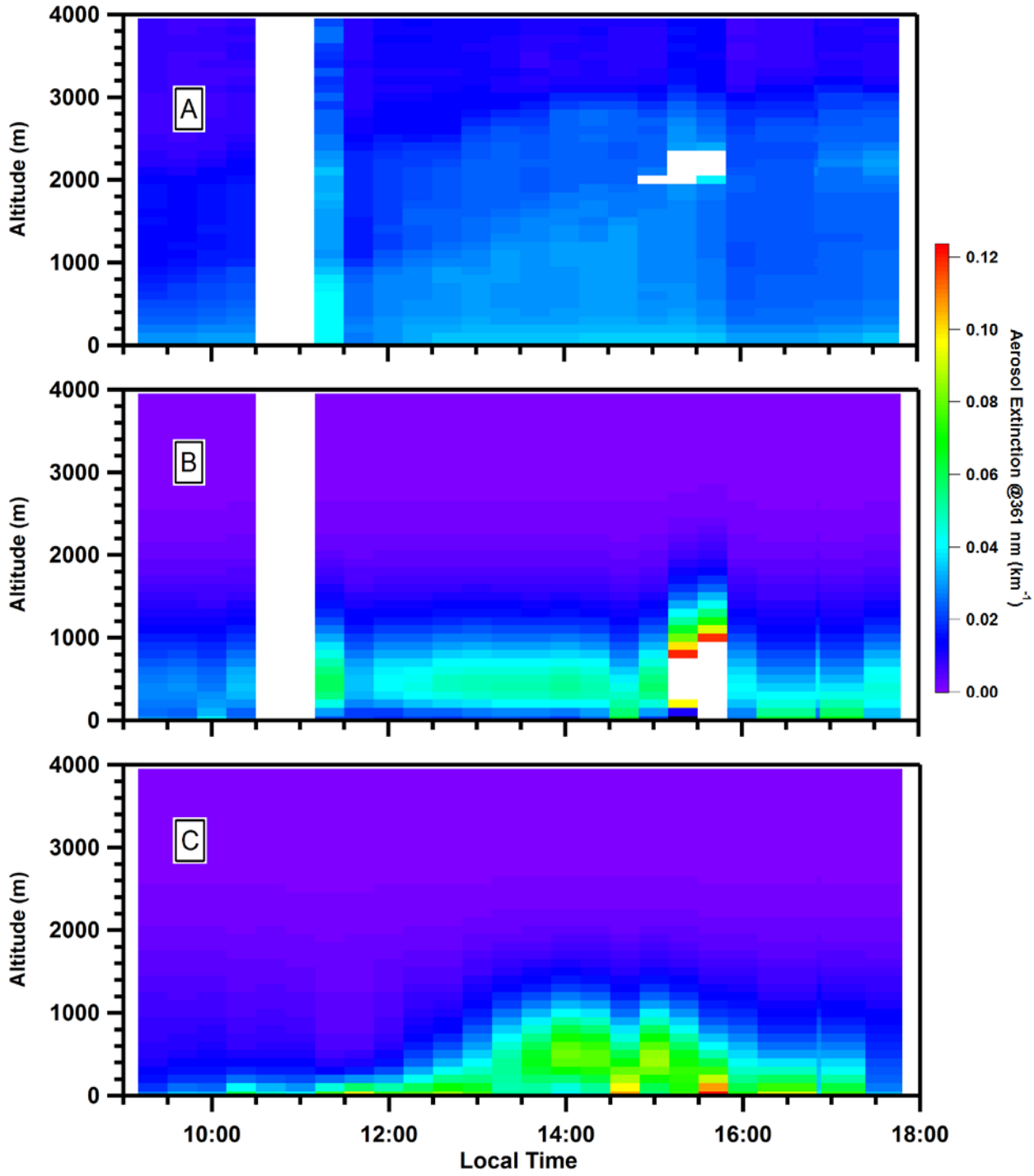

Figure 2-16 Sept. 05 vertical profiles of aerosol extinction (361 nm) from averaged lidar (a), smoothed lidar (b), and MAX-DOAS retrieved (c). Omitted data in the afternoon were measurements of cirrus clouds.

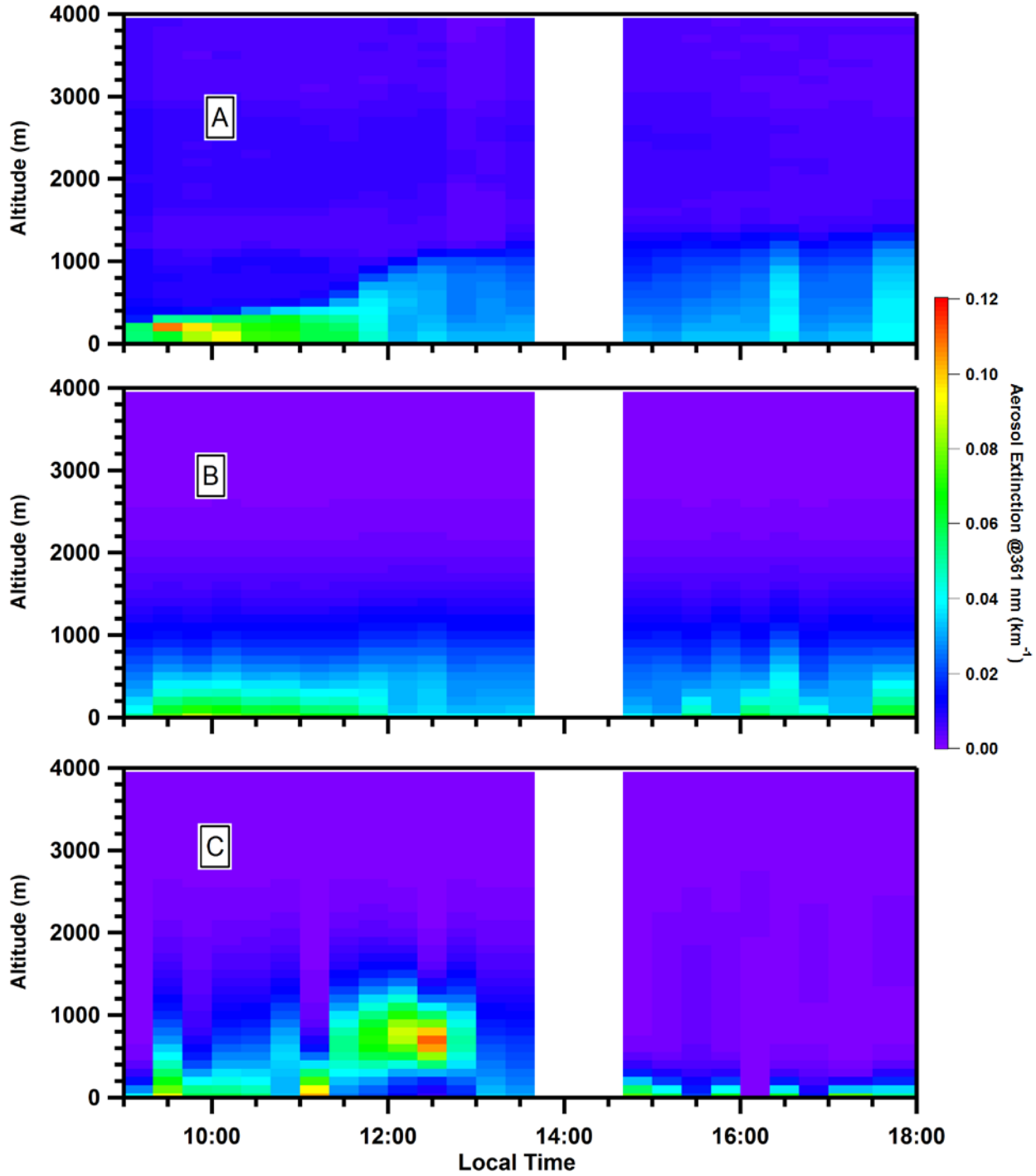

Figure 2-17 Sept. 06 vertical profiles of aerosol extinction (361 nm) from averaged lidar (a), smoothed lidar (b), and MAX-DOAS retrieved (c).

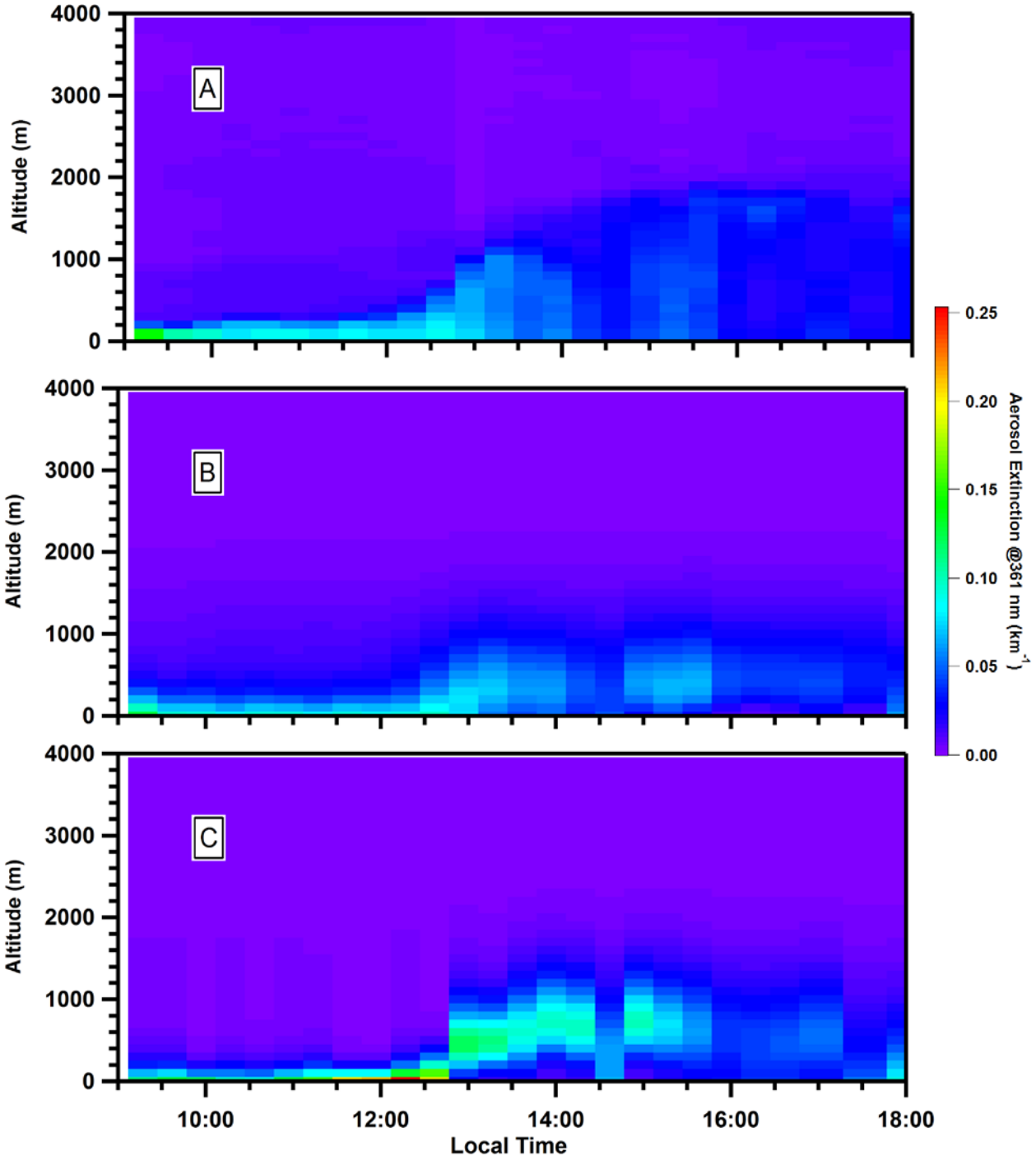

Figure 2-18 Sept. 07 vertical profiles of aerosol extinction (361 nm) from averaged lidar (a), smoothed lidar (b), and MAX-DOAS retrieved (c).

2.3.2 Evaluation of MAX-DOAS Trace gas Retrievals

2.3.2.1 Comparison of MAX-DOAS and Pandora Trace gas VCDs

The MAX-DOAS and Pandora SO_2 and NO_2 VCDs exhibited similar temporal trends over the four days of comparison, except during the afternoon of Sept. 07 (Figure 2-4 (c, d); (b, c) in Figure 2-5, Figure 2-6, & Figure 2-8).

On Aug. 23 the MAX-DOAS and Pandora VCDs were strongly correlated ($R^2 > 0.80$) with linear regression slopes of 1.55±0.07 and 2.20±0.07 for SO_2 and NO_2 VCDs, respectively (Table A4). Greater trace gas enhancements were also observed near the surface at Fort McKay South compared to Oski-Ôtin through in-situ measurements by the Wood Buffalo Environmental Association (WBEA) (Wood Buffalo Environmental Association, 2019) (Figure A10) with slopes of the linear regressions of 1.42±0.05 (R^2=0.91) and 1.93±0.07 (R^2=0.61) for SO_2 and NO_2, respectively (Table A2). The strong correlations between the trace gas measurements between the sites indicate that the same airmass impacted both sites but that a more central (higher concentration) portion of the plume impacted Fort McKay South or significant horizontal dilution of the plume occurred during transport.

The NO_2 VCDs had a slope of the regression greater than that of the in-situ NO_2 measurements (Table A2). NO_x may have been lost at a faster rate near the surface during transport due to deposition to the surface (e.g., the boreal forests). Transport times between the sites were relatively long (~30 minutes) on this day due to low wind-speeds below 600 m a.g.l. (Figure 2-2). NO_x is lost through surface deposition and photochemical conversion to HONO and HNO_3 (Finlayson-Pitts et al., 2003; Wojtal et al., 2011). HONO might be subsequently released as NO and OH, but the HNO_3 loss will be virtually permanent.

$$NO_2 + NO_2 + H_2O \rightarrow HNO_{3_{(aq.surface)}} + HONO_{(g)} \quad (8)$$

$$HONO + h\nu \rightarrow NO + OH \quad (9)$$

On Sept. 04 the MAX-DOAS and Pandora VCDs exhibited similar temporal trends and were often equal within error (Figure 2-6 (b, c)). The slopes of the linear correlations of the SO_2 and NO_2 VCDs were 1.10±0.33 (R^2=0.51) and 0.95±0.07 (R^2=0.85), respectively (Table A6). The greater variability in SO_2 between the sites compared to NO_2 is consistent with the in-situ data between Fort McKay South and the WBEA Bertha Ganter site (Fort McKay North; 57.189428, -111.640583) with R^2= 0.7 and 0.92 for SO_2 and NO_2, respectively (Table A6) (Wood Buffalo Environmental Association, 2019). SO_2 plumes are more localized in the AOSR, originating mostly from large industrial stacks and fewer sources compared to NO_2 (Zhang et al., 2018) (Tables A1 & A2). Note that when MAX-DOAS SO_2 VCDs were significantly greater than Pandora SO_2 VCDs around noon, the SO_2 mixing ratios at Fort McKay South were approximately double those at the Bertha Ganter (Fort McKay) site (Figure A11). These results suggest that the MAX-DOAS performed well in retrieving accurate VCDs of SO_2 despite the weaker linear correlation with the Pandora VCDs. The two sites appear to have largely experienced the same air-masses within a small temporal period (<20 minutes) due to higher wind-speeds relative to Aug. 23 and Sept. 03 (Figure 2-2 (a, c)).

Higher wind speeds likely reduced the maximum enhancements in trace gas VCDs compared to Aug. 23 and Sept. 03 due to greater dispersion. Wind shear on Sept. 04 (Figure 2-3 (c)) may also have transported only certain altitudes of the elevated plumes from south of Fort McKay South to the sites. In contrast, wind shear on Aug. 23 was limited within 500 m a.g.l. (Figure 2-3(a)).

On Sept. 03 and Sept. 07, the MAX-DOAS and Pandora VCDs demonstrated weak linear correlations (R^2 <0.2) (Tables A5 and A9).

The Sept. 03 VCD correlations are inconclusive due to the limited number of data points and relatively little variation in the Pandora VCDs. The MAX-DOAS VCDs tended to be higher than the Pandora VCDs. Unlike on Aug. 23, an examination of the in-situ data between sites is not helpful due to the significant wind-shear on Sept. 03 and the presence of elevated plumes. Based on the good agreement between the MAX-DOAS and Pandora VCDs on Sept. 04 with similar VCD magnitudes, the apparent overestimation could be due to different air-masses experienced by the two sites.

On Sept. 07 the MAX-DOAS were similar to the Pandora trace gas VCDs before 13:30 but were much larger after (Figure 2-9 (b, c)). The deviation of the MAX-DOAS VCDs is an expected result given the rapid spatial and temporal variation in the wind profiles (discussed in 3.1.3). Errors of the trace gas retrievals can be expected to be even greater than the aerosol retrieval errors because the retrieved aerosol profiles were used as forward model parameters in the trace gas retrieval. The afternoon MAX-DOAS trace gas retrievals on Sept. 07 are not expected to represent the true atmospheric state.

Inter-comparisons of the Pandora and MAX-DOAS VCDs show that the MAX-DOAS retrievals of trace gas VCDs performed well under low to moderate wind-speeds and when vertical profiles of pollution were relatively constant within the retrieval period.

2.3.2.2 Comparison of MAX-DOAS 0-100 m Retrieval with Active-DOAS Mixing Ratios

The 0-100 m a.g.l. MAX-DOAS trace gas retrievals are shown with the Active-DOAS mixing ratios in Figures 4 (e, f) and Figures 5-9 (d, e). The MAX-DOAS retrievals generally captured the Active-DOAS temporal trends but tended to overestimate the magnitudes. The MAX-DOAS retrieval yields an estimate of the average concentration within the 0-100 m layer, which is larger than the surface value in case of uplifted layers. Therefore, in-situ near-ground instruments, such as Active-DOAS, are required when accurate surface mixing ratios are required.

The MAX-DOAS retrievals were most consistent with the Active-DOAS measurement during the late afternoon of Aug. 23 (Figure 2-4 (e, f)). SO_2 was at its highest levels and assumed to be relatively well-mixed within the boundary layer based on the similarity in the temporal trends in SO_2 VCDs and surface mixing ratios (Figure 2-4 (g)) and the uniformity of the lidar vertical profiles <1 km a.g.l. (Figure 2-13(a)). The mixing ratios were equal within error during the morning and after 14:00 with some differences in the early afternoon that may be due to the different viewing geometry. On days other than Aug. 23, the uncertainty in the surface retrieval is often too high for reliable comparison when the near-surface when SO_2 and NO_2 were <20 ppbv and <10 ppbv, respectively. Overall,

the MAX-DOAS retrievals of 0-1000 m performed well, considering the frequently complex vertical profiles observed during the study.

2.3.2.3 Temporal trends of MAX-DOAS Trace gas VCDs and Active-DOAS Mixing Ratios

Active-DOAS mixing ratios are shown with MAX-DOAS VCDs in Figure 2-4 (g, h) and in Figures 2-5 to 2-9 (f, g). The VCDs and mixing ratios exhibited similar temporal trends on Aug. 23, Sept. 04-06 (Figure 2-4 (g, h); Figure 2-6; Figure 2-7 (f, g)), but not on Sept. 03 and Sept. 07 ((f, g) in Figure 2-5 &Figure 2-8). The similar temporal trends in VCDs and mixing ratios observed on Aug. 23 are consistent with the limited vertical wind-shear and low to moderate wind-speeds, as discussed previously. In contrast, the ratio of VCDs to mixing ratios sometimes varied even during short periods on Sept. 04 and Sept. 06. If the boundary layer is well-mixed, the Active-DOAS mixing ratios and MAX-DOAS VCDs are expected to have similar temporal trends during short periods since the boundary layer is expected to be effectively constant. On Sept. 04, the temporal trends were very similar until ~13:30, when the rapid decrease in trace gas mixing ratios was not reflected in the VCDs (Figure 2-6 (f, g)), indicating elevated pollution plumes that are apparent in the lidar measurements (Figure A7 (a)). These observations are a testament to the ability of MAX-DOAS to observe elevated pollution plumes not detectable at the surface. The differences in the short-term trends in VCDs and mixing ratios are consistent with the wind profile data around 13:30 on Sept. 04, which indicates Westerly to Northwesterly wind directions <300 m a.gl. that are expected to result in relatively clean air near the surface (Figure 2-3(c)). Although measurements of the wind profiles above ~250 m a.g.l. were unavailable, southerly winds aloft are suggested by the trace gas VCDs remaining enhanced until ~15:00. While significant enhancements of trace gas near the surface tend to contribute to enhanced VCDs, the opposite may not always occur: elevated plumes that cause enhanced VCDs may not result in large surface mixing ratios (Fioletov et al., 2016a). The observations in this study indicate that elevated enhancements may also result from vertical wind shear. Techniques for estimating emissions from industrial facilities must account for the possibility that different vertical portions of plumes can be transported in different directions. Such complex pollution conditions require pollution monitoring techniques such as MAX-DOAS that can detect elevated pollution plumes. In addition to being able to observe elevated plumes that are under-sampled by in-situ, ground instruments, MAX-DOAS can be used to estimate emissions when deployed using the mobile-MAX-DOAS technique (Davis et al., 2019).

2.3.2.4 MAX-DOAS Retrievals of Vertical profiles of SO_2 and NO_2

MAX-DOAS retrievals of vertical profiles of SO_2 and NO_2 are shown in Figure 19. Unlike the aerosol profiles, co-located measurements of the trace gas vertical profiles were generally not available. The magnitude and vertical location of the pollution were highly dependent on wind direction and wind shear. The greatest trace gas enhancements occurred under South-South-Easterly wind-directions (Figure 2-3 &Figure 2-19) where pollution originated from the greatest sources of SO_2 and NO_2 to the South (Figure 2-1; Tables A1 & A2). The MAX-DOAS retrievals performed well in terms of the profile shapes expected based on the wind profiles or evidence of elevated plumes. For example, trace gas pollutants in the MAX-DOAS retrievals were confined largely to <200 m on the mornings of Sept. 04 and Sept. 07 (Figure 2-19 (c) & (f)) as expected from the wind-shear (Figure 2-3). The

elevated profiles of SO_2 on Sept. 03 before noon and during the afternoon of Sept. 04 are consistent with the results discussed previously.

Aircraft measurements of trace gases on Sept. 03 allow some comparison of the MAX-DOAS retrieved profiles. A vertical profile of SO_2 measured during an aircraft spiral ascent at ~14:27 in the vicinity of Fort McKay South (Figure 2-20) is consistent in magnitude and shape with the MAX-DOAS retrieved vertical profile for 11:00-11:20 (Figure 2-20). The MAX-DOAS 11:10 profile was used for comparison because it appears to have observed the same plume as the aircraft spiral. Although these two profiles cannot be directly compared due to the differences in time and vertical resolutions, the aircraft profile indicates that the magnitudes and elevated shape of the MAX-DOAS profiles of SO_2 are reasonable. The elevated SO_2 plumes measured by the aircraft and MAX-DOAS could have originated from upgrader stacks at either the Syncrude or Suncor facilities south of Fort McKay South. The aircraft also passed over Fort McKay South at 16:32, measuring 30 ppbv of SO_2 and 5 ppbv of NO_2 at 395 m a.g.l. The MAX-DOAS retrieval for 16:20-16:40 had maximum SO_2 values of 57 (±19) ppbv at 350 m and maximum NO_2 values of 10 (±5) ppbv at 650 m. Note that the Active-DOAS measured 20 (±0.1) ppbv of SO_2 and 4.3 (±0.1) ppbv of NO_2 near the surface. These measurements, therefore, suggest that elevated plumes were present and that the MAX-DOAS retrieved magnitudes are reasonable.

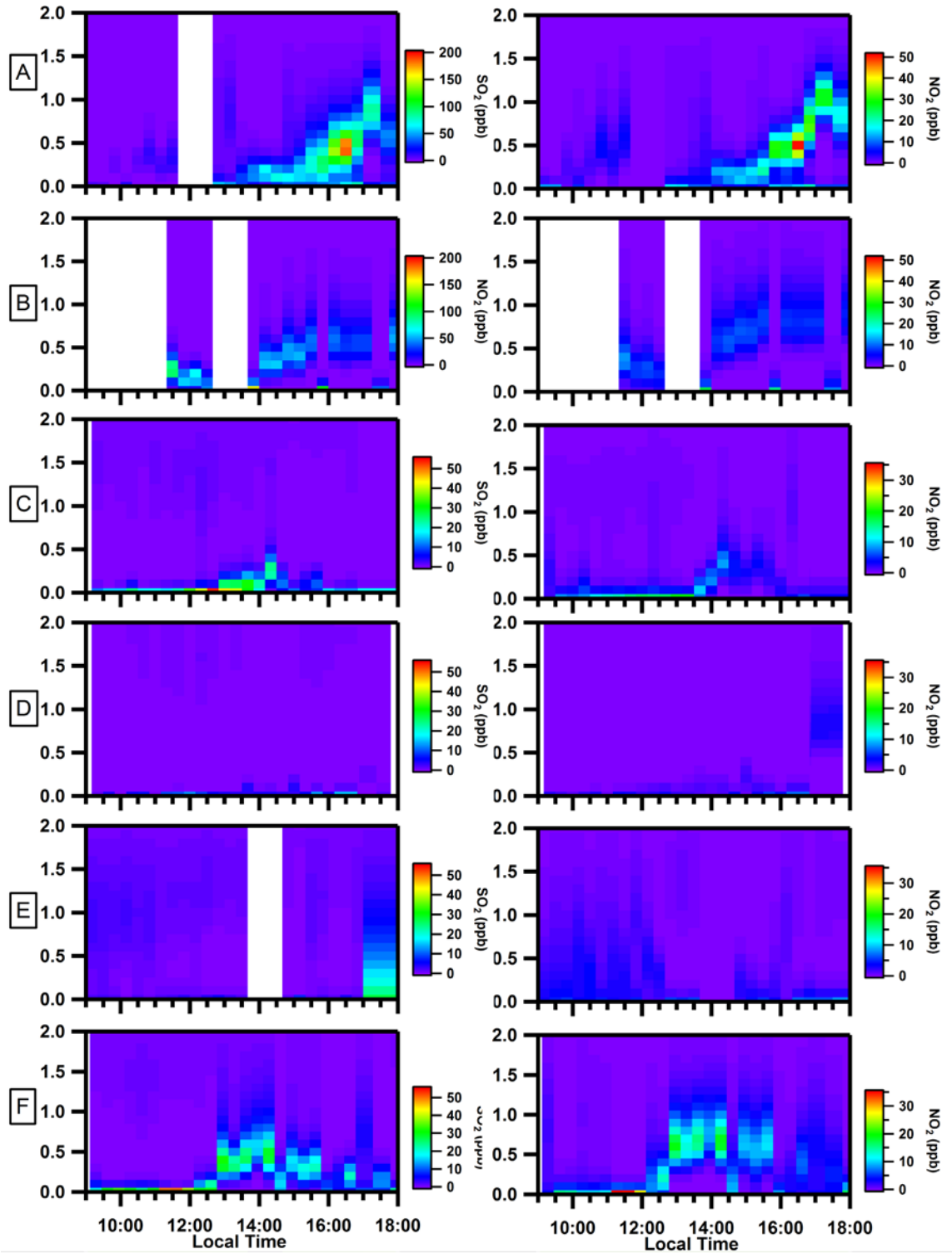

Figure 2-19 MAX-DOAS vertical profiles of SO_2 (left column) and NO_2 (right column): Aug. 23 (A), Sept. 03 (B), Sept. 04 (C), Sept. 05 (D), Sept. 06 (E), and Sept. 07 (F). Note the different colour scale maximum for Aug. 23 and Sept. 03.

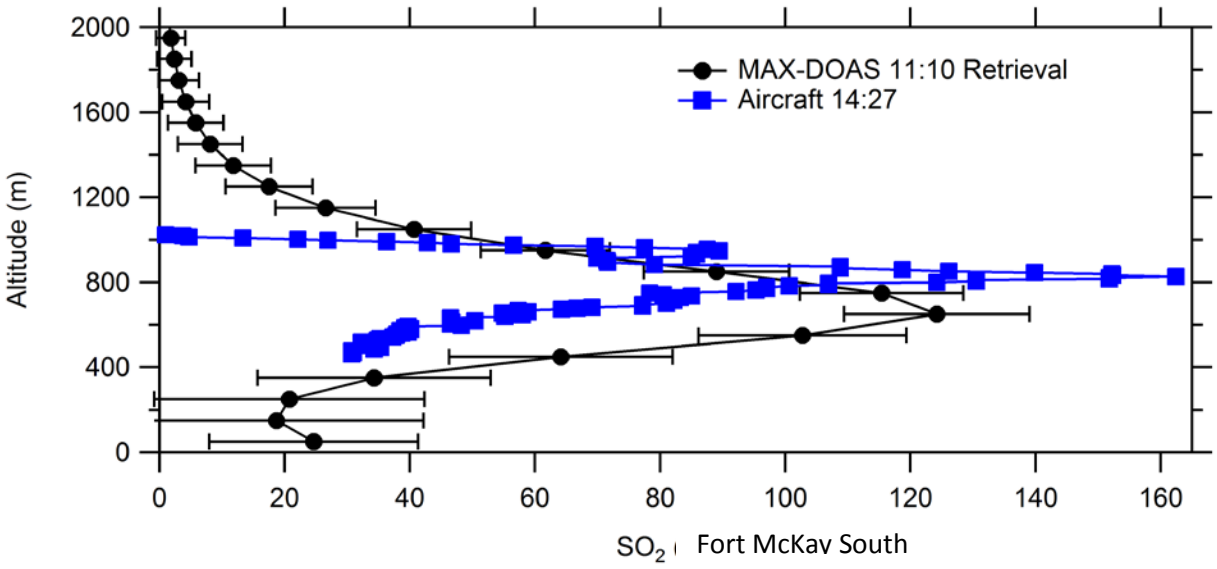

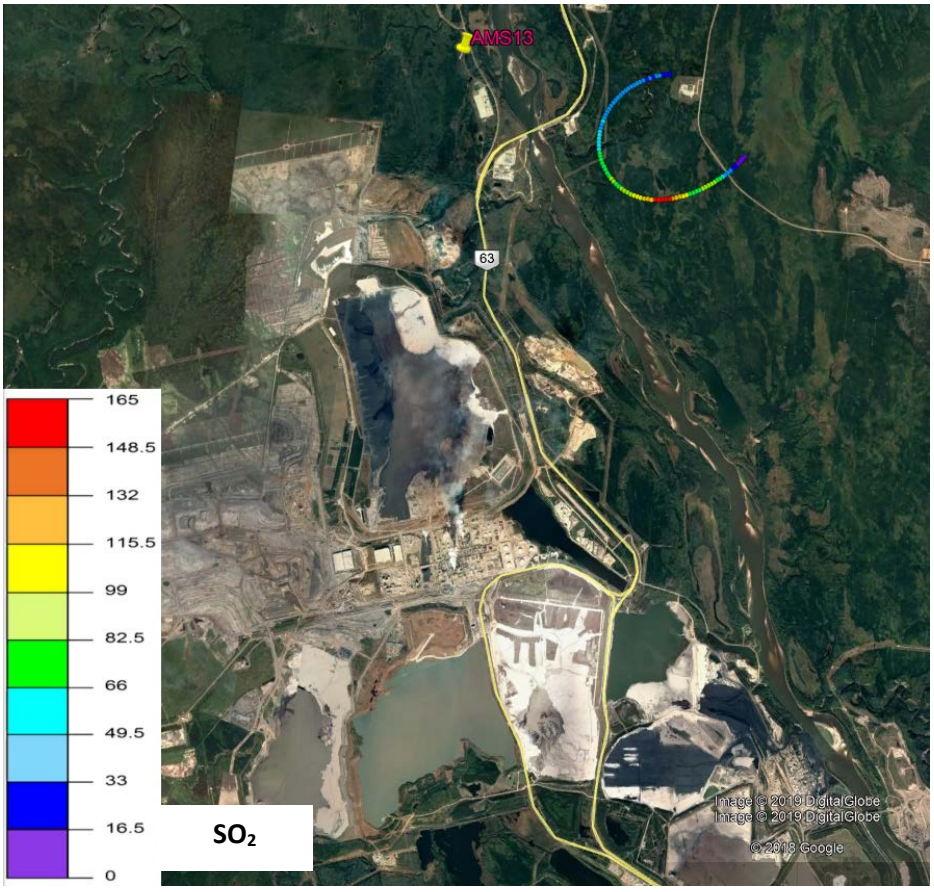

Figure 2-20 Sept. 03 vertical profiles of SO_2 (ppbv) from an aircraft spiral measurement (14:26-14:28 local time) and MAX-DOAS retrieved SO_2 vertical profile (local time 11:10). Aircraft spiral shown in Google Earth plot (bottom).

2.3.3 Advantages of MAX-DOAS

MAX-DOAS has an advantage over the zenith lidar technique in detecting aerosol extinction since lidar retrievals cannot detect close to the surface due to challenges with signal overlap (Zieger et al., 2011). Quantifying aerosol extinction from lidar measurements also requires additional knowledge (i.e., the S-ratio) (Wagner et al., 2004), as has been highlighted in this paper. The advantage of the MAX-DOAS over the sun photometer (in direct-sun viewing mode) is the ability to determine vertical profiles of pollutants versus only total columns. The MAX-DOAS is complementary to Active-DOAS and other point-source measurements when pollution within the boundary layer is vertically inhomogeneous (see 3.2.3). While surface level, local measurements of pollutants are often important for applications such as health exposure studies, they may fail to provide the full picture of the total boundary layer pollution. Such in-situ measurements provide highly localized information with little information about elevated plumes that may mix down to the surface down-wind. MAX-DOAS allows remote sensing of airmasses over longer path-lengths, even if plumes are elevated. The MAX-DOAS method is advantageous over satellite measurements when plumes are localized and can provide more information on near-surface trends.

2.3.4 Limitations of the Inter-Comparisons in this Study

A limitation to validating the MAX-DOAS AODs against lidar and sun photometer data was the different viewing geometry and slightly different locations. Also, Angstrom exponents used to convert the lidar extinctions to the MAX-DOAS retrieval wavelength would ideally be measured at Fort McKay South. Application of a single S-ratio modelled from particle measurements from the near-surface to the entire lidar vertical profile can introduce errors since the S-ratio may vary vertically (Figure A6). The S-ratio can be significantly non-uniform with altitude when the vertical profile is composed of layers of anthropogenic (urban, biomass burning), and/or biogenic aerosols or mixtures of them. Even if a layer is well-mixed, the lidar ratio can change with height if the vertical profile of relative humidity is non-uniform (Weitkamp, 2005).

The MAX-DOAS trace gas VCDs should ideally be compared with a co-located Pandora instrument given the possibility of horizontal inhomogeneity between the sites. Validation of the MAX-DOAS 0-100 m retrieval using the Active-DOAS mixing ratios was complicated by the lowest viewing elevation angle observing 5 m above the Active-DOAS light path. The MAX-DOAS “surface” retrieved values are only expected to be equal to the Active-DOAS values when the air masses were well-mixed within 0-100 m a.g.l. A more thorough validation of the MAX-DOAS near-surface retrievals could be achieved with trace gas measurements at multiple heights within 100 m a.g.l. from a tall tower.

2.4 Summary

In this study, data from a diverse range of instruments have allowed an expansive characterization of the MAX-DOAS retrievals of aerosol extinction, NO_2 and SO_2. The retrievals performed well at capturing the aerosol loading within the boundary layer. The exception was under conditions of rapid variation in the vertical profiles of pollutants during the retrieval period. The ratio of the MAX-DOAS to sun photometer AODs depended on the vertical location of the aerosol extinction within the atmospheric column. Direct inter-comparisons of AODs between instruments must account for the relative spatial extents observed. The comparison of MAX-DOAS and lidar data combined

with S-ratio modelling indicated that accurate S-ratio values are essential to retrieve accurate profiles of aerosol extinction from lidar measurements when particle composition or size distribution varies significantly temporally or spatially. Direct comparison of MAX-DOAS and lidar AODs should be made with caution when knowledge of the S-ratio value(s) is limited. S-ratios can be estimated from measurements of particle size distribution and composition using Mie scattering modelling. However, near-surface measurements of particles should only be used to model S-ratios when the boundary layer is well mixed. Lidar extinction profiles should ideally be determined using a technique that accounts for the vertical and temporal variation in the S-ratio such as in Strawbridge et al. (2018). When the S-ratio variability was accounted for, the results of this study indicate that the MAX-DOAS retrievals of aerosol extinction performed well compared to the smoothed lidar results.

Comparisons of averaged and smoothed lidar profiles of aerosol extinction indicated that the vertical sensitivity of the MAX-DOAS retrievals smoothed the true atmospheric profiles towards the surface. This smoothing can transform vertical profiles that are relatively uniform within the boundary layer into apparently elevated profiles and vice versa. This shape change depends on the location of extinction within the true vertical profile and the averaging kernel matrix of the retrieval. Interpretation of the shape of the MAX-DOAS vertical profiles must account for the instrument's sensitivity to the true vertical profile (i.e., the averaging kernel matrix).

MAX-DOAS retrievals of NO_2 and SO_2 VCDs performed well in comparison to the Pandora VCDs. The exception was when the aerosol retrievals were inaccurate due to rapidly varying vertical profiles. This was an expected result since the aerosol retrievals are used as forward model parameters in the trace gas retrieval. The MAX-DOAS trace gas retrievals within 0-100 m a.g.l. captured the temporal trends observed by the Active-DOAS measurements, but the MAX-DOAS mixing ratios were statistically greater than the Active-DOAS values, particularly when SO_2 and NO_2 were <20 ppbv and <10 ppbv, respectively. Differences between the instruments' values can be attributed to variability in the trace gas profiles within 150 m a.g.l. The MAX-DOAS observed elevated enhancements of pollution undetected by ground-based techniques such as the Active-DOAS, perhaps its greatest asset. Pollution enhancements at surface-level did not always coincide with total boundary layer enhancements, and vice versa, due to elevated plumes and/or significant wind-shear. The MAX-DOAS vertical profiles of trace gases were consistent with the profiles expected based on the wind direction and -shear conditions. Aircraft measurements of SO_2 near Fort McKay South on Sept. 03 indicated that the magnitudes and elevated shape of the retrievals were reasonable.

A major advantage of the MAX-DOAS technique is the ability to simultaneously retrieve total column and vertical profiles of trace gases and aerosol extinction from spectral measurements without requiring prior knowledge of the aerosols or the vertical profiles of trace gases. These advantages are important in industrial regions where the vertical profiles of pollutants vary temporally and spatially, and in-situ monitoring can under-sample plumes. In the AOSR and similar industrial regions, a full understanding of the air quality conditions requires instruments, such as MAX-DOAS, capable of observing the total boundary layer on a horizontal scale of a few kilometers, in addition to traditional in-situ instruments.

2.5 Acknowledgements

Funding for this study was provided by Environment and Climate Change Canada and the Canada-Alberta Oil Sands Monitoring program. Zoe Davis, Akshay Lobo and Sabour Baray acknowledge the financial support provided by the Natural Sciences and Engineering Research Council of Canada (NSERC) Collaborative Research and Training Experience Program (CREATE) Integrating Atmospheric Chemistry and Physics from Earth to Space (IACPES).

2.6 References

Adams, C., Normand, E. N., McLinden, C. A., Bourassa, A. E., Lloyd, N. D., Degenstein, D. A., Krotkov, N. A., Belmonte Rivas, M., Boersma, K. F. and Eskes, H.: Limb–nadir matching using non-coincident NO2 observations: proof of concept and the OMI-minus-OSIRIS prototype product, Atmospheric Meas. Tech., 9(8), 4103–4122, doi:10.5194/amt-9-4103-2016, 2016.

Aggarwal, M., Whiteway, J., Seabrook, J., Gray, L., Strawbridge, K., Liu, P., O'Brien, J., Li, S.-M. and McLaren, R.: Airborne lidar measurements of aerosol and ozone above the Canadian oil sands region, Atmospheric Meas. Tech., 11(6), 3829–3849, doi:10.5194/amt-11-3829-2018, 2018.

Amiri, N., Ghahremaninezhad, R., Rempillo, O., Tokarek, T. W., Odame-Ankrah, C. A., Osthoff, H. D. and Norman, A.-L.: Stable sulfur isotope measurements to trace the fate of SO2 in the Athabasca oil sands region, Atmospheric Chem. Phys., 18(11), 7757–7780, doi:10.5194/acp-18-7757-2018, 2018.

Baray, S., Darlington, A., Gordon, M., Hayden, K. L., Leithead, A., Li, S.-M., Liu, P. S. K., Mittermeier, R. L., Moussa, S. G., O'Brien, J., Staebler, R., Wolde, M., Worthy, D. and McLaren, R.: Quantification of methane sources in the Athabasca Oil Sands Region of Alberta by aircraft mass balance, Atmospheric Chem. Phys., 18(10), 7361–7378, doi:10.5194/acp-18-7361-2018, 2018.

Bogumil, K., Orphal, J., Homann, T., Voigt, S., Spietz, P., Fleischmann, O. C., Vogel, A., Hartmann, M., Kromminga, H., Bovensmann, H., Frerick, J. and Burrows, J. P.: Measurements of molecular absorption spectra with the SCIAMACHY pre-flight model: instrument characterization and reference data for atmospheric remote-sensing in the 230–2380 nm region, J. Photochem. Photobiol. Chem., 157(2–3), 167–184, doi:10.1016/S1010-6030(03)00062-5, 2003.

Browaeys, J.: Linear fit with both uncertainties in x and in y - File Exchange - MATLAB Central, [online] Available from: https://www.mathworks.com/matlabcentral/fileexchange/45711 (Accessed 26 February 2019), 2017.

Canadian Council of Ministers of the Environment: Sulphur Dioxide, Sulphur Dioxide [online] Available from: https://www.ccme.ca/en/resources/air/air/sulphur-dioxide.html (Accessed 28 May 2019), 2014.

Clemer, K., Van Roozendael, M., Fayt, C., Hendrick, F., Hermans, C., Pinardi, G., Spurr, R., Wang, P. and De Maziere, M.: Multiple wavelength retrieval of tropospheric aerosol optical properties from MAXDOAS measurements in Beijing, Atmospheric Meas. Tech., 3(4), 863–878, doi:10.5194/amt-3-863-2010, 2010.

Davis, Z. Y. W., Baray, S., McLinden, C. A., Khanbabakhani, A., Fujs, W., Csukat, C., Debosz, J. and McLaren, R.: Estimation of NOx and SO2 Emissions from Sarnia, Ontario using Mobile-MAX-DOAS and a NOx-Analyzer, Atmospheric Chem. Phys. Discuss., 1–40, doi:https://doi.org/10.5194/acp-2019-442, 2019.

Degenstein, D. A., Bourassa, A. E., Roth, C. Z. and Llewellyn, E. J.: Limb scatter ozone retrieval from 10 to 60 km using a multiplicative algebraic reconstruction technique, Atmos Chem Phys, 9, 2009.

Deutschmann, T., Beirle, S., Frieß, U., Grzegorski, M., Kern, C., Kritten, L., Platt, U., Prados-Roman, C., Pukite, J., Wagner, T., Werner, B. and Pfeilsticker, K.: The Monte Carlo atmospheric radiative transfer model McArtim: Introduction and validation of Jacobians and 3D features, J. Quant. Spectrosc. Radiat. Transf., 112(6), 1119–1137, doi:10.1016/j.jqsrt.2010.12.009, 2011.

ECCC: Environment and Climate Change Canada - NPRI Data Search, NPRI Data Search [online] Available from: https://pollution-waste.canada.ca/national-release-inventory/archives/index.cfm?lang=en (Accessed 24 April 2019a), 2018.

ECCC: Environment and Climate Change Canada - NPRI Data Search - Facility Search Results, Facil. Search Results - Nitrogen Oxides [online] Available from: https://pollution-waste.canada.ca/national-release-inventory/archives/index.cfm?do=results&lang=en&opt_facility_name=&opt_facility=&opt_npri_id=&opt_report_year=2017&opt_chemical_type=ALL&opt_industry=&opt_cas_name=11104-93-1&opt_cas_num=&opt_location_type=ALL&opt_province=&opt_postal_code=&opt_community=&opt_csic=&opt_csi2=&opt_asic=&opt_naics3=&opt_naics4=&opt_naics6=&opt_nai6code=&community1=&opt_urban_center=&opt_province_comm=&opt_media=all&opt_sort_order=TOTAL_RELEASE&opt_sort_direction=DESC&submit=Sort (Accessed 24 April 2019b), 2018.

ECCC: Environment and Climate Change Canada - NPRI Data Search - Facility Search Results, Facil. Search Results- Sulphur Dioxide [online] Available from: https://pollution-waste.canada.ca/national-release-inventory/archives/index.cfm?do=results&lang=en&opt_facility_name=&opt_facility=&opt_npri_id=&opt_report_year=2017&opt_chemical_type=ALL&opt_industry=&opt_cas_name=7446-09-5&opt_cas_num=&opt_location_type=ALL&opt_province=&opt_postal_code=&opt_community=&opt_csic=&opt_csi2=&opt_asic=&opt_naics3=&opt_naics4=&opt_naics6=&opt_nai6code=&community1=&opt_urban_center=&opt_province_comm=&opt_media=all&opt_sort_order=TOTAL_RELEASE&opt_sort_direction=DESC&submit=Sort (Accessed 24 April 2019c), 2018.

Fenn, M. E., Bytnerowicz, A., Schilling, S. L. and Ross, C. S.: Atmospheric deposition of nitrogen, sulfur and base cations in jack pine stands in the Athabasca Oil Sands Region, Alberta, Canada, Environ. Pollut., 196, 497–510, doi:10.1016/j.envpol.2014.08.023, 2015.

Finlayson-Pitts, B. J., Wingen, L. M., Sumner, A. L., Syomin, D. and Ramazan, K. A.: The heterogeneous hydrolysis of NO2 in laboratory systems and in outdoor and indoor atmospheres: An integrated mechanism, Phys. Chem. Chem. Phys., 5(2), 223–242, doi:10.1039/b208564j, 2003.

Fioletov, V. E., McLinden, C. A., Cede, A., Davies, J., Mihele, C., Netcheva, S., Li, S.-M. and O'Brien, J.: Sulfur dioxide (SO2) vertical column density measurements by Pandora spectrometer over the Canadian oil sands, Atmos Meas Tech, 9(7), 2961–2976, doi:10.5194/amt-9-2961-2016, 2016.

Frieß, U., Monks, P. S., Remedios, J. J., Rozanov, A., Sinreich, R., Wagner, T. and Platt, U.: MAX-DOAS O4 measurements: A new technique to derive information on atmospheric aerosols: 2. Modeling studies, J. Geophys. Res.-Atmospheres, 111(D14), D14203, doi:10.1029/2005JD006618, 2006.

Frieß, U., Deutschmann, T., Gilfedder, B. S., Weller, R. and Platt, U.: Iodine monoxide in the Antarctic snowpack, Atmospheric Chem. Phys., 10(5), 2439–2456, doi:10.5194/acp-10-2439-2010, 2010.

Frieß, U., Sihler, H., Sander, R., Poehler, D., Yilmaz, S. and Platt, U.: The vertical distribution of BrO and aerosols in the Arctic: Measurements by active and passive differential optical absorption spectroscopy, J. Geophys. Res.-Atmospheres, 116, D00R04, doi:10.1029/2011JD015938, 2011.

Frieß, U., Klein Baltink, H., Beirle, S., Clémer, K., Hendrick, F., Henzing, B., Irie, H., Leeuw, G. de, Li, A., Moerman, M. M., Roozendael, M. van, Shaiganfar, R., Wagner, T., Wang, Y., Xie, P., Yilmaz, S. and Zieger, P.: Intercomparison of aerosol extinction profiles retrieved from MAX-DOAS measurements, Atmospheric Meas. Tech., 9(7), 3205–3222, doi:https://doi.org/10.5194/amt-9-3205-2016, 2016.

Frieß, U., Beirle, S., Alvarado Bonilla, L., Bösch, T., Friedrich, M. M., Hendrick, F., Piters, A., Richter, A., Roozendael, M. van, Rozanov, V. V., Spinei, E., Tirpitz, J.-L., Vlemmix, T., Wagner, T. and Wang, Y.: Intercomparison of MAX-DOAS vertical profile retrieval algorithms: studies using synthetic data, Atmospheric Meas. Tech., 12(4), 2155–2181, doi:https://doi.org/10.5194/amt-12-2155-2019, 2019.

Gordon, M., Li, S.-M., Staebler, R., Darlington, A., Hayden, K., O'Brien, J. and Wolde, M.: Determining air pollutant emission rates based on mass balance using airborne measurement data over the Alberta oil sands operations, ATMOSPHERIC Meas. Tech., 8(9), 3745–3765, doi:10.5194/amt-8-3745-2015, 2015.

Gordon, M., Makar, P. A., Staebler, R. M., Zhang, J., Akingunola, A., Gong, W. and Li, S.-M.: A Comparison of Plume Rise Algorithms to Stack Plume Measurements in the Athabasca Oil Sands, Atmos Chem Phys Discuss, 2017, 1–27, doi:10.5194/acp-2017-1093, 2017.

Government of Canada: Canadian Environmental Sustainability Indicators - Canada.ca, [online] Available from: http://indicators-map.canada.ca/App/CESI_ICDE?keys=AirAmbient_AvgPM&GoCTemplateCulture=en-CA (Accessed 6 February 2019), 2018.

Health Canada: Human Health Risk Assessment for Sulphur Dioxide, [online] Available from: http://publications.gc.ca/collections/collection_2016/sc-hc/H144-29-2016-eng.pdf (Accessed 1 January 2019), 2016.

Heckel, A., Richter, A., Tarsu, T., Wittrock, F., Hak, C., Pundt, I., Junkermann, W. and Burrows, J. P.: MAX-DOAS measurements of formaldehyde in the Po-Valley, Atmospheric Chem. Phys., 5, 909–918, doi:10.5194/acp-5-909-2005, 2005.

Holloway, A. M. and Wayne, R.: Atmospheric Chemistry, RSC Publishing, Cambridge, UK., 2010.

Honninger, G. and Platt, U.: Observations of BrO and its vertical distribution during surface ozone depletion at Alert, Atmos. Environ., 36(15–16), 2481–2489, doi:10.1016/S1352-2310(02)00104-8, 2002.

Honninger, G., von Friedeburg, C. and Platt, U.: Multi axis differential optical absorption spectroscopy (MAX-DOAS), ATMOSPHERIC Chem. Phys., 4, 231–254, 2004.

Hsu, Y.-M.: Trends in Passively-Measured Ozone, Nitrogen Dioxide and Sulfur Dioxide Concentrations in the Athabasca Oil Sands Region of Alberta, Canada, Aerosol Air Qual. Res., 13(5), 1448–1463, doi:10.4209/aaqr.2012.08.0224, 2013.

Irie, H., Kanaya, Y., Akimoto, H., Iwabuchi, H., Shimizu, A. and Aoki, K.: First retrieval of tropospheric aerosol profiles using MAX-DOAS and comparison with lidar and sky radiometer measurements, Atmospheric Chem. Phys., 8(2), 341–350, doi:10.5194/acp-8-341-2008, 2008.

Irie, H., Takashima, H., Kanaya, Y., Boersma, K. F., Gast, L., Wittrock, F., Brunner, D., Zhou, Y. and Van Roozendael, M.: Eight-component retrievals from ground-based MAX-DOAS observations, Atmospheric Meas. Tech., 4(6), 1027–1044, doi:10.5194/amt-4-1027-2011, 2011.

Irie, H., Nakayama, T., Shimizu, A., Yamazaki, A., Nagai, T., Uchiyama, A., Zaizen, Y., Kagamitani, S. and Matsumi, Y.: Evaluation of MAX-DOAS aerosol retrievals by coincident observations using CRDS, lidar, and sky radiometer in Tsukuba, Japan, Atmospheric Meas. Tech., 8(7), 2775–2788, doi:10.5194/amt-8-2775-2015, 2015.

Jin, J., Ma, J., Lin, W., Zhao, H., Shaiganfar, R., Beirle, S. and Wagner, T.: MAX-DOAS measurements and satellite validation of tropospheric NO2 and SO2 vertical column densities at a rural site of North China, Atmos. Environ., 133, 12–25, doi:10.1016/j.atmosenv.2016.03.031, 2016.

Keller-Rudek, H., Moortgat, G. K., Sander, R. and Sörensen, R.: The MPI-Mainz UV/VIS Spectral Atlas of Gaseous Molecules of Atmospheric Interest, Earth Syst. Sci. Data, 5(2), 365–373, doi:10.5194/essd-5-365-2013, 2013.

Kulmala, M., Vehkamäki, H., Petäjä, T., Dal Maso, M., Lauri, A., Kerminen, V.-M., Birmili, W. and McMurry, P. H.: Formation and growth rates of ultrafine atmospheric particles: a review of observations, J. Aerosol Sci., 35(2), 143–176, doi:10.1016/j.jaerosci.2003.10.003, 2004.

Lee, A. K. Y., Adam, M. G., Liggio, J., Li, S.-M., Li, K., Willis, M. D., Abbatt, J. P. D., Tokarek, T. W., Odame-Ankrah, C. A., Osthoff, H. D., Strawbridge, K. and Brook, J. R.: A Large Contribution of Anthropogenic Organo-Nitrates to Secondary Organic Aerosol in the Alberta Oil Sands, Atmospheric Chem. Phys. Discuss., 1–25, doi:https://doi.org/10.5194/acp-2018-1177, 2019.

Levenberg, K.: A method for the solution of certain non-linear problems in least squares, Quart Appl Math, 2, 164–168, doi:https://doi.org/10.1090/qam/10666, 1944.

Li, X., Brauers, T., Shao, M., Garland, R. M., Wagner, T., Deutschmann, T. and Wahner, A.: MAX-DOAS measurements in southern China: retrieval of aerosol extinctions and validation using ground-based in-situ data, Atmospheric Chem. Phys., 10(5), 2079–2089, doi:10.5194/acp-10-2079-2010, 2010.

Liggio, J., Li, S.-M., Hayden, K., Taha, Y. M., Stroud, C., Darlington, A., Drollette, B. D., Gordon, M., Lee, P., Liu, P., Leithead, A., Moussa, S. G., Wang, D., O'Brien, J., Mittermeier, R. L., Brook, J. R., Lu, G., Staebler, R. M., Han, Y., Tokarek, T. W., Osthoff, H. D., Makar, P. A., Zhang, J., Plata, D. L. and Gentner, D. R.: Oil sands operations as a large source of secondary organic aerosols, Nature, 534(7605), 91-94, doi:10.1038/nature17646, 2016.

Liggio, J., Li, S.-M., Staebler, R. M., Hayden, K., Darlington, A., Mittermeier, R. L., O'Brien, J., McLaren, R., Wolde, M., Worthy, D. and Vogel, F.: Measured Canadian oil sands CO 2 emissions are higher than estimates made using internationally recommended methods, Nat. Commun., 10(1), 1863, doi:10.1038/s41467-019-09714-9, 2019.

Marquardt, D. W.: An algorithm for lesat squares estimation of non-linear parameters, J Soc Inudst Appl Math, 11(2), 431–441, 1963.

McLaren, R., Wojtal, P., Majonis, D., McCourt, J., Halla, J. D. and Brook, J.: NO3 radical measurements in a polluted marine environment: links to ozone formation, Atmospheric Chem. Phys., 10(9), 4187–4206, doi:10.5194/acp-10-4187-2010, 2010.

McLaren, R., Wojtal, P., Halla, J. D., Mihele, C. and Brook, J. R.: A survey of NO2:SO2 emission ratios measured in marine vessel plumes in the Strait of Georgia, Atmos. Environ., 46, 655–658, doi:10.1016/j.atmosenv.2011.10.044, 2012.

McLinden, C. A.: Stratospheric ozone in 3-D models: A simple chemistry and the cross-tropopause flux., J. Geophys. Res., 105(D11), 14653–14665, doi:10.1029/2000JD900124, 2000.

McLinden, C. A., Fioletov, V., Boersma, K. F., Krotkov, N., Sioris, C. E., Veefkind, J. P. and Yang, K.: Air quality over the Canadian oil sands: A first assessment using satellite observations, Geophys. Res. Lett., 39, L04804, doi:10.1029/2011GL050273, 2012.

McLinden, C. A., Fioletov, V., Boersma, K. F., Kharol, S. K., Krotkov, N., Lamsal, L., Makar, P. A., Martin, R. V., Veefkind, J. P. and Yang, K.: Improved satellite retrievals of NO2 and SO2 over the Canadian oil sands and

comparisons with surface measurements, Atmospheric Chem. Phys., 14(7), 3637–3656, doi:10.5194/acp-14-3637-2014, 2014.

McLinden, C. A., Fioletov, V., Krotkov, N. A., Li, C., Boersma, K. F. and Adams, C.: A Decade of Change in NO2 and SO2 over the Canadian Oil Sands As Seen from Space, Environ. Sci. Technol., 50(1), 331–337, doi:10.1021/acs.est.5b04985, 2016.

Platt, U., Perner, D. and Patz, H.: Simultaneous Measurement of Atmospheric CH2O, O3, and NO2 by Differential Optical-Absorption, J. Geophys. Res.-Oceans Atmospheres, 84(NC10), 6329–6335, doi:10.1029/JC084iC10p06329, 1979.

Platt, U., Stutz, J., Springer E-books - York University and SpringerLink (Online service): Differential optical absorption spectroscopy: principles and applications, Springer Verlag, Berlin. [online] Available from: http://www.library.yorku.ca/eresolver/?id=1261530, 2008.

Psenner, R.: Environmental impacts on freshwaters: acidifaction as a global problem., Sci. Total Environ., 143(1), 53–61, doi:10.1016/0048-9697(94)90532-0, 1994.

Pui, D. Y. H., Chen, S.-C. and Zuo, Z.: PM 2.5 in China: Measurements, sources, visibility and health effects, and mitigation, Particuology, 13, 1–26, doi:10.1016/j.partic.2013.11.001, 2014.

Rodgers, C. D.: Inverse methods for atmospheric sounding: theory and practice, World Scientific, Singapore., 2000.

Rodgers, C. D. and Connor, B. J.: Intercomparison of remote sounding instruments, J. Geophys. Res. Atmospheres, 108(D3), doi:10.1029/2002JD002299, 2003.

Rozanov, A., Bovensmann, H., Bracher, A., Hrechanyy, S., Rozanov, V., Sinnhuber, M., Stroh, F. and Burrows, J. P.: NO2 and BrO vertical profile retrieval from SCIAMACHY limb measurements: Sensitivity studies, in Atmospheric Remote Sensing: Earth's Surface, Troposphere, Stratosphere and Mesosphere - I, vol. 36, edited by J. P. Burrows and K. U. Eichmann, pp. 846–854, Elsevier Science Ltd, Oxford., 2005.

Seinfeld, J. H. and Pandis, S. N.: Atmospheric Chemistry and Physics: From Air Pollution to Climate Change, John Wiley & Sons., 2006.

Simpson, I. J., Blake, N. J., Barletta, B., Diskin, G. S., Fuelberg, H. E., Gorham, K., Huey, L. G., Meinardi, S., Rowland, F. S., Vay, S. A., Weinheimer, A. J., Yang, M. and Blake, D. R.: Characterization of trace gases measured over Alberta oil sands mining operations: 76 speciated C-2-C-10 volatile organic compounds (VOCs), CO2, CH4, CO, NO, NO2, NOy, O-3 and SO2, Atmospheric Chem. Phys., 10(23), 11931–11954, doi:10.5194/acp-10-11931-2010, 2010.

Sioris, C. E., Abboud, I., Fioletov, V. E. and McLinden, C. A.: AEROCAN, the Canadian sub-network of AERONET: Aerosol monitoring and air quality applications, Atmos. Environ., 167, 444–457, doi:10.1016/j.atmosenv.2017.08.044, 2017.

Strawbridge, K. B.: Developing a portable, autonomous aerosol backscatter lidar for network or remote operations, Atmos Meas Tech, 6(3), 801–816, doi:10.5194/amt-6-801-2013, 2013.

Strawbridge, K. B., Travis, M. S., Firanski, B. J., Brook, J. R., Staebler, R. and Leblanc, T.: A fully autonomous ozone, aerosol and nighttime water vapor lidar: a synergistic approach to profiling the atmosphere in the Canadian oil sands region, Atmospheric Meas. Tech., 11(12), 6735–6759, doi:10.5194/amt-11-6735-2018, 2018.

Stutz, J. and Platt, U.: Problems in Using Diode-Arrays for Open Path Doas Measurements of Atmospheric Species, edited by H. I. Schiff and U. Platt, Spie - Int Soc Optical Engineering, Bellingham., 1993.

Tan, W., Liu, C., Wang, S., Xing, C., Su, W., Zhang, C., Xia, C., Liu, H., Cai, Z. and Liu, J.: Tropospheric NO2, SO2, and HCHO over the East China Sea, using ship-based MAX-DOAS observations and comparison with OMI and OMPS satellite data, Atmospheric Chem. Phys., 18(20), 15387–15402, doi:10.5194/acp-18-15387-2018, 2018.

Tokarek, T. W., Odame-Ankrah, C. A., Huo, J. A., McLaren, R., Lee, A. K. Y., Adam, M. G., Willis, M. D., Abbatt, J. P. D., Mihele, C., Darlington, A., Mittermeier, R. L., Strawbridge, K., Hayden, K. L., Olfert, J. S., Schnitzler, E. G., Brownsey, D. K., Assad, F. V., Wentworth, G. R., Tevlin, A. G., Worthy, D. E. J., Li, S.-M., Liggio, J., Brook, J. R. and Osthoff, H. D.: Principal component analysis of summertime ground site measurements in the Athabasca oil sands with a focus on analytically unresolved intermediate-volatility organic compounds, Atmospheric Chem. Phys., 18(24), 17819–17841, doi:10.5194/acp-18-17819-2018, 2018.

Wagner, T., von Friedeburg, C., Wenig, M. O., Otten, C. and Platt, U.: UV-visible observations of atmospheric O-4 absorptions using direct moonlight and zenith-scattered sunlight for clear-sky and cloudy sky conditions., J. Geophys. Res.-ATMOSPHERES, 107(D20), doi:10.1029/2001JD001026, 2002.

Wagner, T., Dix, B., von Friedeburg, C., Frieß, U., Sanghavi, S., Sinreich, R. and Platt, U.: MAX-DOAS O-4 measurements: A new technique to derive information on atmospheric aerosols - Principles and information content, J. Geophys. Res.-Atmospheres, 109(D22), D22205, doi:10.1029/2004JD004904, 2004.

Wagner, T., Deutschmann, T. and Platt, U.: Determination of aerosol properties from MAX-DOAS observations of the Ring effect, Atmos Meas Tech, 18, 2009.

Wagner, T., Beirle, S., Brauers, T., Deutschmann, T., Frieß, U., Hak, C., Halla, J. D., Heue, K. P., Junkermann, W., Li, X., Platt, U. and Pundt-Gruber, I.: Inversion of tropospheric profiles of aerosol extinction and HCHO and NO2 mixing ratios from MAX-DOAS observations in Milano during the summer of 2003 and comparison with independent data sets, Atmospheric Meas. Tech., 4(12), 2685–2715, doi:10.5194/amt-4-2685-2011, 2011.

Wagner, T., Beirle, S., Benavent, N., Bösch, T., Chan, K. L., Donner, S., Dörner, S., Fayt, C., Frieß, U., García-Nieto, D., Gielen, C., González-Bartolome, D., Gomez, L., Hendrick, F., Henzing, B., Jin, J. L., Lampel, J., Ma, J., Mies, K., Navarro, M., Peters, E., Pinardi, G., Puentedura, O., Puķīte, J., Remmers, J., Richter, A., Saiz-Lopez, A., Shaiganfar, R., Sihler, H., Roozendael, M. V., Wang, Y. and Yela, M.: Is a scaling factor required to obtain closure between measured and modelled atmospheric O_4 absorptions? An assessment of uncertainties of measurements and radiative transfer simulations for 2 selected days during the MAD-CAT campaign, Atmos. Meas. Tech., 12(5), 2745–2817, doi:https://doi.org/10.5194/amt-12-2745-2019, 2019.

Wang, T., Hendrick, F., Wang, P., Tang, G., Clemer, K., Yu, H., Fayt, C., Hermans, C., Gielen, C., Muller, J.-F., Pinardi, G., Theys, N., Brenot, H. and Van Roozendael, M.: Evaluation of tropospheric SO2 retrieved from MAX-DOAS measurements in Xianghe, China, Atmospheric Chem. Phys., 14(20), 11149–11164, doi:10.5194/acp-14-11149-2014, 2014.

Wang, Y., Beirle, S., Lampel, J., Koukouli, M., De Smedt, I., Theys, N., Li, A., Wu, D., Xie, P., Liu, C., Van Roozendael, M., Stavrakou, T., Mueller, J.-F. and Wagner, T.: Validation of OMI, GOME-2A and GOME-2B tropospheric NO2, SO2 and HCHO products using MAX-DOAS observations from 2011 to 2014 in Wuxi, China: investigation of the effects of priori profiles and aerosols on the satellite products, Atmospheric Chem. Phys., 17(8), 5007–5033, doi:10.5194/acp-17-5007-2017, 2017.

Weitkamp, C.: Lidar: range-resolved optical remote sensing of the atmosphere., Springer Science+Business Media, New York., 2005.

WHO: WHO Air quality guidelines for particulate matter, ozone, nitrogen dioxide and sulfur dioxide. Global update 2005. Summary of Risk Assessment. [online] Available from: https://apps.who.int/iris/bitstream/handle/10665/69477/WHO_SDE_PHE_OEH_06.02_eng.pdf?sequence=1 (Accessed 18 April 2019), 2006.

Wojtal, P., Halla, J. D. and McLaren, R.: Pseudo steady states of HONO measured in the nocturnal marine boundary layer: a conceptual model for HONO formation on aqueous surfaces, Atmospheric Chem. Phys., 11(7), 3243–3261, doi:10.5194/acp-11-3243-2011, 2011.

Wood Buffalo Environmental Association: Historical Environmental Monitoring Data, Wood Buffalo Environ. Assoc. [online] Available from: https://wbea.org/historical-monitoring-data/ (Accessed 29 April 2019), 2019.

Wu, F., Xie, P., Li, A., Mou, F., Chen, H., Zhu, Y., Zhu, T., Liu, J. and Liu, W.: Investigations of temporal and spatial distribution of precursors SO2 and NO2 vertical columns in the North China Plain using mobile DOAS, Atmospheric Chem. Phys., 18(3), 1535–1554, doi:10.5194/acp-18-1535-2018, 2018.

Wu, F. C., Xie, P. H., Li, A., Chan, K. L., Hartl, A., Wang, Y., Si, F. Q., Zeng, Y., Qin, M., Xu, J., Liu, J. G., Liu, W. Q. and Wenig, M.: Observations of SO2 and NO2 by mobile DOAS in the Guangzhou eastern area during the Asian Games 2010, Atmospheric Meas. Tech., 6(9), 2277–2292, doi:10.5194/amt-6-2277-2013, 2013.

Zhang, J., Moran, M. D., Zheng, Q., Makar, P. A., Baratzadeh, P., Marson, G., Liu, P. and Li, S.-M.: Emissions preparation and analysis for multiscale air quality modeling over the Athabasca Oil Sands Region of Alberta, Canada, Atmospheric Chem. Phys., 18(14), 10459–10481, doi:10.5194/acp-18-10459-2018, 2018.

Zhao, Y., Duan, L., Xing, J., Larssen, T., Nielsen, C. P. and Hao, J.: Soil Acidification in China: Is Controlling SO 2 Emissions Enough?, Environ. Sci. Technol., 43(21), 8021–8026, doi:10.1021/es901430n, 2009.

Zhong, S. and Zaveri, R.: Atmospheric Aerosols, in International Encyclopedia of Geography, pp. 1–5, American Cancer Society., 2017.

Zieger, P., Weingartner, E., Henzing, J., Moerman, M., de Leeuw, G., Mikkila, J., Ehn, M., Petaja, T., Clemer, K., van Roozendael, M., Yilmaz, S., Frieß, U., Irie, H., Wagner, T., Shaiganfar, R., Beirle, S., Apituley, A., Wilson, K. and Baltensperger, U.: Comparison of ambient aerosol extinction coefficients obtained from in-situ, MAX-DOAS and LIDAR measurements at Cabauw, Atmospheric Chem. Phys., 11(6), 2603–2624, doi:10.5194/acp-11-2603-2011, 2011.

Chapter 3

Recommendations for Spectral Fitting of SO_2 from MAX-DOAS Measurements.

Zoë Y. W. Davis[1], and Robert McLaren[2].

[1] Department of Earth and Space Science, York University, Toronto, M3J 1P3, Canada

[2] Department of Chemistry York University, Toronto, M3J 1P3, Canada

In Review: Atmospheric Measurement Techniques (2019) Ref. No.: ATMENV-D-19-01588.

Author Contributions. ZYWD: Study concept, design, investigation and data analysis, data visualization, and writing of manuscript and modifications of the same. RM: MAX-DOAS supervision and editing of the manuscript.

Abstract. Fitting SO_2 dSCDs from MAX-DOAS measurements of scattered sunlight is challenging because actinic light intensity is low in wavelength regions where the SO_2 absorption features are strongest. SO_2 dSCDs were fit with different wavelength windows (λ_{low} to λ_{high}) from ambient measurements with high and low concentration calibration cells inserted in the light path at different viewing elevation angles. SO_2 dSCDs were the least accurate and fit errors were the largest for fitting windows with λ_{low} < 307 nm or λ_{low} >312 nm. The SO_2 dSCDs also exhibited an inverse relationship with the SO_2 absorption cross-section for fitting windows with λ_{low} < 307 nm. Spectra measured at low viewing elevation angles (i.e., $\alpha = 2^o$) exhibited less accurate SO_2 dSCDs for the same fitting windows compared to higher angles. The use of a 400 nm short-pass filter or a polynomial to account for stray light (the offset function), increased the accuracy of the SO_2 dSCDs for many different fitting windows, decreased fit errors, and decreased the dSCDs' dependence on the SO_2 absorption features. The inaccuracies at lower fitting wavelengths were increased by stray light originating from light with λ > 400 nm. Deviation of the SO_2 dSCD from the true value depended on the SO_2 concentration for some fitting windows rather than exhibiting a consistent bias. Uncertainties of the SO_2 dSCD reported by the fit algorithm were significantly less than the true error for many windows, particularly for the measurements without the filter or offset function. For retrievals with the filter or offset function, increasing λ_{high}> 320 nm tended to decrease the reported fit uncertainty but did not increase the accuracy. Based on the results of this study, a short-pass filter and a fitting window of 307.5 < λ <319 nm are recommended. If a filter is not available or conflicts with other species to be determined (NO_2, HCHO, etc.), the offset function should be enabled, and a fit window 307.5 < λ <319 nm is still recommended.

3.1 Introduction

Retrieving differential Slant Column Densities (SCDs) of SO_2 from MAX-DOAS measurements is challenging because the SO_2 absorption features are strongest in the wavelength region where the intensity of solar light becomes relatively small. There are three major regions of photo-absorption by SO_2 in the UV range: the very weak absorption in the A band ranges from 340-390 nm, the moderately strong B band ranges from 260-340 nm, and the strongest C band ranges from 180-240 nm. MAX-DOAS spectroscopy uses the SO_2 "B band" in the near UV, which has absorption peaks of increasing strength with decreasing wavelength (Hermans et al., 2009; Xie et al., 2013). Actinic flux at the surface level of the earth decreases by several orders of magnitude in the 320-290 nm region due to a steep increase in O_3 absorption with decreasing wavelengths (Kreuter and Blumthaler, 2009). O_3 absorption features can also cause interference in the fit because of the similarity to the SO_2 absorption features between 315 and 325 nm (Rix et al., 2012). Stray light in spectrometers, which reduces fit accuracy, can be a major challenge in near UV spectral region due to the low signal-to-noise ratio (Kreuter and Blumthaler, 2009). The ideal fitting window for retrieval of SO_2 must have a lower wavelength (λ_{low}) small enough to include strong features of SO_2 absorption but large enough to ensure enough solar signal. The upper wavelength of the fit range (λ_{high}) should ensure that the fitting window includes multiple SO_2 absorption structures while excluding wavelengths where SO_2 absorption features are so weak that degrees of freedom (DOF) are unnecessarily increased, increasing fitting uncertainty. MAX-DOAS fit windows must also be relatively narrow compared to direct sun viewing applications because the air mass factors used to convert SCDs to vertical column densities (VCD) differ with wavelength due to scattering (Fioletov et al., 2016b).

Fitting windows for SO_2 in previous MAX-DOAS studies have varied: 305-317.5 nm (Wang and Christopher, 2003), 307.5-328 (Schreier et al., 2015), 307.6-325 nm (Jin et al., 2016), 310-320 nm (Irie et al., 2011), and Bobrowski and Platt (2007) used 307.5 to 315.0 with a short-pass filter to block visible light >400 nm to reduce stray light. In this study, MAX-DOAS measurements of scattered sunlight were made with two different calibration gas cells inserted in the light path to examine the variation in the SO_2 dSCDs with 1) different fitting windows, 2) different viewing elevation angles (α), 3) the use of a 400 nm short-pass filter, and 4) the offset function enabled.

3.2 Methods

The mini-MAX-DOAS instrument (Hoffmann Messtechnik GmbH model #16127) consisted of a sealed metal box with a UV fibre-coupled spectrometer and all electronics inside. Incident scattered sunlight received by the cylindrical black telescope in front of the entrance optics is focused into the quartz fibre by a cylindrical quartz lens with a focal length of 40 mm. The spectrometer (OceanOptics USB2000 spectrograph) has a 50 µm wide entrance slit and a Sony ILX511 linear silicon Charge-Coupled Device (CCD) array detector (2048 pixels, pixel size 14x200 microns, signal-to-noise ratio at full signal 250:1). The spectral range of the spectrometer is 290-433 nm with a resolution of ~0.6 nm FWHM. A Peltier stage cooled the spectrograph to maintain the chosen temperature of 5ºC. A stepper motor mounted underneath allows the instrument to point at different α above the horizon. The instrument was connected to a laptop via USB to transfer spectrometer data and allow automated measurements by Jscript programs using the DOASIS software package.

MAX-DOAS spectra of scattered solar light were recorded with an SO_2 calibration gas cell (Resonance Ltd.) inserted in the light path (in the telescope tube). The two cylindrical gas cells with a 22 mm diameter and 14.13 mm thickness had calibrated slant column densities (SCDs) of 2.2×10^{17} molec cm^{-2} (high) and 2.2×10^{16} (low) (± 10%) molec cm^{-2}. Active-DOAS measurements of the SO_2 gas cells confirmed the SCDs. These SCDs would be equivalent to an air mass with SO_2 mixing ratios of 87 and 9 ppbv, respectively, for a $\alpha=30^o$ measurement within a homogeneous boundary layer of 1 km. For each cell, spectra were recorded around solar noon in September in Toronto, Ontario (43.773 N, -79.506 W) at $\alpha = 2^o$, 4^o, 8^o, 30^o, and 90^o above the horizon, followed by a 90^o measurement without the gas cell. This second zenith measurement was used as the Fraunhofer Reference Spectrum (FRS) in the fit. Each recorded spectrum was the average of 1000 spectra with an integration time of ~115 ms. The experiment was repeated for both gas cells by placing a 400 nm short-pass filter (Edmund Optics TECHSPEC® OD 2 #47-285**)** within the telescope between the MAX-DOAS lens and the SO_2 gas cell. The fused silica filter had a thickness of 3 mm, a cutoff wavelength of 400 nm, and a transmission wavelength range of 250-385 nm. The blocking optical density was ≥2.0, and the transmission was >85% in the transmission range. Spectra collected using the filter were fit against a FRS collected by measuring a 90^o spectrum without a gas cell but including the filter.

Trace gas differential Slant Column Densities (dSCDs) were obtained using the DOAS technique (Platt and Stutz, 2008) with DOASIS software (Institute of Environmental Physics, Heidelberg University, 2009). All spectra were corrected for dark current and electronic offset, and wavelength calibrated using measurements of a Mercury (Hg) lamp. Included in all fits were a Fraunhofer Reference Spectrum (FRS), Ring spectrum, a 3^{rd} order polynomial, and

cross-sections of SO_2 at 293K and O_3 at 293 and 223 K (Bogumil et al., 2003a). The cross-sections were obtained from the MPI-MAINZ UV/VIS Spectral Atlas of Gaseous Molecules of Atmospheric Interest (Keller-Rudek et al., 2013). The reported uncertainty in the SO_2 absorption cross-section is ~3% (Bogumil et al., 2003a). The SO_2 dSCDs were fit in DOASIS with varying fitting windows using λ_{low}= 303-316 nm and λ_{high}= 310-340 nm in ~0.2 nm increments. DOASIS fits dSCDs using an iterative algorithm based on the Levenberg-Marquardt method that finds the optimal solution by minimizing a cost function. The cost function includes the deviation between the measured spectrum and the spectrum modelled using the components included in the fit. Details on the DOASIS fitting algorithm can be found in Kraus (2006).

For each calibration gas cell (high and low), four scenarios were fit: i) the base case (B) with no filter and no offset function, ii) no filter with offset function enabled (B+O), iii) with filter and offset disabled (B+F), and iv) with both filter and offset enabled (B+ F+O). The offset function enabled in DOASIS was used with a fixed polynomial order of zero. SO_2 dSCDs were considered "accurate" if within ±10% of the high calibration cell value and ±50% of the low calibration cell value, 2.2×10^{17} and 2.2×10^{16} molec cm^{-2}, respectively. The background SO_2 in the atmosphere in Toronto was assumed to be negligible (<1 ppbv) because there are currently no significant sources in Toronto (ECCC, 2018d). A few industrial sources of <1600 tonnes of SO_2 yr^{-1} were present south-west of Toronto (ECCC, 2018d), but the measurements were conducted under North-Easterly wind conditions. Typical hourly average mixing ratios of SO_2 in northern Toronto are <0.5 ppbv (Ontario Ministry of the Environment, 2019).

3.3 Results

Examples of spectral retrievals of SO_2 from the $\alpha=2^o$ spectrum in the base case (no filter and offset function disabled) are shown in Figure 3-1.

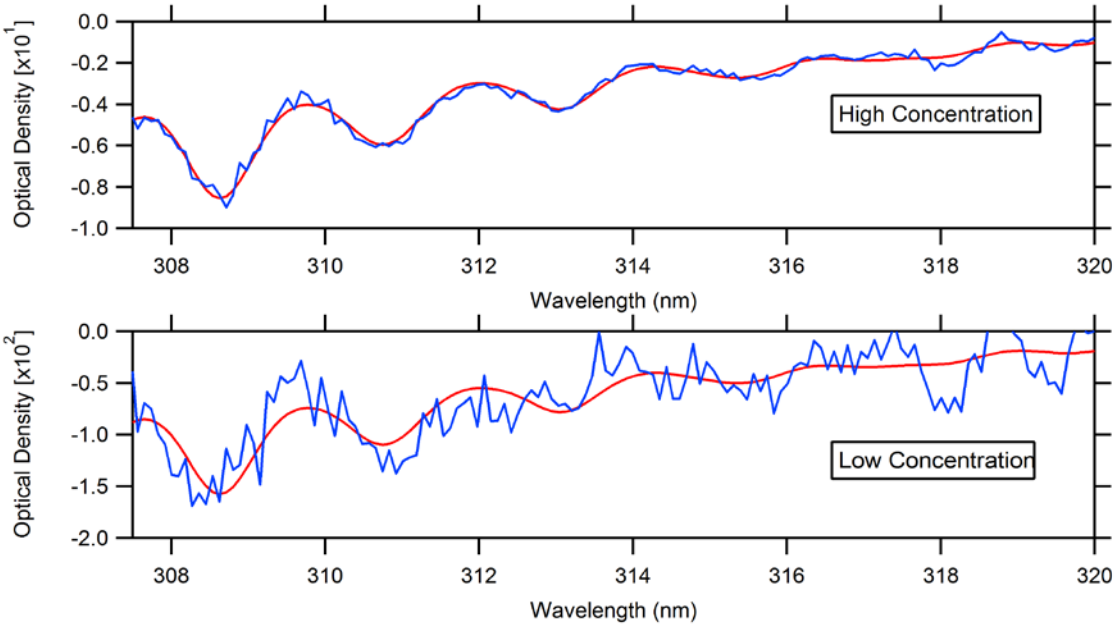

Figure 3-1 Examples of spectral retrievals of SO_2 from the base case (no filter and offset function disabled) from spectra measured at 2^o viewing elevation angle using the fitting window 307.5-320 nm. Retrieved dSCDs were $2.23(\pm0.08)\times10^{17}$ molec cm^{-2} and $4.10(\pm0.66)\times10^{16}$ molec cm^{-2} for the high and low concentration measurements, respectively.

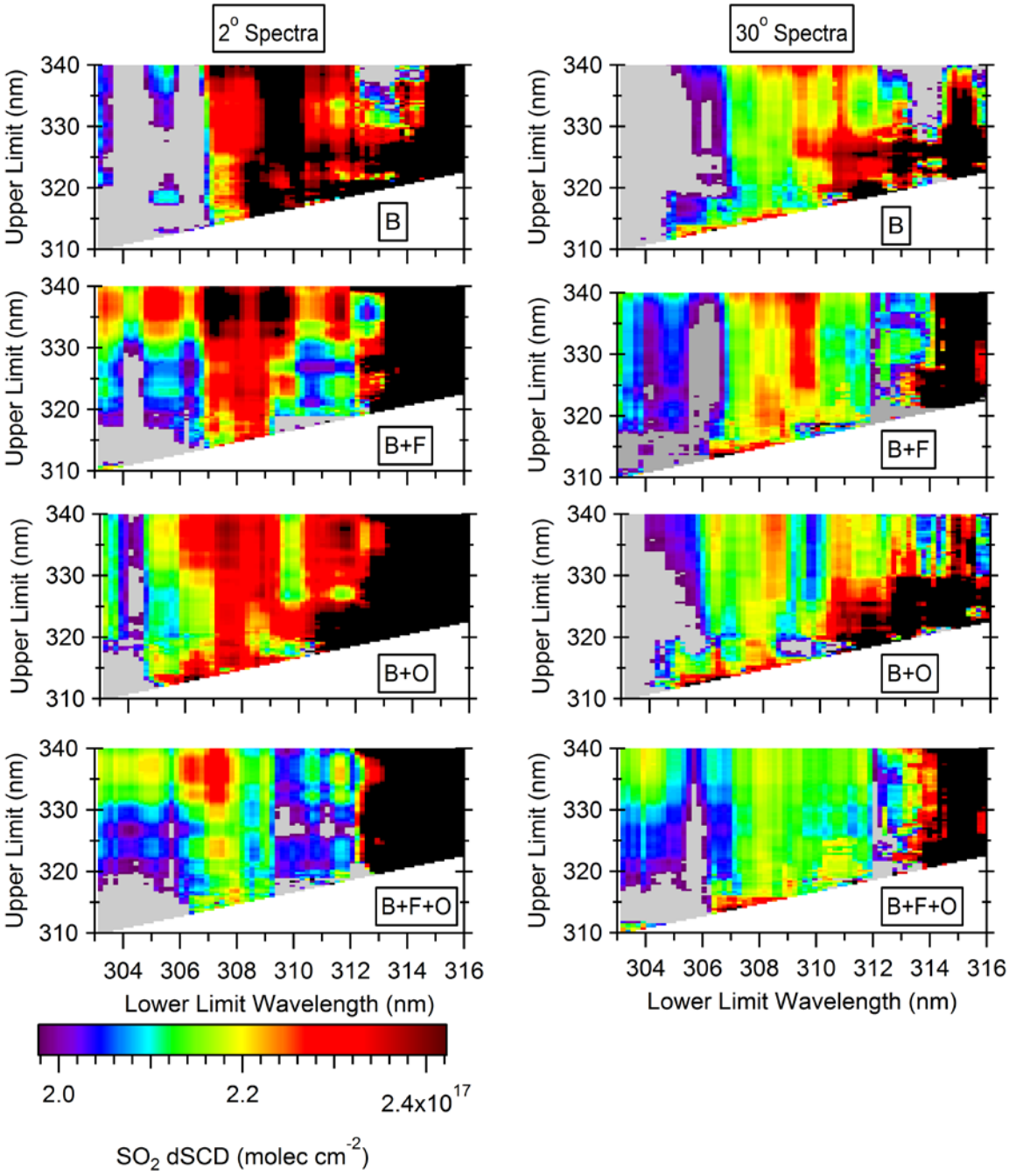

Figure 3-2 SO_2 dSCDs fit from high concentration measurements at 2° (left) and 30° (right) elevation angles for the base case (B), with offset (B+O), with filter (B+F), and with filter and offset (B+F+O). Grey and black areas indicate dSCDs were <10% less and >10% more than the expected value, respectively. The true value of the cell is 2.2×10^{17} molec cm^{-2} (yellow).

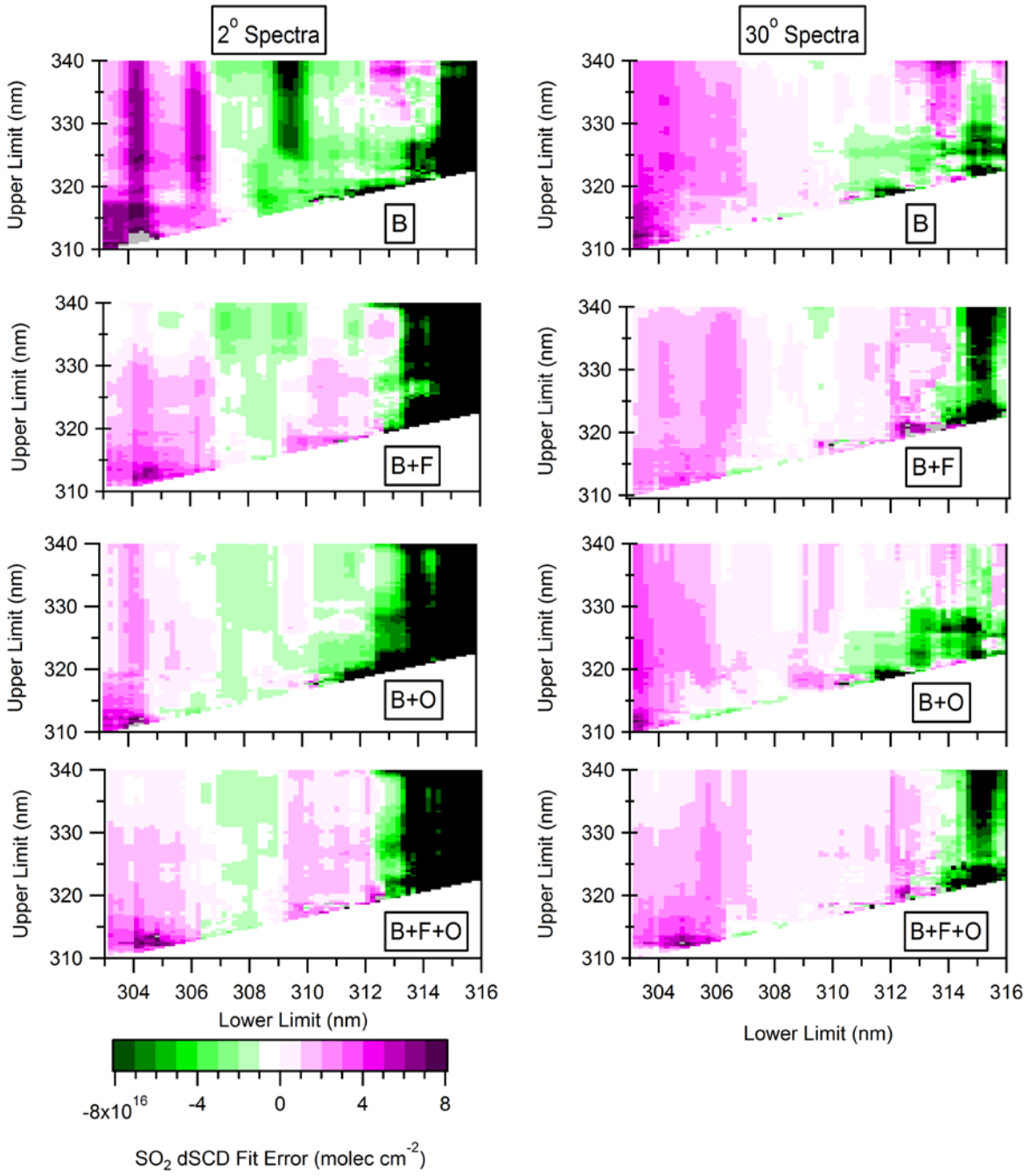

Figure 3-3 High concentration fit errors (deviations of SO_2 dSCDs from the expected value of 2.2×10^{17} molec cm^{-2}) from the measurements at 2° (left) and 30° (right) elevation angles for the base case (B), with offset (B+O), with filter (B+F), and with filter and offset (B+F+O). Purple and green areas indicate under- and over-estimation of the expected value, respectively. Black and grey areas indicate dSCDs over- and under-estimated by more than 8.0×10^{16} molec cm^{-2}, respectively.

3.3.1 High Concentration Reference Cell

SO_2 dSCDs fit from the $\alpha=2^o$ and $\alpha=30^o$ measurements using the high concentration cell are shown in Figure 3-2 with varying fitting windows for the four scenarios. The deviations of the SO_2 dSCDs from the expected value of 2.2×10^{17} molec cm^{-2} (fit errors) are shown in Figure 3-3, where purple and green colours indicate under- and over-estimation, respectively. Grey and black areas indicate that the dSCD under- and over-estimated the expected value by more than 8×10^{16} molec cm^{-2}, respectively. For the base case, the windows with λ_{low} <307 nm ("low wavelengths") underestimated the expected SO_2 dSCD as indicated by the grey areas in Figure 3-2(B) and the purple areas in Figure 3-3 (B). The addition of the short-pass filter increased the accuracy of the SO_2 dSCDs for most windows, especially in the low wavelengths (Figure 3-2 & Figure 3-3 (B+F)). These results suggest that stray light originating from wavelengths >400 nm increased the underestimation of SO_2 dSCDs at low wavelengths.
Stray light is a well-known source of interference in spectroscopic measurements that reduces accuracy and can obscure weak spectral lines (Kristensson et al., 2014). Ideally, a spectrometer's detector receives only light with the correct spectral bandwidth window at each pixel (Lindon et al., 2000). Stray light is additional light of incorrect wavelength that enhances the background signal in ways that can vary across the spectral range (Kristensson et al., 2014). Sources of stray light include imperfections in the diffraction grating, leakage of light into the instrument, and scattering off mirrors and dust inside the instrument (Lindon et al., 2000). Stray light results in apparent negative deviations from Beer's law (Choudhury et al., 2015), causing an underestimation of the retrieved SO_2 dSCD by "filling-in" the measured intensity reduced by SO_2 absorption features. Stray light has an enhanced effect at low wavelengths because of the low measured signal and sensitivity near the lower end of the actinic spectral range (Choudhury et al., 2015). Many fitting windows with λ_{low}<307 nm and λ_{high}< 320 nm still underestimated the SO_2 dSCD even with the filter, suggesting that significant stray light from <400 nm remained (Figure 3-2 (B+F)).
Enabling the offset function increased the accuracy of the SO_2 dSCDs of many windows compared to the base case (Figure 3-2Figure 3-3(B+O)). The offset function resulted in slightly more windows with accurate dSCDs than the filter for windows with λ_{low} <311 nm because the offset function attempts to compensate for all the stray light, not just the stray light originating from >400 nm (Figure 3-2 (B+F) & (B+O)). The use of both the offset function and the filter slightly improved the dSCD accuracy for a few windows compared to the filter or offset function alone (Figure 3-2 (B+F+O)). However, the effect for the lower angles was mostly for windows with large λ_{high} (>324 nm) that are unlikely to be utilized due to unnecessarily increased DOF.

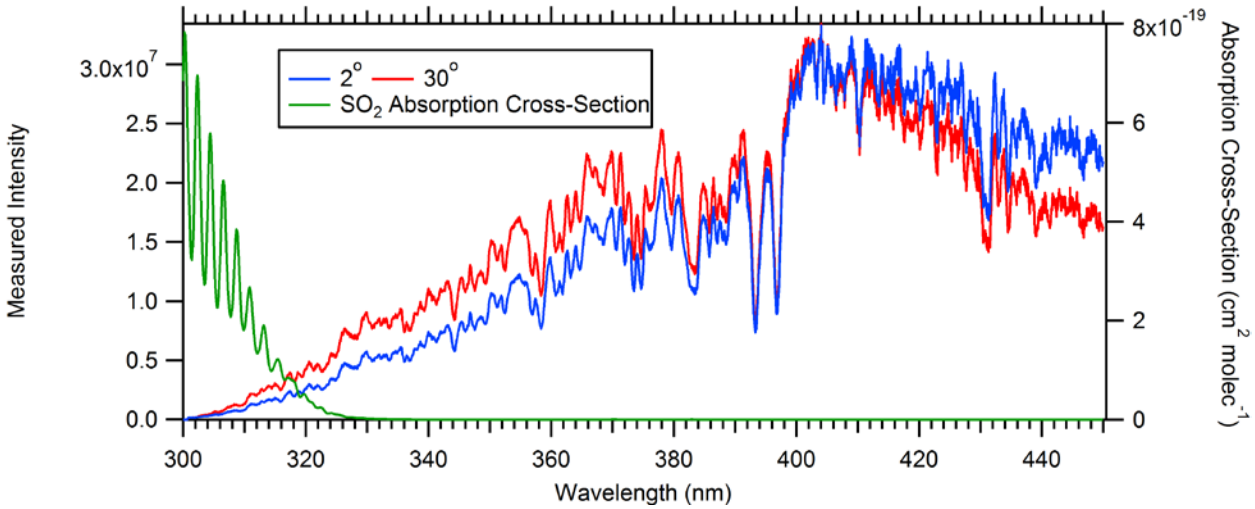

Figure 3-4 Comparison of the measured spectral intensity for the 2º and 30º viewing elevation angle spectra with the low concentration cell without the short-pass filter, and the absorption cross-section of SO_2 smoothed to the spectral resolution of the instrument.

Fitting windows produced more accurate SO_2 dSCDs from spectra measured at higher α (90º & 30º) compared to the lowest α (2º & 4º) in the base case (Figure 3-2,Figure 3-3 (B) & B1). Windows with λ_{low} <307 nm underestimated SO_2 dSCDs more from the 2º compared to the 30º measurements (Figure 3-3(B)). The spectra collected at higher α are expected to produce more accurate SO_2 dSCDs because of the greater UV signal intensity (Figure 3-3 &Figure 3-4). Spectra measured at lower α have longer light paths closer to the ground, experiencing more Rayleigh scattering that preferentially scatters away shorter wavelengths and reduces the UV intensity. The impact of stray light on fits from the lower angle spectra is further increased because the visible light intensity, a potential source of stray light, is the same or higher compared to measurements at higher α (Figure 3-4). The difference in the accuracy of SO_2 dSCDs between low and high α spectra decreased with the use of the filter or the offset function (Figure 3-2 & Figure 3-3), an expected result.

Fitting windows with λ_{low} >312 nm often overestimated the SO_2 dSCDs for all scenarios, as indicated by the green and black areas in Figure 3-3, probably because the SO_2 absorption features become relatively weak (Figure 3-4). The SO_2 dSCDs exhibited a dependence on the features of the SO_2 absorption cross-section for λ_{low} <307 nm for the base case (Figure 3-2 &Figure 3-3) that will be discussed in section 5.3.3.

3.3.2 Low Concentration Reference Cell

Figure 3-5 and Figure 3-6 show the SO_2 dSCDs and their deviations from the expected value (fit error), respectively, for the low concentration measurements for all the scenarios. Purple and green areas in Figure 3-6 indicate dSCDs were under- and over-estimation, respectively. Black and grey areas indicate dSCDs over- and under-estimated by more than 2.0×10^{16} molec cm^{-2}, respectively.

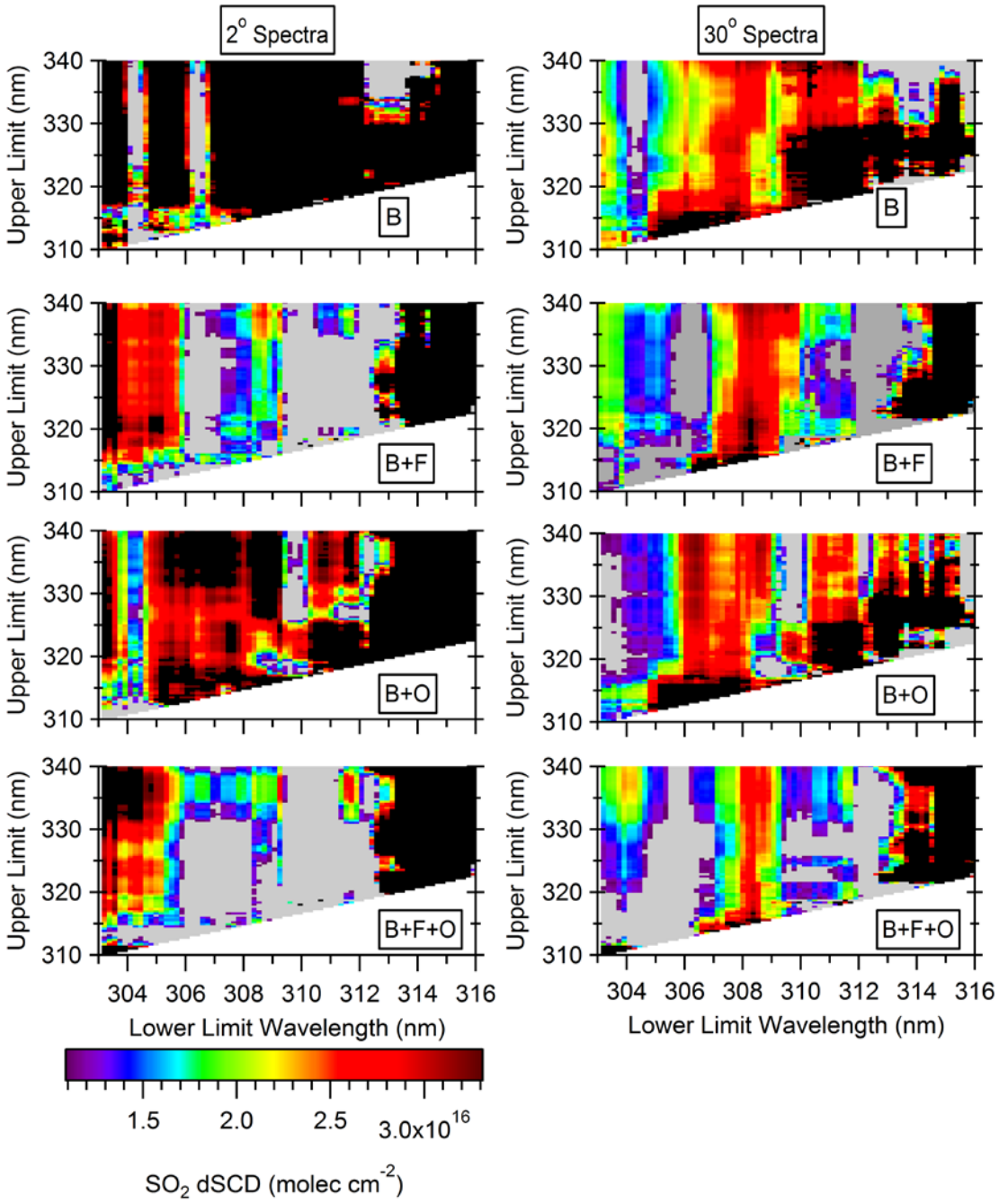

Figure 3-5 SO_2 dSCDs fit from the low concentration measurements at 2° (left) and 30° (right) elevation angles for the base case (B), with offset (B+O), with filter (B+F), and with filter and offset (B+F+O). Grey and black areas indicate dSCDs that were <50% less and >50% more than the expected value, respectively. The true value of the high concentration cell is 2.2×10^{16} molec cm^{-2} (yellow).

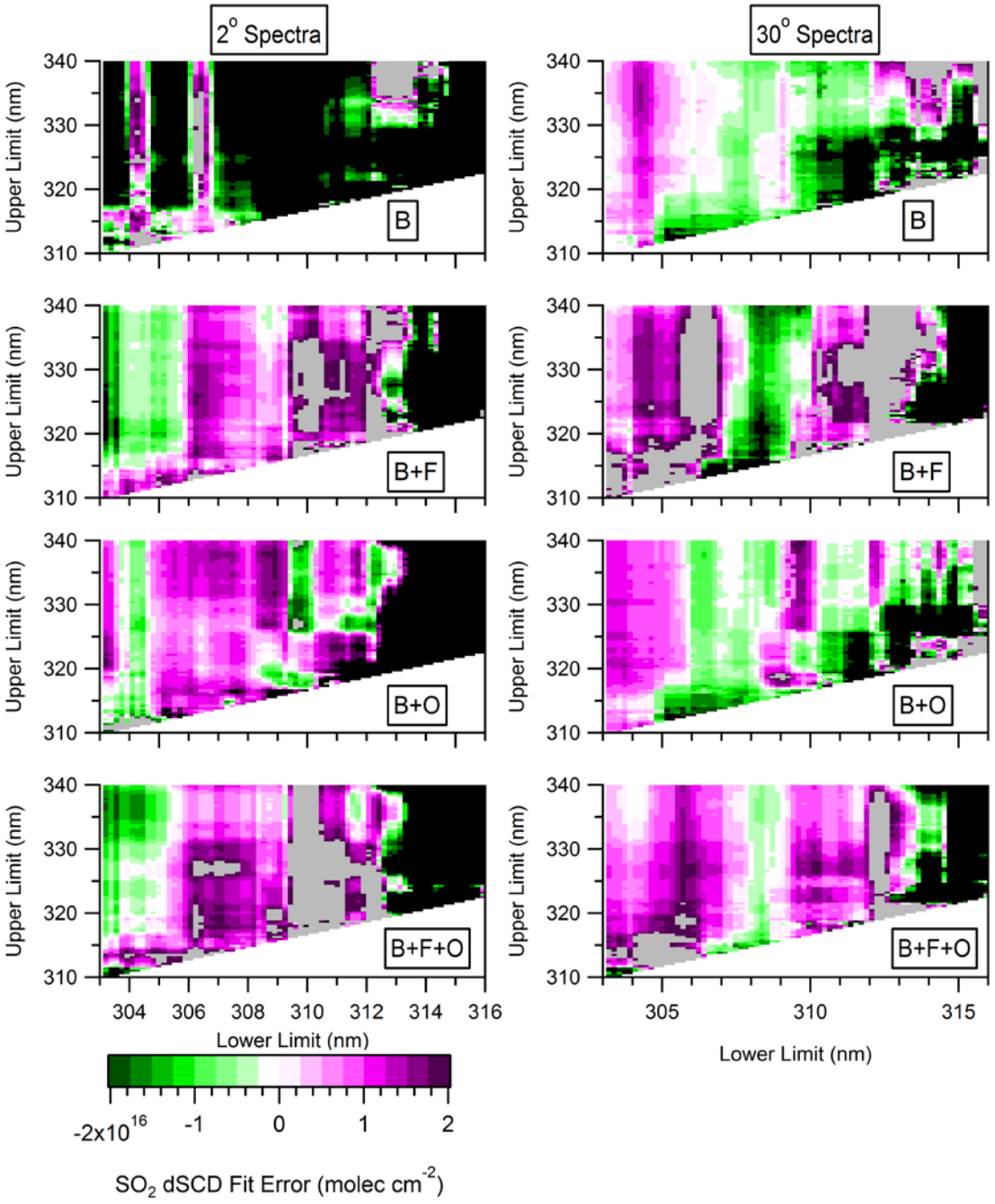

Figure 3-6 Low concentration fit errors (deviations of SO_2 dSCDs from the expected value of 2.2×10^{16} molec cm^{-2}) from the measurements at 2° (left) and 30° (right) elevation angles for the base case (B), with offset (B+O), with filter (B+F), and with filter and offset (B+F+O). Purple and green areas indicate dSCDs were under- and over-estimation, respectively. Black and grey areas indicate dSCDs over- and under-estimated by more than 2.0×10^{16} molec cm^{-2}, respectively.

The SO_2 dSCDs from the base case exhibited a dependence on the SO_2 absorption that will be discussed in section 5.3.3. In the base case, the low concentration measurements had fewer windows that produced accurate SO_2 dSCDs compared to the high concentration measurements (Figure 3-2 & Figure 3-5 (B)). Most of the fitting windows produced SO_2 dSCDs that were >100% over- or under-estimated for the low concentration 2° spectrum (Figure 3-5 Figure 3-6(B) & B1). In contrast, the low concentration 90° measurement exhibited accurate SO_2 dSCDs for all fitting windows with λ_{low} < 311 nm (Figure B1). This difference highlights that measurements at lower α experience greater inaccuracies from the reduced solar intensity and greater impact of stray light. While the high concentration dSCDs from the 2° measurements were consistently underestimated for windows with λ_{low} <307 nm, the low concentration measurements often overestimated the dSCDs (Figure 3-5 &Figure 3-6(B)). This overestimation in spite of the influence of stray light could be due to interference from O_3 since the similarity between the absorption features of SO_2 and O_3 can introduce instability in the retrieval (Kraus, 2006; Rix et al., 2012). The deviation of the dSCD from the true value can depend on the SO_2 concentration rather than exhibiting a consistent bias for a fitting window.

The use of the filter or offset function increased the accuracy of the SO_2 dSCDs for most windows for spectra measured at angles ≤15° (Figure 3-3 & Figure 3-6 (B+F), (B+O)). The improved accuracy due to the filter indicates that stray light originating from wavelengths >400 nm significantly decreased the accuracy of the SO_2 dSCDs for fitting windows at both lower and higher wavelengths. Unexpectedly, use of both the filter and offset function for the 30° measurement reduced the accuracy of the SO_2 dSCDs compared to the base case for some windows with λ_{low}<307 nm and λ_{high}<320 nm (Figure 3-6 (B+F+O)). Since the stray light to signal ratio is expected to be lower for the higher elevation measurements, and the filter already reduced the stray light, the offset function may have incorrectly estimated the relatively small amount of remaining stray light at some wavelengths. The offset function may have added unnecessary freedom to the fit, increasing instability and inaccuracy in the dSCD. Also, the offset function compensates for stray light by assuming the stray light is proportional to the measured intensity (see Eqs. 11-12 in Appendix B). If light from wavelengths outside the fitting window contributes to stray light, this assumption is invalid, and the offset function may increase uncertainty in the fit. The short-pass filter may be the preferred method of reducing the impact of stray light compared to the offset function because the filter directly addresses rather than modelling the source of the problem. However, the problems from using both the filter and offset function can be mitigated by using a fitting window with λ_{low}<307 nm.

3.3.3 Dependence of the dSCD on the SO_2 Absorption Features

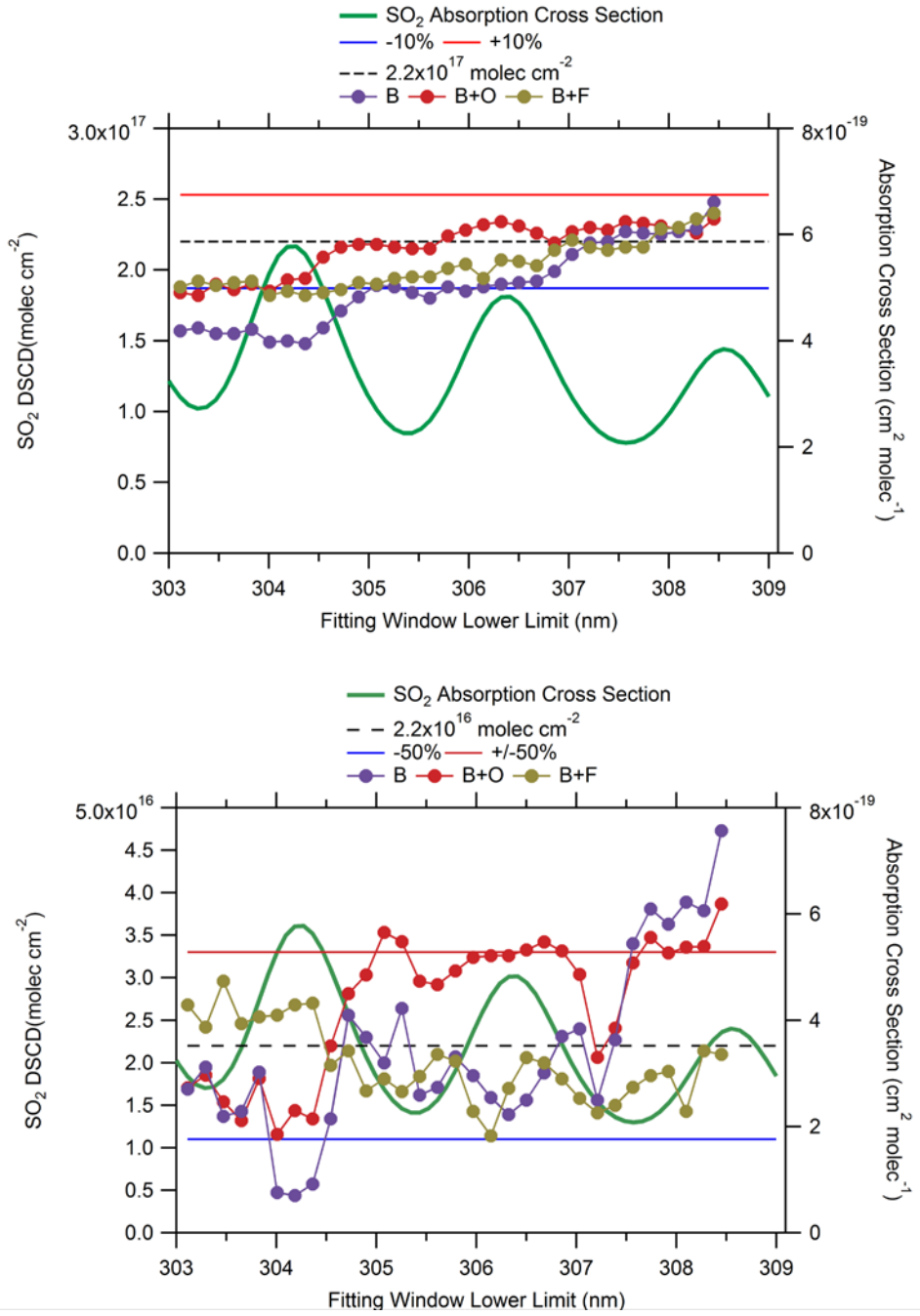

Figure 3-7 SO_2 absorption cross-section and variation in the SO_2 dSCD with λ_{low} with λ_{high} = 315 nm for high (top) and low (bottom) concentration measurements for the base case (B), with offset (B+O), and with filter (B+F).

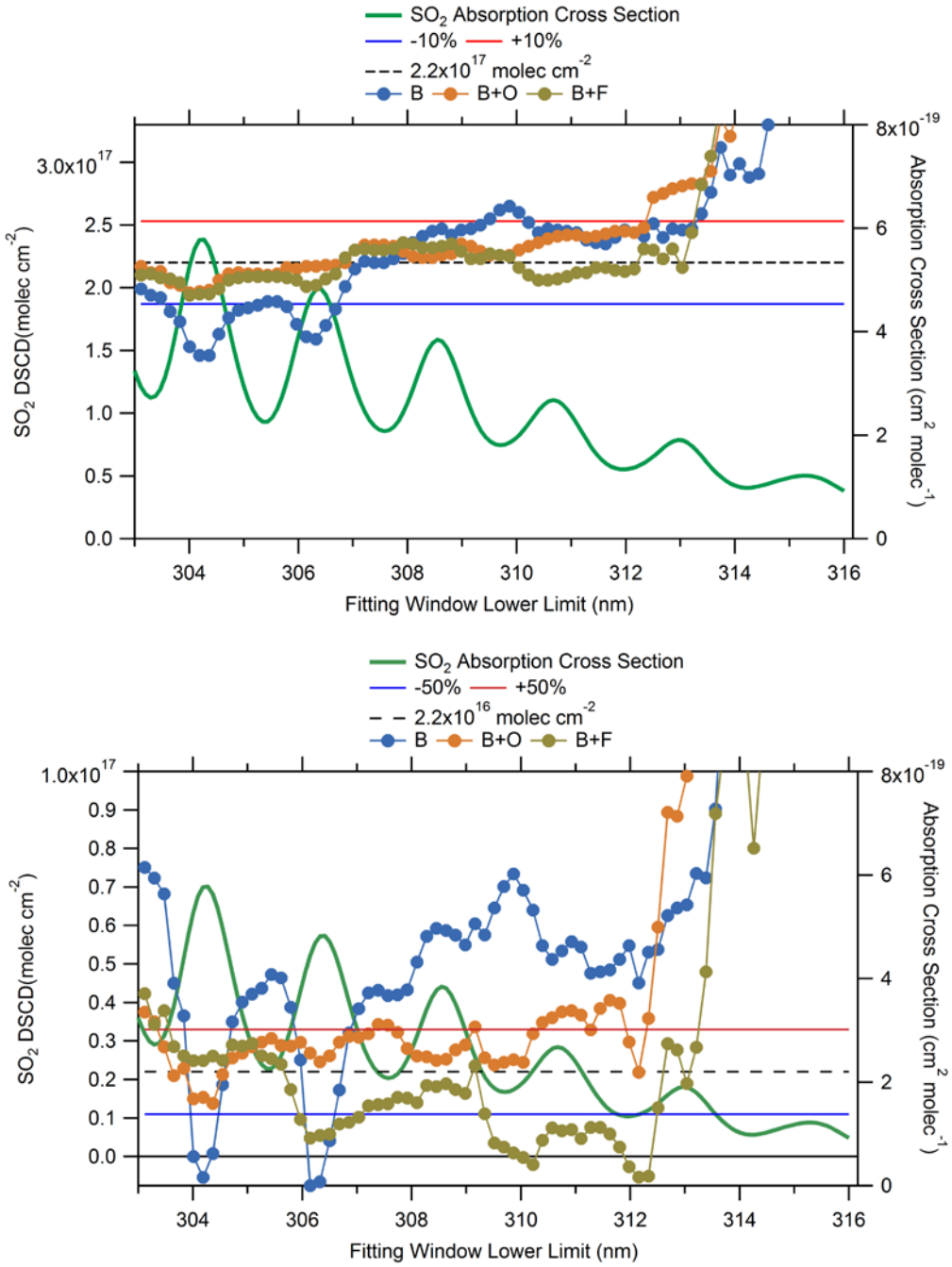

Figure 3-8 SO_2 absorption cross-section and variation in the SO_2 dSCD with λ_{low} with λ_{high}= 324 nm for high (top) and low (bottom) concentration measurements for the base case (B), with offset (B+O), and with filter (B+F).

In the base case, the SO_2 dSCDs exhibited an inverse relationship with the SO_2 absorption features for windows with λ_{low}< 307 nm and λ_{high}<330 nm for non-zenith measurements (Figure 3-2& Figure 3-5(B)). The variation in the SO_2 dSCD as a function of λ_{low} from the $\alpha=2^o$ measurements, given λ_{high} of 315 nm and 324 nm, are shown in Figure 3-7 andFigure 3-8, respectively. The SO_2 dSCDs varied up to 3.4×10^{16} and 3.0×10^{16} molec cm^{-2} for a 0.4 nm change in λ_{low} for the high and low concentration measurements, respectively (Figure 3-7 &Figure 3-8). For both concentrations, using the filter or enabling the offset function reduced the dependence of the dSCDs on λ_{low} (Figure 3-7 &Figure 3-8) and increased the accuracy of many of the low wavelength fitting windows (Figure 3-3 Figure 3-6). The SO_2 dSCD dependency was increased by stray light, exhibiting the greatest underestimation when λ_{low} coincided with an SO_2 absorption peak. Errors due to stray light are enhanced in wavelength regions where absorption is high (Choudhury et al., 2015). The measured signal was further reduced surrounding an SO_2 absorption peak (e.g., ~304.4 nm) compared to an absorption minimum and stay light "filled-in" the decreased intensity due to the absorption maxima. If an absorption peak is the strongest SO_2 feature included in the fit, the resultant deviation between the modelled and measured spectrum in the peak region requires the fit algorithm to underestimate the SO_2 dSCD to minimize the cost function (see Appendix B for fitting algorithm details). The inverse relationship between the dSCD and the SO_2 absorption features was strongest at λ_{low} <307 nm because absorption was greatest and solar signal was smallest (Figure 3-4,Figure 3-7 &Figure 3-8). The dSCDs exhibit less dependence on the λ_{low} when λ_{low} = 307-311 nm due to increased solar intensity and weaker SO_2 absorption (Figure 3-4). For both high and low concentration measurements, the anti-correlation of the SO_2 dSCD in the base case was more pronounced for windows with the λ_{high}= 324 nm than λ_{high}= 315 nm (Figure 3-7 &Figure 3-8).

3.3.4 Fit Uncertainties and Accuracy

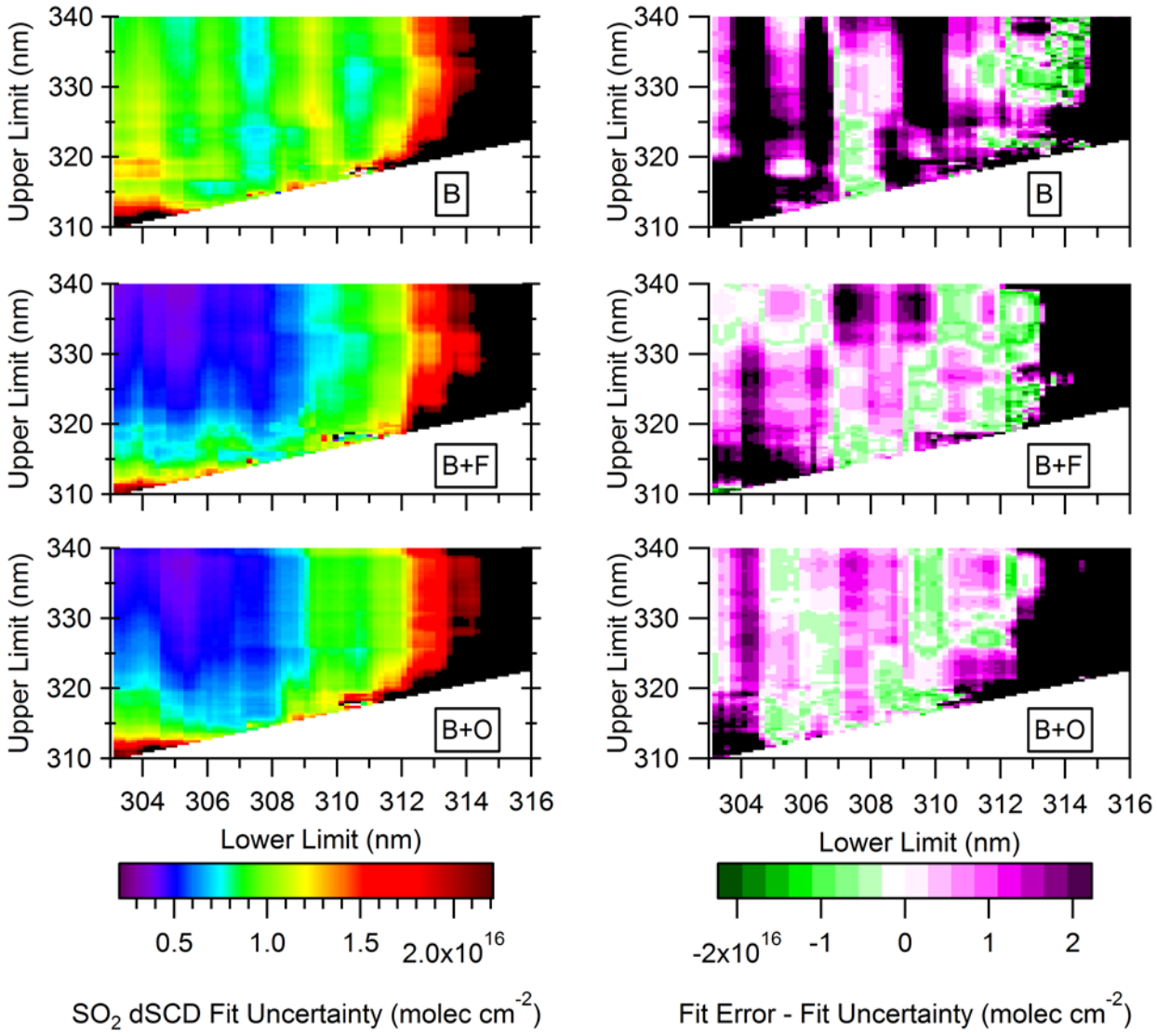

Figure 3-9 High concentration SO_2 dSCDs fit uncertainties (left) and difference between fit error and uncertainty (right) from spectra measured at 2° elevation angle for the base case (B), with offset (B+O), and with filter (B+F). Black areas indicate errors >1.1×10^{16} molec cm^{-2} for absolute error (left) and >2.2×10^{16} molec cm^{-2} for the difference (under-estimation) between actual and fit error.

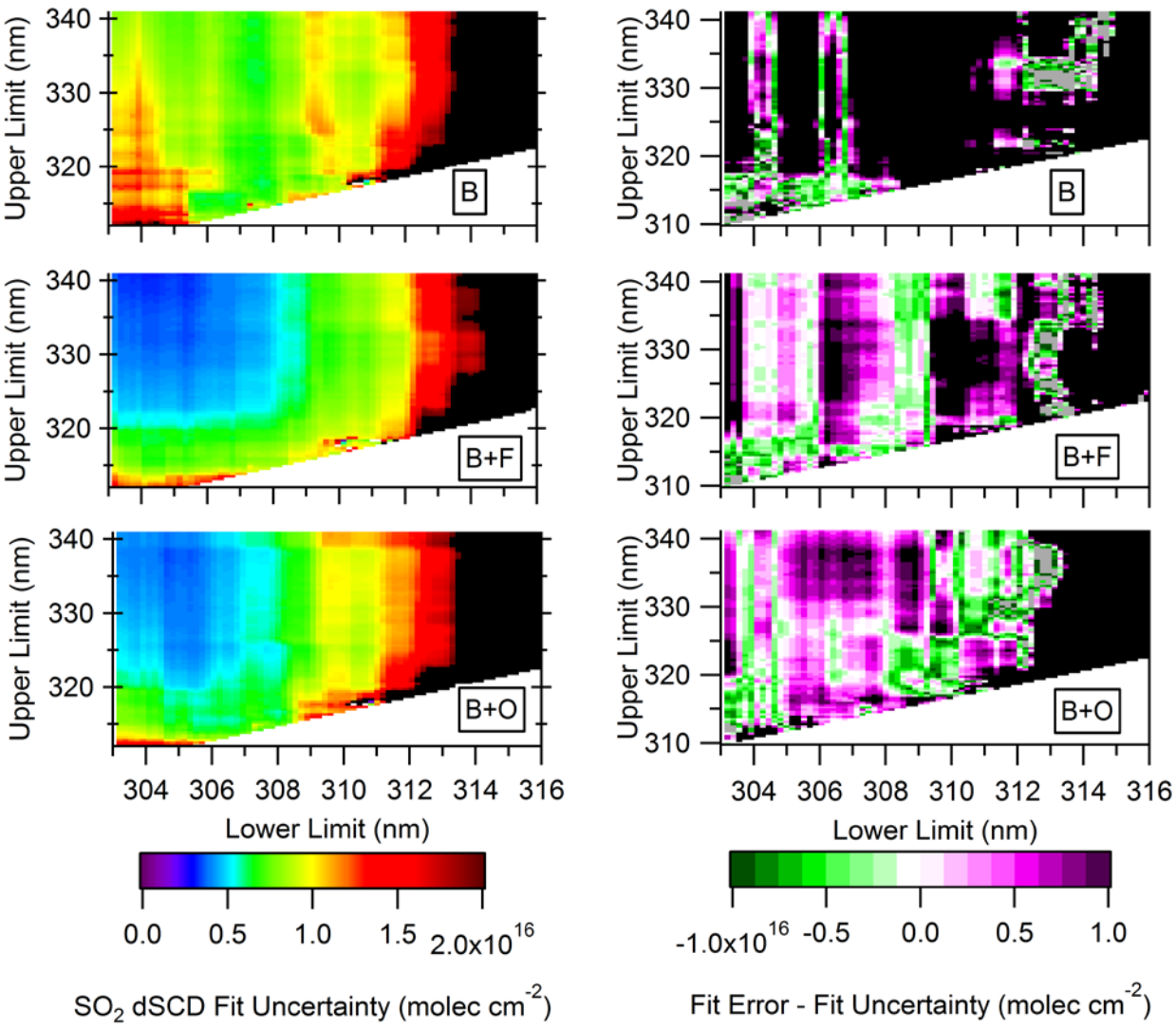

Figure 3-10 Low concentration SO_2 dSCDs fit errors (left) and difference between fit uncertainty and error (right) from spectra measured at 2° elevation angle for the base case (B), with offset (B+O), and with filter (B+F). Black areas indicate errors of $>2.2\times10^{16}$ molec cm^{-2} for absolute error (left) and $>1.1\times10^{16}$ molec cm^{-2} under-estimation of the fit error by the fit uncertainty.

The uncertainty in the SO_2 dSCD reported by the fitting algorithm and the actual deviation from the expected value shall be referred to as the "fit uncertainty" and the "fit error," respectively. The fit uncertainties from the 2° spectrum are shown for the high and low concentration measurements in the left column of Figure 3-9 and Figure 3-10, respectively. The fit uncertainties for the base case were the greatest for windows with λ_{low} <306 nm and λ_{high} < 315 nm, and with λ_{low} >312 nm (Figure 3-9Figure 3-10 (B)). The difference between fit uncertainty and error are shown in the right column of Figure 3-9 and Figure 3-10. The purple and black regions indicate that fit error was greater than the fit uncertainty, and the green regions indicate that fit error was less than fit uncertainty. For the high concentration measurement, the fit error was significantly greater than the fit uncertainty (by $>2.2\times10^{16}$ molec cm^{-2}) when λ_{low} <305 nm in the base case (black regions in Figure 3-9 (B)). Therefore, fitting windows in low wavelength

regions (impacted by stray light) not only produce less accurate SO_2 dSCDs but also significantly underestimate the fit error (Figure 3-2Figure 3-3 Figure 3-9 (B)). For the low concentration measurement, the fit error was greater $>1.1\times10^{16}$ molec cm^{-2} greater than the fit uncertainty for most windows in the base case (black regions in Figure 3-10 (B)). The use of the filter or enabling the offset function reduced the fit uncertainties by up to 50% and decreased the difference between the fit errors and uncertainties, particularly for windows with λ_{low} <309 nm. Note that when the filter or offset function was used, increasing λ_{high} > ~ 320 nm or decreasing the λ_{low} < ~307 nm decreased the fit uncertainty but not the fit error for some windows (Figure 3-6 and Figure 3-8).

3.4 Summary and Recommendations

SO_2 dSCDs in the base case were least accurate and had the largest fit uncertainties for fitting windows with λ_{low} <307 nm and >312 nm due to stray light and low solar signal, and weak SO_2 absorption, respectively. Fitting windows exhibited less accurate SO_2 dSCDs for spectra recorded at lower compared to higher α due to reduced UV signal. Therefore, choosing an accurate fitting window is particularly important for measurements at low α. Windows with λ_{low} <307 nm generally underestimated SO_2 dSCDs from high concentration measurements for all scenarios but could be overestimated by the same windows for the low concentration measurements. In the base, the SO_2 fit uncertainties were significantly less than the actual fit error for many windows case for both concentration measurements. Using the short-pass filter or the offset function increased the accuracy of the SO_2 dSCDs, decreased fit uncertainty, and decreased the difference between the fit uncertainty and error compared to the base case for most windows. Some low wavelength windows continued to underestimate the SO_2 dSCDs despite the filter for the high concentration measurements, suggesting that significant stray light originated from <400 nm. A low pass filter with lower cutoff wavelength (i.e., λ_{cutoff} = 340 nm) may aid in this respect, as may the use of spectrometers with reduced stray light. SO_2 dSCDs exhibited an inverse dependence on the features in the SO_2 absorption cross-section in the base case. The dependence decreased with the use of the short-pass filter or offset function, implying that stray light contributed to the dependence. Using both the filter and offset function decreased the accuracy of the low concentration dSCDs of SO_2 for some windows with λ_{low}<307 nm and λ_{high}<320 nm compared to the base case. Increasing the λ_{high} greater than ~ 320 nm tended to decrease the fit uncertainty but not necessarily the fit error for measurements with the filter or offset function.
Note that are a number of other parameters that can be varied in the SO_2 dSCD fit that were not varied in this study. These parameters include the order of the DOAS and offset function polynomials, and the choice of the literature cross-sections for the trace gases. The experiments in this study would ideally also be repeated at different solar zenith and azimuth angles. Variation of these parameters and measurement conditions was outside the scope of this study, which focused on the fitting window wavelength range, but could be the focus of future studies.

Based on the results of this study, it is recommended that fitting windows for SO_2 have λ_{low} >307 nm to avoid the effects of stray light and low solar signal, and λ_{low} <312 nm because of weak SO_2 features. Fitting windows should have λ_{high} less than ~320 nm to avoid increased underestimation of the fit error. A fitting window should not be chosen because it has a smaller fit uncertainty since it does not guarantee a more accurate dSCD. A short-pass filter

with a cutoff close to the λ_{high} of the SO_2 fitting window improves the accuracy of MAX-DOAS SO_2 measurements. In the absence of a filter or if a filter would conflict with other species to be determined (e.g., NO_2), the offset function should be used to compensate for stray light. Even in the case that SO_2 and NO_2 are to be fit simultaneously, a filter with λ_{cutoff} = 550 nm may reduce stray light. A short-pass filter may be preferred over the offset function for reducing stray light impacts because the filter removes stray light while the offset function mathematically compensates for stray light by assuming it is proportional to the measured intensity (see Eqs. 11-12 in Appendix B). The offset function may increase fit error if this assumption is invalid or if little stray light is present. If a short-pass filter or the offset function is used, the 307.5-319 nm fitting window for SO_2 is recommended. Ultimately, the use of higher quality spectrometers with reduced stray light for MAX-DOAS measurements is desirable, but a higher expense.

3.5 Acknowledgements

This research was funded by a Discovery Grant from the Natural Science and Engineering Research Council of Canada (NSERC) and a NSERC CREATE Grant- Integrating Atmospheric Chemistry and Physics from Earth to Space (IACPES).

3.6 References

Bobrowski, N. and Platt, U.: SO2/BrO ratios studied in five volcanic plumes, J. Volcanol. Geotherm. Res., 166(3–4), 147–160, doi:10.1016/j.jvolgeores.2007.07.003, 2007.

Bogumil, K., Orphal, J., Homann, T., Voigt, S., Spietz, P., Fleischmann, O. C., Vogel, A., Hartmann, M., Kromminga, H., Bovensmann, H., Frerick, J. and Burrows, J. P.: Measurements of molecular absorption spectra with the SCIAMACHY pre-flight model: instrument characterization and reference data for atmospheric remote-sensing in the 230–2380 nm region, J. Photochem. Photobiol. Chem., 157(2–3), 167–184, doi:10.1016/S1010-6030(03)00062-5, 2003.

Choudhury, A. K. R., Prayagi, K. P., Engineering Pro - York University, Skillsoft Books - York University and Textile Institute (Manchester, England): Principles of colour appearance and measurement. Volume 2: Visual measurement of colour, colour comparison and management, Woodhead Publishing Limited in association with The Textile Institute, Sawston, Cambridge, UK : [online] Available from: http://ezproxy.library.yorku.ca/login?url=http://ezproxy.library.yorku.ca/sso/skillport?context=78779 (Accessed 20 August 2019), 2015.

ECCC: NPRI Data Search - Facility and Substance Information, [online] Available from: https://pollution-waste.canada.ca/national-release-inventory/archives/index.cfm?lang=en (Accessed 17 September 2018), 2018.

Fioletov, V. E., McLinden, C. A., Cede, A., Davies, J., Mihele, C., Netcheva, S., Li, S.-M. and O'Brien, J.: Sulfur dioxide (SO2) vertical column density measurements by Pandora spectrometer over the Canadian oil sands, Atmospheric Meas. Tech., 9(7), 2961–2976, doi:10.5194/amt-9-2961-2016, 2016.

Hermans, C., Vandaele, A. C. and Fally, S.: Fourier transform measurements of SO2 absorption cross-sections:: I. Temperature dependence in the 24000–29000cm−1 (345–420nm) region, J. Quant. Spectrosc. Radiat. Transf., 110(9–10), 756–765, doi:10.1016/j.jqsrt.2009.01.031, 2009.

Institute of Environmental Physics, Heidelberg University: DOASIS - DOAS Intelligent System - Home, DOASIS [online] Available from: https://doasis.iup.uni-heidelberg.de/bugtracker/projects/doasis/ (Accessed 13 September 2019), 2009.

Irie, H., Takashima, H., Kanaya, Y., Boersma, K. F., Gast, L., Wittrock, F., Brunner, D., Zhou, Y. and Van Roozendael, M.: Eight-component retrievals from ground-based MAX-DOAS observations, Atmospheric Meas. Tech., 4(6), 1027–1044, doi:10.5194/amt-4-1027-2011, 2011.

Jin, J., Ma, J., Lin, W., Zhao, H., Shaiganfar, R., Beirle, S. and Wagner, T.: MAX-DOAS measurements and satellite validation of tropospheric NO2 and SO2 vertical column densities at a rural site of North China, Atmos. Environ., 133, 12–25, doi:10.1016/j.atmosenv.2016.03.031, 2016.

Keller-Rudek, H., Moortgat, G. K., Sander, R. and Sörensen, R.: The MPI-Mainz UV/VIS Spectral Atlas of Gaseous Molecules of Atmospheric Interest, Earth Syst. Sci. Data, 5(2), 365–373, doi:10.5194/essd-5-365-2013, 2013.

Kraus, S. G.: DOASIS A Framework Design for DOAS, Mannheim University, Mannheim, Germany. [online] Available from: https://pdfs.semanticscholar.org/c091/cbb709447d3b5b778e7bf4aff9d6a2e25861.pdf, 2006.

Kreuter, A. and Blumthaler, M.: Stray light correction for solar measurements using array spectrometers, Rev. Sci. Instrum., 80(9), 096108, doi:10.1063/1.3233897, 2009.

Kristensson, E., Bood, J., Alden, M., Nordstrom, E., Zhu, J., Huldt, S., Bengtsson, P.-E., Nilsson, H., Berrocal, E. and Ehn, A.: Stray light suppression in spectroscopy using periodic shadowing, Opt. Express, 22(7), 7711–7721, doi:10.1364/OE.22.007711, 2014.

Lindon, J. C., Tranter, G. E. and Koppenaal, D. W.: Encyclopedia of Spectroscopy and Spectrometry, 2nd ed., Elsevier, Oxford; Sand Diego, CA., 2000.

Ontario Ministry of the Environment: Toronto North: Hourly Sulphur Dioxide Concentrations 34021, Air Qual. Ont. [online] Available from: http://www.airqualityontario.com/history/pollutant.php?stationid=34021&pol_code=9 (Accessed 13 September 2019), 2019.

Platt, U., Stutz, J., Springer E-books - York University and SpringerLink (Online service): Differential optical absorption spectroscopy: principles and applications, Springer Verlag, Berlin. [online] Available from: http://www.library.yorku.ca/eresolver/?id=1261530, 2008.

Rix, M., Valks, P., Hao, N., Loyola, D., Schlager, H., Huntrieser, H., Flemming, J., Koehler, U., Schumann, U. and Inness, A.: Volcanic SO2, BrO and plume height estimations using GOME-2 satellite measurements during the

eruption of Eyjafjallajökull in May 2010, J. Geophys. Res. Atmospheres, 117(D20), doi:10.1029/2011JD016718, 2012.

Schreier, S. F., Peters, E., Richter, A., Lampel, J., Wittrock, F. and Burrows, J. P.: Ship-based MAX-DOAS measurements of tropospheric NO2 and SO2 in the South China and Sulu Sea, Atmos. Environ., 102, 331–343, doi:10.1016/j.atmosenv.2014.12.015, 2015.

Wang, J. and Christopher, S. A.: Intercomparison between satellite-derived aerosol optical thickness and PM2.5 mass: Implications for air quality studies, Geophys. Res. Lett., 30(21), doi:10.1029/2003GL018174, 2003.

Xie, C., Hu, X., Zhou, L., Xie, D. and Guo, H.: Ab initio determination of potential energy surfaces for the first two UV absorption bands of SO2, J. Chem. Phys., 139(1), 014305, doi:10.1063/1.4811840, 2013.

Chapter 4

Enhanced NO_2 and aerosol extinction observed in the tropospheric column behind lake-breeze fronts in Toronto using MAX-DOAS.

Zoë Y. W. Davis[1], David M. L. Sills[2], and Robert McLaren[3].

[1]Department of Earth and Space Science, York University, Toronto, M3J 1P3, Canada

[2] Department of Civil and Environmental Engineering, University of Western Ontario, London, Ontario, Canada, N6A 3K7

[3]Centre for Atmospheric Chemistry, York University, Toronto, M3J 1P3, Canada

In Review: Atmospheric Environment (2019).

Author Contributions. ZYWD: MAX-DOAS study concept, design, investigation and data analysis, data visualization, and writing of manuscript and modifications of the same with contribution from all co-authors. DMLS: Mesoscale analysis and visualization of LBFs. RM: MAX-DOAS supervision.

Abstract. The lake breezes that frequently occur in Southern Ontario impact the levels of pollutants experienced by the populations in urban areas. The effects of lake breeze circulations on pollution transport and processing are not well understood. Few studies have measured the circulations' impact on pollutants both at the surface and within the tropospheric column. In this study, pollutants in the tropospheric column (NO_2 VCDs and AODs) were measured using MAX-DOAS concurrent with near-surface measurements of NO_x, O_3, and $PM_{2.5}$ on lake breeze days in Toronto in September and October. The arrival of lake-breeze fronts (LBF) was identified using co-located meteorological data. The presence of lake breezes was confirmed using mesoscale analyses of radar, satellite and a network of meteorological stations. NO_2 VCDs exhibited short-term increases 0.8-3.4×10^{16} molecules cm^{-2} above the pre-LBF levels following the arrival of a LBF. These measurements are the first confirmation of the theorized presence of enhanced total burden of pollution within the total column behind the front within a lake-breeze circulation on multiple lake-breeze days. Rapid decreases of O_3 of up to 13 ppbv at the arrival of the lake-breeze front were unexpected based on observed increases in O_3 in other studies, but can be attributed to reduced photochemical O_3 production during late summer and fall compared to mid-summer. AODs exhibited delayed enhancements compared to NO_2 VCDs, appearing to be driven by enhanced humidity following the front, in addition to enhanced particle concentration. Our measurements highlight the complex 3-D structure of lake-breeze circulations.

4.1 Introduction

The presence of oceans and large lakes have long been known to influence meteorology as well as formation and transport of pollutants in populated areas close to coastlines (Levy et al., 2008; Lyons and Cole, 1973; & others). This influence is especially true in the Great Lakes Region in Canada and USA, where numerous populated cities exist along the shorelines of the Great Lakes. This region has been the subject of many investigations of the effect of the lakes on complex meteorological phenomena (Comer and Mckendry, 1993; Estoque, 1981; Keen and Lyons, 1978; Laird et al., 2001; Lyons, 1972; Lyons and Cole, 1973, 1976; Sills et al., 2011; Sills and King, 1998), including their role in the initiation of thunderstorms and the associated development of severe weather (Alexander et al., 2018; King et al., 2003; Moroz, 1967; Sills, 1998; Sills et al., 2002), as well as their modification of air quality in southern Ontario (Brook et al., 2013; Hastie et al., 1999; Hayden et al., 2011; Lyons and Olsson, 1973; Reid et al., 1996; Sills et al., 2011; Wentworth et al., 2015). Air quality is modified by the presence of the lakes primarily via lake-breeze circulations (LBC) as well as the extended lifetime of ozone (O_3) and other pollutants over the lakes as opposed to land surface (Lyons et al., 1995; Lyons and Cole, 1973, 1976; Sillman et al., 1993; & others).

The LBCs can enhance the formation of secondary ozone (O_3) and aerosols, transport emissions of air pollutants from industrial and large urban areas (i.e., Toronto, Hamilton, Windsor, Detroit, Chicago,), and re-circulate primary and secondary pollutants (Brook et al., 2013). LBCs arise from a difference in heating between the land and lake that creates horizontal gradients in pressure at the surface and aloft. An idealized LBC under calm synoptic winds (Figure 4-1) consists of an inflow layer transporting cool lake air towards land, an updraft at the leading edge of the onshore flow at the lake-breeze front (LBF), and a return flow that subsides over the lake and results in a capping inversion (Sills et al., 2011). A lake breeze head (LBH), a raised component of the circulation approximately twice the depth of

the flow following behind, may be present above and directly behind the LBF (Simpson et al., 1977). The region of mixing within the LBC is the thermal internal boundary layer (TIBL), which is shallower than the convective boundary layer (CBL) but grows vertically with inland distance (Hayden et al., 2011). The LBC typically forms a few hours after sunrise and tends to penetrate inland throughout the day (Sills et al., 2011), but opposing synoptic flow can slow or even prevent inland movement of the LBF (Mariani et al., 2018). The synoptic flow in the lower troposphere impacts the structure, formation, and inland penetration of the LBF (Comer and Mckendry, 1993; King et al., 2003; Sills et al., 2011). Onshore synoptic flow promotes greater inland penetration of the LBF, and vice versa (Mariani et al., 2018; Sills et al., 2011). In Southern Ontario, LBFs have been observed to penetrate as far as 200 km inland (Sills et al., 2011). While lake breezes can develop in any season under favourable conditions, LBCs occur more frequently during spring and summer. Meteorological conditions associated with the formation of a LBC include clear skies and light synoptic winds. Lake breezes have been observed around Lake Michigan even in January and February but occurred with the greatest frequency during late spring and summer (Lyons, 1972). In the spring and early summer, the air temperature differential between the land and the lake is typically at its largest. During midsummer, the synoptic conditions favouring the formation of lake breezes are often present. For example, during the Border Air Quality and Meteorology Study in southern Ontario, lake breezes were observed somewhere in the domain on one of the associated lakes on 90% of the days in July-August 2007 (Sills et al., 2011). In another analysis of lake breezes impacting Toronto, it was determined lake breezes for Lake Ontario were observed on 74% of summer days in the summers of 2010-2012 (Wentworth et al., 2015). In late summer and fall and into winter, the frequency of lake breezes decreases as insolation decreases, reducing the lake-water temperature difference and other conditions conducive to lake breeze formation.

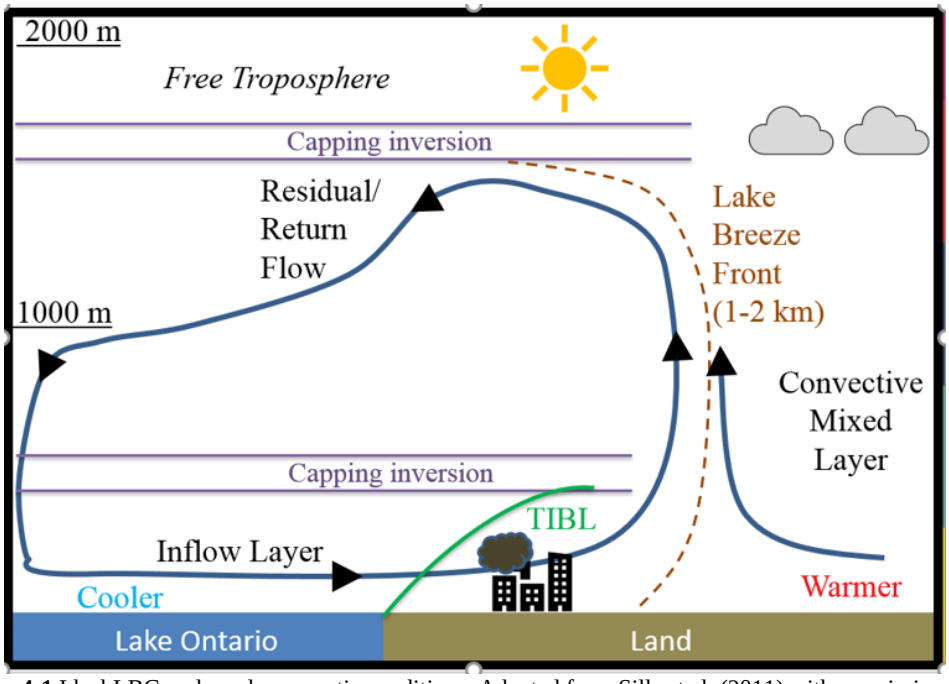

Figure 4-1 Ideal LBC under calm synoptic conditions. Adapted from Sills et al. (2011) with permission.

LBCs can influence pollution transport in three dimensions through multiple effects: fumigation of elevated pollution plumes downwind of the shoreline, trapping of pollutants within the shallow TIBL, re-circulation of pollutants, and advection inland of pollutants accumulated over the lake (Sills et al., 2011). The complex pattern of wind in 3-dimensions caused by the lakes can lead to pollutant concentrations that vary rapidly over small spatial distances (Hayden et al., 2011; Levy et al., 2008) with an enhancement of pollutant concentrations or mixing ratios in the re-circulating regions just behind the front on the lake side. The timing of both the lake breeze and pollutant release determines the fate of the pollutants (Harris and Kotamarthi, 2005). Conditions that favour lake breeze formation also tend to produce air stagnation, allowing pollutants such as NO_x to build-up and later photolyze to produce ozone (O_3) and secondary aerosols (Fosco and Schmeling, 2006). Dry deposition rates of O_3 over water surfaces are lower compared to over land (Monks et al., 2015), allowing O_3 to accumulate in the shallow boundary layer over the surface of a lake (Brook et al., 2013). In 2015, hourly O_3 in the Greater Toronto area only exceeded the Ontario Ambient Air Quality Criteria (AAQC) of 80 ppbv on days with lake breezes (Wentworth et al., 2015). Increases of up to 30 ppbv of O_3 at the arrival of LBFs have been observed in Ontario in the Greater Toronto Area (GTA) and at a rural location (Hastie et al., 1999; Sills, 1998; Wentworth et al., 2015). Short-term increases in NO_x in Ontario (Hastie et al., 1999) and Chicago (Fosco and Schmeling, 2006) have been observed concurrent with the arrival of LBFs. Motions at LBFs in the vertical and horizontal cause re-circulation of primary and secondary pollutants (Brook et al., 2013; Harris and Kotamarthi, 2005), and enhance aerosol formation rates compared to the background air (Brook et al., 2013; Hayden et al., 2011). Increased concentrations of secondary pollutants (e.g., sulphate and nitrate) have been observed post-LBF (Fosco and Schmeling, 2006).

Our current understanding of the interaction between chemical processes, transport and LBCs is limited (Hayden et al., 2011). Observing the chemical and physical structure of LBCs, and how they evolve in time would be ideal, especially their vertical extent, although limited means exist to do this. Information on the vertical extent of chemical pollution in lake and ocean breeze circulations can be obtained using balloon measurement (Bottenheim et al., 1997; Hayden et al., 1997; McKendry et al., 1998; Steyn et al., 1997) and aircraft studies (Hayden et al., 2011), the latter of which can be prohibitively expensive. One observation of the vertical extent of a suspected lake breeze enhanced pollution event was observed with vertical column densities (VCD) of NO_2 determined using ground-based Multi Axis-Differential Optical Absorption Spectroscopy (MAX-DOAS) measurements and radiative transfer modelling (Halla et al., 2011). MAX-DOAS is a remote sensing technique that measures column integrated densities of aerosol extinction and chemical pollutants (NO_2, SO_2, etc.) using ground-based measurements of sky scattered sunlight (Honninger et al., 2004; Davis et al., 2019).

In this study, the passages of lake-breeze fronts at York University were identified using typical associated meteorological signals: a sharp decrease in air temperatures, an increase in relative humidity and a shift to onshore flow (wind direction from 160-180^o) near the surface. Though temperature and humidity signals tend to weaken as lake air is modified while travelling inland, a clear wind shift is often still observed (Lyons, 1972). The existence of the lake breezes was confirmed via mesoscale meteorological analysis on most days, allowing additional contextual data to be obtained. Pollutants in the lower tropospheric column and near the surface were measured using a MAX-

DOAS instrument and in-situ instruments, respectively, on lake breeze days in Toronto during September and October 2015. Tropospheric aerosol optical depths (AODs) and vertical column densities (VCDs) of NO_2 were retrieved using optimal estimation inverse modelling from the MAX-DOAS measurements.

Our study objectives were to 1) determine the meteorological and chemical factors that drive changes in pollutants in the tropospheric column (NO_2 VCDs & AODs) and near the surface (NO-NO_2-NO_x, O_3, $PM_{2.5}$) when a LBF passes, 2) compare trends in trace-gases and aerosol levels in the tropospheric column, and 3) compare the trends in pollutants (VCD and surface) for our fall days with previous summertime measurements. The study presents the first observations of the changes to aerosol and trace-gas pollutants both near the surface and integrated within the lower tropospheric column due to LBCs on multiple days.

4.2 Experimental

4.2.1 Field Site and Instrumentation

The mini-MAX-DOAS instrument (Hoffmann Messtechnik GmbH) measured spectra of scattered sunlight during September and October 2015 at York University, Keele Campus (43.773 N, -79.506 W) (Figure 4-2). Measurements were also made in July and August, but cloud-free days were absent. A narrow band of cumulus clouds typically develops along the LBF (Hayden et al., 2011; Sills et al., 2011).

The instrument was mounted on a rooftop, ~15 m a.gl., pointing North, and located ~14 and ~17 km north of downtown Toronto and Lake Ontario, respectively. MAX-DOAS spectra were collected at a continuous sequence of viewing elevation angles above the horizon: 2°, 4°, 8°, 15°, 30° and 90° (zenith). The instrument had a field of view of ~0.6°, and incident light was focused on a cylindrical quartz lens with a focal length of 40 mm into a quartz fibre. The fibre transmitted the light into the OceanOptics USB2000 spectrograph with a Sony ILX511 linear silicon Charge-Coupled Device (CCD) detector array (2048 pixels, pixel size 14x200 microns, signal-to-noise ratio at full signal 250:1). The spectrograph had a 50 µm wide entrance slit, a spectral resolution of ~0.6 nm FWHM, and a spectral range of 290-433 nm. A Peltier stage cooled the spectrograph to maintain the selected temperature of +5 °C. A USB cable transferred spectrometer data to a laptop computer. The software package DOASIS was used to control the instrument and allowed automated measurements using JScript programs. Each recorded spectrum was an average of 1000 spectra if exposure time was greater than 110 milliseconds and 1500 averages if exposure time was less than 110 milliseconds. The exposure time depended on the ambient light levels.

Figure 4-2 Location of field site (indicated by the yellow star) and Lake Ontario.

Co-located measurements of NO_x species, O_3, and $PM_{2.5}$ were made in the Centre for Atmospheric Chemistry Air Quality Research Station at York University, Keele campus. Ozone was measured using UV absorption spectroscopy with a TECO Model 49 Ozone Analyzer, NO_x species were measured using chemical luminescence with a TECO model 42 NO_x analyzer, and $PM_{2.5}$ mass concentration was measured with nephelometry and beta attenuation using a Model 5030 SHARP instrument. All data were available at 1 min time resolution. Infrastructure containing the in-situ instruments was installed at York University by the Ontario Ministry of the Environment to conduct enhanced monitoring of the air quality during the 2015 Pan and Para-pan American Games (Joe et al., 2018; Mariani et al., 2018).

A meteorological station located at the surface level measured temperature, relative humidity (RH), short-wave radiation, and wind speed and -direction with a 5-minute time resolution (Taylor, 2015). Absolute humidity was calculated from RH and temperature using equations found in Vaisala (2013). The presence and inland progression of

the LBF was confirmed through mesoscale analyses that used data from radar, GOES-13 satellite imagery, and the network of surface meteorological stations in the Toronto area (see Joe et al. (2018)) on all days except Sept. 01 because of an absence of recorded data. The methods used for the mesoscale analysis are described in Alexander et al. (2018). The synoptic-scale flow was estimated using the MSL pressure contours depicted on the NWS Daily Weather Map valid at 12 UTC for each day. Maps of lake surface temperature from Great Lakes Surface Environmental Analysis (GLSEA) and near-surface temperatures at the site are shown in the Appendix Figures C6 and C7, respectively.

AODs at 380 nm and 340 nm were obtained from Level 2.0 AERONET data, measured by sun photometer 3.5 km East of the site (43.790 N, 79.470 W). The uncertainty in the AERONET data is estimated to be 0.01 (Sinyuk et al., 2012). The AERONET AODs at wavelength λ_1 were converted to AODs at 361 nm, the MAX-DOAS aerosol retrieval wavelength, following Eq. (1):

$$E(361nm) = E(\lambda_1) * \left(\frac{361nm}{\lambda_1}\right)^{-\propto} \quad (1)$$

Equation (1) accounts for the wavelength dependence of aerosol extinction using the Angstrom exponent, $\propto$. The AERONET 340-440nm Angstrom exponent was used to convert the two AERONET AODs, which were then averaged. AERONET AODs had a time resolution of ~3 minutes.

4.2.2 MAX-DOAS Data Analysis

DOAS Fitting

Trace gas Differential Slant Column Densities (dSCDs) were obtained using the DOAS technique (Platt and Stutz, 2008) with DOASIS software (Institute of Environmental Physics, Heidelberg, Germany). All spectra were corrected for dark current and electronic offset and wavelength calibrated using a measurement of a Hg lamp. The fitting window for NO_2 was 410-435 nm and for O_4 was 350-375 from McLaren et al. (2010) and Frieß et al. (2011), respectively. Table 4-1 lists the components included for the fitting of each gas. Absorption cross-sections were obtained from the MPI-MAINZ UV/VIS Spectral Atlas of Gaseous Molecules of Atmospheric Interest (Keller-Rudek et al., 2013). Each non-zenith measured spectrum was fit against the Fraunhofer Reference Spectrum (FRS), the closest zenith spectrum in time. The statistical error of the O_4 dSCDs was $<1.0 \times 10^{42}$ molecules cm^{-2}, and the O_4 fit error for off-axis measurements relative to the FRS was <4%. The statistical fit errors of the NO_2 dSCDs were $0.5\text{-}3.0 \times 10^{15}$ molecules cm^{-2}. The reported uncertainty in the absorption cross-section of NO_2 of approximately 3% (Bogumil et al., 2003a) results in systematic errors in the retrieved dSCDs. The absolute value of the O_4 cross-section and its dependence on temperature is uncertain. While some studies suggest a scaling factor for the O_4 cross-section because the absolute value of the cross-section may be overestimated (by up to 25%) (Clemer et al., 2010; Wagner et al., 2002, 2009), others found that the best results for measured O_4 dSCDs and aerosol extinction retrieved from them were achieved without a scaling factor (Frieß et al., 2011). In this study, a scaling factor was not used for the O_4 fitting.

Table 4-1 Information on MAX-DOAS spectral fitting.

Gas	Fitting Window	Included in the Fit
NO_2	410-435nm	FRS, Ring, Bogumil 2003 NO_2 (293K) and Bogumil 2003 (293K and 243K) O_3, 3rd order polynomial
O_4	350-375nm	FRS, Ring, Hermans 2011 O_4 Bogumil 2003 (293K) NO_2, Bogumil 2003 (293K and 223K) O_3, 3rd order polynomial

Optimal Estimation Retrievals

Tropospheric aerosol optical depths (AODs) and vertical column densities (VCDs) of NO_2 were retrieved using optimal estimation inverse modelling from the MAX-DOAS measurements of O_4 dSCDs and NO_2 dSCDs, respectively (Frieß et al., 2011, 2016, 2019). The retrievals consisted of a two-step approach: 1) vertical profiles of aerosol extinction were retrieved from MAX-DOAS O_4 dSCDs and 2) NO_2 vertical profiles were retrieved from NO_2 dSCDs using the aerosol extinction profiles as forward model parameters. A-priori state vectors that decreased exponentially with a scale height of 0.6 km and surface magnitudes of 0.1 km^{-1} and 10 ppbv were used to retrieve the aerosol extinction and NO_2 profiles, respectively. The wavelengths for the optimal estimation retrievals of O_4 and NO_2 were 360.8 and 422.5, respectively. Vertical profiles of NO_2 mixing ratio and aerosol extinction were integrated vertically to produce NO_2 VCDs and AODs, respectively. The time resolution of the VCD and AOD retrievals was 15 -20 minutes, depending on light conditions. Note that VCD and AOD data points were removed from the plots if were retrieved from a set of angles that included spectral measurements from both before and after the arrival of a LBF. The technique for retrieving NO_2 vertical profiles by optimal estimation has been described previously in Davis et al. (2019).

Only cloud-free MAX-DOAS measurements were used in the retrievals. Cloud-free periods were identified from measurements of down-welling short-wave radiation from the York University meteorological station and a pyranometer mounted on top of the MAX-DOAS. LBFs passed the site on five largely cloud-free days during the study period: Sept. 01, Sept. 15, Sept. 16, Sept. 17, and Oct. 23.

4.3 Results and Discussion

4.3.1 Trace Gases

Near the surface, the arrival of the LBF was associated with a rapid increase in mixing ratios of NO and NO_2 but a decrease in O_3 (Figure 4-3 toFigure 4-7 (b)). During the subsequent ~1-2 hours, NO_x decreased while O_3 increased, excepting Oct. 23 where O_3 remained constant (Figure 4-7 (b)). The observed short-term maxima in NO_x is consistent with previous studies of LBCs (Fosco and Schmeling, 2006; Hastie et al., 1999). However, the decrease in O_3 contrasts to prior studies in Toronto during July and August where the LBF arrival was associated with increases of up to 30

ppbv of O_3 within a few minutes (Hastie et al., 1999) and an increase in the hourly O_3 mixing ratio (Wentworth et al., 2015). In this study, a rapid increase of ~30 ppbv of O_3 was also observed at the arrival of a LBF that was identified by Mariani et al. (2018) on Jul 28 (Figure C2), but MAX-DOAS data was not available due to clouds. On the days with MAX-DOAS data, O_3 mixing ratios decreased by up to 13 ppbv upon arrival of LBF and remained lower than pre-LBF levels for 30-90 minutes (Figure 4-3 to Figure 4-6 (b)). Odd oxygen (O_3 + NO_2) tended to be conserved on most days, before and after the LBF arrival (Figure 4-3 to Figure 4-7 (c)). These trends suggest that the decrease in O_3 seen at the LBF was due to increased NO titration in the air mass on the lake side of the front. It also suggests that photochemical ozone formation was limited and that O_3 was present at regional background levels on both sides of the front at the time of LBF passage on most days, i.e. 40-50ppbv. The exceptions were Sept 01 and 16, where odd oxygen actually dropped at the LBF arrival (Figure 4-3 & Figure 4-5 (c)).

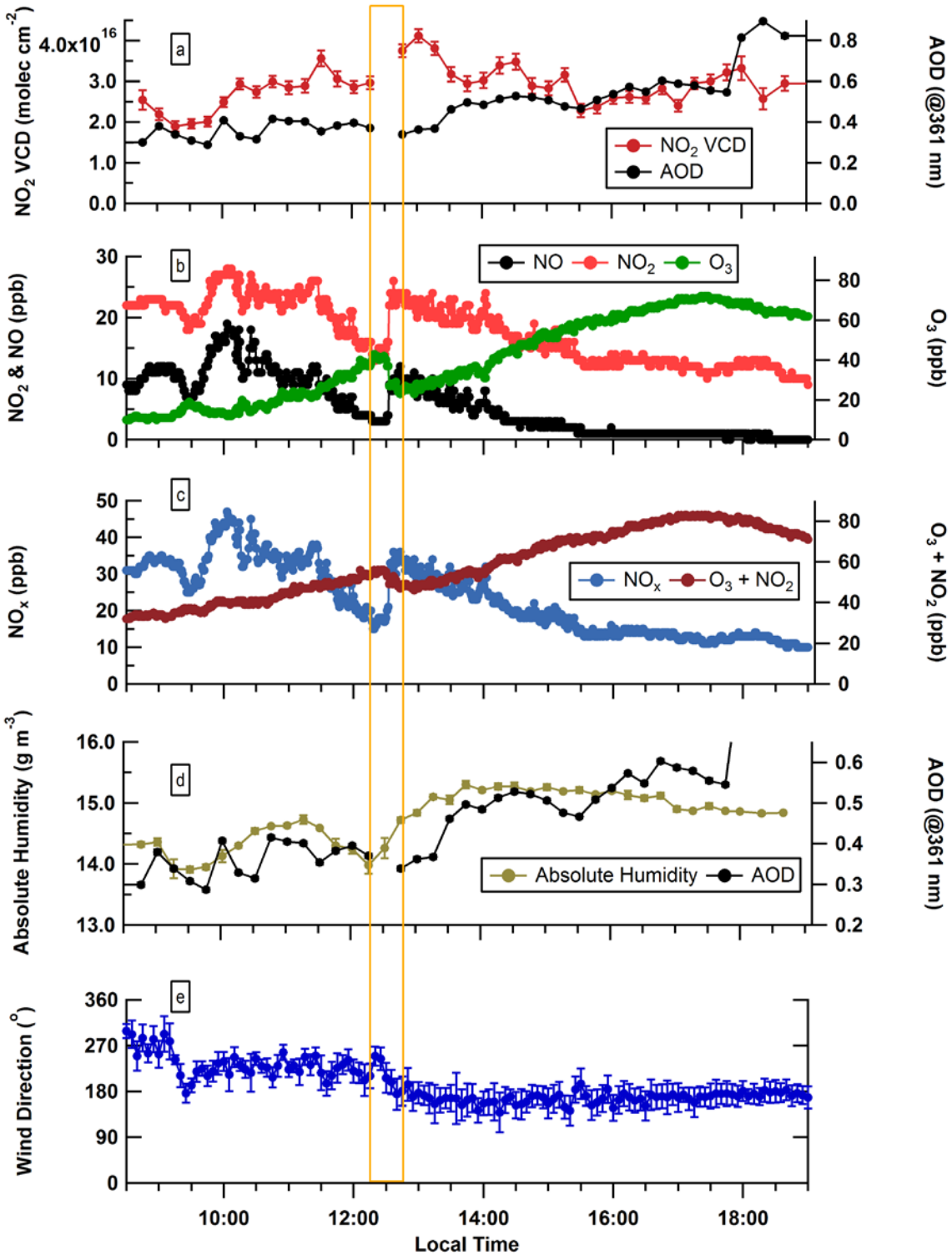

Figure 4-3 Sept. 01 NO_2 VCDs, AODs, mixing ratios of NO, NO_2, O_3, and odd oxygen, absolute humidity, and wind direction. The orange box indicates the estimated timing of the LBF arrival (± 15 mins).

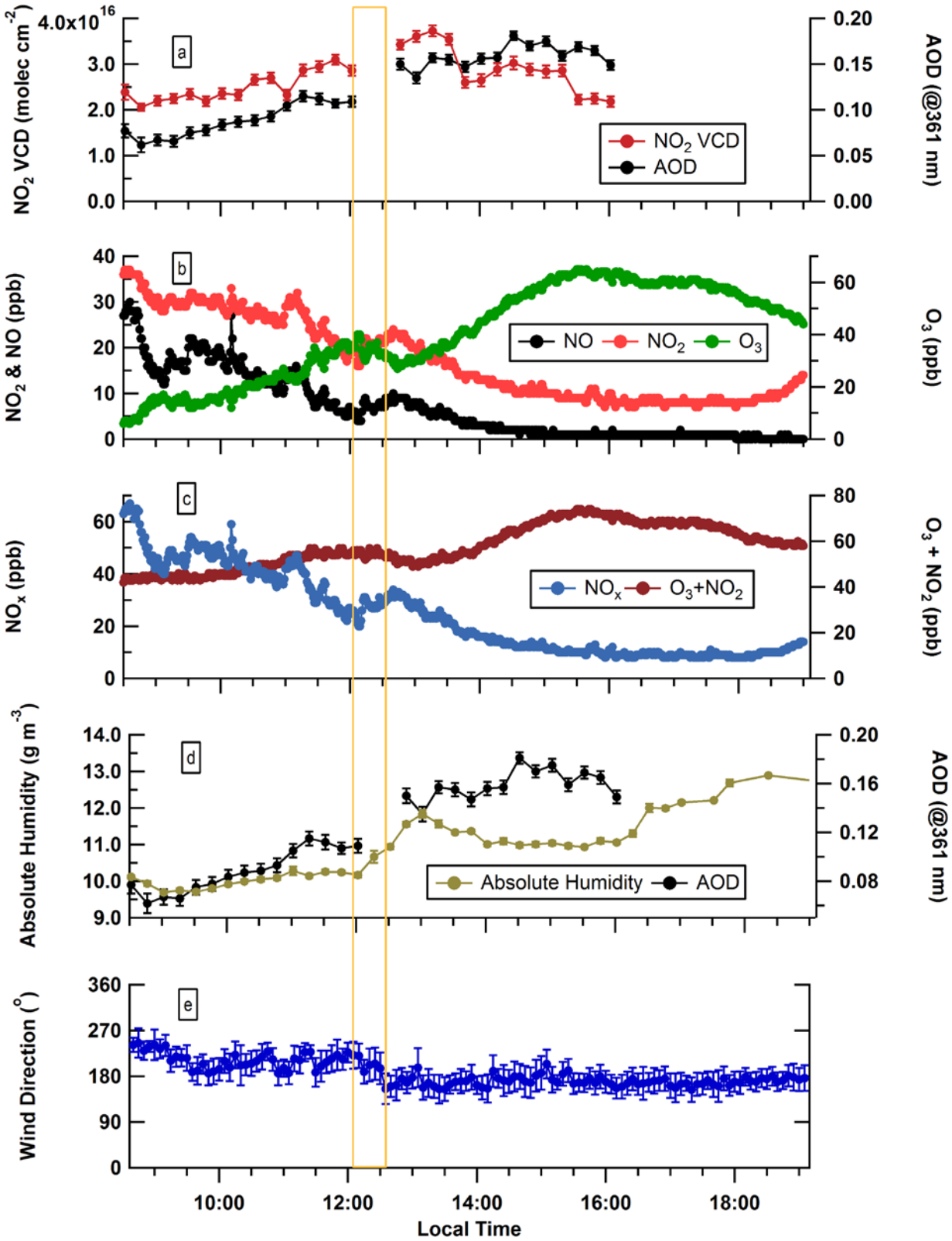

Figure 4-4 Same as Figure 3 but for Sept. 15.

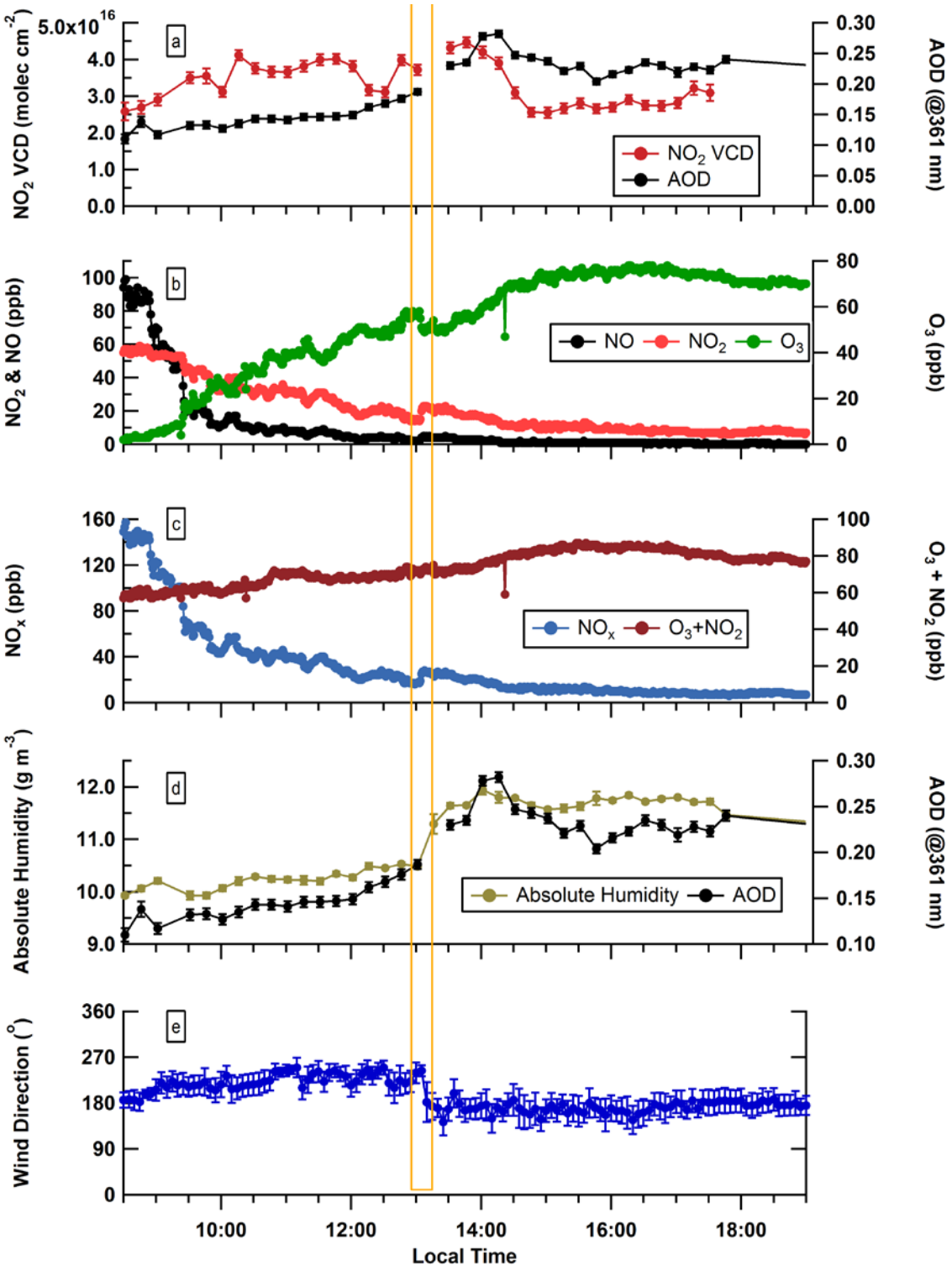

Figure 4-5 Same as Figure 3 but for Sept. 16.

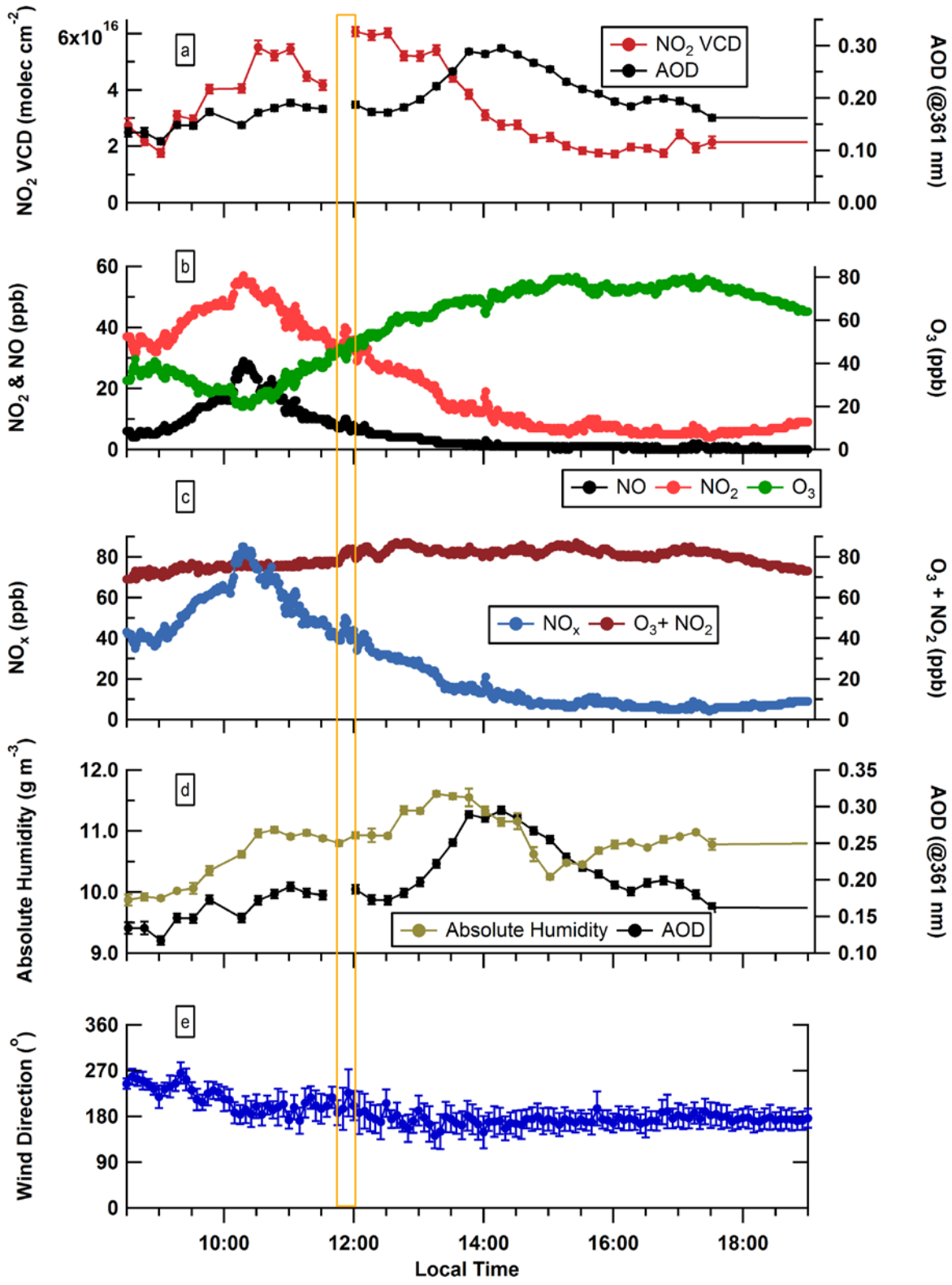

Figure 4-6 Same as Figure 3 but for Sept. 17.

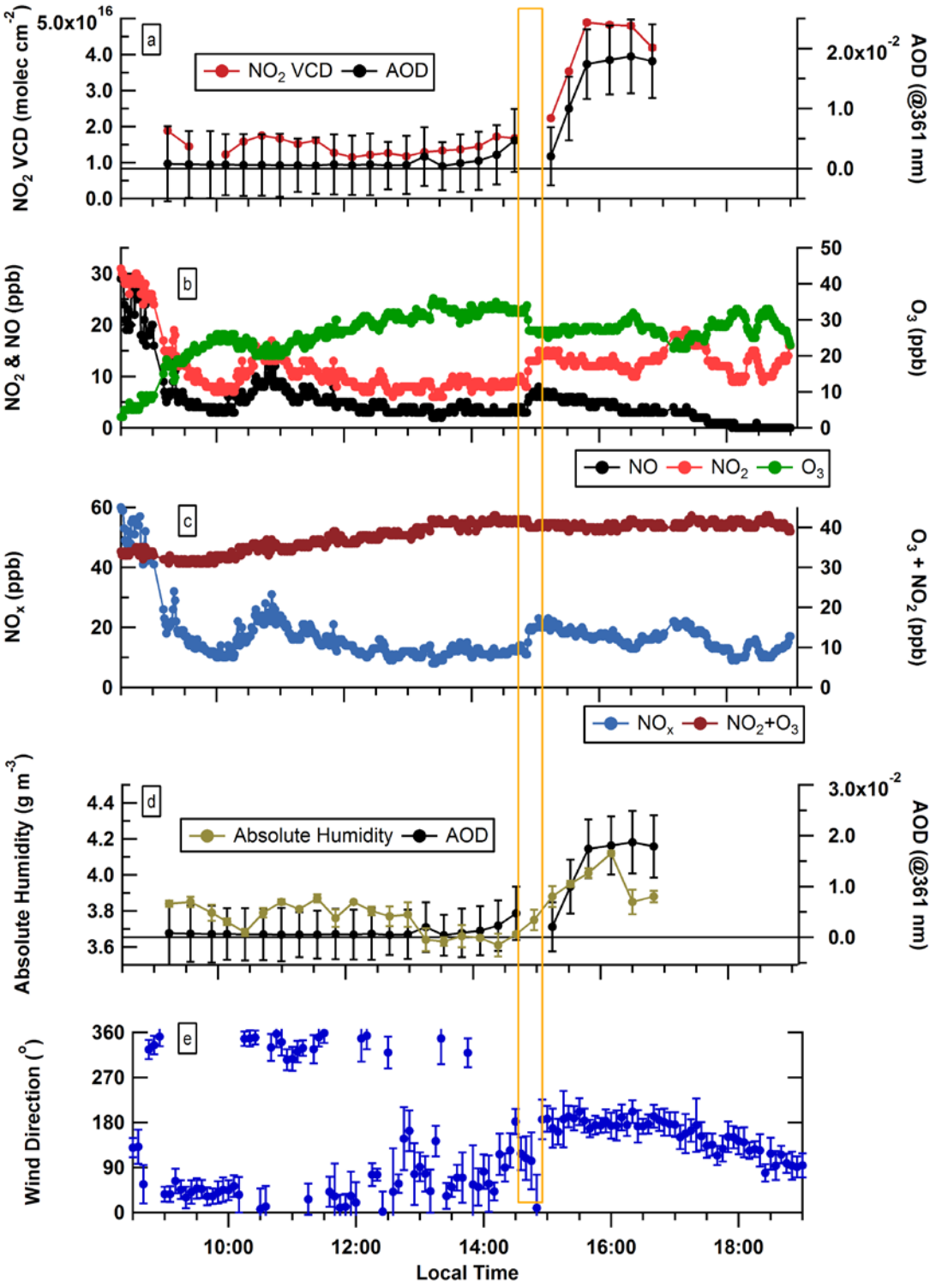

Figure 4-7 Same as Figure 3 but for Oct. 23.

This difference in O_3 trends may be seasonal since photochemical formation is much faster during the summer period compared to the fall. The tendency towards photochemical formation of tropospheric O_3 decreases from early September to late October and further into winter, primarily due to decreased photolysis rates of NO_2, lower temperatures, and decreased emission rates of biogenic VOC emissions. Under the fall conditions, the increase in NO_x at the LBF arrival probably resulted in O_3 titration. On September days, the arrival of the LBF appears to delay the increase in O_3 for ~1 hour simultaneous with NO_x being enhanced above pre-LBF levels (Figure 4-3 & Figure 4-4). On Oct. 23, O_3 remained lower than pre-LBF concentrations despite the wind-direction having shifted from cleaner to more polluted origins (Figure 4-7).

The rapid increase in NO_x mixing ratios at the LBF can be attributed to two factors: i) the LBF acts as a separation barrier of two different air masses, one lake side (that is more polluted) and one inland, that have experienced different anthropogenic emission rates over the previous several hours, and ii) the decreased mixing height due to the shallower TIBL within the lake breeze (Kitada and Kitagawa, 1990; Sills et al., 2011). The shallowest TIBL tends to occur at the leading edge of the LBF as observed by Mariani et al. (2018) in the Greater Toronto area and in sea-breezes (Simpson et al., 1977). Despite TIBL growth with inland penetration, the TIBL can remain relatively small compared to the CBL on the inland side of the LBF (Lyons and Cole, 1973). LBC flow depths of ~ 300 m have been observed even 31 km inland in the GTA (Mariani et al., 2018). Examination of the trends in NO_2 VCDs can help determine which factors enhanced NO_x mixing ratios since VCDs are independent of boundary layer height.

NO_2 VCDs experienced diurnal maximums shortly following the passage of a LBF on every day including Oct. 23 (Figure 4-3 to Figure 4-7 (a)). This trend contrasts with a typical diurnal trend on non-LBC days of the NO_2 VCDs peaking late morning and early evening, following the morning and afternoon rush-hours, respectively (Figure D3 (a)). The NO_2 VCD increased 0.75-1.9x10^{16} molecules cm^{-2} and 3.4 x10^{16} molecules cm^{-2} above the pre-LBF levels for the September and October case study days, respectively. The Oct. 23 increase was expected to be the largest, given that the air mass on the inland side of the LBF was clean (northerly synoptic winds) (Figure 4-7). The enhancements in NO_2 VCDs are expected to occur at least 15 minutes after the increase in NO_2 concentrations because of the time required for the LBF to penetrate sufficiently north for all the angles in a retrieval to observe within the LBC. The delay, therefore, depends on the speed of the inland penetration of the LBF and the pathlength of the MAX-DOAS viewing path (~1-3 km, depending on aerosol loading).

Table 4-2 Synoptic wind speed and direction, timing of and change in surface wind at LBF, and MAX-DOAS delay on lake breeze days.

Date	Synoptic Wind Direction & Speed	Change in Surface Wind Direction due to LBF (°)	LBF Timing	Max-DOAS NO_2 Delay after NO_x Peak at LBF (minutes)	Speed & Behaviour of LBF Passing Site
Sept. 01	From South-West (SW) at 5 (±2.5) m s^{-1}	55	~12:33	~15	Slow & decelerating
Sept. 15	From SW at 7.5 (±2.5) m s^{-1}	40	~12:12	30	Slow & decelerating
Sept. 16	From SW at 5 (±2.5) m s^{-1}	60	~13:07	15-30	Moderate & steady
Sept. 17	From SW at 5 (±2.5) m s^{-1}	30	~11:52	~15	Fast & Decelerating
Oct. 23	From North-East (NE) at 5 (±2.5) m s^{-1}	150	~14:54	30-50 mins	Moderate & steady

The increase in NO_2 VCDs following the LBF can be attributed to two factors: 1) the TIBL is deepest within the lake breeze head, behind the leading edge of the LBF (see Figure 4-1, Figure 10 in Mariani et al. (2018), & Figure 5 in Simpson et al. (1977)), and 2) micro-scale transport within the LBC may accumulate and confine pollutants in the lake-modified air behind the front (Hayden et al., 2011; Kitada and Kitagawa, 1990). The maxima in NO_2 VCDs following the brief enhancements in NO_x mixing ratio at the LBF suggests that the peaks in the NO_x were due to both the shallower TIBL compared to the CBL and an increased accumulation of pollutants within the vertical column behind the LBF. On the September days, the NO_2 VCD returned to approximately pre-LBF values after the short-term diurnal maximum following the LBF (Figure 4-3 to Figure 4-6 (a)). The exception was Sept. 15, where NO_2 VCDs were smaller than pre-LBF levels following the diurnal maximum (Figure 4-4(a)). The NO_2 VCD was likely comparable on both sides of the LBF (excepting the peak) because the South-West synoptic winds directions lead to transport from polluted regions (Table 4-2). Therefore, both the TIBL (lake side air) and lofted layers (inland air) can be expected to have been polluted (Figure 4-3 to Figure 4-6 (e)). If a region of increased loading of NO_2 within the vertical column behind the LBF were absent, the surface NO_x would still exhibit a rapid increase, but the NO_2 VCD would be expected to remain relatively constant following the LBF arrival. Our results are consistent with numerical simulations of sea breezes that suggested circulation behind the sea breeze front creates a high-concentration zone of pollutants that are partially trapped within the re-circulating flow (Kitada and Kitagawa, 1990). Aircraft observations also found that high concentrations of pollutants were confined close behind the LBF (Hayden et al., 2011).

On Oct. 23, the synoptic winds were off-shore (North-Easterly), opposing the passage of the LBF by ~150°, in contrast to other days (i.e., $\Delta WD = 30\text{-}60^{o}$) (Table 4-2). These conditions likely produced a wedge-shaped LBF with a steep frontal gradient (Sills et al., 2011) previously observed under opposing synoptic conditions in lake breezes in Canada (Curry et al., 2017; Mariani et al., 2018) and in sea-breeze fronts in Athens (Helmis et al., 1987). While NO_x increased

rapidly at the LBF arrival (Figure 4-7c), the increase in the NO_2 VCDs and AODs was much slower. The NO_2 VCD started increasing by 15:15, but the maximum occurred at 15:50. The delayed VCD maximum is consistent with the moderate speed of advance of the LBF (Table 4-2) and the lake breeze head being located further behind the front due to deformation likely caused by the opposing synoptic winds.

4.3.2 Aerosols

The MAX-DOAS AODs exhibited different temporal trends from the NO_2 VCDs post LBF arrival (Figure 4-3 & Figure 4-7 (a)). The AODs exhibited a small increase during the VCD peak but then further increased to maximize later than the VCDs. Increased AOD can be due to greater particle loading (Wang and Christopher, 2003), change in particle chemical composition to particles with greater aerosol extinction coefficients (Jung et al., 2016), and/or increased humidity (Altaratz et al., 2013) that causes hygroscopic growth of particles. Changes in particle loading may be indicated by the trends in $PM_{2.5}$ since it is a measurement of dry particle loading. For the September days, $PM_{2.5}$ exhibited small peaks with increases of a few μg m^{-3} concurrent with the NO_x peaks at the LBF (Figure C4). This increase was likely at least partly due to the reduced boundary layer depth, similar to the NO_x mixing ratios, and as previously observed at sea-breeze fronts (Boyouk et al., 2011). After the short-term peak, when the flow depth can be expected to have been relatively constant, the $PM_{2.5}$ tended to decrease or remain constant while the AOD increased (Figure 4-3 to Figure 4-6 (a) & C4). Therefore, particle loading seems unlikely to have been the main driver for increased AOD unless enhanced $PM_{2.5}$ was present aloft. Such elevated vertical profiles of aerosols are possible based on simulations of transport of particles by LBCs where approximately one-third of surface particles were uplifted at the LBF and transported to 300-700+ m a.g.l. (Harris and Kotamarthi, 2005). In the absence of $PM_{2.5}$ measurements aloft, it is unclear whether elevated particles contributed significantly to the AOD trends. Increased proportion of particles with greater coefficients of extinction, such as nitrate, could also have increased the AOD. Previous studies have observed post-LBF increases in nitrate (Harris and Kotamarthi, 2005) and secondary aerosols (Brook et al., 2013; Hayden et al., 2011). However, nitrate is a main component of $PM_{2.5}$ (Jung et al., 2016), which did not remain significantly enhanced post LBF.

The trends in AOD post-LBF may have been driven by increasing humidity that caused hygroscopic growth of particles (Wang and Christopher, 2003). The trends in AODs and humidity were similar: the AOD maximized shortly after the relative/absolute humidity maximized (Figure 4-3 to Figure 4-7 (d) & Figure C1). Increased extinction in accumulation mode particles from change in relative humidity measured at the surface (40-60%) (Figure C1) should have been small (Randriamiarisoa et al., 2006) but may have been significant near the top of the mixed layer where relative humidity increases to close to saturation (Dupont et al., 1994). Interpreting the impact of humidity on AOD is complicated by only having humidity measurements from near the surface since humidity likely varied with altitude. However, the similarity in temporal trends in AOD and absolute humidity may be explained based on the observations of the vertical profile of absolute humidity within sea-breezes in Figure 17 of Simpson et al. (1977) where absolute humidity at the surface maximized ~6 kilometres behind the sea-breeze front. This result is consistent with our observations of relative and absolute humidity maximizing 45-90 minutes after the LBF arrival (Figure 4-3 to Figure 4-7 & C1). Therefore, the AODs may have maximized when the MAX-DOAS observed the section of the LBC with

the maximum surface humidity because humidification within the total vertical column was also the greatest. In contrast, on Oct. 23 the probable wedge shape of the LBF and the relatively clean air lofted above the LBF circulation resulted in the AODs, NO_2 VCDs and absolute humidity maximizing around the same time with greater $PM_{2.5}$ on the lake side of the LBF (Figure 4-7(a, d) & C4). On this day, the AOD trend was likely driven by both increased humidity and particle loading.

The AERONET AODs exhibited small increases at LBF arrival (Figure 4-8 & C5). In contrast to the MAX-DOAS AODs, the AERONET AODs were not always greater post-LBF, such as on Sept. 16 (Figure 4-8 & C5). The AERONET AODs are expected to exhibit different temporal trends from the MAX-DOAS AODs because the AERONET AOD viewed the total of the tropospheric and stratospheric columns while the MAX-DOAS AODs represents ~0-2 km a.g.l. The MAX-DOAS AODs, therefore, tend to be less than the AERONET AODs except when the contribution of the aerosol extinction in the lower troposphere dominated the total column AOD. AERONET AODs are expected to change significantly due to LBCs only when the atmospheric column was relatively clean because flow depths of LBCs in the GTA have been observed to be shallow, 120-900 m (Mariani et al., 2018). Consequently, the most noticeable difference in the AERONET AODs following the LBF arrival was on Oct. 23 because of the relatively clean conditions before the LBF (Figure 4-7, Figure 4-8, & C5). The MAX-DOAS instrument is better suited to observing changes in LBCs in the troposphere compared to satellite and sun photometer because the MAX-DOAS is most sensitive closest to the surface and represents the lower troposphere where the circulations have the most impact.

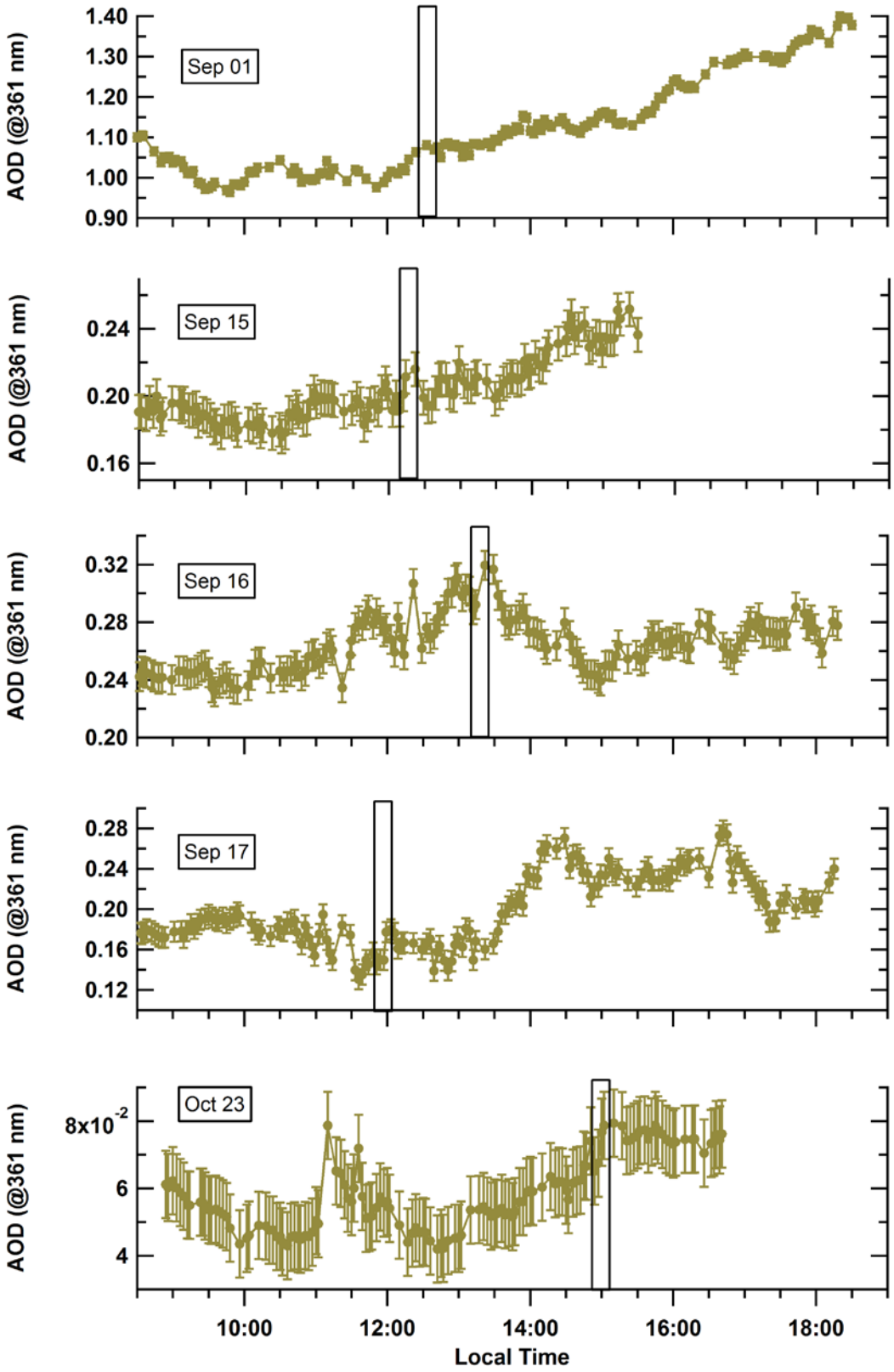

Figure 4-8 Diurnal trends in AERONET AOD (non-averaged) on lake breeze days. The black rectangle indicates the arrival of the LBF.

4.4 Summary

In this study, we report on, for the first time, the changes in pollutants in the lower tropospheric column (AODs and NO_2 VCDs) and near the surface (NO-NO_2-NO_x, O_3, $PM_{2.5}$) following the arrival of LBFs. Short-term enhancements in NO_x mixing ratios following the LBF arrival were consistent with previous studies. Observed decreases in O_3 mixing ratios of up to 12 ppbv post-LBF contrast with previous summertime studies but were attributed to decreased photochemical activity and more O_3 titration by NO in our late summer to fall study period. NO_2 VCDs exhibited diurnal maximums following the LBF arrival with short-term increases above pre-LBF levels of 0.8-3.4×10^{16} molecules cm^{-2}. Short-term increases in both mixing ratios and VCDs of NO_2 indicate that the increased pollution at the LBFs is due to not only a shallower boundary layer but also a region of enhanced NO_2 loading behind the LBF. The increase in NO_2 VCD was slower under opposing wind conditions, likely due to deformation of the front (steep frontal gradient). AODs exhibited a small increase concurrent with the NO_2 VCD but continued to increase to maximums that peaked later. The delayed maxima in AOD appeared to be driven by humidification within the vertical profile of the LBC rather than only increased particle loading based on the $PM_{2.5}$ trends. AERONET AODs exhibited small increases at the LBF arrival but were sometimes smaller post-LBF because the AERONET AOD represents the total atmospheric column. The MAX-DOAS instrument is well suited to observing the impacts of LBCs on pollutants in the lower troposphere compared to satellite or sun photometer because the MAX-DOAS sensitivity increases towards the surface and the retrievals represent the lower troposphere. MAX-DOAS compliments in-situ measurements in a way that improves our understanding of the transport of pollutants within LBCs.

4.5 Acknowledgements

This research was funded by a Discovery Grant from the Natural Science and Engineering Research Council of Canada and a NSERC CREATE Grant- Integrating Atmospheric Chemistry and Physics from Earth to Space. We thank the Ontario Ministry of the Environment for the in-situ measurements of pollutants at York University and Dr. Peter Taylor for meteorological measurements available from the York University Weather Station (https://www.yorku.ca/pat/weatherStation/index.php).

4.6 References

Alexander, L. S., Sills, D. M. L. and Taylor, P. A.: Initiation of Convective Storms at Low-Level Mesoscale Boundaries in Southwestern Ontario, Weather Forecast., 33(2), 583–598, doi:10.1175/WAF-D-17-0086.1, 2018.

Altaratz, O., Bar-Or, R. Z., Wollner, U. and Koren, I.: Relative humidity and its effect on aerosol optical depth in the vicinity of convective clouds, Environ. Res. Lett., 8(3), 034025, doi:10.1088/1748-9326/8/3/034025, 2013.

Bogumil, K., Orphal, J., Homann, T., Voigt, S., Spietz, P., Fleischmann, O. C., Vogel, A., Hartmann, M., Kromminga, H., Bovensmann, H., Frerick, J. and Burrows, J. P.: Measurements of molecular absorption spectra with the SCIAMACHY pre-flight model: instrument characterization and reference data for atmospheric remote-sensing in the 230–2380 nm region, J. Photochem. Photobiol. Chem., 157(2–3), 167–184, doi:10.1016/S1010-6030(03)00062-5, 2003.

Bottenheim, J. W., Brickell, P. C., Dann, T. F., Wang, D. K., Hopper, F., Gallant, A. J., Anlauf, K. G. and Wiebe, H. A.: Non-methane hydrocarbons and CO during Pacific '93, Atmos. Environ., 31(14), 2079–2087, doi:10.1016/S1352-2310(96)00303-2, 1997.

Boyouk, N., Leon, J.-F., Delbarre, H., Augustin, P. and Fourmentin, M.: Impact of sea breeze on vertical structure of aerosol optical properties in Dunkerque, France, Atmospheric Res., 101(4), 902–910, doi:10.1016/j.atmosres.2011.05.016, 2011.

Brook, J. R., Makar, P. A., Sills, D. M. L., Hayden, K. L. and McLaren, R.: Exploring the nature of air quality over southwestern Ontario: main findings from the Border Air Quality and Meteorology Study, Atmospheric Chem. Phys., 13(20), 10461–10482, doi:10.5194/acp-13-10461-2013, 2013.

Clemer, K., Van Roozendael, M., Fayt, C., Hendrick, F., Hermans, C., Pinardi, G., Spurr, R., Wang, P. and De Maziere, M.: Multiple wavelength retrieval of tropospheric aerosol optical properties from MAXDOAS measurements in Beijing, Atmospheric Meas. Tech., 3(4), 863–878, doi:10.5194/amt-3-863-2010, 2010.

Comer, N. and Mckendry, I.: Observations and Numerical Modeling of Lake-Ontario Breezes, Atmosphere-Ocean, 31(4), 481–499, doi:10.1080/07055900.1993.9649482, 1993.

Curry, M., Hanesiak, J., Kehler, S., Sills, D. M. L. and Taylor, N. M.: Ground-Based Observations of the Thermodynamic and Kinematic Properties of Lake-Breeze Fronts in Southern Manitoba, Canada, Bound.-Layer Meteorol., 163(1), 143–159, doi:10.1007/s10546-016-0214-1, 2017.

Dupont, E., Pelon, J. and Flamant, C.: Study of the moist Convective Boundary Layer structure by backscattering lidar, Bound.-Layer Meteorol., 69(1), 1–25, doi:10.1007/BF00713292, 1994.

Estoque, M. A.: Further Studies of a Lake Breeze Part I: Observational Study, Mon. Weather Rev., 109(3), 611–618, doi:10.1175/1520-0493(1981)109<0611:FSOALB>2.0.CO;2, 1981.

Fosco, T. and Schmeling, M.: Aerosol ion concentration dependence on atmospheric conditions in Chicago, Atmos. Environ., 40(34), 6638–6649, doi:10.1016/j.atmosenv.2006.05.061, 2006.

Frieß, U., Sihler, H., Sander, R., Poehler, D., Yilmaz, S. and Platt, U.: The vertical distribution of BrO and aerosols in the Arctic: Measurements by active and passive differential optical absorption spectroscopy, J. Geophys. Res.-Atmospheres, 116, D00R04, doi:10.1029/2011JD015938, 2011.

Frieß, U., Klein Baltink, H., Beirle, S., Clémer, K., Hendrick, F., Henzing, B., Irie, H., Leeuw, G. de, Li, A., Moerman, M. M., Roozendael, M. van, Shaiganfar, R., Wagner, T., Wang, Y., Xie, P., Yilmaz, S. and Zieger, P.: Intercomparison of aerosol extinction profiles retrieved from MAX-DOAS measurements, Atmospheric Meas. Tech., 9(7), 3205–3222, doi:https://doi.org/10.5194/amt-9-3205-2016, 2016.

Frieß, U., Beirle, S., Alvarado Bonilla, L., Bösch, T., Friedrich, M. M., Hendrick, F., Piters, A., Richter, A., Roozendael, M. van, Rozanov, V. V., Spinei, E., Tirpitz, J.-L., Vlemmix, T., Wagner, T. and Wang, Y.: Intercomparison of MAX-DOAS vertical profile retrieval algorithms: studies using synthetic data, Atmospheric Meas. Tech., 12(4), 2155–2181, doi:https://doi.org/10.5194/amt-12-2155-2019, 2019.

Halla, J. D., Wagner, T., Beirle, S., Brook, J. R., Hayden, K. L., O'Brien, J. M., Ng, A., Majonis, D., Wenig, M. O. and McLaren, R.: Determination of tropospheric vertical columns of NO2 and aerosol optical properties in a rural setting using MAX-DOAS, ATMOSPHERIC Chem. Phys., 11(23), 12475–12498, doi:10.5194/acp-11-12475-2011, 2011.

Harris, L. and Kotamarthi, V. R.: The characteristics of the Chicago Lake breeze and its effects on trace particle transport: Results from an episodic event simulation, J. Appl. Meteorol., 44(11), 1637–1654, doi:10.1175/JAM2301.1, 2005.

Hastie, D. R., Narayan, J., Schiller, C., Niki, H., Shepson, P. B., Sills, D. M. L., Taylor, P. A., Moroz, W. J., Drummond, J. W., Reid, N., Taylor, R., Roussel, P. B. and Melo, O. T.: Observational evidence for the impact of the lake breeze circulation on ozone concentrations in Southern Ontario, Atmos. Environ., 33(2), 323–335, doi:10.1016/S1352-2310(98)00199-X, 1999.

Hayden, K. L., Anlauf, K. G., Hoff, R. M., Strapp, J. W., Bottenheim, J. W., Wiebe, H. A., Froude, F. A., Martin, J. B., Steyn, D. G. and McKendry, I. G.: The vertical chemical and meteorological structure of the boundary layer in the Lower Fraser Valley during Pacific '93, Atmos. Environ., 31(14), 2089–2105, doi:10.1016/S1352-2310(96)00300-7, 1997.

Hayden, K. L., Sills, D. M. L., Brook, J. R., Li, S.-M., Makar, P. A., Markovic, M. Z., Liu, P., Anlauf, K. G., O'Brien, J. M., Li, Q. and McLaren, R.: Aircraft study of the impact of lake-breeze circulations on trace gases and particles during BAQS-Met 2007, Atmospheric Chem. Phys., 11(19), 10173–10192, doi:10.5194/acp-11-10173-2011, 2011.

Helmis, C., Asimakopoulos, D., Deligiorgi, D. and Lalas, D.: Observations of Sea-Breeze Fronts Near the Shoreline, Bound.-Layer Meteorol., 38(4), 395–410, doi:10.1007/BF00120854, 1987.

Honninger, G., von Friedeburg, C. and Platt, U.: Multi axis differential optical absorption spectroscopy (MAX-DOAS), Atmospheric Chem. Phys., 4, 231–254, 2004.

Joe, P., Belair, S., Bernier, N. B., Bouchet, V., Brook, J. R., Brunet, D., Burrowsws, W., Charlandnd, J.-P., Dehghan, A., Driedger, N., Duhaime, C., Evansns, G., Filion, A.-B., Frenette, R., de Grandpndpndpre, J., Gultepe, I., Hendnderson, D., Herdt, A., Hilker, N., Huang, L., Hung, E., Isaac, G., Jeong, C.-H., Johnsnston, D., Klaassssen, J., Leroyer, S., Lin, H., MacDonald, M., MacPhee, J., Mariani, Z., Munoz, T., Reid, J., Robichaud, A., Rochon, Y., Shairsingh, K., Sills, D., Spacek, L., Stroud, C., Su, Y., Taylor, N., Vanos, J., Voogt, J., Wang, J. M., Wiechers, T.,

Wren, S., Yang, H. and Yip, T.: The Environment Canada Pan and Parapan American Science Showcase Project, Bull. Am. Meteorol. Soc., 99(5), 921–953, doi:10.1175/BAMS-D-16-0162.1, 2018.

Jung, C. H., Shin, H. J., Lee, J. Y. and Kim, Y. P.: Sensitivity and Contribution of Organic Aerosols to Aerosol Optical Properties Based on Their Refractive Index and Hygroscopicity, Atmosphere, 7(5), 65, doi:10.3390/atmos7050065, 2016.

Keen, C. S. and Lyons, W. A.: Lake/Land Breeze Circulations on the Western Shore of Lake Michigan, J. Appl. Meteorol., 17(12), 1843–1855, doi:10.1175/1520-0450(1978)017<1843:LBCOTW>2.0.CO;2, 1978.

Keller-Rudek, H., Moortgat, G. K., Sander, R. and Sörensen, R.: The MPI-Mainz UV/VIS Spectral Atlas of Gaseous Molecules of Atmospheric Interest, Earth Syst. Sci. Data, 5(2), 365–373, doi:10.5194/essd-5-365-2013, 2013.

King, P. W. S., Leduc, M. J., Sills, D. M. L., Donaldson, N. R., Hudak, D. R., Joe, P. and Murphy, B. P.: Lake Breezes in Southern Ontario and Their Relation to Tornado Climatology, Weather Forecast., 18(5), 795–807, doi:10.1175/1520-0434(2003)018<0795:LBISOA>2.0.CO;2, 2003.

Kitada, T. and Kitagawa, E.: Numerical-Analysis of the Role of Sea Breeze Fronts on Air-Quality in Coastal and Inland Polluted Areas, Atmospheric Environ. Part -Gen. Top., 24(6), 1545–1559, doi:10.1016/0960-1686(90)90063-S, 1990.

Laird, N. F., Kristovich, D. A. R., Liang, X.-Z., Arritt, R. W. and Labas, K.: Lake Michigan Lake Breezes: Climatology, Local Forcing, and Synoptic Environment, J. Appl. Meteorol., 40(3), 409–424, doi:10.1175/1520-0450(2001)040<0409:LMLBCL>2.0.CO;2, 2001.

Levy, I., Dayan, U. and Mahrer, Y.: A five-year study of coastal recirculation and its effect on air pollutants over the East Mediterranean region, J. Geophys. Res.-Atmospheres, 113(D16), D16121, doi:10.1029/2007JD009529, 2008.

Lyons, W., Pielke, R., Tremback, C., Walko, R., Moon, D. and Keen, C.: Modeling Impacts of Mesoscale Vertical Motions Upon Coastal Zone Air-Pollution Dispersion, Atmos. Environ., 29(2), 283–301, doi:10.1016/1352-2310(94)00217-9, 1995.

Lyons, W. A.: The Climatology and Prediction of the Chicago Lake Breeze, J. Appl. Meteorol., 11(8), 1259–1270, doi:10.1175/1520-0450(1972)011<1259:TCAPOT>2.0.CO;2, 1972.

Lyons, W. A. and Cole, H. S.: Fumigation and Plume Trapping on the Shores of Lake Michigan During Stable Onshore Flow, J. Appl. Meteorol., 12(3), 494–510, doi:10.1175/1520-0450(1973)012<0494:FAPTOT>2.0.CO;2, 1973.

Lyons, W. A. and Cole, H. S.: Photochemical Oxidant Transport: Mesoscale Lake Breeze and Synoptic-Scale Aspects, J. Appl. Meteorol., 15(7), 733–743, doi:10.1175/1520-0450(1976)015<0733:POTMLB>2.0.CO;2, 1976.

Lyons, W. A. and Olsson, L. E.: Detailed Mesometeorological Studies of Air Pollution Dispersion in the Chicago Lake Breeze, Mon. Weather Rev., 101(5), 387–403, doi:10.1175/1520-0493(1973)101<0387:DMSOAP>2.3.CO;2, 1973.

Mariani, Z., Dehghan, A., Joe, P. and Sills, D.: Observations of Lake-Breeze Events During the Toronto 2015 Pan-American Games, Bound.-Layer Meteorol., 166(1), 113–135, doi:10.1007/s10546-017-0289-3, 2018.

McKendry, I. G., Steyn, D. G., Banta, R. M., Strapp, W., Anlauf, K. and Pottier, J.: Daytime photochemical pollutant transport over a tributary valley lake in southwestern British Columbia, J. Appl. Meteorol., 37(4), 393–404, doi:10.1175/1520-0450(1998)037<0393:DPPTOA>2.0.CO;2, 1998.

McLaren, R., Wojtal, P., Majonis, D., McCourt, J., Halla, J. D. and Brook, J.: NO3 radical measurements in a polluted marine environment: links to ozone formation, Atmospheric Chem. Phys., 10(9), 4187–4206, doi:10.5194/acp-10-4187-2010, 2010.

Monks, P. S., Archibald, A. T., Colette, A., Cooper, O., Coyle, M., Derwent, R., Fowler, D., Granier, C., Law, K. S., Mills, G. E., Stevenson, D. S., Tarasova, O., Thouret, V., von Schneidemesser, E., Sommariva, R., Wild, O. and Williams, M. L.: Tropospheric ozone and its precursors from the urban to the global scale from air quality to short-lived climate forcer, Atmospheric Chem. Phys., 15(15), 8889–8973, doi:10.5194/acp-15-8889-2015, 2015.

Moroz, W. J.: A Lake Breeze on the Eastern Shore of Lake Michigan: Observations and Model, J. Atmospheric Sci., 24(4), 337–355, doi:10.1175/1520-0469(1967)024<0337:ALBOTE>2.0.CO;2, 1967.

Platt, U., Stutz, J., Springer E-books - York University and SpringerLink (Online service): Differential optical absorption spectroscopy: principles and applications, Springer Verlag, Berlin. [online] Available from: http://www.library.yorku.ca/eresolver/?id=1261530, 2008.

Randriamiarisoa, H., Chazette, P., Couvert, P., Sanak, J. and Megie, G.: Relative humidity impact on aerosol parameters in a Paris suburban area, Atmospheric Chem. Phys., 6, 1389–1407, doi:10.5194/acp-6-1389-2006, 2006.

Reid, N. W., Niki, H., Hastie, D., Shepson, P., Roussel, P., Meld, O., Mackay, G., Drummond, J., Schiff, H., Poissant, L. and MOROZ, W.: The Southern Ontario Oxidant Study (SONTOS): Overview and case studies for 1992, Atmos. Environ., 30, 2125–2132, doi:10.1016/1352-2310(95)00121-2, 1996.

Sillman, S., Samson, P. J. and Masters, J. M.: Ozone production in urban plumes transported over water: Photochemical model and case studies in the northeastern and midwestern United States, J. Geophys. Res. Atmospheres, 98(D7), 12687–12699, doi:10.1029/93JD00159, 1993.

Sills, D. M.: Lake and land breezes in southwestern Ontario: Observations, analyses and numerical modelling, PhD, York University, CRESS, Toronto, Ontario, Canada., 1998.

Sills, D. M. L. and King, P.: The 1997 ELBOW Project: an experiment to study the Effects of Lake Breezes On Weather in southern Ontario., vol. Preprints, pp. 317–320, Amer. Meteorol. Soc., Minneapolis, MN., 1998.

Sills, D. M. L., Taylor, P. A., King, P., Hocking, W. and Nichols, I.: ELBOW 2001 – studying the relationship between lake breezes and severe weather: project overview and preliminary results., vol. Preprints, pp. 611–614, Amer. Meteorol. Soc., San Antonio, TX., 2002.

Sills, D. M. L., Brook, J. R., Levy, I., Makar, P. A., Zhang, J. and Taylor, P. A.: Lake breezes in the southern Great Lakes region and their influence during BAQS-Met 2007, Atmospheric Chem. Phys., 11(15), 7955–7973, doi:10.5194/acp-11-7955-2011, 2011.

Simpson, J., Mansfield, D. and Milford, J.: Inland Penetration of Sea-Breeze Fronts, Q. J. R. Meteorol. Soc., 103(435), 47–76, doi:10.1256/smsqj.43503, 1977.

Sinyuk, A., Holben, B. N., Smirnov, A., Eck, T. F., Slutsker, I., Schafer, J. S., Giles, D. M. and Sorokin, M.: Assessment of error in aerosol optical depth measured by AERONET due to aerosol forward scattering, Geophys. Res. Lett., 39(23), doi:10.1029/2012GL053894, 2012.

Steyn, D. G., Bottenheim, J. W. and Thomson, R. B.: Overview of tropospheric ozone in the Lower Fraser Valley, and the Pacific ’93 field study, Atmos. Environ., 31(14), 2025–2035, doi:10.1016/S1352-2310(97)00018-6, 1997.

Taylor, P. A.: EMOS, ESSE Meteorol. Obs. Stn. [online] Available from: https://www.yorku.ca/pat/weatherStation/index.php (Accessed 15 August 2019), 2015.

Vaisala, O.: HUMIDITY CONVERSION FORMULAS Calculation formulas for humidity, [online] Available from: https://www.vaisala.com/sites/default/files/documents/Humidity_Conversion_Formulas_B210973EN-F.pdf, 2013.

Wagner, T., von Friedeburg, C., Wenig, M. O., Otten, C. and Platt, U.: UV-visible observations of atmospheric O-4 absorptions using direct moonlight and zenith-scattered sunlight for clear-sky and cloudy sky conditions., J. Geophys. Res.-ATMOSPHERES, 107(D20), doi:10.1029/2001JD001026, 2002.

Wagner, T., Deutschmann, T. and Platt, U.: Determination of aerosol properties from MAX-DOAS observations of the Ring effect, Atmos Meas Tech, 18, 2009.

Wang, J. and Christopher, S. A.: Intercomparison between satellite-derived aerosol optical thickness and PM2.5 mass: Implications for air quality studies, Geophys. Res. Lett., 30(21), doi:10.1029/2003GL018174, 2003.

Wentworth, G. R., Murphy, J. G. and Sills, D. M. L.: Impact of lake breezes on ozone and nitrogen oxides in the Greater Toronto Area, Atmos. Environ., 109, 52–60, doi:10.1016/j.atmosenv.2015.03.002, 2015.

Chapter 5

Estimation of NO_x and SO_2 Emissions from Sarnia, Ontario using Mobile-MAX-DOAS and a NO_x-Analyzer.

Zoë Y. W. Davis[1], Sabour Baray[2], Chris A. McLinden[3], Aida Khanbabakhani[2], William Fujs[2], Csilla Csukat[2], Jerzy Debosz[4], and Robert McLaren[2].

[1]Department of Earth and Space Science, York University, Toronto, M3J 1P3, Canada
[2]Centre for Atmospheric Chemistry, York University, Toronto, M3J 1P3, Canada
[3]Environnment and Climate Change Canada, Toronto, M3H 5T4, Canada
[4]Air Quality Monitoring and Assessment Unit, Ontario Ministry of the Environment, Conservation and Parks, Etobicoke, M9P 3V6, Canada

Journal of Atmospheric Chemistry and Physics (2019), https://doi.org/10.5194/acp-19-13871-2019

Author Contributions. ZYWD conceived of and organized the field campaign with aid from RM. ZYWD, SB, AK, WF, CC, and RM carried out the experiments in Sarnia. CM modelled conditions for the satellite retrievals of NO_2 in the region of Sarnia, and provided useful advice. ZYWD and RM prepared the manuscript, with contributions from all co-authors.

Abstract. Sarnia, ON experiences pollutant emissions disproportionate to its relatively small size. The small size of the city limits traditional top-down emission estimate techniques (e.g., satellite) but a low-cost solution for emission monitoring is Mobile-MAX-DOAS. Measurements were made using this technique from 21/03/2017 to 23/03/2017 along various driving routes to retrieve vertical column densities (VCDs) of NO_2 and SO_2 and to estimate emissions of NO_x and SO_2 from the Sarnia region. A novel aspect of the current study was the installation of a NO_x analyzer in the vehicle to allow real time measurement and characterization of near-surface NO_x/NO_2 ratios across the urban plumes, allowing improved accuracy of NO_x emission estimates. Confidence in the use of near-surface measured NO_x/NO_2 ratios for estimation of NO_x emissions was increased by relatively well-mixed boundary layer conditions. These conditions were indicated by similar temporal trends in NO_2 VCDs and mixing ratios when measurements were sufficiently distant from the sources. Leighton ratios within transported plumes indicated peroxy radicals were likely disturbing the $NO\text{-}NO_2\text{-}O_3$ photostationary state through VOC oxidation. The average lower limit emission estimate of NO_x from Sarnia was 1.60 ± 0.34 tonnes hr^{-1} using local 10 m elevation wind-speed measurements. Our estimates were larger than the downscaled annual 2017 NPRI reported industrial emissions of 0.9 tonnes NO_x hr^{-1}. Our lower limit estimate of SO_2 emissions from Sarnia was 1.81 ± 0.83 tonnes SO_2 hr^{-1}, equal within uncertainty to the 2017 NPRI downscaled value of 1.85 tonnes SO_2 hr^{-1}. Satellite-derived NO_2 VCDs over Sarnia from the Ozone Monitoring Instrument (OMI) were lower than Mobile-MAX-DOAS VCDs, likely due to the large pixel size relative to the city's size. The results of this study support the utility of the Mobile-MAX-DOAS method for estimating NO_x and SO_2 emissions in relatively small, highly industrialized regions especially when supplemented with mobile NO_x measurements.

5.1 Introduction

Differential Optical Absorption Spectroscopy (DOAS) is a remote sensing technique that quantifies tropospheric trace-gases using light spectra and the unique spectral absorption cross-sections of trace-gases. DOAS has been used since its introduction by (Platt et al., 1979) to measure small molecular species including NO_2, SO_2, OH, BrO, NO_3, NH_3, ClO and others. One advantage of the technique is the potential for simultaneous quantification of multiple trace-gases (e.g., SO_2 and NO_2) (Platt and Stutz, 2008). The Multi-Axis DOAS (MAX-DOAS) method allows sensitive quantification of tropospheric pollutants by measuring scattered sunlight spectra at multiple viewing directions and/or elevation angles. Spectra measured at elevation angles close to horizon-pointing have high sensitivity to ground-level

gases since the light paths are longer near the surface (Honninger et al., 2004b). Ground-based MAX-DOAS measurements quantify total boundary layer pollution loading by determining tropospheric vertical column densities (VCDs) of trace-gases. These measurements are, therefore, well suited to measuring total emissions into an air mass. VCDs are independent of boundary layer height, unlike mixing ratios, and are spatially averaged (horizontally and vertically) on the order of a few kilometres along the light path. Ground-based MAX-DOAS can also retrieve vertical profiles of aerosol extinction and trace-gases by combining MAX-DOAS data with radiative transfer modelling (Frieß et al., 2006; Heckel et al., 2005; Honninger et al., 2004; Honninger and Platt, 2002; Irie et al., 2008; Wagner et al., 2004, 2011).

The recently developed Mobile-MAX-DOAS technique allows measurement of trace-gas emissions from a region of interest by driving the instrument around the region. The method can estimate emissions on a nearly hourly basis in a region with a spatial resolution of ~1 km. Mobile MAX-DOAS has been used to estimate NO_x emissions from a shipping and industrial areas (Rivera et al., 2010), power-plants (Wu et al., 2017a) and cities (Ibrahim et al., 2010; Shaiganfar et al., 2011, 2017), validate satellite and air quality modelled VCDs (Dragomir et al., 2015; Shaiganfar et al., 2015), estimate surface NO_2 mixing ratios from NO_2 VCDs (Shaiganfar et al., 2011), and determine the horizontal variability of trace-gas VCDs within satellite pixels (Wagner et al., 2010). Mobile-MAX-DOAS is a "top-down" approach for quantifying real-world emissions that can be used to validate "bottom-up" emission inventories (Shaiganfar et al., 2011).

Sarnia, Ontario, a small Canadian city, experiences pollutant emissions due to a large number of industrial chemical and oil processing facilities, vehicular exhaust from the Canada-U.S.A. international border crossing, emissions from large ships travelling through the St Clair River, vehicular traffic, residential heating and other anthropogenic emissions from the city populace, and transnational air pollution from Ohio, Illinois and Michigan (Oiamo et al., 2011). These sources contribute to increased levels of air pollutants such as NO_x, VOC's and SO_2, which are precursors of $PM_{2.5}$ and O_3 (Ministry of the Environment and Climate Change, 2015). Traditional "top-down" methods for quantifying pollutant emissions from small cities (e.g., satellite monitoring, aircraft studies) are limited by the small footprint. Additionally, in-situ air quality monitoring stations are limited by the bias towards near-surface emissions and under-sampling of elevated emissions (Tokarek et al., 2018a).

The Mobile-MAX-DOAS method has advantages over satellite, aircraft and in-situ techniques. Major advantages over satellite techniques include 1) emissions can be estimated without the need for an a-priori vertical profile, 2) accuracy of estimates can increase rather than decrease for smaller source regions, and 3) emissions may be estimated many times per day. Satellite retrievals are useful for estimating "top-down" emissions on regional and global scales over long periods of time (Huang et al., 2014; Kim et al., 2014; Liu et al., 2016; McLinden et al., 2012). However, accuracy over small regions can be limited by insufficient pixel resolution due to horizontal averaging and retrieval reliance on modelled a-priori vertical profiles that may not resolve small regions (Heckel et al., 2011). Aircraft studies can quantify emissions from cities but are relatively expensive. The major advantage of emissions estimates using aircraft measurements is that one can in principle fully characterize the vertical profile of trace gas concentration as well as the vertical profile of wind vectors for an accurate horizontal flux measurement downwind of a source (Baray et al., 2018; Gordon et al., 2015). Major advantages of the Mobile-MAX-DOAS method over aircraft techniques are that 1) MAX-DOAS VCDs are already vertically integrated, reducing the uncertainties due to interpolation of measurements at multiple flight altitudes and 2) MAX-DOAS studies are logistically easier to conduct. However, one is still left with the uncertainty of the vertical profile of wind vector fields. The Mobile-MAX-DOAS technique is a solution for quantifying pollutant emissions that complements the aforementioned techniques as well as in-situ monitoring, through the ability to observe localized surface based and elevated emissions.

An uncertainty associated with MAX-DOAS and satellite methods when estimating NO_x emissions from NO_2 measurements is the assumptions concerning the NO_x/NO_2 relationship in the air mass, which can be variable both spatially and temporally. The NO_x/NO_2 ratio is often assumed to be spatially constant, taken from literature based on the season, estimated using atmospheric modelling or occasionally taken from aircraft measurements when available (Rivera et al., 2010). In this study, we combined the Mobile-MAX-DOAS method with simultaneous mobile NO_x measurements (NO, NO_2, NO_x) to increase knowledge of the NO_x/NO_2 ratio in the air mass spatially and temporally in order to improve the accuracy of the NO_x emission estimates obtained from NO_2 measurements. A stationary modular meteorological station was deployed in the airshed provided auxillary meteorological information, typically a major source of uncertainty in Mobile-MAX-DOAS emission estimations. Hourly wind data measured at 10 m elevation (agl) were also available from local, permanent monitoring stations. Vertical wind profiles were modelled in high resolution (1 km x 1 km) using the version 3.9.1 Weather Research and Forecasting model (WRF) centered on Sarnia (42.9745^o N, 82.4066^o W) in an attempt to improve upon emissions values calculated using near-surface

wind-speed, since wind-speeds are expected to increase with altitude. However, inter-comparison of WRF modelled winds with measured near-surface winds during the study period indicated poor model performance (see Appendix D Section 2.2 for detailed results). Emissions in this study were therefore calculated using the 10 m measured winds to provide lower limit estimates of the hourly emissions.

Our study objectives were to 1) examine the relationship between the NO_2 near-ground mixing ratios and the NO_2 tropospheric VCDs, 2) determine NO_x and SO_2 emissions from the city of Sarnia including industrial sources, 3) determine the impact of NO_x/NO_2 variability on the accuracy of NO_x emission estimates, and 4) examine OMI satellite intrapixel NO_2 homogeneity. This study aims to demonstrate the utility of this method for determining trace-gas emissions and monitoring pollutant transportation in Sarnia and similar urban/industrial areas.

5.2 Experimental

5.2.1 Location and Instruments

Measurements were conducted in and around the city of Sarnia (42.9745° N, 82.4066° W), located in southwestern Ontario, Canada at the border with Port Huron, MI, U.S.A (Figure 1-1). The routes driven in the vehicle aimed to capture major NO_x and SO_2 emission sources at different distances downwind, dependent on the prevailing wind conditions. The metro area has a population of ~72,000 (2016 census) and an area of ~165 km^2. Sources of air pollution in this region include emissions from large ships, anthropogenic emissions from the cities of Sarnia and Port Huron, transport from the cities of Windsor and Detroit (60 km SW), the St Clair and Belle River power-plants (20 km SSW), oil refineries and chemical industry in Sarnia, and the cross-border traffic between Canada and the U.S.A. along Highway 402. Emissions from ships along the St. Clair River, normally a major source, were absent during the time of our study since the canal had not opened for the season.

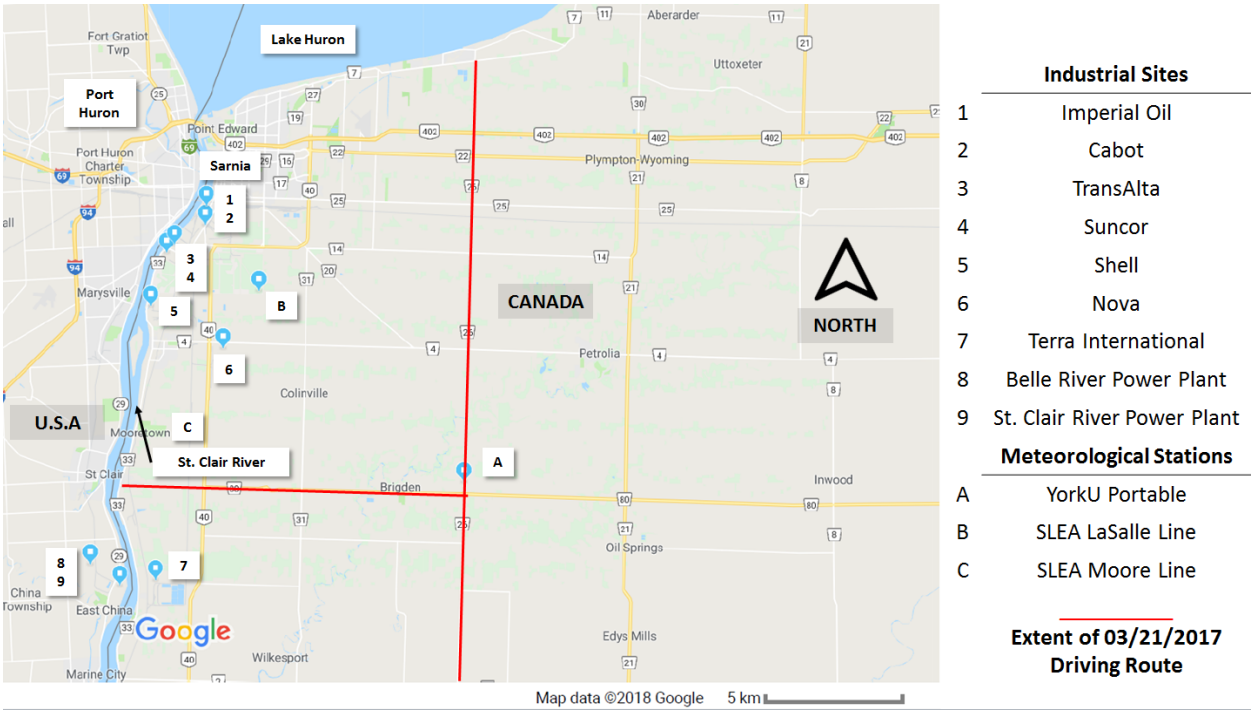

Figure 5-1 Location of industrial NO_x and SO_2 emission sources and meteorological stations in the Sarnia area.

A mini-MAX-DOAS instrument (Hoffmann Messtechnik GmbH) measured scattered sunlight spectra during three days: 21/03/2017 to 23/03/2017 ("Days 1 to 3") while mounted on top of a car in a backwards pointing direction. The instrument has a sealed metal box containing entrance optics, UV fibre coupled spectrometer and electronics. Incident light is focused on a cylindrical quartz lens (focal length = 40 mm) into a quartz fibre optic that transmits light into the spectrometer (OceanOptics USB2000) with a field of view approximately 0.6º. The spectrometer has a spectral range of 290-433 nm, a 50µm wide entrance slit yielding a spectral resolution was ~0.6 nm. The spectrometer is cooled and stabilized by a Peltier cooler. Spectrometer data was transferred to a laptop computer via USB cable. Spectra were obtained with an integration time of ~1 minute with the continuously repeating sequence of viewing elevation angles (30º, 30º, 30º, 30º, 40º, 90º). The vehicle was driven at a low but safe target speed of 50 km hr^{-1} when possible to provide a spatial resolution of ~ 1 km, but speeds were occasionally up to 80 km hr^{-1} when necessary. Tropospheric VCDs were estimated from the 30º and 40º elevation angle spectra. The 40º spectra allow verification that aerosol levels were sufficiently low to determine VCDs without radiative transfer modelling since VCDs obtained from both angles should be equal within ±15% under low to moderate aerosol loading conditions (Wagner et al., 2010). The cool temperatures in March aided in this as secondary organic aerosol loading tends to be low in this season due to an absence of biogenic emissions.

A Model 42 chemiluminescence NO-NO_2-NO_x Analyzer (Thermo Environmental Instruments Inc.) mounted in the vehicle measured NO, NO_2, and NO_x ($NO+NO_2$) near-surface mixing ratios. A PTFE inlet tube (5m length and ID=1/4") was mounted above the front vehicle window on the passenger side (~1.5 m above ground). The instrument alternately recorded average NO-NO_2-NO_x mixing ratios with a temporal resolution of 1 minute. Most of the routes were driven downwind of Sarnia on rural remote roads with little to no traffic such that NO_x emissions from other vehicles were not a concern. When NO_x from other vehicles was a potential concern, data was filtered out via careful note taking. The instrument indirectly measures NO_2 by subtracting the NO chemiluminescence signal obtained when air bypasses a heated Molybdenum (Mo) convertor from the successive total NO_x chemiluminescence signal obtained when air passes over the Mo-convertor. The NO_x analyzer can overestimate NO_x and NO_2 due to the potential contribution of other non-NO_x reactive nitrogen oxides (NO_z) other than NO_2 that can also be reduced to NO by the Mo converter (HNO_3, HONO, organic nitrates, etc.), leading to an overestimation (Dunlea et al., 2007). Since this overestimation is more important in low NO_x regions, only data with NO_x mixing ratios > 3 ppbv were used. Mixing ratios of <3ppbv NO_2 were only measured outside of plume-impacted regions when NO_2 VCDs were also low. The potential error in NO_x/NO_2 ratios is addressed further in section 5.3.2. NO_x mixing ratios can also have an error when successive NO and NO_x measurements occurred in areas with a significant temporal gradient in the NO_x emissions. Such gradients were seen due to passing vehicles or localized industrial NO_x plumes. These data were removed based on records of passing vehicles and other local near-surface sources or whenever the NO_2 mixing ratios were reported as negative. Few data points were removed because the routes driven were primarily rural roads with extremely low traffic density.

Aura satellite Ozone Monitoring Instrument (OMI) data were obtained for overpasses of the Sarnia, Ontario area for Days 1 and 3. Tropospheric NO_2 VCDs are the NASA Standard Product Version 3.0 with AMFs recalculated using the Environment and Climate Change Canada regional air quality forecast model GEM-MACH. The OMI instrument makes UV-vis solar backscatter radiation measurements with a spatial resolution of 13x24 km^2 at nadir and up to 28×150 km^2 at swath edges (Ialongo et al., 2014). The NO_2 detection limit of OMI is 5×10^{14} molec cm^{-2} (Ialongo et al., 2016). The OMI data used were screened for row anomalies that have affected OMI data since June 2007 (Boersma et al., 2007).

5.2.2 MAX-DOAS Determination of VCDs

Trace-gas Differential Slant Column Densities (DSCDs) were obtained using the DOAS technique (Platt and Stutz, 2008) with the spectral fitting range of 410-435 nm for NO_2 at 293 K and 307.5-318 nm for SO_2 at 293 K. All trace-gas cross-sections used were from (Bogumil et al., 2003b). For both gases, spectral fits also included a Fraunhofer Reference Spectrum (FRS), Ring Spectrum created from the FRS, O_3 cross-sections at 223 K and 297 K, and a third-order polynomial. The NO_2 cross-section was included in the SO_2 fits. Formaldehyde (HCHO) was not included in the fits for SO_2 as it was expected to be very low, and did not affect the residuals for the SO_2 fits. NO_2 DSCDs from Day 1 were fit against a single, same-day FRS obtained in a low-pollutant region near solar-noon time. These DSCDs were corrected for SCD(FRS) and SCD(Solar Zenith Angle (SZA)) contributions using the $DSCD_{offset}$ method (Wagner et al., 2010). The SCD(FRS) is the constant tropospheric trace-gas SCD component present in the FRS that causes an underestimation in the fitted DSCD. The SCD(SZA) is the difference between the stratospheric trace-gas component in the FRS and the measured non-zenith spectra. SCD(SZA) varies over time of day (t_i), maximizing overestimation in the DSCD early and late in the day. The sum of SCD(FRS) and SCD(SZA) is collectively known as the $DSCD_{offset}$. The $DSCD_{offset}(t_i)$ function was estimated by fitting a second order polynomial to multiple pairs of DSCDs of spectra (non-zenith and zenith from the same sequence), described in detail in (Wagner et al., 2010).

The $DSCD_{offset}$ polynomial is most accurate when successive spectra in each sequence observe similar mixing ratio fields, and measurements obtained many data-points over most of the daylight hours. However, routes on Days 2 and 3 included driving in and out of both high and low NO_x regions within short time-periods and thus met neither of the requirements listed above for the $DSCD_{offset}$ method. On these days, a second method was used where NO_2 DSCDs were fit against an FRS spectrum obtained close in time (<25 minutes) along each respective route in a low-pollutant region. The impacts of SCD(FRS) and SCD(SZA) on the retrieved DSCDs can be assumed to be negligible since each FRS was from a low-pollutant area and obtained close in time, respectively. This method was also used for the Day 1 SO_2 route since limited data were available but included background SO_2 measurements close in time.

For all routes trace-gas tropospheric VCDs were determined by assuming a single scattering event occurred for each photon such that the air-mass factor (AMF) depended only on the viewing elevation angle, $\propto$, $AMF_{trop}(\propto) \approx \frac{1}{\sin(\alpha)}$ (Brinksma et al., 2008)(Wagner et al., 2010). This “geometric approximation” is most valid under low to moderate aerosol loading and has been shown to deviate from the typically more accurate radiative transfer modelling by up to ±20% under moderate aerosol loading (Shaiganfar et al., 2011). Day 1 VCDs were calculated following Eq. (1):

$$VCD_{trop} = \frac{DSCD_{meas}(\propto,t_i)+DSCD_{offset}(t_i)}{\frac{1}{\sin(\alpha,t_i)}} \quad (1)$$

Days 2 and 3 NO_x and Day 1 SO_2 VCDs were calculated following Eq. (2):

$$VCD_{trop} \approx \frac{DSCD_{meas}(\propto, t_i)}{\frac{1}{\sin(\alpha, t_i)}} \quad (2)$$

The VCD of SO_2 was above detection limit on only two occasions in this study (both on Day 1), in contrast to NO_2. The detection limit of SO_2 is higher than NO_2 for several reasons, first, it's differential cross-section is less than that of NO_2 and, second, its absorption features are in the UV wavelength region where scattered sunlight intensity is much less than that in the visible region. The fast measurements required in mobile DOAS also allow limited averaging of spectra compared to stationary measurements (Davis et al., 2019), where detection of industrial SO_2 plumes is easier. Therefore, SO_2 DSCDs were only above detection limits for Day 1 Routes 3 & 4 when the light levels were highest, and the vehicle observed the combined plumes of the largest SO_2 sources in the area.

5.2.3 Estimating Trace-gas Emissions from MAX-DOAS VCDs

Trace-gas emission estimates were calculated following a flux integral approximation Eq. (3):

$$E = \left[(\sum_i \left(VCD_{outflow,i} - VCD_{influx,i}\right) w_i \sin(\beta_i)\, ds \right] \frac{MW}{Av} \quad (3)$$

where $VCD_{outflow,i}$ is the VCD measured at position i along the route s for distance ds, $VCD_{influx,i}$ is either the measured influx values or the estimated background VCD value, w_i is the wind-speed, β_i is the angle between the driving direction and the wind-direction, MW is the molecular weight of the target gas, and Av is Avogadro's number. Transect routes were designed to observe both within and beyond emission impacted areas since routes encircling the emission sources were often not possible. Flux integrals were calculated using portions of the transects impacted only by the Sarnia urban/industrial plume in cases where plumes from other sources impacted the transect (i.e., Day 1; U.S.A. power-plant plumes). In these cases, the end-points of integration were chosen judiciously where NO_2 VCDs and surface mixing ratios decreased to a minimum at the edge of the Sarnia emissions. This method assumes that the wind-field and trace-gas emission rates are constant during the time required to drive a route. The validity of this assumption improves with decreased time for driving route completion. The Sarnia region is ideal for this method

since a small geographical area contains the majority of the emissions and is surrounded on three sides by rural regions with low anthropogenic emissions.

A potential source of uncertainty in Mobile-MAX-DOAS emission estimates is variation in the wind fields and/or source emission rates while driving (Ibrahim et al., 2010; Wu et al., 2017a). Previous studies have estimated wind-fields from local meteorology stations (Ibrahim et al., 2010), meteorological models (Shabbir et al., 2016; Shaiganfar et al., 2011, 2017) or LIDAR measurements (Wu et al., 2017a). In our study, wind field information was obtained from a Modular Weather Station (Nova Lynx 110-WS-25DL-N) we deployed near one of the driving routes at (42.8148^{o}, -82.2381^{o}) (Figure 5-1) and from meteorological ground stations in the area (Figure 5-1, Table D1, Figure D1). The modular weather station measured wind-speed and direction, temperature, relative humidity, and barometric pressure at 2 m above the surface every 30 seconds. Wind data was available from the Sarnia-Lambton Environmental Association (SLEA) LaSalle Road (42.911330°, -82.379900°) and Moore Line (42.83954°, -82.4208°) meteorological stations that are located near the driving routes (Figure 5-1). These stations were surrounded by fallow, flat farm-land for at least 4 km on each side and thus should reflect total boundary layer for plumes transported away from the city more than the urban stations (Figure D1). The hourly wind-direction data from the modular and permanent stations exhibited similar values (±10^{o}) and trends on Day 1 (Figure D2). Wind-directions for Days 2 and 3 were obtained by determining the angle of a vector drawn between the geographical locations of the maximum NO_2 VCD enhancements and the industrial facilities expected to have emitted the plumes. These map-determined wind-directions were consistent (±10^{o}) with the data from the station(s) closest to the driving route. Comparison of wind-speed data on Days 2 and 3 was not possible due to a technical issue with the modular weather station on these days.

The NO_2 VCD influx (background VCD) was estimated on Day 1 since measurement was impossible along the western border of Sarnia due to the road configuration and proximity of industrial emissions. A NO_2 VCD_{influx} = 2×10^{15} molec cm^{-2} was estimated based on OMI satellite VCDs of ~1.5-3.5$\times10^{15}$ molec cm^{-2} from the area east of Sarnia that are expected to be similar to the NO_2 regime west of Sarnia. These pixels are expected to be unaffected by other sources. The influx would be expected to be impacted by vehicular and residential emissions from the small city of Port Huron, U.S.A., on the west side of the St Clair River (Figure 5-1), which has limited industry but a moderate level of commercial vehicle activity due to border-crossings. A first order emission estimate of vehicular NO_x emissions from Port Huron from daily reported traffic counts results in an upper limit of NO_2 influx VCD of ~1×10^{15}

molec cm^{-2} (see Appendix D Section 4). True influx would vary along the length of the measurement transect, depending on what sources are upwind of the location. Halla et al. (2011) measured NO_2 tropospheric VCDs using MAX-DOAS in a similar region approximately 70 km south-east of Sarnia. The observed NO_2 VCDs in that study ranged from 0.01 to 1.25×10^{16} molec cm^{-2} with a median value of 2×10^{15} molec cm^{-2}, which is expected to be representative of background NO_2 columns in this region. The highest VCD in that study was attributed to the transport of industrial emissions from the Sarnia area and/or from Detroit, MI to the northwest and west of the site respectively (Halla et al., 2011). Based on the range of VCDs from literature, vehicular emission estimates and satellite measurements, a background VCD of 2×10^{15} molec cm^{-2} is a reasonable estimate, and emissions sensitivity tests were conducted using influx VCDs of $0.5\text{-}3\times10^{15}$ molec cm^{-2} (see Appendix D Section 5). In contrast, the NO_2 VCD_{influx} on Days 2 and 3 and SO_2 VCD_{influx} on Day 1 were determined from the average VCDs measured in the low-pollution area of each transect.

5.2.3.1 Determination of NO_x emission estimates from NO_2 measurements

NO_x emissions were estimated using Equation 4 from the NO_2 flux integral and the average NO_x/NO_2 ratio (NO_x > 3 ppbv) measured by the NO_x-analyzer along the route. The emission values were then corrected for expected NO_x loss during transport using a NO_x lifetime, τ. NO_x emission estimates were calculated as follows:

$$\boldsymbol{E_{NOx} = E_{NO_2} * \frac{\overline{NO_x}}{NO_2} * e^{\left(\frac{y/w}{\tau}\right)}} \quad (4)$$

where τ is NO_x lifetime, w is wind-speed, and y is the distance between the NO_x source and the measurement location. For routes where individual NO_x/NO_2 ratios deviated significantly from the route average, the NO_x emission estimates were calculated by applying 1) the route-averaged NO_x/NO_2 ratio and 2) individual NO_x/NO_2 ratios associated with each NO_2 VCD point by point. Multiple factors determine NO_x lifetime in a plume. A NO_x lifetime of 6 hours was used in this study based on considerations given in section 5.3.3. A sensitivity analysis was performed varying the lifetimes between 4-8 hours (Appendix D Section 7). The conversion factors used to calculate NO_x emissions for each route can be found in Table D 8. The NO_x/NO_2 ratios are more fully addressed in Section 5.3.2 and the NO_x lifetime is addressed in Section 5.3.3.

5.3 Results & Discussion

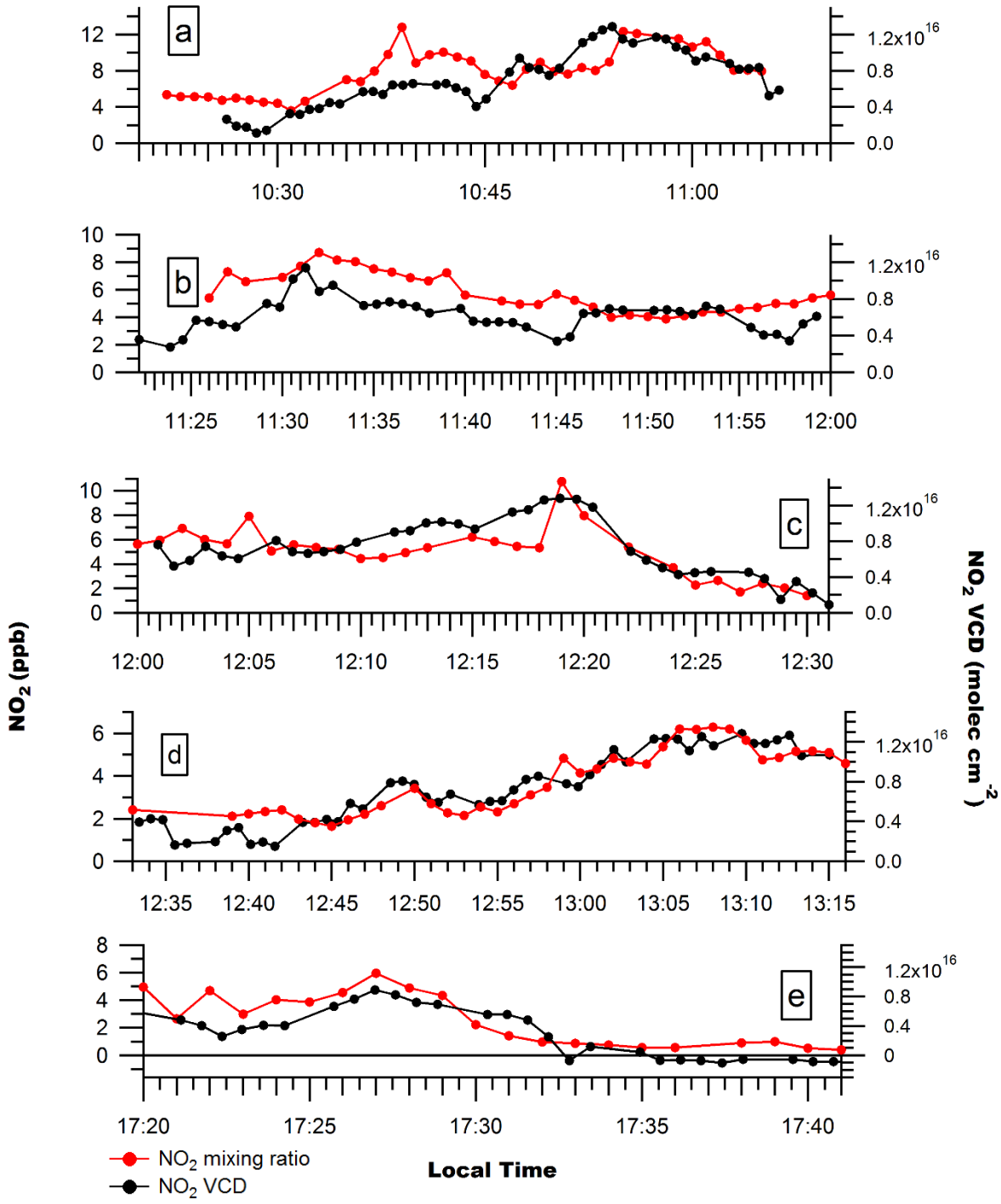

Figure 5-2 NO_2 mixing ratios and NO_2 VCDs along routes 1-4 on Day 1 (a) – (d) and route 1 on Day 2 (e). Uncertainties in measured NO_2 mixing ratios are ± 0.5 ppbv. Uncertainties in the NO_2 VCD are given by $\sigma_{VCD} = [(0.25\ VCD)^2 + (5\times10^{14}\ molec\ cm^{-2})^2]^{½}$.

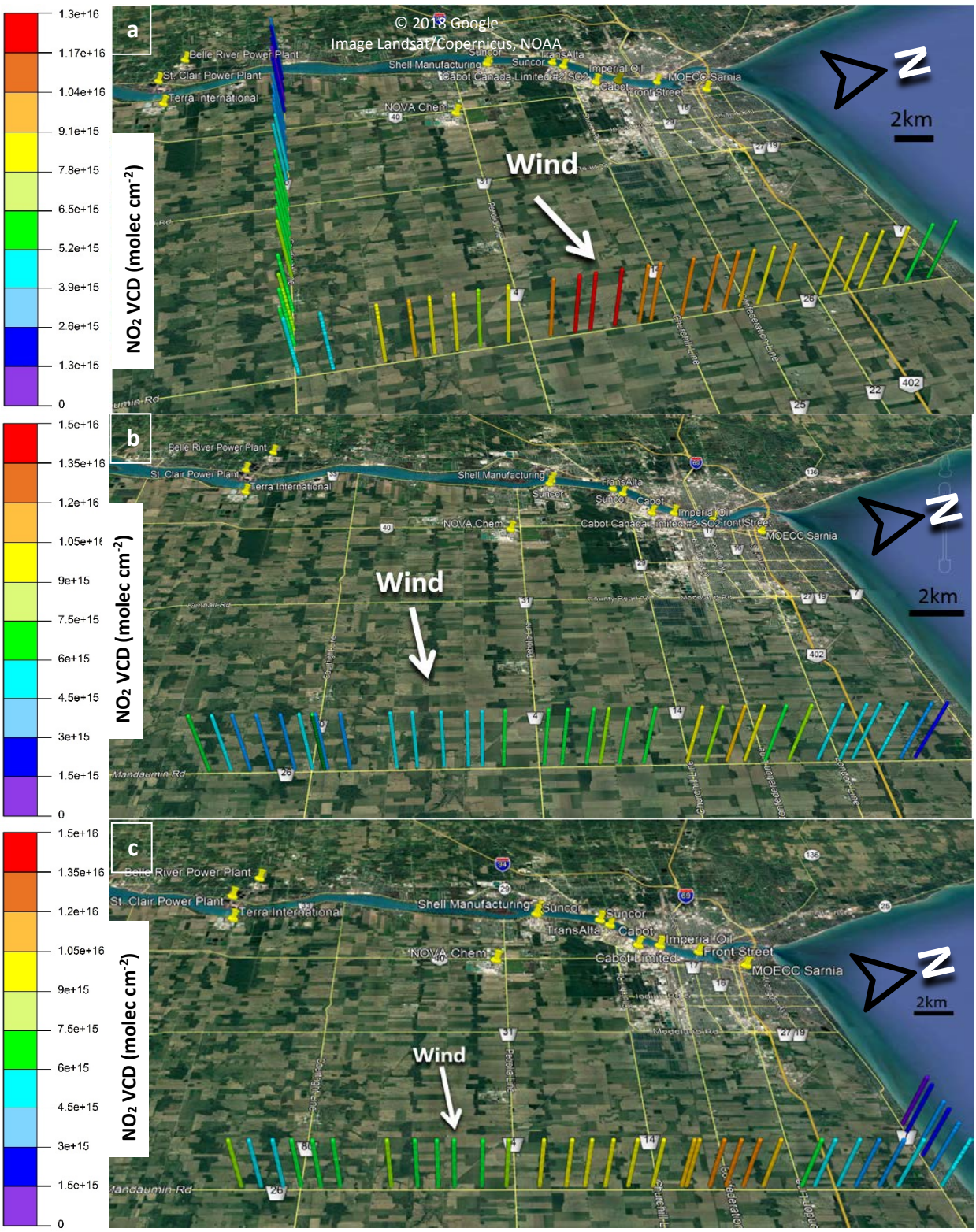

Figure 5-3 Day 1 driving routes; (a) route 1, (b) route 2 and (c) route 3, used to estimate NO_x emissions from Sarnia.

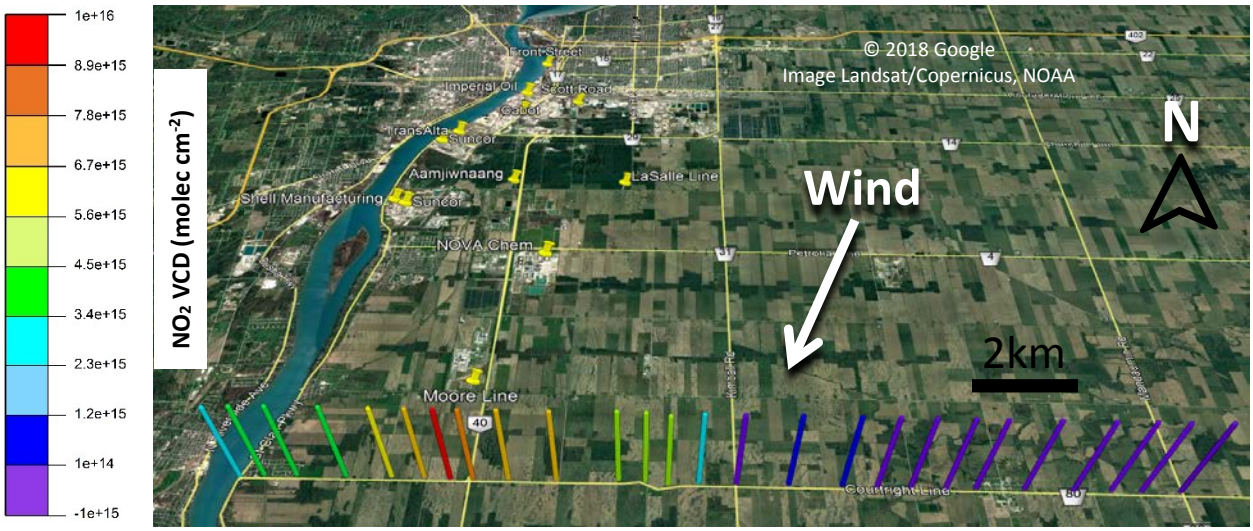

Figure 5-4 NO_2 VCDs measured on Day 2 route 1.

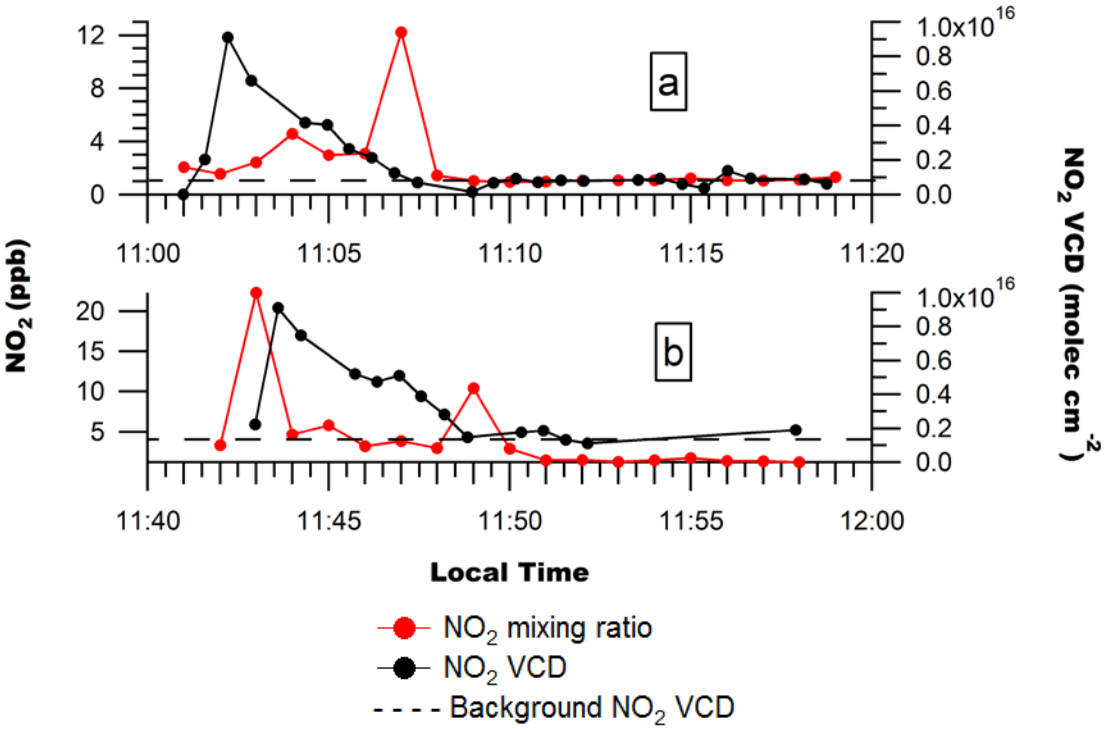

Figure 5-5 NO_2 mixing ratios and NO_2 VCDs measured on Day 3 along (a) driving route 1 and (b) driving route 2. Uncertainties in measured NO_2 mixing ratios are ± 0.5 ppbv. Uncertainties in the NO_2 VCD are given by $\boldsymbol{\sigma}_{VCD} = [(0.25\ VCD)^2 + (5\times10^{14}\ molec\ cm^{-2})^2]^{½}$.

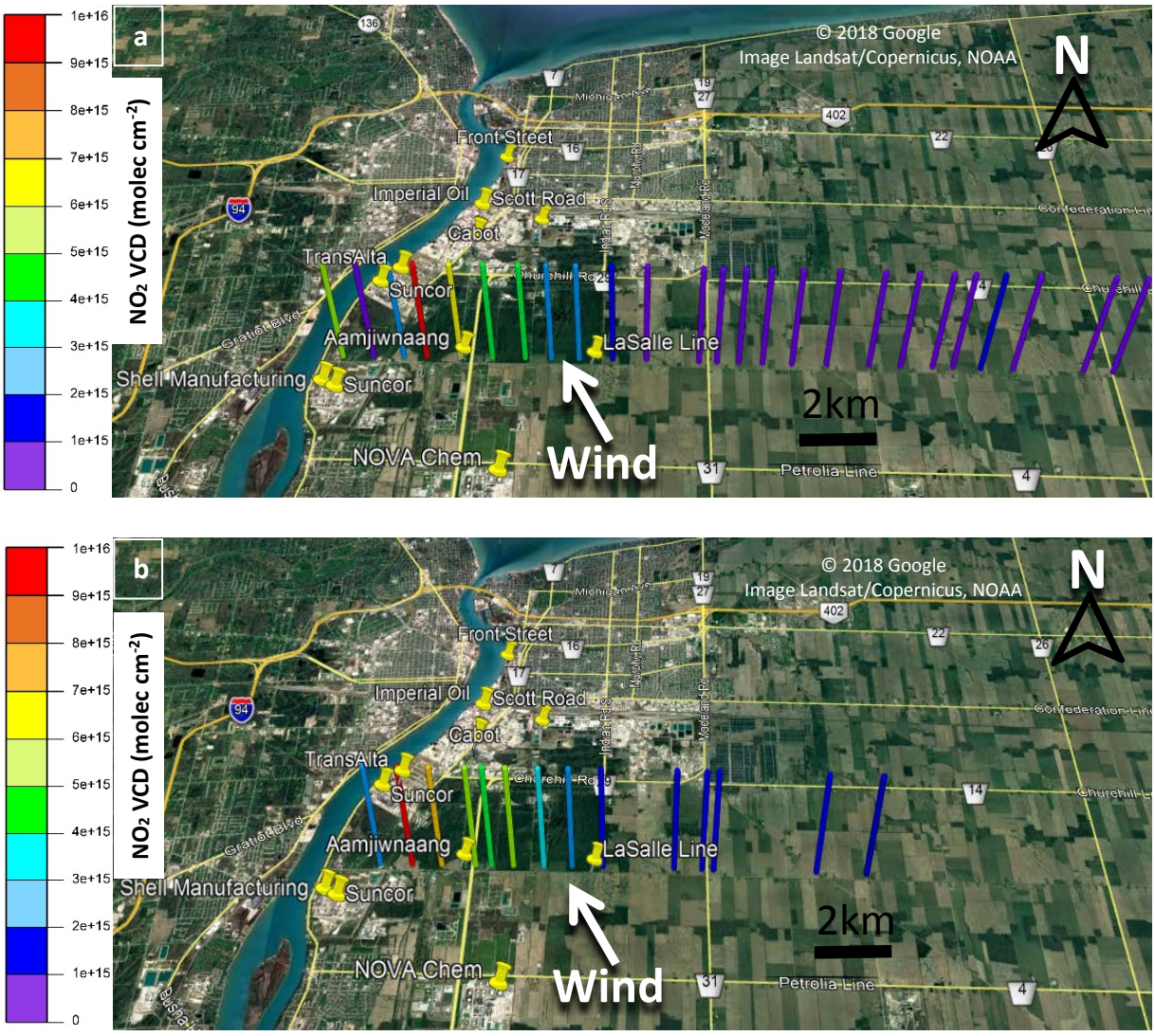

Figure 5-6 NO_2 VCDs measured on Day 3 along (a) driving route 1 and (b) driving route 2.

5.3.1 Relationship between NO_2 VCDs & NO-NO_2-NO_x Analyzer Measurements

Figure 2 shows that enhancements in NO_2 VCDs downwind of Sarnia were generally associated with NO_2 surface mixing ratios enhancements during Days 1 and 2. This suggests that pollution from Sarnia was well-mixed within the boundary layer at the measurement locations, typically 14-23 km downwind of sources (Figure 5-3 &Figure 5-4). However, the ratio of NO_2 VCD to NO_2 mixing ratio was sometimes variable even during relatively short time periods when the boundary layer height was expected to be constant (Figure 5-2a). This variability was probably due to the presence of multiple NO_x plumes that had originated from sources with different heights (i.e., stacks and surface sources) and emission rates.

In contrast to Days 1 and 2, NO_2 VCD enhancements on Day 3 were not consistently associated with NO_2 surface mixing ratio enhancements (Figure 5-5 & Figure 5-6). A large surface enhancement (NO_x=22 ppbv) was observed at the location of the VCD NO_2 enhancements (~2.5×10^{16} molec cm^{-2}) associated with the NOVA Chemicals industrial plume on route 2 (Figure 5-5b & Figure 5-6b) but not on route 1 (Figure 5-5a & Figure 5-6a). This discrepancy is likely due to the closer proximity of the driving route to the source compared with Day 1, combined with limited vertical mixing of the plume. The relatively long sampling time of the NO_x analyzer with a relatively fast driving speed on this route may also have led to an underestimation of the true NO_x values for this localized plume.

Table 5-1 Daily meteorological conditions, number of routes and time period of routes driven. Wind-speed from SLEA LaSalle Road; Temperature and Relative Humidity from portable meteorological station Day 1 and Day 2 and from Moore Line station Day 2.

Date	Number of Routes Driven	Measurement Local Time Period	Average Wind-speed ($km\ hr^{-1}$)	Prevailing Wind-Direction	Average Temperature (^oC)	Average Relative Humidity (%)	Emission Area Measured
3/21/2017	4	10:26-13:16	15	Westerly	10	50	City of Sarnia
3/22/2017	1	17:22-17:41	8	Northerly	-3	52	City of Sarnia
3/23/2017	2	11:10-11:57	15	Southerly	1	42	NOVA Chemicals Industries Facility

5.3.2 NO_x/NO_2 Ratios

The NO_x/NO_2 ratio is necessary to estimate NO_x emissions from the source, given measurements of NO_2 VCD's (Eq. 4). Ratios of NO_x/NO_2 (Table 5-2) measured along the routes on Days 1 and 3 were within 20% of the route-averaged value with a relative standard deviation of less than 12%. NO_x/NO_2 ratios tended to increase at locations associated with transported plumes' centerlines, as expected due to an increase in NO emissions from the sources (Figure 5-7), and exhibited the greatest variability in air-masses affected by sources with different altitudes and emission rates. Day 1, route 1 exhibited variable NO_x/NO_2 ratios due to emissions from the power-plants across the river in Michigan, residential and vehicular traffic, and industrial emissions (Figure 5-3a & Figure 5-7).

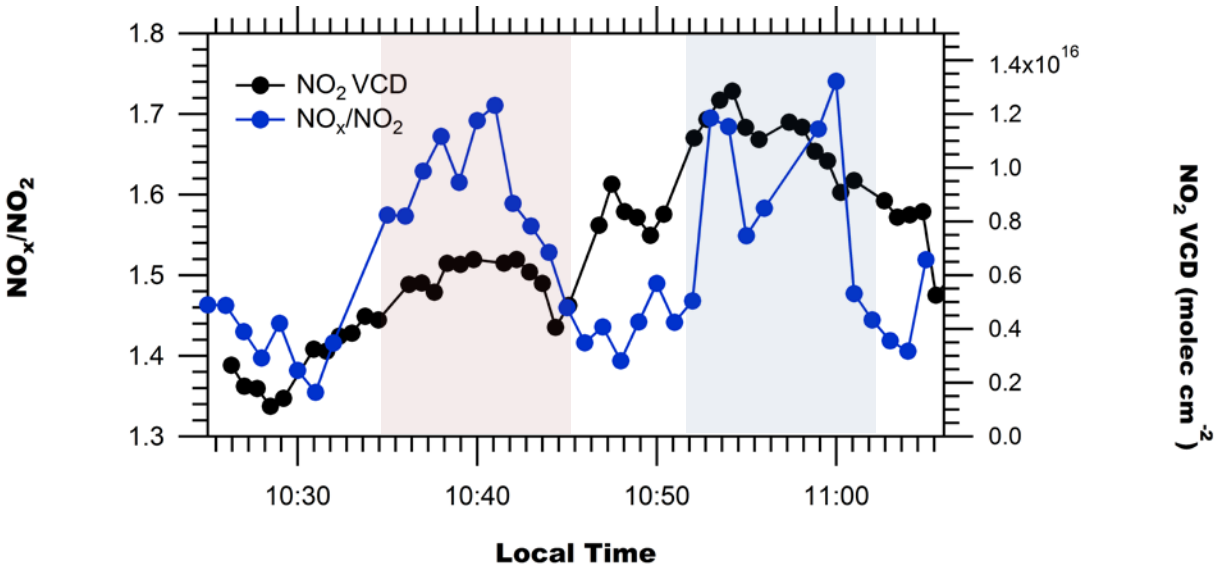

Figure 5-7 NO_2 VCDs and NO_x/NO_2 ratios on Day 1 route 1. Detection of Michigan power plants' plume(s) (left) on East-West transect & Sarnia plume (right) on North-South transect are highlighted in pink and blue, respectively. Uncertainties in measured NO_x/NO_2 ratios are ± 5% (~±0.075). Uncertainties in the NO_2 VCD are given by $\sigma_{VCD} = [(0.25\ VCD)^2 + (5\times10^{14}\ molec\ cm^{-2})^2]^{½}$.

Table 5-2 NO_x/NO_2 ratios for routes driven.

Date	Day's Route Number	Measurement Local Time Period	Number of Points	Average ±1σ	Median
3/21/2017	1	10:26-11:06	37	1.53±0.12	1.49
3/21/2017	2	11:22-11:45	23	1.45±0.06	1.44
3/21/2017	3	12:09-12:28	18	1.36±0.07	1.37
3/21/2017	4	12:34-13:16	24	1.29±0.06	1.31
3/22/2017	1	17:22-17:41	10	1.49±0.53	1.30
3/22/2017	1	17:22-17:41*	9	1.32±0.08	1.30
3/23/2017	1	11:10-11:19	5	1.39±0.09	1.39
3/23/2017	2	11:42-11:57	9	1.46±0.17	1.52

The 3/22/2017 17:22-17:41* data had the peak NO_2 plume location NO_x/NO_2 value removed.

Potential errors may exist in the NO_x/NO_2 ratio due to the presence of other NO_z species in the air mass (e.g., HNO_3, HONO, NO_3, N_2O_5, organic nitrates, etc.) that are also converted to NO by the Mo-convertor in addition to NO_2 (Dunlea et al., 2007). However, these errors are smaller than might be expected due to the presence of the error in both the numerator and the denominator of the ratio, $NO_x/NO_2 = (NO+NO_2)/NO_2$, thus partially offsetting each other. For example, at an apparent NO_x/NO_2 ratio of 1.40 (average in Table 5-2), a 10% and 30% error in the reported NO_2 due the presence of other NO_z species gives rise to errors of only -2.6% and -6.6% in the measured NO_x/NO_2 ratio

respectively. Mathematically, the error in the NO_x/NO_2 ratio gets larger as the percentage of NO in the total NO_x increases. However, since most of the interfering NO_z species are generated photochemically, or only at night (NO_3, N_2O_5) increasing with reaction time and distance away from the source, the percentage of interfering species is smaller at higher values of total NO and NO_x. Under significantly intense photochemical conditions in the MCMA-2003 field campaign in Mexico, the interference in the chemiluminescence monitors resulted in average NO_2 concentrations being 22% higher than those determined from spectroscopic measurements (Dunlea et al., 2007), which would give rise to an error in the NO_x/NO_2 ratio of <5%. In the current study we estimate that the resultant negative bias in the measured NO_x/NO_2 ratio does not exceed -5% for several reasons; i) we filter out low NO_x data (<3ppbv), ii) the emission integral is dominated by regions with high NO_x that are spatially and temporally close to the sources and, iii) photochemistry was reduced during this spring campaign. The uncertainty that arises from potential errors in the NO_x/NO_2 ratio is insignificant compared to other errors (Table D9). It is also worth noting that NO_2 measurements by the NO_x analyzer are not directly used for the calculation of emissions; only the NO_x/NO_2 ratio is used.

Previous Mobile-MAX-DOAS studies have relied on literature estimates of the NO_x/NO_2 ratio (Shabbir et al., 2016; Shaiganfar et al., 2011) or estimated the ratio from a Leighton ratio calculated using local air quality station data (Ibrahim et al., 2010). In regions with many pollutant sources throughout (e.g., megacities), this ratio is expected to be horizontally and vertically inhomogeneous. The ratio can therefore be challenging to estimate and can increase the uncertainty of the NO_x emission estimate. Estimation of NO_x/NO_2 ratios from near-surface monitoring stations can be problematic because the ratios are applied to a VCD but may reflect only local emissions (e.g., nearby vehicular exhaust) rather than the total boundary layer. In this study, NO_x data impacted by local emissions were removed. Also, the Sarnia emissions were expected to be well mixed to the surface since most of the transects were driven sufficiently far from the sources. Therefore, the near-surface NO_x/NO_2 ratios should be representative for the altitude range of the dispersed NO_x plume(s). This hypothesis is supported by the similarity between the NO_2 surface and VCD temporal trends during the study, especially on Days 1 and 2 (Figure 5-2).

5.3.3 NO_x Lifetime

Various lifetimes of NO_x, τ, have been used in previous mobile MAX-DOAS studies for the calculation of NO_x emissions from NO_2 measurements: 6 hr in Germany (Ibrahim et al., 2010), 5 hr in Delhi (Shaiganfar, 2011), 5 hr in China (Wu et al., 2017) and 3 hr summer – 12 hr winter in Paris (Shaiganfar, 2017). In Beirle et al. (2011), the

daytime lifetime of NO_x was quantified by analyzing the downwind patterns of NO_2 measured by satellite instruments and shown to vary from ~4 hr in low to mid-latitude locations (e.g., Riyadh, Saudia Arabia) to ~8hr in northern locations in wintertime (e.g., Moscow, Russia). In a follow up study, Valin et al (2013) showed that one cannot assume that τ is independent of wind speed and derived values of τ from the satellite observations over Riyadh to be 5.5hr to 8 hr, corresponding to OH levels of $5\text{-}8\times10^6$ molec cm^{-3}at high and low wind speeds.

Multiple factors determine NO_x lifetime in a plume, including season (e.g., insolation) (Liu et al., 2016), latitude, wind-driven dilution (Nunnermacker et al., 2000; Valin et al., 2013), NO_x emission rate and initial dilution (Nunnermacker et al., 2000), temperature, hydroxyl radical levels (OH) and precursors to OH including O_3, H_2O, and HONO. Very importantly, the daytime lifetime of NO_x is a nonlinear function of the NO_x concentration itself, having longer lifetimes at high and low concentrations with the shortest lifetimes at intermediate NO_x concentrations due to the impact on OH levels in a non-linear feedback on its own lifetime (Valin et al., 2013). The NO_x lifetime is ultimately dependent on the OH levels since this dictates the loss rate of NO_2 to its terminal sink ($NO_2 + OH \rightarrow HNO_3$). However, the presence of VOC's in the urban plume, which are catalytically oxidized forming O_3 in the presence of NO_x and HO_x ($OH + HO_2$), can decrease the NO_x lifetime due to their acceleration of the conversion of NO to NO_2 via peroxy radical reactions ($RO_2\cdot + NO \rightarrow NO_2 + RO\cdot$). Therefore, NO_x lifetimes can vary both spatially and temporally (Liu et al., 2016), even within the same plume (Valin et al., 2013). Underestimation of the true NO_x lifetime leads to overestimation of the NO_x emissions, while an overestimate leads to an underestimation of the emissions.

While photolysis of HONO is often the major source of OH in the morning boundary layer (Platt et al., 1980; Alicke et al., 2002), midday production of OH via photolysis of O_3 and subsequent reaction of O (^1D) with water is frequently the dominant source of OH. Assuming O(^1D) is in steady-state, it can be shown that when ozone photolysis is the main source of OH, the product of the mixing ratios of H_2O and O_3 is proportional to the production rate of OH. In this study, the $[H_2O]*[O_3]$ product was calculated using surrounding station measurements (see Appendix D Section 8.1). The $[H_2O]*[O_3]$ product indicates that mid-day OH production under the spring-conditions for Days 1 and 2 is only 10-25% of the expected OH production under warmer more humid summer-conditions, presuming that O_3 photolysis predominates. This might suggest OH levels were lower in our study than

during summer, and hence NO_x lifetimes longer. However we assume this with caution as the HONO production is not known nor are the loss rates of OH.

As mentioned, the presence of VOC's can decrease the lifetime of NO_x under conditions where NO_x is sufficiently high to dominate the peroxy radical reaction path. To test for the presence of VOC's in the plumes (in the absence of measurements), Leighton ratios, ϕ (Leighton, 1961), were calculated at locations of maximum NO_2 VCD associated with Sarnia plumes. Leighton ratios were calculated following Eq. (5) (see Appendix D Section 8.2 for details):

$$\phi = \frac{\boldsymbol{j_{NO_2}[NO_2]}}{\boldsymbol{k_1[NO][O_3]}} \quad (5)$$

where j_{NO2} is the NO_2 photolysis rate, k_8 is the temperature-dependent rate constant for the reaction between NO and O_3. Leighton ratios equal to 1.0 indicate that NO, NO_2 and O_3 are in steady state with no significant interference from other species, while ratios of ϕ greater than 1.0 imply the role of other peroxy radical species (e.g., RO_2, HO_2) in the conversion of NO to NO_2 (Pitts and Finlayson-Pitts, 2000). The NO_2/NO ratios were calculated from the NO_x analyzer measurements, O_3 mixing ratios were obtained from local monitoring stations during the same daytime periods as the transects. Values of j_{NO2} were estimated using SLEA Moore Line station solar irradiance data (Figure 5-1; Table D1) and solar zenith angle following the method in Wiegand and Bofinger (2000).

Table 5-3 Calculated Leighton Ratios for selected plume maximums on Day 1 and 2.

Date	Local Time	J_{NO2} ($\times 10^{-3}$ s^{-1})	Solar Irradiance (W m^{-2})	SZA	O_3 mixing ratio (ppbv)	Measured NO_2/NO (ppbv $ppbv^{-1}$)	Calculated Leighton Ratio*
21/03/2017	11:00	5.23	564	35	18	1.7	1.61
21/03/2017	11:30	5.65	600	40	23	2.2	1.76
21/03/2017	12:15	6.44	675	43	23	2.2	2.01
22/03/2017	17:28	2.71	300	23	10	0.5	0.44

*** Note that Leighton ratios, ϕ** , could be biased high by as much as +20% from the the NO_z component of NO_y measured by the NO_x analyzer, but likely much lower due to it being a fresh urban/industrial NO_x plume.

Table 5-3 shows Leighton ratios calculated at the locations of maximum NO_2 VCD enhancements. Calculated Leighton ratios were significantly greater than 1 (ϕ = 1.7-2.3) at peak NO_x locations on Day 1 (Table 5-3). Even if we consider a potential bias of + 20% in the NO_2 measurements by the NO_x analyzer for reasons outlined in Section 5.3.2 (highly unlikely in a fresh NO_x plume), a +20% bias in the Leighton ratio would still give (ϕ = 1.4-1.9). We interpret this as an indication that significant levels of peroxy radicals were present in the plume, presumably from

VOC oxidation by the OH radical. This is consistent with high VOC emissions from the petrochemical facilities in Sarnia, with emission rates >300 tonnes yr^{-1} each for four of the top six industrial NO_x emitters in Sarnia (ECCC, 2018g). The Day 2 Leighton ratio of less than 1.0 in Table 5-3 suggests a relatively fresh plume (only 4 km downwind of a facility) that had not come to photo-stationary state.

Thus, we have indications that OH production may be lower than summer time leading to longer NO_x lifetimes and we have indications that VOC oxidation in the plume may be significant leading to shorter NO_x lifetimes than air masses where the photo-stationary state in NO_x is valid. Without further information, we have opted to assume a central NO_x lifetime assume of ~ 6 hr. Sensitivity calculations were conducted for NO_x emission estimates using a range of lifetimes of 4-8 hours (Appendix D Section 7). Varying the lifetime from ± 2 hours changed the emission estimates by <15% for all routes except for Day 1 route 1 due to low wind-speeds during that route (30% change).

For the calculation of SO_2 emissions, SO_2 was assumed to have a sufficiently long lifetime in the boundary layer so as to be conserved between the emission and measurement location. Note that cloud processing of SO_2 was assumed to be negligible since SO_2 measurements were completed on a mostly cloud-free day.

5.3.4 Emission Estimates

5.3.4.1 Emission Estimates of Sarnia

The VCDs measured are shown in Figure 5-3 and Figure 5-6 while the NO_x emissions calculated using Eqs. (3) and (4) are shown in Table 5-4. The values of VCD_{influx} required for the calculations were typically determined from measurements of VCD in low pollution transect areas. However, the VCD_{influx} on Day 2 was not determined in this way since these DSCDs were close to zero within error (Figure 5-2 &Figure 5-4). The VCD_{influx} is expected to be low on Day 2 because the north wind-direction indicates that the air-masses originated from over Lake Huron. These low values were probably due to low light levels during measurement, insufficiently long integration times (low signal to noise ratio), and NO_2 background VCD values below the instrument's limit of detection. A low value of VCD_{influx} = $0.5(\pm 0.5)\times 10^{15}$ molec cm^{-2} was therefore assumed.

Table 5-4 Lower limit NO_x Emission Estimates from 10 m elevation wind-speeds.

Date	Emission Source	Daily Route Number	Lower-limit NO_x (tonnes hr^{-1})	NPRI NO_x (tonnes hr^{-1})
21/03/2017	Sarnia	1	1.6±0.8	0.9
21/03/2017	Sarnia	2	1.2±0.5	0.9
21/03/2017	Sarnia	3	1.4±0.5	0.9
22/03/2017	Sarnia	1	1.5±0.6	0.9
22/03/2017	Sarnia	1*	2.2±0.8	0.9
23/03/2017	NovaChem	1	0.27±0.1	0.14
23/03/2017	NovaChem	2	0.29±0.1	0.14

* calculated using individual NO_x/NO_2 ratios.

The emissions were calculated in two ways i) using a route-average NO_x/NO_2 ratio value for each route estimate and ii) using individual NO_x/NO_2 ratios co-located with each VCD measurement. For Day 1 route, the route average NO_x/NO_2 ratio was 1.53 ± 0.12 ppbv $ppbv^{-1}$ with the difference between the calculated emission rates using the two methods being only 3%. Day 1 transects 2-4 exhibited small variability in NO_x/NO_2 (Table 5-2) and the variation in the NO_x/NO_2 ratio impacted emission estimates by less than 5%.

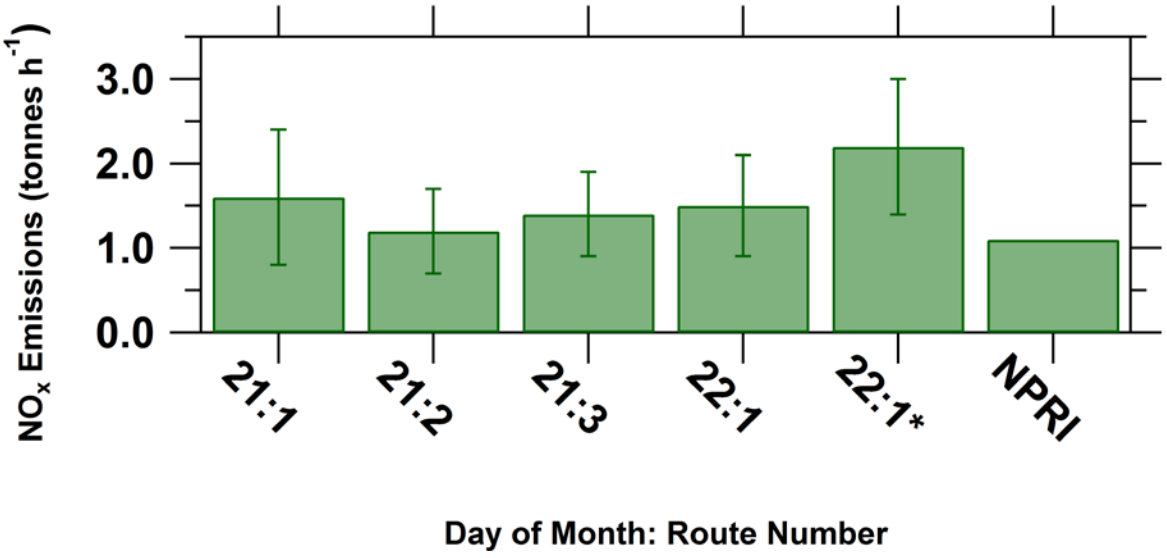

Figure 5-8 Lower limit estimates of NO_x Emissions from Sarnia on Day 1 and Day 3 and 2016 NPRI emissions. The 22:1* NO_x emission estimate used individual NO_x/NO_2 ratio values for each VCDs rather than a single average ratio.

However, the difference between emission estimates calculated using individual NO_x/NO_2 ratios versus a route-averaged value can be non-trivial, as observed with the Day 2 route 1. Day 2 had consistent northerly wind conditions, and east-west transects were driven south of Sarnia to capture the urban plume and background regions to the east (Figure 5-4). The resultant Sarnia NO_x emission using the first method is consistent with the first three

Day 1 emission estimates but the application of the second method (individual NO_x/NO_2 ratios collocated with each VCD) increased the emission estimate by ~50% (Table 5-4 and Figure 5-8). The NO_x/NO_2 ratio was generally consistent with the averaged value of 1.3 (maximum NO_x/NO_2 removed) but increased to 3 in the region of maximum NO_2 VCD enhancements 7 km south of the NOVA Chemicals facility (Table 5-2). The calculated Leighton ratio for this peak NO_x/NO_2 ratio location is less than 1 (see 5.3.4.2 and Table 5-3). The Leighton ratio suggests the plume from the NOVA Chemical facility had significant NO that had not had sufficient time to come to a photostationary state. The emission estimate using individual NO_x/NO_2 ratios is considered the more accurate value for this route compared to the emission value calculated using the route-averaged ratio.

The importance of measuring the local NO_x/NO_2 ratio is also illustrated by observing variation of the ratio due to the impact of the Michigan power-plants' plume, apparent in the Day 1 route 1 East-West transect (Figure 5-3a). The NO_x/NO_2 ratio along this transect increased to ~1.7 (Figure 5-7), higher than the maximum NO_x/NO_2 ratio observed in the North-South transect downwind of Sarnia. A higher ratio is somewhat unexpected because the distance between the source and receptor measurement for the power plant source was greater than the source-receptor distance for the Sarnia sources. Thus, the power-plant plume would have been expected to be more aged, but the results suggest that the power-plants' plumes had a slower conversion of NO to NO_2 perhaps due to higher initial mixing ratios of NO_x (Nunnermacker et al., 2000). Very high NO mixing ratios in a power plant plume (i.e., > 40ppbv) could completely titrate the ambient O_3 in the air entrained into the plume, an observation previously seen in power plant plumes (Brown et al., 2012).

The East-West transect appears to have captured approximately half of the power-plants' plume since the NO_2 VCDs and the NO_2 mixing ratios increase from background to a plateau at a maximum (Figure 5-2a). A preliminary estimation of the NO_x and SO_2 emissions from the power-plants can be determined by scaling up the flux integral from the appropriate section of the East-West transect by a factor of two. While this is highly uncertain, we do this to make a first order estimate of the power plant plumes on the US side of the border. In this case, we have used VCD_{influx} = 2-3×10^{15} molec cm^{-2} for NO_x and zero for SO_2 since the background region SO_2 DSCDs were at or below detection limits. The NO_x estimate used individual NO_x/NO_2 ratios because the NO_x/NO_2 ratio was significantly higher in the plume than outside the plume. This illustrates the importance of in-situ instruments of NO_x/NO_2, especially when close to the source where plume NO_x/NO_2 ratios can be variable (Valin et al., 2013).

Given the above assumptions, a tentative first order estimate of the total emissions from the power plants are 0.31-0.46 tonnes NO_x hr^{-1} and 0.77 tonnes SO_2 hr^{-1}, respectively. The hourly emissions of the power-plants from reported 2015 annual values are 0.74 tonnes NO_x hr^{-1} and 2.56 tonnes SO_2 hr^{-1} (United States EPA, 2018). Our hourly estimates are only preliminary since only half of the plume (approximately) was captured by the measurement transect.

The NO_x emission estimates from Sarnia from Day 1 are consistent within 25% and are consistent with the Day 2 estimates within the calculated error of approximately ±45% (Figure 5-8, Table 5-4). Some variability between the emission estimates is expected due to wind-data uncertainties, NO_x/NO_2 vertical profile variability, errors introduced by using a constant VCD_{influx} and NO_x lifetime, and temporal variations in emissions from the source.

Conversion of the hourly measured emissions to annual emissions would require knowledge and application of daily, weekly and seasonal emission profiles, which is beyond the scope of this work. The Mobile-MAX-DOAS emission estimates are reported in units of tonnes per hour since routes were completed within <40 minutes. Events such as flaring can significantly increase the instantaneous emission rate but are excluded from the annual emission inventory data. However, there was no reported flaring during the measurement period (MOECC 2017; personal communication). NO_x emissions from petrochemical facilities, excluding flaring, typically have low variability during periods of continuous operation. According to Ryerson et al. (2003), variation in average hourly NO_x emissions from a petrochemical facility reported by industry (CEMS data) was <10% from an average of the hourly average emissions over 11 days in Houston, Texas. However, this trend may be different for the chemical industry. A first-order comparison to the 2017 National Pollution Release Inventory (NPRI) values (downscaled by assuming constant emissions) was made to determine whether our measured Sarnia emissions are reasonable. The NPRI value is the sum of the NO_x emissions from the top nine industrial emitters of NO_x in Sarnia whose emissions would have been captured along the driving routes. The NPRI requires significant point source industry facilities to report their pollutant emissions, but the method of estimating emissions can vary by facility (ECCC, 2015). The NPRI emission value does not include mobile and area sources from the Sarnia region. Thus, the NPRI emission inventory values for Sarnia would be expected to be smaller than our measured emissions because of this exclusion. The measured NO_x emissions are larger than the 2017 NPRI value but not statistically so (Figure 5-8; Table 5-4). The exception is the Day 1 route 1* value, which is statistically higher. The average of the four NO_x emission estimates from Sarnia is greater than the

2017 NPRI value. These results demonstrate that our measured emission rates are reasonable. Future Mobile-MAX-DOAS studies could focus on determining diurnal trends in emissions by driving multiple routes at as many times of the day as possible on multiple days, seasons and weekdays/weekends. Measurements of vertical wind profiles could reduce emission uncertainty to allow identification of temporal trends by comparing same-day measurements.

Table 5-5 Average emission estimates from Mobile MAX_DOAS using 10 m wind-speeds and from NPRI.

	Gas	Lower Limit Emission Estimate (tonnes hr^{-1})	2017 NPRI Value (tonnes hr^{-1})
Sarnia	NO_x	1.60±0.34	0.9
Sarnia	SO_2	1.81±0.83	1.85
NOVA Chemicals-Corunna Site	NO_x	0.28±0.06	0.14

Figure 5-9 SO_2 VCDs along route for emission estimate (Day 1 Route 3).

Apart from NO_x, we were also able to estimate SO_2 emissions from the Sarnia urban/industrial region during one route when the SO_2 DSCDs were detectable, Day 1 route 3 (Table 5-5). Our SO_2 emission estimate using the 10 m wind-speed is consistent within error with the 2017 NPRI value (Table 5-5). We expect our SO_2 emission estimate to be closer to the NPRI values compared to the NO_x estimates because SO_2 emissions from area and mobile sources in Sarnia are expected to be small relative to industrial sources (Ministry of the Environment and Climate Change, 2016). Since ships were not operating in the St. Clair River at this time of year, shipping emissions of SO_2 were absent. Thus, SO_2 plumes in this region are localized to the major industrial emissions sources. Therefore, the VCDs from the areas

unaffected by the Sarnia plumes are representative of background values, VCD_{influx}. While the Mobile-MAX-DOAS was able to capture these plumes (Figure 5-9), only 1 of 7 local monitoring stations (LaSalle Road, Figure D1) observed elevated levels of SO_2 during this period. The under-sampling by stations is due to the highly localized nature of the SO_2 plumes that are from stacks where the plume is frequently elevated above the surface. These results illustrate the complementary nature of Mobile-MAX-DOAS and in-situ measurements and the importance of monitoring techniques that can capture localized plumes independent of the wind direction.

5.3.4.2 Emission Estimates of NOVA Chemicals Industrial Facility

NO_x emissions were opportunistically measured from a single facility on Day 3 because the southerly wind-directions isolated this plume (ECCC, 2018e) from other industrial sources in Sarnia. The plume originated from Nova Chemicals, the 2nd highest emitter of NO_x in the region in 2017. These conditions allowed us to test the mobile-MAX-DOAS method in isolating a single plume. The wind-direction on Day 3 indicated that the air-masses originated from rural areas south of Sarnia and the VCD_{influx} was expected to be low, ~ 1×10^{15} molec cm^{-2}.

The emission estimates of NO_x from the two routes on Day 3 from the NOVA Chemicals industrial site (Table 5-4Table 5-5) are consistent with each other within 10%. The consistency increases confidence in fitting the spectra in each transect against a local FRS and removing influx using the average "background" VCDs rather than using the "$DSCD_{Offset}$" method in this case. The use of "background" VCDs is appropriate because vehicular traffic upwind of the measurement transect is minimal in the local area. Upwind emissions were unlikely to have contributed significantly to the total measured emissions. The emission estimates from NOVA Chemicals are larger than the 2017 NPRI value (Table 5-4Table 5-5). This comparison merely indicates that the Mobile-MAX-DOAS values are reasonable given that there was likely diurnal variability and the measurements were taken only during a single hour on a single day.

5.3.5 Comparison of OMI Satellite and MAX-DOAS VCDs

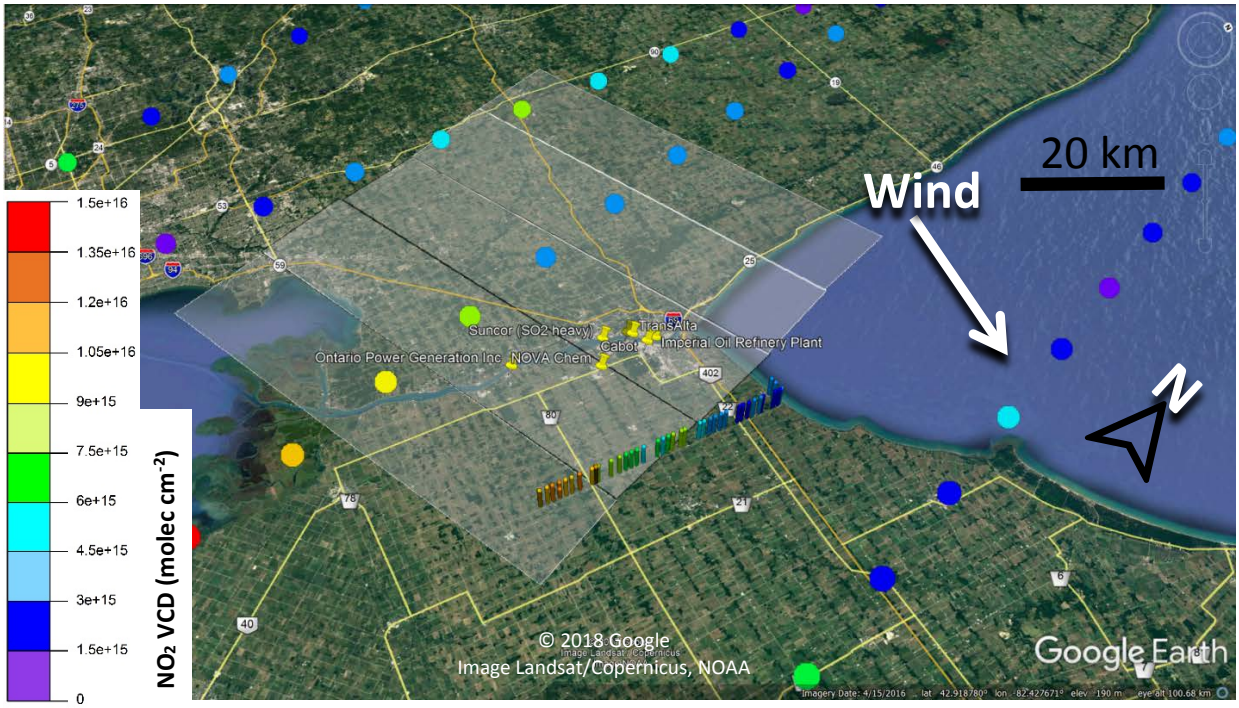

Figure 5-10 Day 1 NO_2 VCDs from OMI satellite VCDs and mobile-MAX-DOAS Route 4. OMI satellite pixels closest to Sarnia were measured at ~18:00 local time. Semi-opaque rectangles centered on the coloured dots (indicating satellite VCD value) indicate the spatial extent of the pixel.

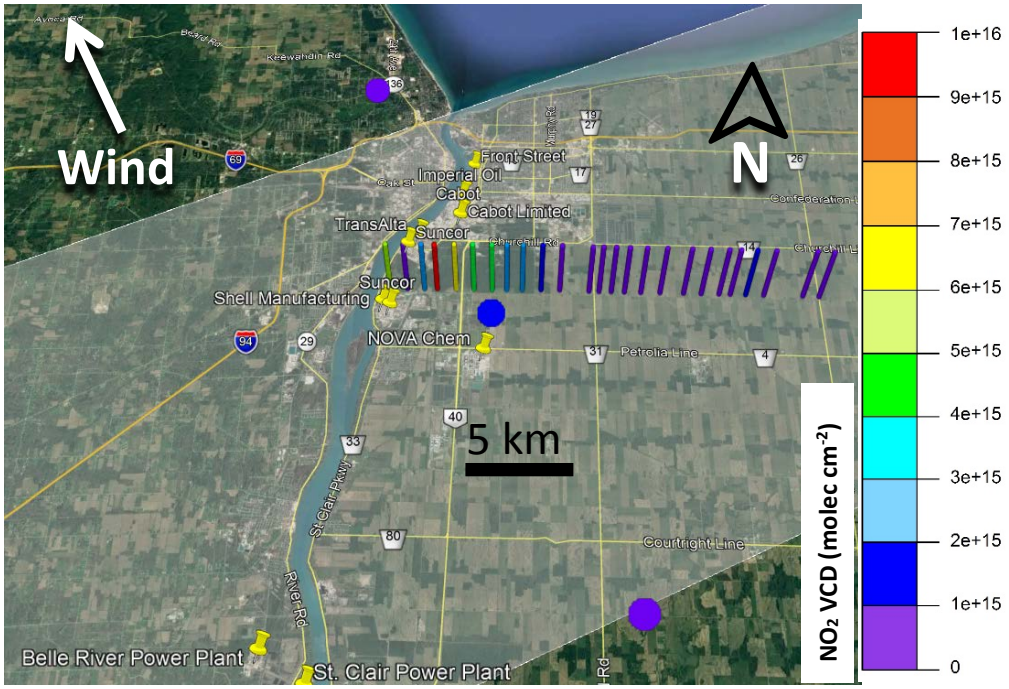

Figure 5-11 Day 3 NO_2 VCDs from OMI satellite and mobile-MAX-DOAS Route 1. OMI pixels shown were measured at ~18:00 local time. Semi-opaque rectangle centered on the coloured dots indicates the spatial extent of the pixel.

The satellite and MAX-DOAS NO_2 VCDs on Day 1 exhibit similar spatial trends in the simple sense that NO_2 VCDs increase towards the south from the background regions north of Sarnia (Fig. 10). This trend is probably due to a combination of emissions from U.S.A. power-plants, the Detroit area as well as Sarnia. The NO_2 VCD of the pixel containing the majority of the Sarnia industrial facilities is comparable to rural area VCDs to the north-west of Sarnia. Only $1/8^{th}$ of the "Sarnia" pixel's footprint region is likely to be impacted by Sarnia emissions, and the remainder observes mostly rural to semi-rural regions. The OMI Pixel from Day 3 (Fig. 11) containing Sarnia exhibits a minimal increase in NO_2 VCD ($1\text{-}2\times10^{15}$ molec cm^{-2}) compared to the surrounding background regions (Fig. 11). In contrast, the Mobile-MAX-DOAS measurements observed VCD enhancements of up to 1×10^{16} molec cm^{-2} within this pixel. The averaging due by the large pixel size (24 km×84 km) causes underestimation of the maximum VCDs. Identification of Sarnia-only emissions without error due to horizontal averaging or inclusion of other sources may require satellite measurements with nadir-viewing pixels centered on Sarnia and/or extremely large averaging times.

5.3.6 Uncertainties in this Study and Recommended Improvements for Mobile-MAX-DOAS Measurements

Many of the factors that increased the uncertainty in the emission values in this study can be significantly reduced in future through relatively small changes in the method. The many factors have been addressed in Appendix D (section 7) and summarized in Table D9. Ideally, accurate horizontal flux measurements would require knowledge of the vertical and horizontal profile of pollutant concentrations as well as the vertical and horizontal profile of wind vectors. Lack of knowledge of the vertical profile of wind-speed increases uncertainty in Mobile-MAX-DOAS emission estimates since elevated plumes and well-mixed plumes are transported by winds with typically higher speeds than those near the surface. Future studies could focus on reducing uncertainty by using measurements from sodar, lidar, tall towers, balloon soundings, or a radio acoustic meteorological profiler. In this study, uncertainty was increased (18-30% based on sensitivity analysis; see Appendix D Sections 5 & 7) because driving routes could not always include measurements along influx regions (Day 1) due to road proximity to sources or obstructions to the viewing field. Future experiments could measure influx values while stationary at multiple locations along the upwind region chosen for an unobstructed viewing field. Very low background trace-gas levels also resulted in SO_2 DSCDs that were below detection limit most of the time, while being occasionally below detection limit for NO_2 (Figure 5-2e). A spectrometer with higher sensitivity giving lower detection limits could solve this issue. Increased averaging of spectra would also improve detectability but at the expense of worse spatial resolution, unless measurements can be made at a slower driving speed. Uncertainty in the NO_x lifetime was a small contribution to uncertainty in this study (up to

±12%) because the distances and transport times between source and measurement locations were relatively small (<25 km). The exception was Day 1 route 1 where uncertainty was up to 30% due to low wind-speeds. The error contribution of NO_x lifetime could be non-trivial if driving routes are far from the sources (e.g., large cities). This error could also be non-trivial if the lifetime that one assumes does not account for the multiple factors discussed in Section 5.3.3. Bias in the emission estimates from an incorrect lifetime could be avoided by determining NO_x lifetimes from photochemical modelling or, for large cities, satellite observations (Beirle et al., 2011) but taking into account wind speeds (Valin et al., 2013).

5.4 Conclusions

In this study, we combined Mobile-MAX-DOAS techniques with mobile NO_x measurements and a modular meteorological station to measure emissions of NO_x and SO_2 from the Sarnia region, a relatively small urban/industrial city. Trace-gas VCDs were determined using the $DSCD_{offset}$ method (Wagner et al., 2010) or by fitting measured spectra against a route-local low pollution spectrum. Both methods provided good results, which suggest that the first method is ideal if there are many hours of measurements while the second method is ideal when short routes contain low-pollution regions. Average lower limit Mobile-MAX-DOAS emissions of NO_x from Sarnia were measured to be 1.60 ± 0.34 tonnes hr^{-1} using 10 m elevation measured wind-speeds. The estimates were larger than the downscaled 2017 NPRI reported industrial emissions of 0.9 tonnes hr^{-1} (ECCC, 2018e) but the NPRI estimate excludes area and mobile emissions. Our lower limit SO_2 emission measurement for Sarnia was 1.81 ± 0.83 tonnes hr^{-1} using 10 m wind-speeds, which is equal within uncertainty to the 2017 NPRI value of 1.85 tonnes hr^{-1} (ECCC, 2018f). Our average lower limit NO_x emission measurement from the NOVA Chemicals Facility was 0.28 ± 0.06 tonnes hr^{-1}, the same order of magnitude as the 2016 NPRI value of 0.14 tonnes hr^{-1} (ECCC, 2018d).

Simultaneous measurements of NO-NO_2-NO_x improved the accuracy of NO_x emission estimates when plumes of varying ages were observed. The NO_x results from Days 1 and 2 suggest that accurate Mobile-MAX-DOAS NO_x emission measurements from routes that observe plumes with differing ages require accurate knowledge of the localized NO_x/NO_2 ratio.

The variability in the ratio of the NO_2 VCDs and mixing ratios indicates that surface NO_2 mixing ratios cannot be reliably estimated from NO_2 VCDs and boundary layer height alone when pollution is emitted from sources of varying heights and chemical composition. A NO_x-analyzer can be an essential component of Mobile-MAX-DOAS NO_2

measurements. The addition of this instrument allows the method to characterize the boundary layer fully and accurately estimate NO_x emissions from NO_2 measurements when multiple NO_x sources are present and when transects are sufficiently distant from the sources.

The modular meteorological station improved knowledge of local wind essential to identify time periods of low temporal variability, ensuring low error due to wind estimation. These time periods would have been difficult to identify with only hourly average or modelled wind data. Accurate knowledge of the vertical wind profile would significantly enhance the accuracy of the Mobile-MAX-DOAS emission estimates. Future studies could obtain vertical wind profiles using sodar, lidar, wind-rass, and radiosonde on a weather balloon or local aircraft soundings.

Mobile-MAX-DOAS measurements identified significant OMI intrapixel inhomogeneity and observed industrial pollution enhancements that were poorly captured by the in-situ ground stations. These results suggest that Mobile-MAX-DOAS has clear advantages in similar industrial regions over other remote sensing techniques used for estimating emissions (e.g., using aircraft or satellite): higher spatial resolution, the potential for multiple emission estimates per day (i.e., observations of diurnal trends), and much lower operational costs. Mobile-MAX-DOAS is a "top-down" low-cost solution for validating bottom-up inventories that compliments in-situ monitoring and has significant utility in smaller regions with significant emissions where satellite applications are limited. Future Mobile-MAX-DOAS studies in such regions can focus on measuring temporal trends in emissions.

5.5 Acknowledgements

This study was completed with collaborative support by the Ontario Ministry of the Environment and Climate Change. Funding for the study was provided by NSERC, CREATE IACPES and the York University Faculty of Graduate Studies. The corresponding author would like to thank Mr. Barry Duffey at the Ontario Ministry of Environment and Climate Change for his support at the project start. We also thank Tony Munoz of OME for his continued support of our research.

5.6 References

Alicke, B., Platt, U., and Stutz, J.: Impact of nitrous acid photolysis on the total hydroxyl radical budget during the limitation of oxidant production/Pianura Padana Produzione di Ozono study in Milan, J. Geophys. Res., 107(D22), 8196,doi:10.1029/2000JD000075, 2002.

Baray, S., Darlington, A., Gordon, M., Hayden, K. L., Leithead, A., Li, S.-M., Liu, P. S. K., Mittermeier, R. L., Moussa, S. G., O'Brien, J., Staebler, R., Wolde, M., Worthy, D. and McLaren, R.: Quantification of methane sources in the Athabasca Oil Sands Region of Alberta by aircraft mass balance, Atmospheric Chem. Phys., 18(10), 7361–7378, doi:10.5194/acp-18-7361-2018, 2018.

Beirle, S., Boersma, K. F., Platt, U., Lawrence, M. G. and Wagner, T.: Megacity Emissions and Lifetimes of Nitrogen Oxides Probed from Space, Science, 333(6050), 1737–1739, doi:10.1126/science.1207824, 2011.

Boersma, K. F., Eskes, H. J., Veefkind, J. P., Brinksma, E. J., Van der A, R. J., Sneep, M., van den Oord, G. H. J., Levelt, P. F., Stammes, P., Gleason, J. F. and Bucsela, E. J.: Near-real time retrieval of tropospheric NO2 from OMI, Atmospheric Chem. Phys., 7(8), 2103–2118, 2007.

Bogumil, K., Orphal, J., Homann, T., Voigt, S., Spietz, P., Fleischmann, O. C., Vogel, A., Hartmann, M., Kromminga, H., Bovensmann, H., Frerick, J. and Burrows, J. P.: Measurements of molecular absorption spectra with the SCIAMACHY pre-flight model: instrument characterization and reference data for atmospheric remote-sensing in the 230-2380 nm region, J. Photochem. Photobiol. -Chem., 157(2–3), 167–184, doi:10.1016/S1010-6030(03)00062-5, 2003.

Brinksma, E. J., Pinardi, G., Volten, H., Braak, R., Richter, A., Schoenhardt, A., van Roozendael, M., Fayt, C., Hermans, C., Dirksen, R. J., Vlemmix, T., Berkhout, A. J. C., Swart, D. P. J., Oetjen, H., Wittrock, F., Wagner, T., Ibrahim, O. W., de Leeuw, G., Moerman, M., Curier, R. L., Celarier, E. A., Cede, A., Knap, W. H., Veefkind, J. P., Eskes, H. J., Allaart, M., Rothe, R., Piters, A. J. M. and Levelt, P. F.: The 2005 and 2006 DANDELIONS NO2 and aerosol intercomparison campaigns, J. Geophys. Res.-Atmospheres, 113(D16), D16S46, doi:10.1029/2007JD008808, 2008.

Brown, S. S., Dube, W. P., Karamchandani, P., Yarwood, G., Peischl, J., Ryerson, T. B., Neuman, J. A., Nowak, J. B., Holloway, J. S., Washenfelder, R. A., Brock, C. A., Frost, G. J., Trainer, M., Parrish, D. D., Fehsenfeld, F. C. and Ravishankara, A. R.: Effects of NOx control and plume mixing on nighttime chemical processing of plumes from coal-fired power plants, J. Geophys. Res.-Atmospheres, 117, D07304, doi:10.1029/2011JD016954, 2012.

Dragomir, C. M., Constantin, D.-E., Voiculescu, M., Georgescu, L. P., Merlaud, A. and Van Roozendael, M.: Modeling results of atmospheric dispersion of NO2 in an urban area using METI-LIS and comparison with coincident mobile DOAS measurements, ATMOSPHERIC Pollut. Res., 6(3), 503–510, doi:10.5094/APR.2015.056, 2015.

ECCC: Using and interpreting data from the National Pollutant Release Inventory, aem [online] Available from: https://www.canada.ca/en/environment-climate-change/services/national-pollutant-release-inventory/using-interpreting-data.html (Accessed 1 August 2018), 2015.

ECCC: NPRI Data Search - Facility and Substance Information - NOVA Chemicals (Canada) Ltd. - Corunna Site 2017, [online] Available from: https://pollution-waste.canada.ca/national-release-inventory/archives/index.cfm?do=facility_substance_summary&lang=en&opt_npri_id=0000001776&opt_report_year=2017 (Accessed 17 September 2018a), 2018.

ECCC: NPRI Data Search - Facility Search Results Nitrogen oxides (expressed as NO2) (11104-93-1), [online] Available from: https://pollution-waste.canada.ca/national-release-inventory/archives/index.cfm?do=results&process=true&lang=en&opt_report_year=2017&opt_facility_name=&opt_npri_id=&opt_cas_name=11104-93-1&opt_cas_num=&opt_province=&opt_postal_code=&opt_urban_center=&opt_province_comm=&opt_naics6=&opt_naics3=&opt_naics4=&opt_nai6code=&opt_csic=&opt_media=all&submit=Submit (Accessed 17 September 2018b), 2018.

ECCC: NPRI Data Search - Facility Search Results Sulphur Dioxide (7446-09-5), [online] Available from: https://pollution-waste.canada.ca/national-release-inventory/archives/index.cfm?do=results&process=true&lang=en&opt_report_year=2017&opt_facility_name=&opt_npri_id=&opt_cas_name=7446-09-5&opt_cas_num=&opt_province=&opt_postal_code=&opt_urban_center=&opt_province_comm=&opt_naics6=&opt_naics3=&opt_naics4=&opt_nai6code=&opt_csic=&opt_media=all&submit=Submit (Accessed 17 September 2018c), 2018.

ECCC: NPRI Facility Search Results - Volatile Organic Compounds (VOCs) (NA-M16), [online] Available from: https://pollution-waste.canada.ca/national-release-inventory/archives/index.cfm?do=results&process=true&lang=en&opt_report_year=2017&opt_facility_name=&opt_npri_id=&opt_cas_name=NA+-+M16&opt_cas_num=&opt_province=&opt_postal_code=&opt_urban_center=&opt_province_comm=&opt_naics6=&opt_naics3=&opt_naics4=&opt_nai6code=&opt_csic=&opt_media=all&submit=Submit (Accessed 17 September 2018d), 2018.

Frieß, U., Monks, P. S., Remedios, J. J., Rozanov, A., Sinreich, R., Wagner, T. and Platt, U.: MAX-DOAS O4 measurements: A new technique to derive information on atmospheric aerosols: 2. Modeling studies, J. Geophys. Res.-Atmospheres, 111(D14), D14203, doi:10.1029/2005JD006618, 2006.

Gordon, M., Li, S.-M., Staebler, R., Darlington, A., Hayden, K., O'Brien, J. and Wolde, M.: Determining air pollutant emission rates based on mass balance using airborne measurement data over the Alberta oil sands operations, ATMOSPHERIC Meas. Tech., 8(9), 3745–3765, doi:10.5194/amt-8-3745-2015, 2015.

Halla, J. D., Wagner, T., Beirle, S., Brook, J. R., Hayden, K. L., O'Brien, J. M., Ng, A., Majonis, D., Wenig, M. O. and McLaren, R.: Determination of tropospheric vertical columns of NO2 and aerosol optical properties in a rural setting using MAX-DOAS, ATMOSPHERIC Chem. Phys., 11(23), 12475–12498, doi:10.5194/acp-11-12475-2011, 2011.

Heckel, A., Richter, A., Tarsu, T., Wittrock, F., Hak, C., Pundt, I., Junkermann, W. and Burrows, J. P.: MAX-DOAS measurements of formaldehyde in the Po-Valley, Atmospheric Chem. Phys., 5, 909–918, doi:10.5194/acp-5-909-2005, 2005.

Heckel, A., Kim, S.-W., Frost, G. J., Richter, A., Trainer, M. and Burrows, J. P.: Influence of low spatial resolution a priori data on tropospheric NO2 satellite retrievals, Atmos Meas Tech, 4(9), 1805–1820, doi:10.5194/amt-4-1805-2011, 2011.

Honninger, G. and Platt, U.: Observations of BrO and its vertical distribution during surface ozone depletion at Alert, Atmos. Environ., 36(15–16), 2481–2489, doi:10.1016/S1352-2310(02)00104-8, 2002.

Honninger, G., von Friedeburg, C. and Platt, U.: Multi axis differential optical absorption spectroscopy (MAX-DOAS), ATMOSPHERIC Chem. Phys., 4, 231–254, 2004.

Huang, M., Bowman, K. W., Carmichael, G. R., Chai, T., Pierce, R. B., Worden, J. R., Luo, M., Pollack, I. B., Ryerson, T. B., Nowak, J. B., Neuman, J. A., Roberts, J. M., Atlas, E. L. and Blake, D. R.: Changes in nitrogen oxides emissions in California during 2005-2010 indicated from top-down and bottom-up emission estimates, J. Geophys. Res.-ATMOSPHERES, 119(22), 12928–12952, doi:10.1002/2014JD022268, 2014.

Ialongo, I., Hakkarainen, J., Hyttinen, N., Jalkanen, J.-P., Johansson, L., Boersma, K. F., Krotkov, N. and Tamminen, J.: Characterization of OMI tropospheric NO2 over the Baltic Sea region, Atmos Chem Phys, 14(15), 7795–7805, doi:10.5194/acp-14-7795-2014, 2014.

Ialongo, I., Herman, J., Krotkov, N., Lamsal, L., Boersma, K. F., Hovila, J. and Tamminen, J.: Comparison of OMI NO2 observations and their seasonal and weekly cycles with ground-based measurements in Helsinki, Atmospheric Meas. Tech., 9(10), 5203–5212, doi:10.5194/amt-9-5203-2016, 2016.

Ibrahim, O., Shaiganfar, R., Sinreich, R., Stein, T., Platt, U. and Wagner, T.: Car MAX-DOAS measurements around entire cities: quantification of NOx emissions from the cities of Mannheim and Ludwigshafen (Germany), ATMOSPHERIC Meas. Tech., 3(3), 709–721, doi:10.5194/amt-3-709-2010, 2010.

Irie, H., Kanaya, Y., Akimoto, H., Iwabuchi, H., Shimizu, A. and Aoki, K.: First retrieval of tropospheric aerosol profiles using MAX-DOAS and comparison with lidar and sky radiometer measurements, Atmospheric Chem. Phys., 8(2), 341–350, doi:10.5194/acp-8-341-2008, 2008.

Kim, N. K., Kim, Y. P., Morino, Y., Kurokawa, J. and Ohara, T.: Verification of NOx emission inventories over North Korea, Environ. Pollut., 195, 236–244, doi:10.1016/j.envpol.2014.06.034, 2014.

Leighton, P. A.: Photochemistry of air pollution. --, Academic Press, New York., 1961.

Liu, F., Beirle, S., Zhang, Q., Doerner, S., He, K. and Wagner, T.: NOx lifetimes and emissions of cities and power plants in polluted background estimated by satellite observations, Atmospheric Chem. Phys., 16(8), 5283–5298, doi:10.5194/acp-16-5283-2016, 2016.

McLinden, C. A., Fioletov, V., Boersma, K. F., Krotkov, N., Sioris, C. E., Veefkind, J. P. and Yang, K.: Air quality over the Canadian oil sands: A first assessment using satellite observations, Geophys. Res. Lett., 39, L04804, doi:10.1029/2011GL050273, 2012.

Ministry of the Environment and Climate Change: Air Quality in Ontario 2014 Report, [online] Available from: http://www.airqualityontario.com/downloads/AirQualityInOntarioReportAndAppendix2014.pdf (Accessed 25 August 2016), 2015.

Ministry of the Environment and Climate Change: Air Quality in Ontario 2016 Report., 2016.

Nunnermacker, L. J., Kleinman, L. I., Imre, D., Daum, P. H., Lee, Y.-N., Lee, J. H., Springston, S. R., Newman, L. and Gillani, N.: NO y lifetimes and O3 production efficiencies in urban and power plant plumes: Analysis of field data, J. Geophys. Res. Atmospheres, 105(D7), 9165–9176, doi:10.1029/1999JD900753, 2000.

Oiamo, T. H., Luginaah, I. N., Atari, D. O. and Gorey, K. M.: Air pollution and general practitioner access and utilization: a population based study in Sarnia, `Chemical Valley,' Ontario, Environ. Health, 10, doi:10.1186/1476-069X-10-71, 2011.

Platt, U., Perner, D. and Patz, H.: Simultaneous Measurement of Atmospheric CH2O, O3, and NO2 by Differential Optical-Absorption, J. Geophys. Res.-Oceans Atmospheres, 84(NC10), 6329–6335, doi:10.1029/JC084iC10p06329, 1979.

Platt, U., Stutz, J., Springer E-books - York University and SpringerLink (Online service): Differential optical absorption spectroscopy: principles and applications, Springer Verlag, Berlin. [online] Available from: http://www.library.yorku.ca/eresolver/?id=1261530, 2008.

Ryerson, T. B., Trainer, M., Angevine, W. M., Brock, C. A., Dissly, R. W., Fehsenfeld, F. C., Frost, G. J., Goldan, P. D., Holloway, J. S., Hubler, G., Jakoubek, R. O., Kuster, W. C., Neuman, J. A., Nicks, D. K., Parrish, D. D., Roberts, J. M., Sueper, D. T., Atlas, E. L., Donnelly, S. G., Flocke, F., Fried, A., Potter, W. T., Schauffler, S., Stroud, V., Weinheimer, A. J., Wert, B. P., Wiedinmyer, C., Alvarez, R. J., Banta, R. M., Darby, L. S. and Senff, C. J.: Effect of petrochemical industrial emissions of reactive alkenes and NOx on tropospheric ozone formation in Houston, Texas, J. Geophys. Res.-Atmospheres, 108(D8), 4249, doi:10.1029/2002JD003070, 2003.

Shabbir, Y., Khokhar, M. F., Shaiganfar, R. and Wagner, T.: Spatial variance and assessment of nitrogen dioxide pollution in major cities of Pakistan along N5-Highway, J. Environ. Sci., 43(Supplement C), 4–14, doi:10.1016/j.jes.2015.04.038, 2016.

Shaiganfar, R., Beirle, S., Sharma, M., Chauhan, A., Singh, R. P. and Wagner, T.: Estimation of NOx emissions from Delhi using Car MAX-DOAS observations and comparison with OMI satellite data, ATMOSPHERIC Chem. Phys., 11(21), 10871–10887, doi:10.5194/acp-11-10871-2011, 2011.

Shaiganfar, R., Beirle, S., Petetin, H., Zhang, Q., Beekmann, M. and Wagner, T.: New concepts for the comparison of tropospheric NO2 column densities derived from car-MAX-DOAS observations, OMI satellite observations and the regional model CHIMERE during two MEGAPOLI campaigns in Paris 2009/10, ATMOSPHERIC Meas. Tech., 8(7), 2827–2852, doi:10.5194/amt-8-2827-2015, 2015.

Shaiganfar, R., Beirle, S., van der Gon, H. D., Jonkers, S., Kuenen, J., Petetin, H., Zhang, Q., Beekmann, M. and Wagner, T.: Estimation of the Paris NOx emissions from mobile MAX-DOAS observations and CHIMERE model simulations during the MEGAPOLI campaign using the closed integral method, Atmospheric Chem. Phys., 17(12), 7853–7890, doi:10.5194/acp-17-7853-2017, 2017.

Tokarek, T. W., Odame-Ankrah, C. A., Huo, J. A., McLaren, R., Lee, A. K. Y., Adam, M. G., Willis, M. D., Abbatt, J. P. D., Mihele, C., Darlington, A., Mittermeier, R. L., Strawbridge, K., Hayden, K. L., Olfert, J. S., Schnitzler, E. G., Brownsey, D. K., Assad, F. V., Wentworth, G. R., Tevlin, A. G., Worthy, D. E. J., Li, S.-M., Liggio, J., Brook, J. R. and Osthoff, H. D.: Principal component analysis of summertime ground site measurements in the Athabasca oil sands: Sources of IVOCs, Atmos Chem Phys Discuss, 2018, 1–53, doi:10.5194/acp-2017-1026, 2018.

United States EPA: Air Pollutant Report | ECHO | US EPA, Air Pollut. Rep. [online] Available from: https://echo.epa.gov/air-pollutant-report?fid=110000404740 (Accessed 2 August 2018), 2018.

Valin, L. C., Russell, A. R. and Cohen, R. C.: Variations of OH radical in an urban plume inferred from NO2 column measurements, Geophys. Res. Lett., 40(9), 1856–1860, doi:10.1002/grl.50267, 2013.

Wagner, T., Dix, B., von Friedeburg, C., Frieß, U., Sanghavi, S., Sinreich, R. and Platt, U.: MAX-DOAS O-4 measurements: A new technique to derive information on atmospheric aerosols - Principles and information content, J. Geophys. Res.-Atmospheres, 109(D22), D22205, doi:10.1029/2004JD004904, 2004.

Wagner, T., Ibrahim, O., Shaiganfar, R. and Platt, U.: Mobile MAX-DOAS observations of tropospheric trace gases, ATMOSPHERIC Meas. Tech., 3(1), 129–140, 2010.

Wagner, T., Beirle, S., Brauers, T., Deutschmann, T., Frieß, U., Hak, C., Halla, J. D., Heue, K. P., Junkermann, W., Li, X., Platt, U. and Pundt-Gruber, I.: Inversion of tropospheric profiles of aerosol extinction and HCHO and NO2 mixing ratios from MAX-DOAS observations in Milano during the summer of 2003 and comparison with independent data sets, Atmospheric Meas. Tech., 4(12), 2685–2715, doi:10.5194/amt-4-2685-2011, 2011.

Wiegand, A. N. and Bofinger, N. D.: Review of empirical methods for the calculation of the diurnal NO2 photolysis rate coefficient, Atmos. Environ., 34(1), 99–108, doi:10.1016/S1352-2310(99)00294-0, 2000.

Wu, F., Li, A., Xie, P., Chen, H., Hu, Z., Zhang, Q., Liu, J. and Liu, W.: Emission Flux Measurement Error with a Mobile DOAS System and Application to NOx Flux Observations, Sensors, 17(2), doi:10.3390/s17020231, 2017.

Chapter 6
Conclusions and Future Directions

This research was conducted to explore the performance of MAX-DOAS techniques to determine their strengths and limitations in monitoring air quality in urban and industrial environments. A second objective was to determine how MAX-DOAS techniques could be applicable in addressing air quality problems in regions where typical monitoring methods are limited. Four separate studies were conducted.

The first study (Chapter 2) identified strengths and limitations of the MAX-DOAS method, retrievals of dSCDs and optimal estimation of aerosol extinction, NO_2, and SO_2 through comparison with data from other instruments under varying pollutant loading conditions in the Athabasca Oil Sands Region. Data from MAX-DOAS measurements collected at a field site north of two major sources of industrial pollution were compared to retrievals from lidar, AERONET and Pandora sun photometers, active-DOAS, and in-situ instruments. Parameters were identified that are important for useful inter-comparisons of MAX-DOAS data with lidar and sun photometer aerosol data. Inter-comparison of MAX-DOAS and sun photometer AODs must account for the greater vertical extent of the atmosphere observed by the sun photometer. Accurate knowledge of S-ratio values is required to derive accurate vertical profiles of aerosol extinction from lidar measurements when atmospheric particles varied, vertically or temporally. MAX-DOAS and lidar profiles of aerosol extinction smoothed using the MAX-DOAS vertical sensitivity showed good agreement when the lidar S-ratio was consistent with values modelled using particle measurements and Mie scattering theory. In general, inter-comparisons indicated that the MAX-DOAS retrievals of aerosol extinction and trace-gases performed well under conditions of relatively constant atmospheric profiles during the retrieval time window.

The results show that the strengths of the MAX-DOAS technique include the ability to simultaneously derive tropospheric column values and vertical profiles of aerosol extinction and trace-gases from one measurement. In contrast, sun photometer measurements provide only total atmospheric column values, and lidar measurements yield vertical profiles of aerosol extinction, but no NO_2 or SO_2 information. Also, the MAX-DOAS tropospheric retrievals are achieved without requiring additional atmospheric knowledge such as the stratospheric column component (e.g., Pandora sun photometer) or particle characteristics of the vertical profile (e.g., lidar S-ratio). A great asset of the MAX-DOAS technique is the ability to observe elevated enhancements of trace-gases undetected by ground-based techniques (e.g., Active-DOAS). A limitation of the MAX-DOAS technique, identified by comparison with lidar profiles of aerosol extinction, is that the retrievals tend to "smooth" the atmospheric profiles towards the ground due to the vertical sensitivity of the MAX-DOAS. Therefore, while the MAX-DOAS retrievals provide information about the vertical profile, the profile shape must be interpreted carefully. Due to the limited vertical resolution of and smoothing by the MAX-DOAS retrievals, accurate measurement of surface mixing ratios still require ground-based instruments under conditions of complex vertical profiles of pollutants.

Fitting SO_2 dSCDs from solar measurements is challenging due to the low actinic intensity at wavelengths where SO_2 absorption features are strong, stray light impacts, and interference by O_3 absorption features. However, an optimal method for fitting SO_2 dSCDs from MAX-DOAS measurements has yet to be developed. In study two (Chapter 3), investigations of fitting SO_2 dSCDs from MAX-DOAS measurements were conducted. Optimal fit settings were determined using measurements of calibration cells with lower and higher SCDs of SO_2 inserted into

the light path at multiple viewing elevation angles, with and without a short-pass filter. The measured spectra were fit with various fitting windows with the offset function enabled or disabled.

The fitted SO_2 dSCDs could vary by up to 100% of the expected value depending on the SO_2 mixing ratio, the fitting window wavelengths, spectral collection method (e.g., use of short-pass filter), and fit settings (i.e., mathematical correction for stray light). Spectra measured at elevation angles close to horizon pointing exhibited SO_2 dSCDs of lower accuracy compared to higher angles for the same fitting windows due to lower UV signal. The SO_2 dSCDs were least accurate for fitting windows with lower limits (λ_{low}) <307 nm due to the effect of stray light and low actinic signal. Retrieved SO_2 dSCDs tended to under-estimate the true value in these regions from the high concentration measurements but over-estimated from the low concentration measurements, indicating that errors exhibited an inconsistent bias. The accuracy of the SO_2 dSCD decreased for fitting windows with λ_{low} >312 nm due to weaker SO_2 absorption features. For spectra measured without a short-pass filter and with the offset function disabled, the SO_2 dSCDs exhibited an inverse dependence on the SO_2 absorption features, and the fit uncertainties were significantly less than the fit error for many windows. The addition of the short-pass filter or the offset function increased the accuracy of the SO_2 dSCDs, and decreased dependency on λ_{low} and the difference between the fit uncertainty and fit error for most windows.

Recommendations for the optimal fitting of SO_2 dSCDs include using a low pass filter with a lower cutoff wavelength as close as possible to the upper limit of the fitting window (i.e., λ_{cutoff} = 340 nm) to prevent error due to stray light. Without a filter or if other species (e.g., NO_2) must be determined in the longer wavelength ranges, a mathematical function such as the offset function should be used to compensate for stray light. A short-pass filter is preferred because it prevents stray light while the offset function attempts to mathematically compensate for stray light by assuming the stray light is proportional to the measured intensity. This study contributes an optimal fitting window of 307.5-319 nm for fitting MAX-DOAS dSCDs SO_2 to maximize the accuracy and consistency of SO_2 measurements in future studies.

A challenge in air quality monitoring is how to effectively monitor air pollution events that have complex 3-D structures in the lower troposphere and evolve relatively quickly, such as lake-breeze circulations (LBC). Traditional techniques such as satellite observations and in-situ or sun photometer instruments are limited by LBCs' spatial and temporal characteristics. In study 3 (Chapter 4), MAX-DOAS observations of NO_2VCDs and AODs simultaneous with in-situ measurements were used to quantify the changes in pollutant loading in the tropospheric column due to lake-breeze events in the urban city of Toronto, Canada.

Short-term enhancements in NO_x mixing ratios observed following the lake-breeze front (LBF) arrival were consistent with previous studies. Observed decreases in O_3 mixing ratios of up to 12 ppbv post-LBF differed with previous summertime studies and were attributed to decreased photochemical activity and more O_3 titration by NO during the late summer to fall study period. The arrival of LBFs was associated with diurnal maximums of NO_2 VCDs and short-term increases above pre-LBF levels of 0.8-3.4×10^{16} molecules cm^{-2}. Increases in both mixing ratios and VCDs of NO_2 indicated that the enhanced pollution at the LBFs was due not only to a decreased boundary

layer height but also to enhanced NO_2 loading behind the LBF. AODs exhibited a small increase concurrent with the NO_2 VCD but continued to increase to peak later than the VCD. The delayed maxima in AOD appears to have been driven by increased humidification within the vertical profile of the LBC rather than only increased particle loading, based on the $PM_{2.5}$ trends. Sun photometer AODs exhibited small increases at the LBF arrival but were sometimes smaller post-LBF because these AODs represent the total atmospheric column. Combining MAX-DOAS measurements with the typically used ground in-situ instruments improved understanding of the 3-D structures of LBCs. This study observed, for the first time, the changes in pollutants in the lower tropospheric column (AODs and NO_2 VCDs) and near the surface (NO-NO_2-NO_x, O_3, $PM_{2.5}$) following the arrival of LBFs on multiple days and identified seasonal differences in LBC impact on tropospheric pollutants. This study illustrates the potential for the stationary MAX-DOAS technique as a low-cost alternative to aircraft measurements to observe the 3-D impacts of meteorological events such as LBCs on tropospheric pollution.

Industrially polluted but geographically small regions pose a technological challenge for effective monitoring of air quality. Ground-level in-situ techniques under-sample localized plumes, the conventional use of aircraft studies can be prohibitively costly, and satellite pixel size is currently too large to capture the scale of the horizontally inhomogeneous pollution in these regions. A final study (Chapter 5) was conducted in the industrial region of Sarnia, Ontario, to advance the Mobile-MAX-DOAS technique and measure emissions of NO_x and SO_2 using concurrent NO-NO_2-NO_x measurements and a modular meteorological station.

Average lower limit emissions of NO_x from Sarnia measured by Mobile-MAX-DOAS were 1.60±0.34 tonnes h^{-1}. The estimate is larger than the downscaled NPRI reported industrial emissions of 0.9 tonnes h^{-1} (ECCC, 2018e), but the NPRI estimate excludes non-industrial emissions. The MAX-DOAS lower limit estimate of SO_2 emissions from Sarnia was 1.81±0.83 tonnes h^{-1}, equal within uncertainty to the NPRI value of 1.85 tonnes h^{-1} (ECCC, 2018f). The average lower limit NO_x emission measurement from the NOVA Chemicals Facility was 0.28±0.06 tonnes h^{-1}, the same order of magnitude as the NPRI value of 0.14 tonnes h^{-1} (ECCC, 2018d). Mobile-MAX-DOAS measurements identified significant inhomogeneity within the OMI satellite pixels and observed industrial pollution enhancements poorly captured by the local network of in-situ monitoring stations.

Two methods were used to determine the trace-gas VCDs used to estimate emissions: 1) the $DSCD_{offset}$ method (Wagner et al., 2010) and 2) fitting measured spectra against a route-local low pollution spectrum. The lower-limit emission estimates of NO_x from Sarnia were consistent within error for the two methods. The results of this study illustrated the Mobile-MAX-DOAS method can estimate emissions when many hours of measurements are possible (method 1) or short routes contain low-pollution regions (method 2). The use of two possible methods increases the flexibility of the technique in terms variable measurement conditions (e.g., number of cloud-free hours in a day). The simultaneous NO_x measurements indicated that accurate NO_x emissions measurements require knowledge of the localized NO_x/NO_2 ratio if routes observe plumes with differing ages. The simultaneous measurements of NO-NO_2-NO_x advanced previous mobile-MAX-DOAS studies by increased the accuracy of the NO_x emissions through better knowledge of NO_x lifetime and variability in the NO_x/NO_2 ratio. The NO_x measurements allowed calculation of Leighton ratios from within transported plumes that indicated peroxy radicals likely disturbed the NO-NO_2-O_3

photostationary state due to VOC oxidation. The modular meteorological station allowed identification of periods of low temporal variability in wind needed to reduce error due to wind estimation. Major conclusions from this study include that the mobile-MAX-DOAS technique has advantages for estimating emissions in small industrial regions compared to conventional techniques (e.g., aircraft, satellite, or in-situ measurements). These advantages include a comparatively high spatial resolution, the potential for measuring emissions multiple times per day (i.e., diurnal trends), and low operational costs. Mobile-MAX-DOAS is a "top-down", low-cost solution for validating "bottom-up" inventories that compliments in-situ monitoring in smaller regions with significant emissions.

These studies illustrate that the MAX-DOAS is capable of capturing industrial pollution enhancements in urban and industrial regions poorly captured by in-situ measurements at the ground or other remote sensing techniques. Significant strengths of MAX-DOAS techniques were highlighted for applications where quantification of aerosol extinction and trace-gases in the lower troposphere is required, especially when elevated pollution profiles are present. In conclusion, the combination of these four studies improved mobile-MAX-DOAS methods for estimating NO_x emission, contributed an optimal method for accuracy fitting MAX-DOAS dSCD of SO_2, and identified additional applications not previously studied.

Future Directions

MAX-DOAS techniques have the potential to contribute to the field of air quality monitoring research when used to study specific polluted regions where traditional techniques are ineffective or too costly. The greatest utility of MAX-DOAS techniques for future studies lies in mobile-MAX-DOAS measurements of pollutant VCDs, emissions, and transboundary fluxes in geographically small areas. As satellite measurements tend towards increasingly better horizontal pixel resolution, MAX-DOAS instruments could be deployed to validate space-based VCDs. Since satellite retrievals of trace-gases depend on modelled a-priori profiles of the gases, which may not resolve small areas, MAX-DOAS could provide important validation for satellite VCDs. These comparisons become especially useful when footprints of satellite pixels become similar to the MAX-DOAS spatial resolution (i.e., a few kilometres). The accuracy of the mobile-MAX-DOAS method for estimating fluxes and emissions could be enhanced in future studies by improving the knowledge of the vertical wind profile. More accurate wind profiles could be obtained through measurements by sodar, lidar, wind-rass, radiosonde on a weather balloon, or local aircraft soundings. A relatively low-cost solution for more accurate local wind measurements is to add a sonic anemometer to the vehicle, such as described in (Belusic et al., 2014), and obtain a vertical wind profile using a balloon deployed in the domain of interest.

Further mobile-MAX-DOAS studies could take advantage of the technique's ability to determine diurnal variability in emissions from area or point sources to validate "bottom-up" emission inventory data. These estimates are essential to ensure industry compliance with air emission standards and to improve atmospheric modelling in areas with complex distributions of pollutants. Simultaneous use of Mobile-MAX-DOAS and near-surface in-situ measurements not only improves emission estimates but also has the broader application of determining pollutant exposure levels in regions where in-situ monitoring stations are often inadequate (e.g., due to industrial plumes).

Specifically, future Mobile-MAX-DOAS studies could focus on determining temporal trends in fluxes of SO_2, NO_x, and formaldehyde (CHCO), an indicator of VOCs, in industrial regions. Mobile-MAX-DOAS studies have the potential to generate maps of pollution exposure, assess trans-boundary pollution fluxes, estimate diurnal trends in emissions, validate satellite VCDs, and validate "bottom-up" inventories in regions where monitoring is challenging.

References

Belusic, D., Lenschow, D. H. and Tapper, N. J.: Performance of a mobile car platform for mean wind and turbulence measurements, Atmospheric Meas. Tech., 7(6), 1825–1837, doi:10.5194/amt-7-1825-2014, 2014.

ECCC: NPRI Data Search - Facility and Substance Information - NOVA Chemicals (Canada) Ltd. - Corunna Site 2017, [online] Available from: https://pollution-waste.canada.ca/national-release-inventory/archives/index.cfm?do=facility_substance_summary&lang=en&opt_npri_id=0000001776&opt_report_year=2017 (Accessed 17 September 2018a), 2018.

ECCC: NPRI Data Search - Facility Search Results Nitrogen oxides (expressed as NO2) (11104-93-1), [online] Available from: https://pollution-waste.canada.ca/national-release-inventory/archives/index.cfm?do=results&process=true&lang=en&opt_report_year=2017&opt_facility_name=&opt_npri_id=&opt_cas_name=11104-93-1&opt_cas_num=&opt_province=&opt_postal_code=&opt_urban_center=&opt_province_comm=&opt_naics6=&opt_naics3=&opt_naics4=&opt_nai6code=&opt_csic=&opt_media=all&submit=Submit (Accessed 17 September 2018b), 2018.

ECCC: NPRI Data Search - Facility Search Results Sulphur Dioxide (7446-09-5), [online] Available from: https://pollution-waste.canada.ca/national-release-inventory/archives/index.cfm?do=results&process=true&lang=en&opt_report_year=2017&opt_facility_name=&opt_npri_id=&opt_cas_name=7446-09-5&opt_cas_num=&opt_province=&opt_postal_code=&opt_urban_center=&opt_province_comm=&opt_naics6=&opt_naics3=&opt_naics4=&opt_nai6code=&opt_csic=&opt_media=all&submit=Submit (Accessed 17 September 2018c), 2018.

Wagner, T., Ibrahim, O., Shaiganfar, R. and Platt, U.: Mobile MAX-DOAS observations of tropospheric trace gases, ATMOSPHERIC Meas. Tech., 3(1), 129–140, 2010.

APPENDIX A: Supplemental to *Validation of MAX-DOAS retrievals of aerosol extinction, SO_2 and NO_2 through comparison with lidar, sun photometer, Active-DOAS and aircraft measurements in the Athabasca Oil Sands Region.*

Section 1 Emissions of NO_2 and SO_2 from AOSR Industrial Facilities

Table A1 Annual Emissions NO_2 in kilotonnes from select facilities.

Facility	NPRI 2013	Off-road vehicle & tail-pipe emissions (Zhang et al., 2018) from 2010	Stack & area sources (Zhang et al., 2018) (2012-2013 period)
Syncrude Mildred Lake Plant	14	8.0	14
Suncor Millennium Plant/Steepbank	8	10.7	11.5
Shell Muskeg River/Jackpine	1.3	7.0	0.7
CNRL Horizon	1.5	5.6	1.8
Imperial Oil Kearl	0.3	1.3	0

Table A2 Annual Emissions SO_2 in kilotonnes from select facilities.

Facility	NPRI 2013	Off-road vehicle & tail-pipe emissions (Zhang et al., 2018) from 2010	Stack & area sources (Zhang et al., 2018) (2012-2013 period)
Syncrude Mildred Lake Plant	63	0.36	77
Suncor Millennium Plant/Steepbank	14	0.06	21
Shell Muskeg River/Jackpine	0	0.13	0
CNRL Horizon	4	0.07	6.5
Imperial Oil Kearl	0	0.03	0

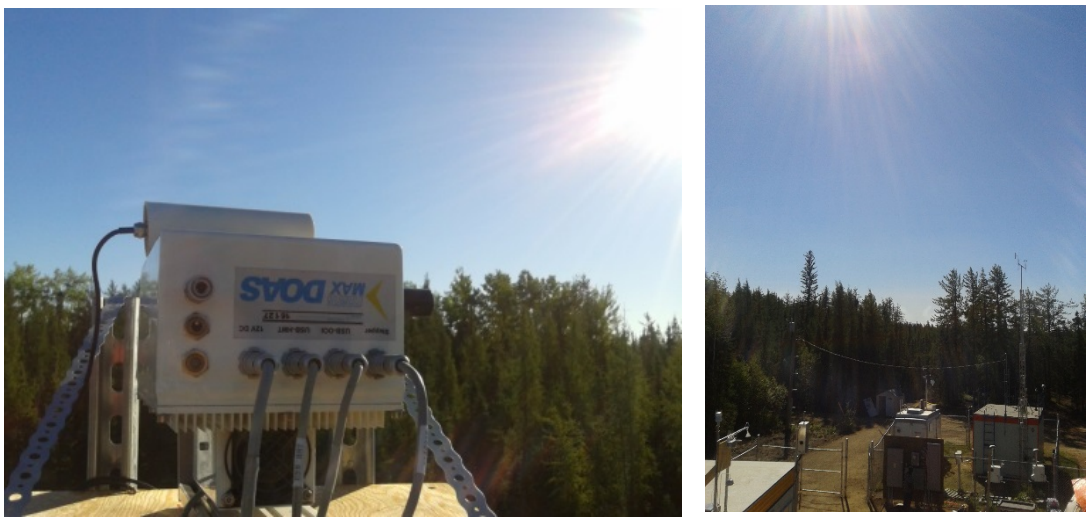

Figure A1 The MAX-DOAS instrument mounted at 5 m a.gl. (left) at Fort McKay South and the view South of the instrument.

Section 2 Additional Information on MAX-DOAS Spectral Fitting

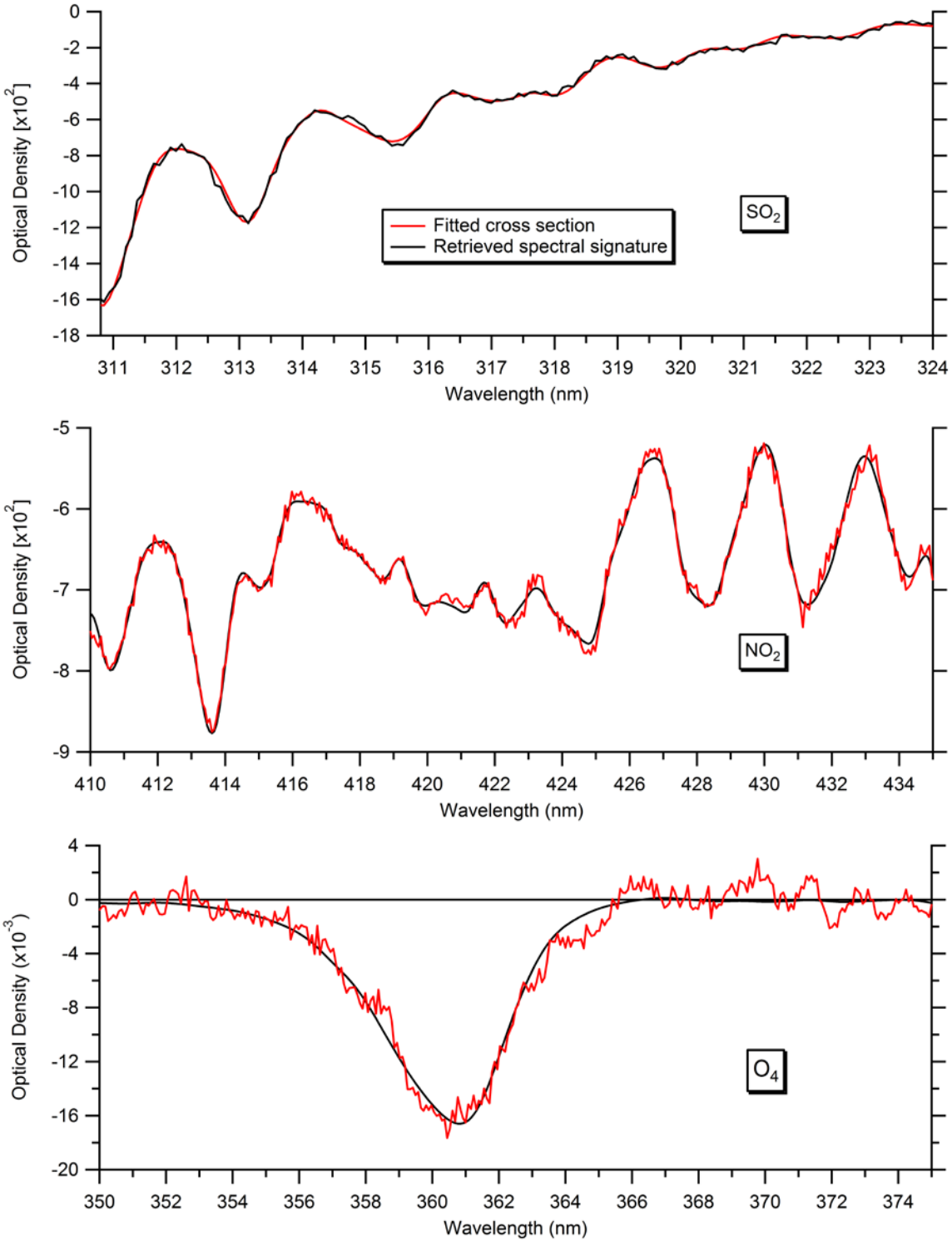

Figure A2 Examples of spectral retrievals of SO_2, NO_2 and O_4 Retrieved dSCDs were 5.79(±0.09)x10^{17} molec cm^{-2}, 1.2(±0.01)x10^{17} molec cm^{-2}, and 3.96(±0.08)x10^{43} molec cm^{-2}, respectively. The spectra were measured under clear sky conditions at 2° in 2013 at 22:37 UTC on Aug. 23 and 18:34 UTC on Sept. 04, respectively.

SO_2 Spectral Fitting Experiments with Calibration Gas Cell

A SO_2 gas cell with a slant column density (SCD) of $2.2e^{17}$ (± 10%) molecules cm^{-2} was placed inside the MAX-DOAS telescope tube. Scattered solar light spectra were recorded around solar noon at viewing elevation angles of 2^o, 4^o, 8^o, 30^o and 90^o above the horizon, followed by a 90^o measurement without the gas cell. This second zenith measurement was used as the FRS. Active-DOAS measurements of the SO_2 gas cell confirmed the SCD. dSCDs of SO_2 were fit in DOASIS with varying fitting windows using a lower limit range of 303-318 nm and an upper limit range of 309-340 nm in ~0.3 nm increments. The fit components can be found in Table 2.

Fitting SO_2 in the measured wavelength region is challenging because the SO_2 absorption features (Figure A3) are strongest where the measured light intensity was small, and the influence of stray light can be large. Increasing O_3 absorption at decreasing wavelengths approaching 300 nm reduces the spectral signal. The lower limit wavelength of the fitting window must balance including strong SO_2 features and enough signal intensity. The upper limit wavelength should ensure that the fitting window includes as many SO_2 absorption features as possible while excluding wavelengths where SO_2 absorption features are so weak that degrees of freedom and fitting uncertainty are increased.

dSCD of SO_2 fitted from the spectra measured at elevation angles closer to horizon-pointing exhibited fewer wavelength fitting windows where the fitted dSCD was within ±15% of the expected value. Spectra measured at lower elevation angles had less UV signal because the longer light path lengths closer to the ground experience more Rayleigh scattering that preferentially scattered away shorter wavelengths. Since the visible light intensity remains the same and is a source of stray light, the reduced UV signal increased the impact of stray light on the dSCD (signal to noise ratio decreases). Stray light artificially increases the measured intensity and tends to cause underestimation of the retrieved dSCD.

Stray light has the largest impact on the signal at the lowest wavelengths where the measured intensity was the lowest. Stray light interference is apparent in the frequent underestimation of the dSCD for the 2^o spectrum with fitting windows with lower limits <307 nm (gray datapoints in Figure A4). The dSCDs were often >15% less than the expected value for fitting windows with a lower limit <308 nm, particularly for the lower elevation angles. The fitted dSCD was sensitive to small changes in the fitting window for lower limits <308 nm and upper limit <330 nm, changing up to ~20% change for a 0.5 nm difference in the lower limit (Figures A4 & A5). The fitted dSCD is inversely proportion to the SO_2 absorption cross-section (Figure A5). When the strongest SO_2 absorption feature included in the fit was an absorption maximum, the measured intensity in lowest wavelength region was even further reduced, leading to up to a 25% reduction in the dSCD compared to a window where the adjacent absorption minimum was the strongest feature included (Figure A5). This result implies that small errors in the wavelength calibration or wavelength shift could significantly deviate the dSCD from the true value. dSCDs exhibited less dependence on the lower limit for windows with lower limit wavelengths of 310.4-311 nm due to increased signal intensity. For lower limit wavelengths >312 nm, the SO_2 absorption features are substantially weaker, leading to dSCDs that tended to be >15% larger than the expected value and varied significantly with relatively small changes

in higher limit wavelength (Figure A4). Since the SO_2 absorption features after 324 nm are very weak, the fitting range upper limit was set to 324 nm.

Based on these results, an SO_2 fitting range of 310.5-324 nm was chosen for this instrument.

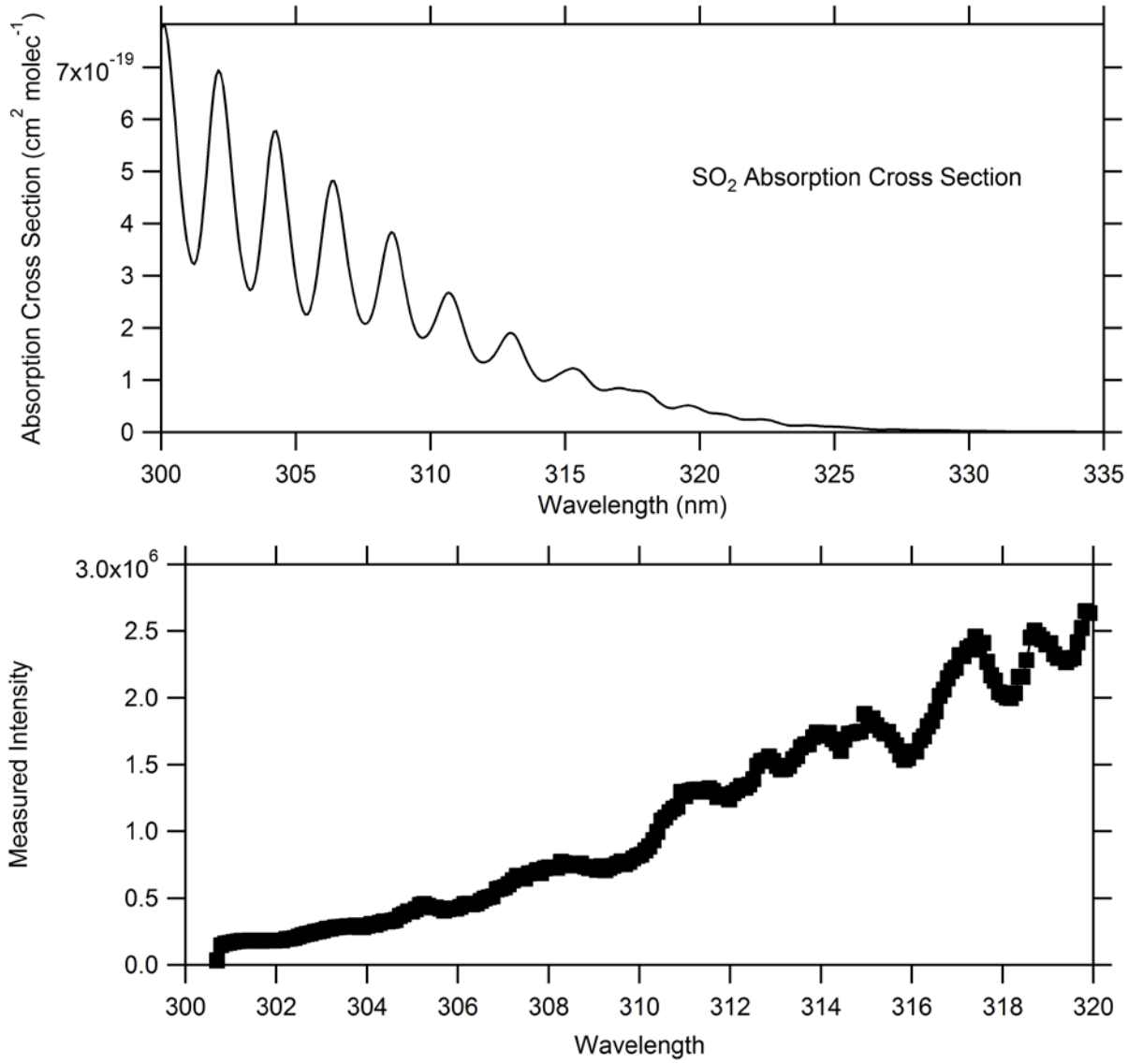

Figure A3 SO_2 Absorption Cross-section from Bogumil 2003 SO_2 (293K) (top) and Measured Intensity from the 2^o Spectrum from 300-320 nm (bottom).

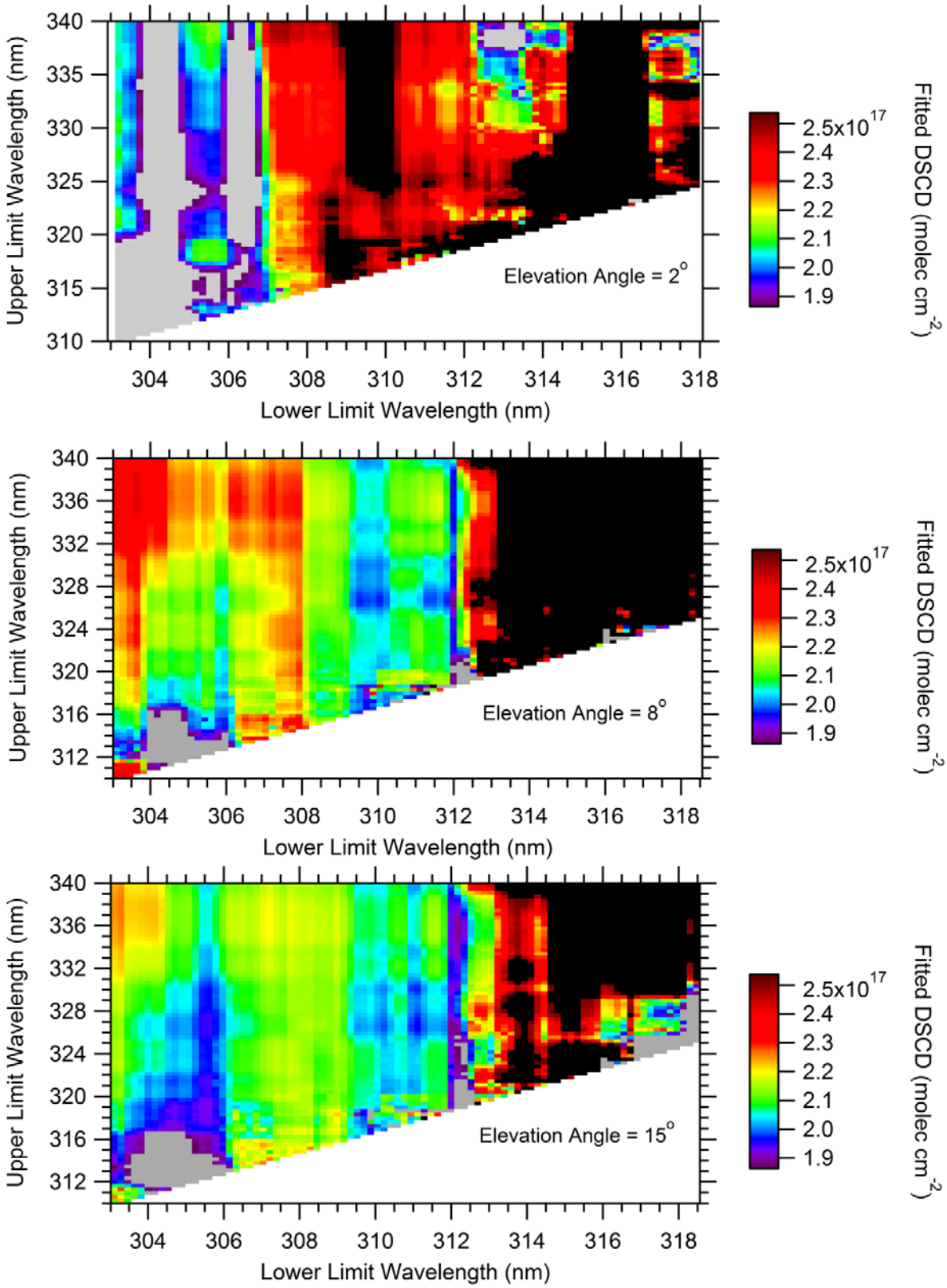

Figure A4 dSCDs of SO2.2x10^{17} molecules cm^{-2} gas cell using varying spectral fitting ranges. Gray and black datapoints indicate that the fitted dSCD was 15% less than and greater than 2.2x10^{17} molec cm^{-2}, respectively.

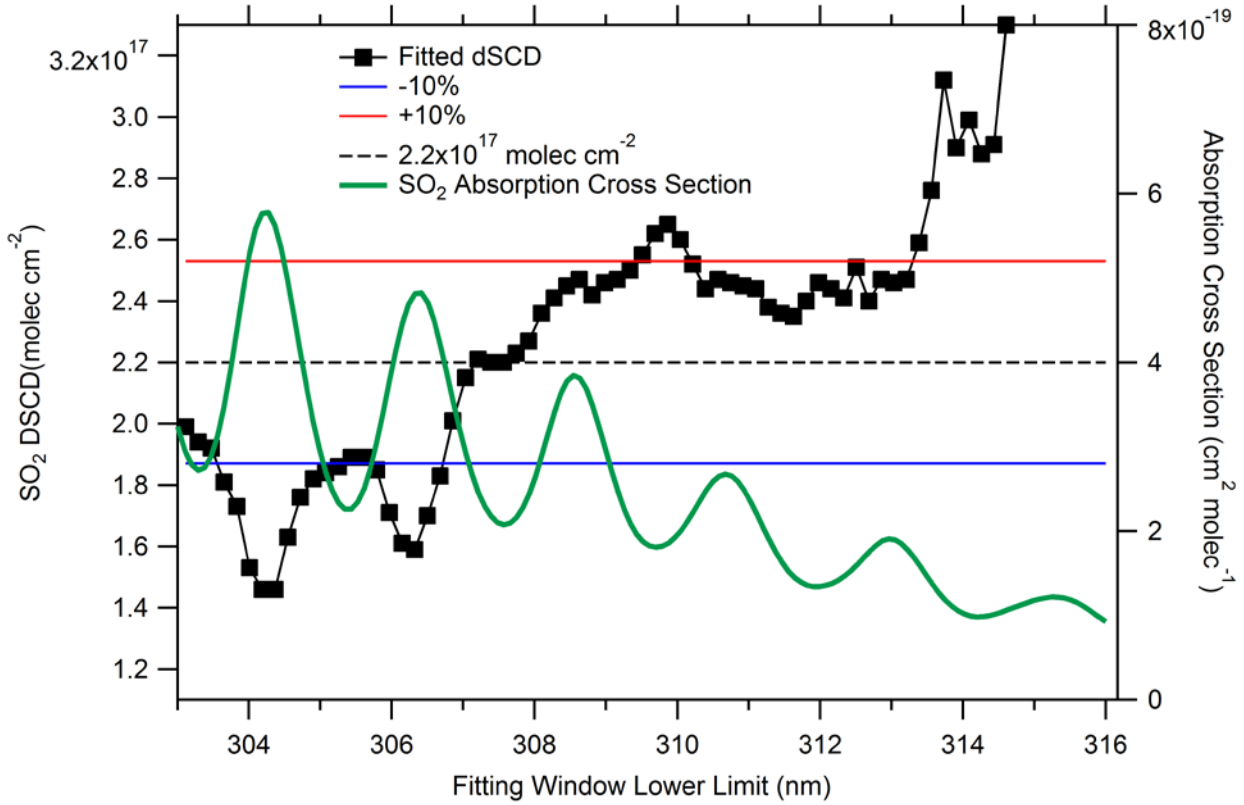

Figure A5 Fitted dSCD of SO_2 with fitting window upper limit of 320 nm from 2° Spectrum using a $2.2x10^{17}$ molec cm^{-2} gas cell (black trace) and SO_2 absorption cross-section degraded to the spectrometer's resolution (green trace).

Section 3 Lidar S-ratio Measurements in the AOSR

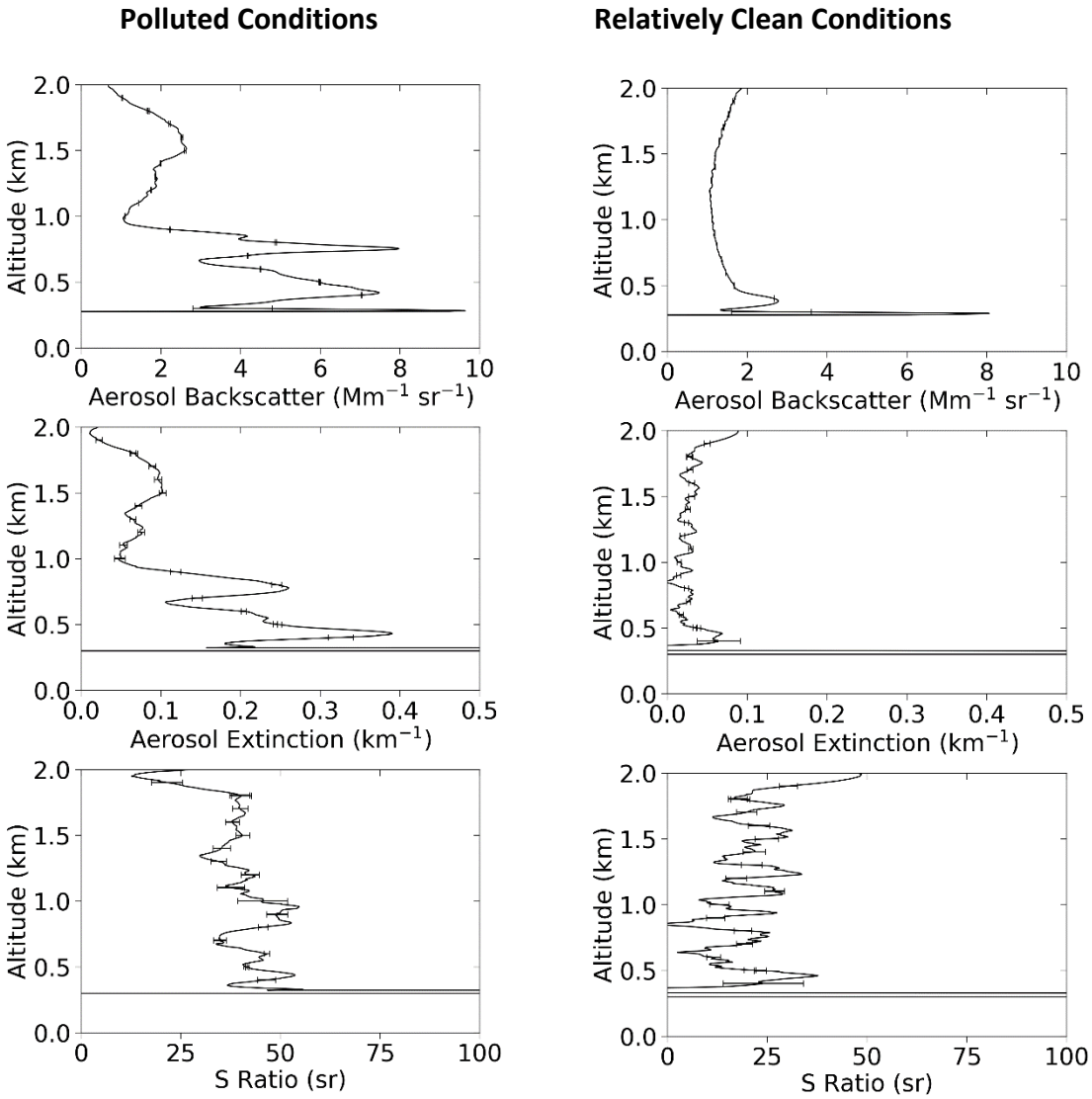

Figure A6 Lidar measurements of vertical profiles of aerosol extinction (middle panels) and S-ratios (bottom panels) under polluted conditions (left column) and relatively clean conditions (right column) at Oski-Ôtin in 2018.

Section 4 Linear Regression Statistics

Table A3 Aug. 23 AOD Linear Regressions.

Y	MAX-DOAS AOD	MAX-DOAS AOD	MAX-DOAS AOD	MAX-DOAS AOD	AERONET AOD -30 mins	AERONET AOD -30 mins
X	AERONET AOD -30mins	AERONET AOD	Lidar AOD S=50 sr in plume	Lidar AOD S=25 sr	Lidar S=50 sr	Lidar S=25 sr
Slope	0.98±0.02	1.03±0.01	1.15±0.02	2.18±0.03	1.08±0.02	2.18±0.01
Intercept	-0.08±0.00	-0.07±0.00	-0.01±0.00	-0.06±0.00	0.07±0.00	0.03±0.01
R^2	0.92	0.80	0.97	0.97	0.98	0.96
N	21	23	21	24	22	22

Table A4 Aug. 23 trace-gas linear regressions. *Denotes the matrix was near-singular or badly conditioned; statistical results may be inaccurate.

Y	MAX-DOAS SO_2 VCD	MAX-DOAS SO_2 VCD	MAX-DOAS NO_2 VCD	MAX-DOAS NO_2 VCD	WBEA Fort McKay South SO_2 mixing ratio	WBEA Fort McKay South NO_2 mixing ratio
X	Pandora SO_2 VCD	Pandora SO_2 VCD -30mins	Pandora NO_2 VCD	Pandora NO_2 VCD -30 mins	WBEA Oski-Ôtin SO_2 mixing ratio - 30 mins	WBEA Oski-Ôtin NO_2 mixing ratio - 30 mins
Slope	*1.61±0.10	*1.55±0.07	*2.03±0.07	*2.20±0.07	1.42±0.05	1.93±0.07
Intercept	*$1.50x10^{16}$±$0.25x10^{16}$	*$1.16x10^{16}$±$0.24x10^{16}$	*-4.56^{15}±$0.51x10^{15}$	*-$6.36x10^{15}$±$0.56x10^{15}$	0.50±0.01	1.95±0.52
R^2	0.51	0.82	0.68	0.87	0.91	0.61
N	24	23	24	23	109	109

Table A5 Sept. 03 AOD and trace-gas linear regressions for data from 11:30 to 18:00. ^Denotes that one or both variables exhibited little variation; the R^2 is not interpretable.

Y	MAX-DOAS AOD	MAX-DOAS AOD	AERONET AOD	MAX-DOAS SO_2 VCD	MAX-DOAS NO_2 VCD	WBEA Fort McKay South SO_2 mixing ratio	WBEA Fort McKay South NO_2 mixing ratio
X	AERONET AOD	Lidar AOD	Lidar AOD	Pandora SO_2 VCD	Pandora NO_2 VCD	WBEA Oski-Ôtin SO_2 mixing ratio	WBEA Oski-Ôtin NO_2 mixing ratio
Slope	0.01±0.01	-0.59±0.36	3.30±0.48	5.27±2.9	-0.19±0.64	0.97±0.10	0.61±0.08
Intercept	-0.01±0.01	0.12±0.02	-0.08±0.03	$-1.5\times10^{17}\pm1.11\times10^{17}$	$1.38\times10^{16}\pm0.44\times10^{15}$	-1.91±1.99	1.82±0.53
R^2	^0.02	^0.05	^0.47	^0.01	^0.00	0.53	0.38
N	16	16	16	13	12	80	80

Table A6 Sept. 04 AOD and trace-gas linear regressions. *Denotes the matrix was near-singular or badly conditioned; statistical results may be inaccurate. . ^Denotes that one or both variables exhibited little variation; the R^2 is not interpretable.

Y	MAX-DOAS AOD	MAX-DOAS AOD	AERONET AOD	MAX-DOAS SO_2 VCD	MAX-DOAS NO_2	WBEA Fort McKay South SO_2 mixing ratio	WBEA Fort McKay South NO_2 mixing ratio
X	AERONET AOD	Lidar AOD	Lidar AOD	Pandora SO_2 VCD	Pandora NO_2 VCD	WBEA Bertha Ganterfort SO_2 mixing ratio	WBEA Bertha Ganterfort NO_2 mixing ratio
Slope	0.39±0.031	0.78±0.08	2.23±0.07	1.10±0.33	*0.95±0.07	0.58±0.04	0.86±0.02
Intercept	-0.01±0.01	0.00±0.01	0.02±0.01	$4.62x10^{15}$±$2.40x10^{15}$	*$9.44x10^{14}$±$3.93x10^{14}$	1.77±0.25	1.00±0.16
R^2	0.31	0.20	0.91	0.51	0.85	0.7	0.92
N	25	25	25	25	25	108	108

Table A7 Sept. 05 AOD linear regressions.

Y	MAX-DOAS AOD	MAX-DOAS AOD	AERONET AOD
X	AERONET AOD	Lidar AOD	Lidar AOD
Slope	1.04±0.08	2.94±0.38	3.24±0.15
Intercept	-0.08±0.01	-0.10±0.02	-0.03±0.01
R^2	0.77	0.51	0.89
N	26	20	20

Table A8 Sept. 06 AOD linear regressions. *Denotes the matrix was near-singular or badly conditioned; statistical results may be inaccurate. ^Denotes that one or both variables exhibited little variation; the R^2 is not interpretable.

Y	MAX-DOAS AOD	MAX-DOAS AOD	AERONET AOD 361
X	AERONET AOD	Lidar AOD	Lidar AOD
Slope	*-2.01±0.93	5.56±1.27	-2.33±0.73
Intercept	0.24±0.09	-0.21±0.06	0.20±0.03
R^2	^0.02	0.02	^0.08
N	24	23	23

Table A9 Sept. 07 AOD and trace-gas linear regressions. *Denotes the matrix was near-singular or badly conditioned; statistical results may be inaccurate.

Y	MAX-DOAS AOD	MAX-DOAS AOD	AERONET AOD	MAX-DOAS SO_2 VCD	MAX-DOAS NO_2 VCD	WBEA Fort McKay South SO_2 mixing ratio	WBEA Fort McKay South NO_2 mixing ratio
X	AERONET AOD	Lidar AOD	Lidar AOD	Pandora SO_2 VCD	Pandora NO_2 VCD	WBEA Bertha Ganterfort SO_2 mixing ratio	WBEA Bertha Ganterfort NO_2 mixing ratio
Slope	0.73±0.06	1.83±0.13	2.34±0.10	*$1.48x10^{14}$±$1.48x10^{14}$	*1.53±3.3	0.99±0.07	1.06±0.03
Intercept	-0.03±0.01	-0.04±0.01	0.00±0.00	*-$1.09x10^{30}$±$1.049x10^{30}$	*$4.10x10^{15}$±$1.75x10^{16}$	-0.04±0.36	1.05±0.23
R^2	0.64	0.67	0.55	^0.00	^0.05	0.64	0.90
N	26	26	26	26	26	108	108

Section 5 Example of Averaging Kernel Matrix from MAX-DOAS Optimal Estimation Retrieval

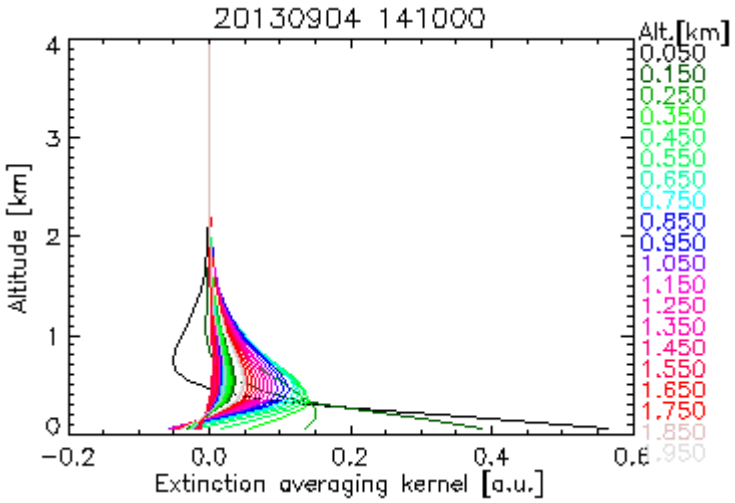

Figure A7 Example of typical averaging kernels from the MAX-DOAS Sept. 04 14:10 retrieval of aerosol extinction.

Section 6 Detailed Plots of Selected Lidar Data

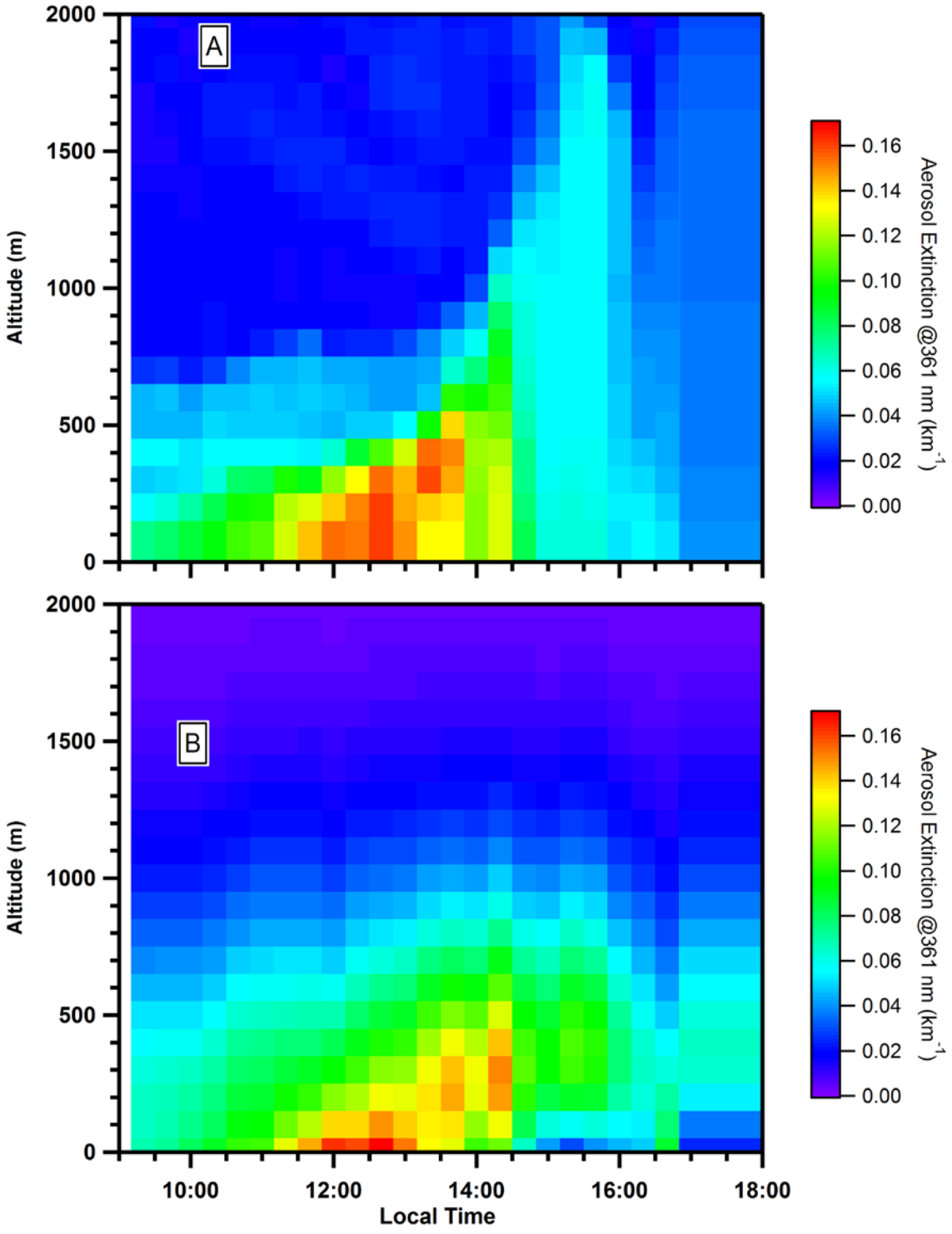

Figure A8 Detail of Sept. 04 averaged (A) and smoothed (B) lidar profiles from 0-2 km.

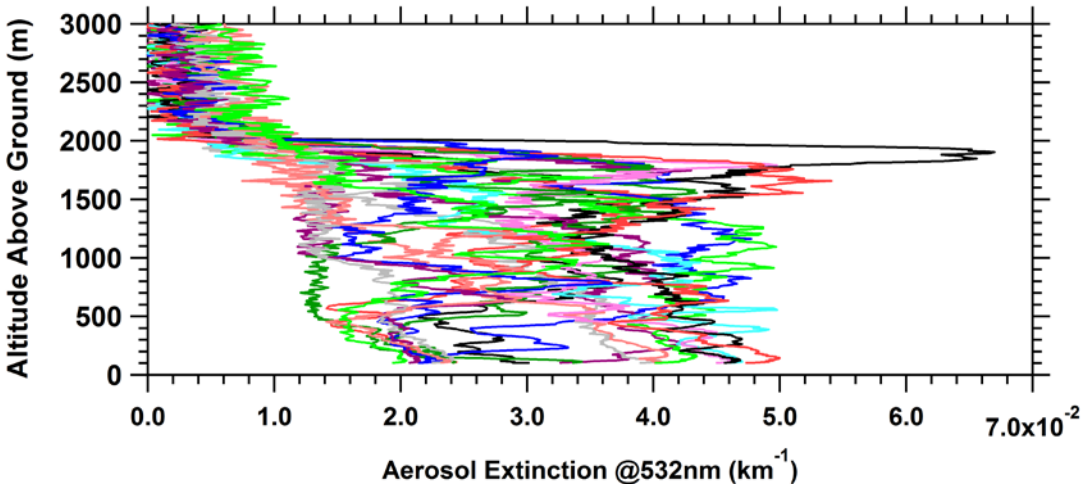

Figure A9 Variability in lidar vertical profiles of aerosol extinction from 15:27 to 15:37 local time on Sept. 07.

WBEA In-Situ Measurements of SO_2 and NO_2 at For McKay South and Fort McKay Sites

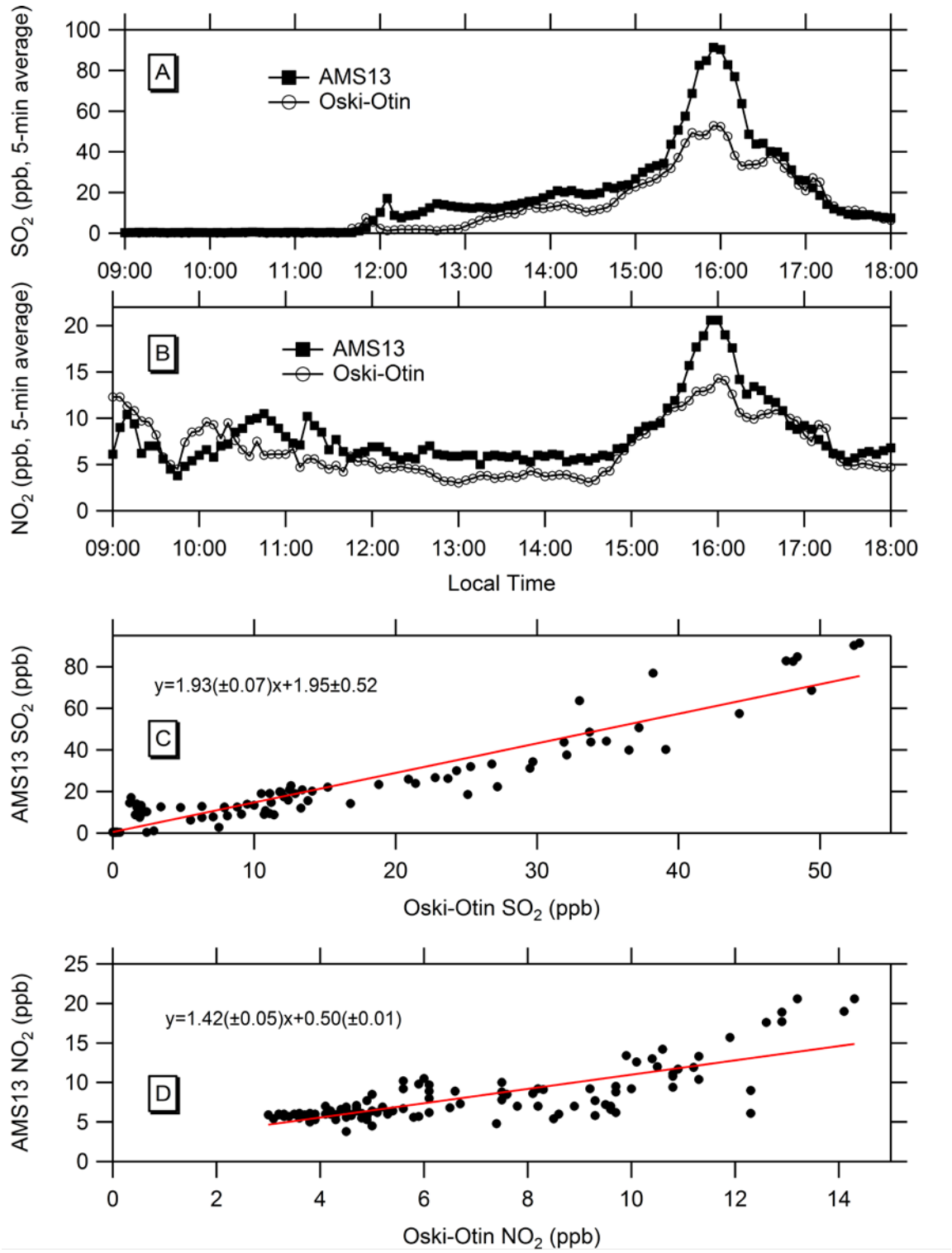

Figure A10 Aug. 23 Time series of 5-minute average mixing ratios of SO_2 (A) and NO_2 (B) at Fort McKay South and Oski-Ôtin and linear regression scatter plots for SO_2 (C) and NO_2 (D).

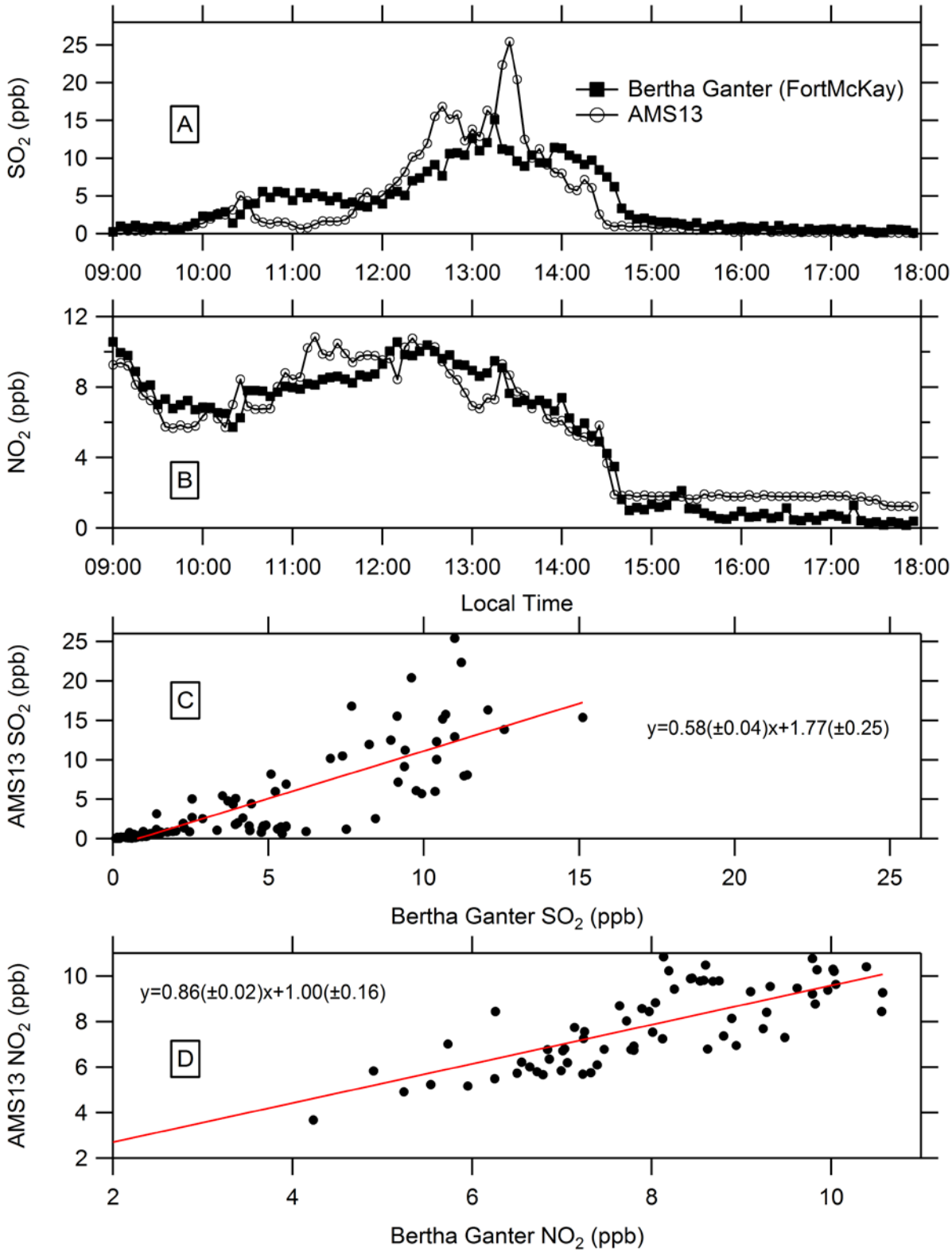

Figure A11 Sept. 04 Time series of 5-minute average mixing ratios of SO_2 (A) and NO_2 (B) at Fort McKay South and Oski-Ôtin and linear regression scatter plots for SO_2 (C) and NO_2 (D).

APPENDIX B: Supplemental to *Recommendations for Spectral Fitting of SO_2* from MAX-DOAS Measurements

Section 1

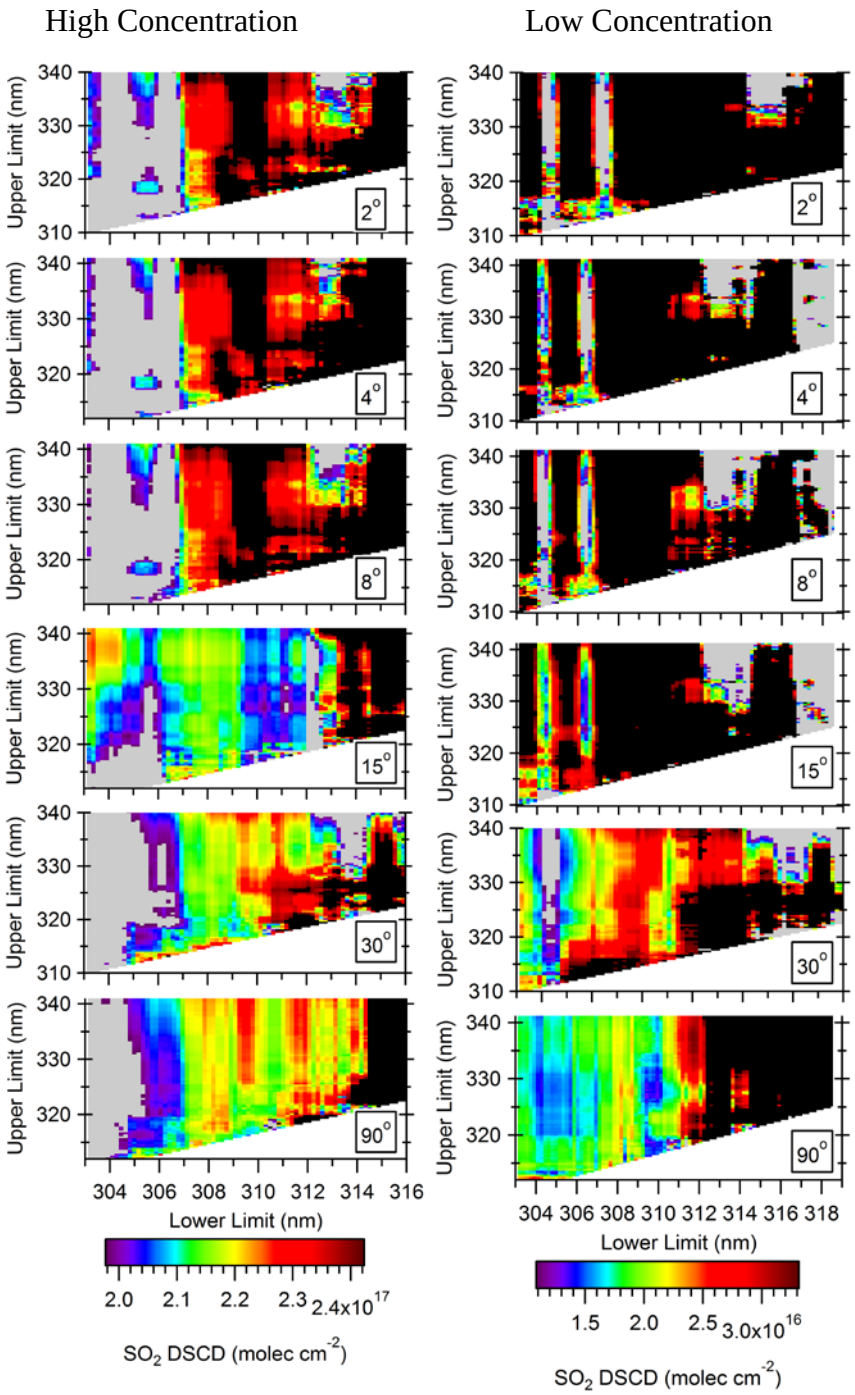

Figure B1 SO_2 dSCDs for the base-case at all the viewing elevation angles for the high (left) and low (right) concentration cells. Grey areas indicate under-estimation of >10% and >50% for the high and low concentration measurements, respectively. Black areas indicate over-estimation of >10% and >50% for the high and low concentration measurements, respectively.

Section 2 DOAS Analysis & Fitting in Trace-Gas dSCDs in the DOASIS software

DOAS analysis is based on the Beer-Lambert law, which describes the attenuation of light with wavelength λ emitted by a radiation source $I_o(\lambda)$ as it passes through the atmosphere along the path length s by an absorber with an absorption cross-section $\sigma(\lambda)$ and number concentration c (Honninger et al., 2004c).

$$I(\lambda) = I_o e^{-\sigma(\lambda)cs} \quad (1)$$

In order to allow interpretation of radiance measurements in the real atmosphere, equation (1) would have to be expanded to include that 1) trace gas absorption cross-sections are a function of temperature and pressure, 2) multiple absorbers are typically present in the atmosphere, and 3) Rayleigh (air molecule) and Mie (aerosol) scattering of light occurs. Determination of trace gas concentration using (1) would require quantification of all factors affecting light intensity including the effect of scattering of light, turbulence, variation in the light source, and changes in spectral sensitivity of the detector (Platt and Stutz, 2008).

For multiple absorbers i and given temperature T

$$I(\lambda) = I_o e^{-\sigma(\lambda,T)\int c_i(s)ds} \quad (2)$$

Given that the SCD of absorber i is $S_i = \int c_i(s)ds$, the integral can be approximated as

$$I(\lambda) = I_o e^{-\sum \sigma_i(\lambda,T)S_i} \quad (3)$$

$$\ln\big(I(\lambda)\big) = \ln(I_o) - \sum \sigma_i(\lambda,T)S_i \quad (4)$$

The DOAS technique eliminates the problem of having to quantify all factors affecting light intensity (see above) by separating absorption structures that vary "slowly" with wavelength (σ^B) from the differential structures (σ').

$$\sigma_i(\lambda) = \sigma_i^B(\lambda) + \sigma_i'(\lambda) \quad (5)$$

The absorption bands unique to each gas are differential features while Rayleigh and Mie scattering, light source variation and spectral sensitivity are broadband features (Honninger et al., 2004c).

The result is the following set of linear equations

$$\ln\big(I(\lambda)\big) = \ln(I_o) - \sum \sigma_i^B(\lambda,T)S_i - \sum \sigma_i'(\lambda,T)S_i \quad (6)$$

The first and second terms on the right-hand side of the equation are low frequency (broadband) and can be modelled as a polynomial function $P(\lambda)$ with coefficients a_j.

$$\ln(I_o) - \sum \sigma_i^B(\lambda,T)S_i = P(\lambda) = \sum_{j=0}^{m} a_j\lambda^j \quad (7)$$

$$\ln\big(I(\lambda)\big) = -\sum \sigma_i'(\lambda,T)S_i + P(\lambda) \quad (8)$$

S_i and a_j can be solved for using the linear least squares method.

However, changes in temperature drift cause wavelength shift (s_i) and squeeze (t_i) so that the wavelength calibration can be slightly inaccurate. Such inaccuracies are non-trivial because absorption features can be only a few detector channels wide (Kraus, 2006). The shift and squeeze parameters are non-linear, preventing a linear solution.

$$\ln\big(I(\lambda)\big) = -\sum \sigma_i'(s_i + t_i\lambda)S_i + P(\lambda) \tag{9}$$

Therefore, DOASIS uses an iterative Levenberg-Marquardt method to obtain the optimal solution. The DOAS retrieval of SCDs finds the best fit of a set of reference spectra to the measured spectrum by minimizing the cost function χ^2.

$$\chi^2 = \int \left[\ln I(\lambda) - P(\lambda) + \sum_i \sigma_i'(s_i + t_i\lambda)S_i\right]^2 d\lambda \tag{10}$$

The first term inside the brackets includes the measured spectrum, and the other two terms include the modelled parameters and absorption cross-sections.

The Levenberg-Marquardt Method combines the gradient descent method, which tends to converge rapidly when the starting conditions are far away from the cost function minimum, and the Gauss-Newton method, which is most effective close to the optimal solution (Kraus, 2006). The methods were combined by Levenberg (1944) because the combined algorithm is more stable and converges faster than the individual methods (Platt and Stutz, 2008). A flow chart of the steps in a DOASIS fit can be found in Figure 7.1 in (Kraus, 2006). The parameters in the model are split into sets of linear (SCDs and polynomial) and nonlinear parameters (shift and squeeze). A first guess of the linear parameters is made, followed by an estimation of the non-linear parameters. A simple least squares method is used to solve for the linear parameters while keeping the nonlinear parameters constant. A step of the iterative algorithm then calculates the nonlinear parameters with the linear parameters kept constant. The linear parameters are now recalculated using the new nonlinear parameters, and the iterations continue until a terminal condition is reached (Kraus, 2006). If an iteration step produces a new estimate with a greater cost function, the gradient method is used to seek a better solution farther away, but if the new estimate is an improvement, the Gauss-Newton method is used. The iteration process stops when the change in the cost function is $<10^{-5}$ or maximum iteration steps have been reached. When the steps become very small, ideally the iteration is close to the cost function minimum. Note that the algorithm may not find the global optimal solution like the least squares method but rather a local minimum in the cost function. Also, the algorithm results are stable and correct if all parameters are independent, but cross-sections containing similar parameters may introduce inter-dependencies that can create instability in the retrieval (Kraus, 2006).

An offset polynomial, $O(\lambda)$ can be enabled in the DOASIS fit to compensate for local broad band structures within the fitting window (e.g., stray light).

$$\ln\big(I(\lambda)\big) = e^{-\sum \sigma_i'(\lambda,T)S_i + P(\lambda)} + O(\lambda) \tag{11}$$

An approximation that $\ln\left(1 + \frac{O(\lambda)}{I(\lambda)}\right) \approx \frac{O(\lambda)}{I(\lambda)}$ for small $\frac{O(\lambda)}{I(\lambda)}$ leads to the equation used by the software as follows:

$$\ln\big(I(\lambda)\big) = -\sum \sigma_i'(s_i + t_i\lambda)S_i + P(\lambda) + \frac{O(\lambda)}{I(\lambda)} \quad (12)$$

References

Honninger, G., von Friedeburg, C. and Platt, U.: Multi axis differential optical absorption spectroscopy (MAX-DOAS), Atmospheric Chem. Phys., 4, 231–254, 2004.

Kraus, S. G.: DOASIS A Framework Design for DOAS, Mannheim University, Mannheim, Germany. [online] Available from: https://pdfs.semanticscholar.org/c091/cbb709447d3b5b778e7bf4aff9d6a2e25861.pdf, 2006.

Platt, U., Stutz, J., Springer E-books - York University and SpringerLink (Online service): Differential optical absorption spectroscopy: principles and applications, Springer Verlag, Berlin. [online] Available from: http://www.library.yorku.ca/eresolver/?id=1261530, 2008.

APPENDIX C: Supplement to *Enhanced NO2 and aerosol extinction observed in the tropospheric column behind lake-breeze fronts in Toronto using MAX-DOAS.*

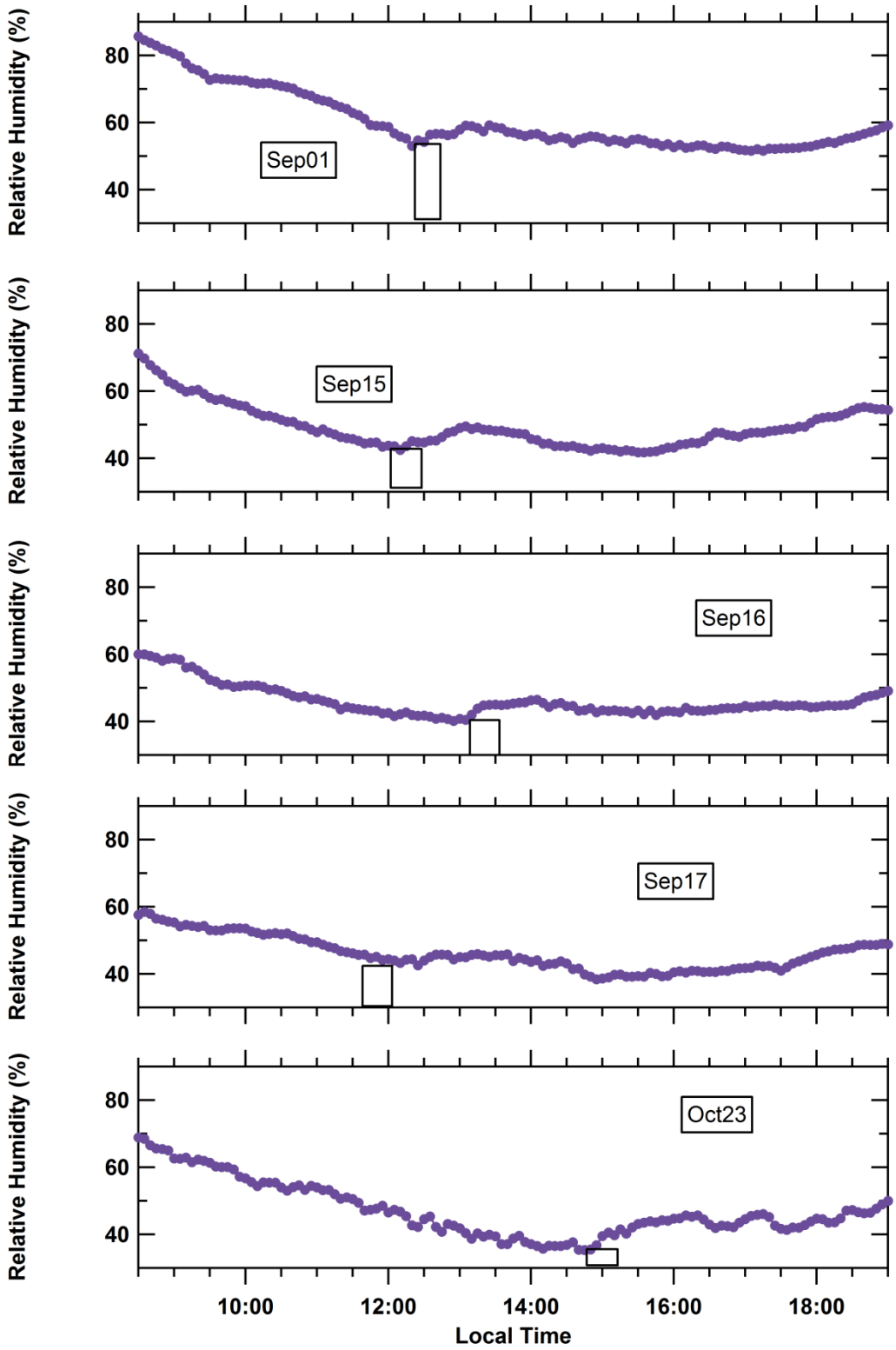

Figure C1 Diurnal trends in RH on lake breeze days. The black rectangle indicates the LBF arrival.

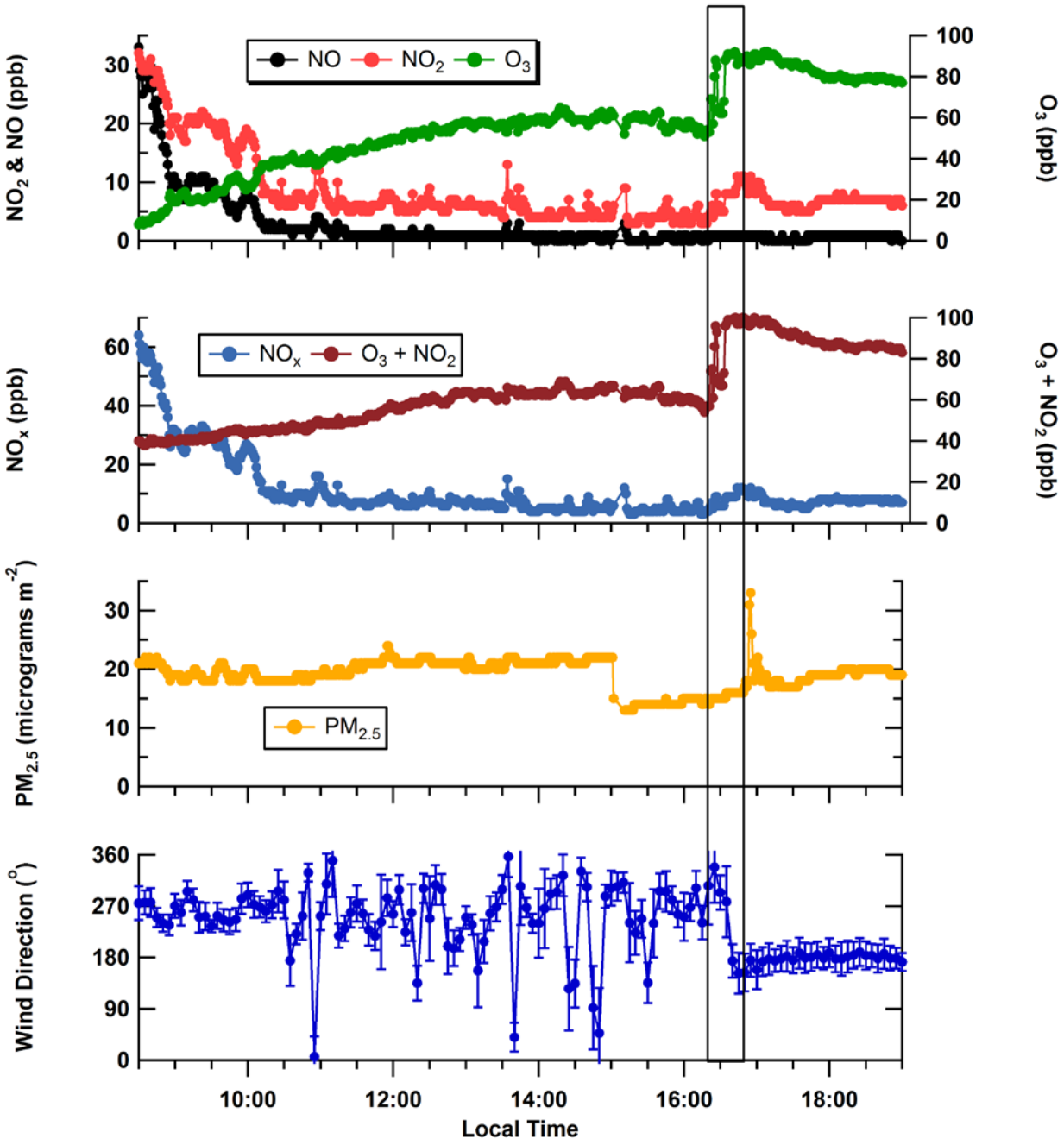

Figure C2 Jul 28 mixing ratios of NO, NO_2, NO_x, O_3, and odd oxygen, and wind direction. The black rectangle indicates the approximate timing of the LBF arrival.

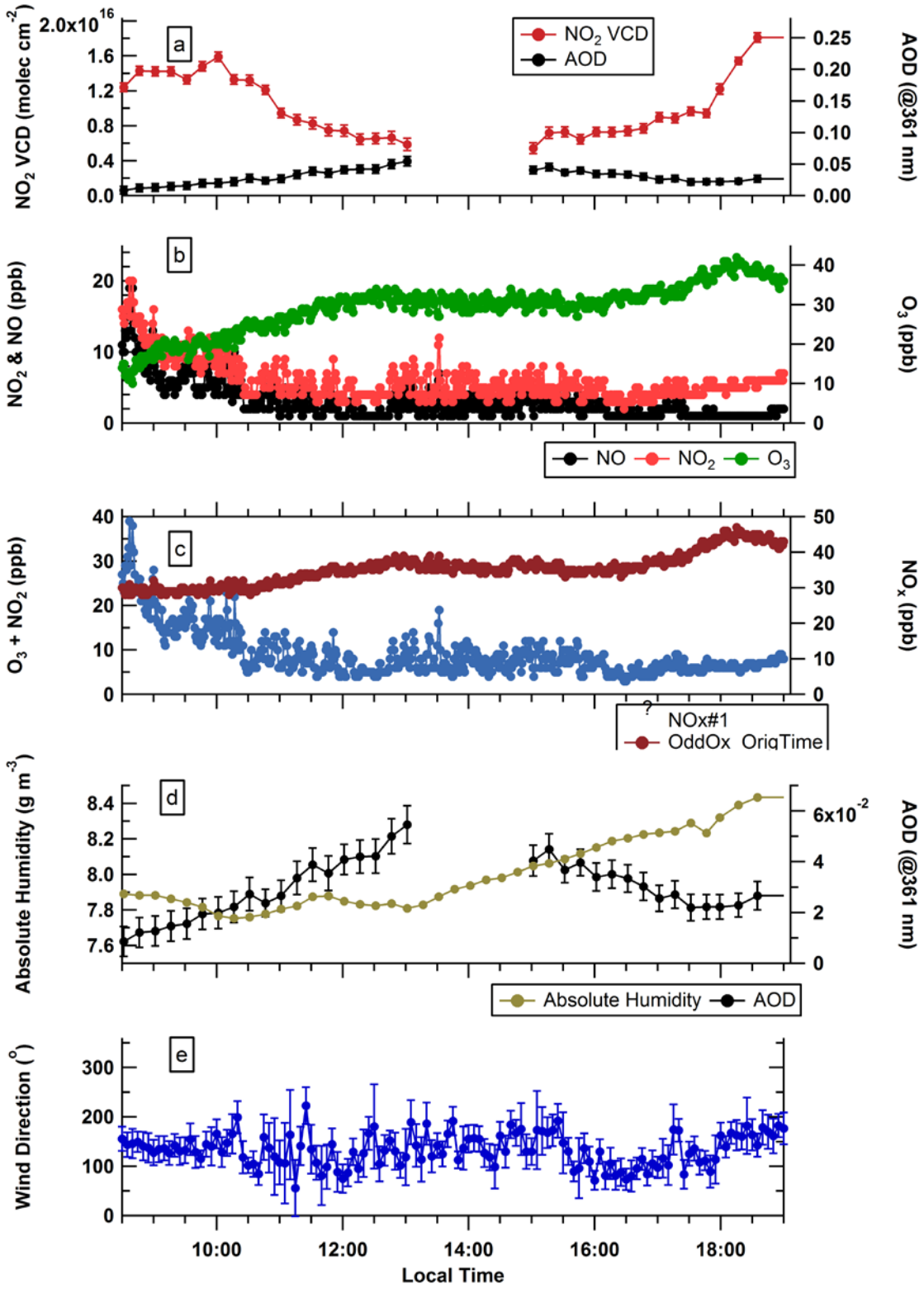

Figure C3 Same as Figure 3 but for July 16, 2015 (a non-lake-breeze day).

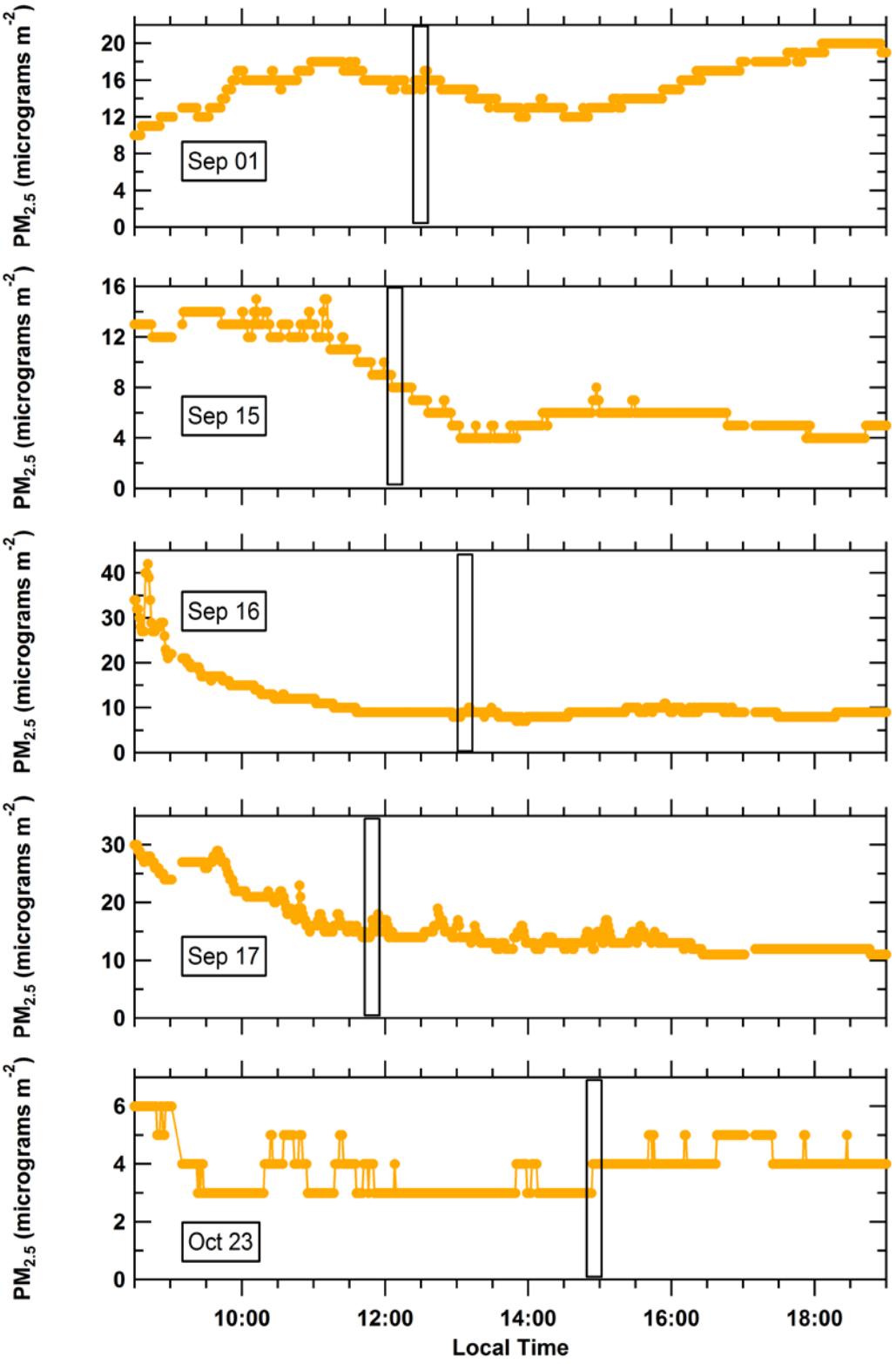

Figure C4 Diurnal trends in $PM_{2.5}$ on lake breeze days. The black rectangle indicates the arrival of the LBF.

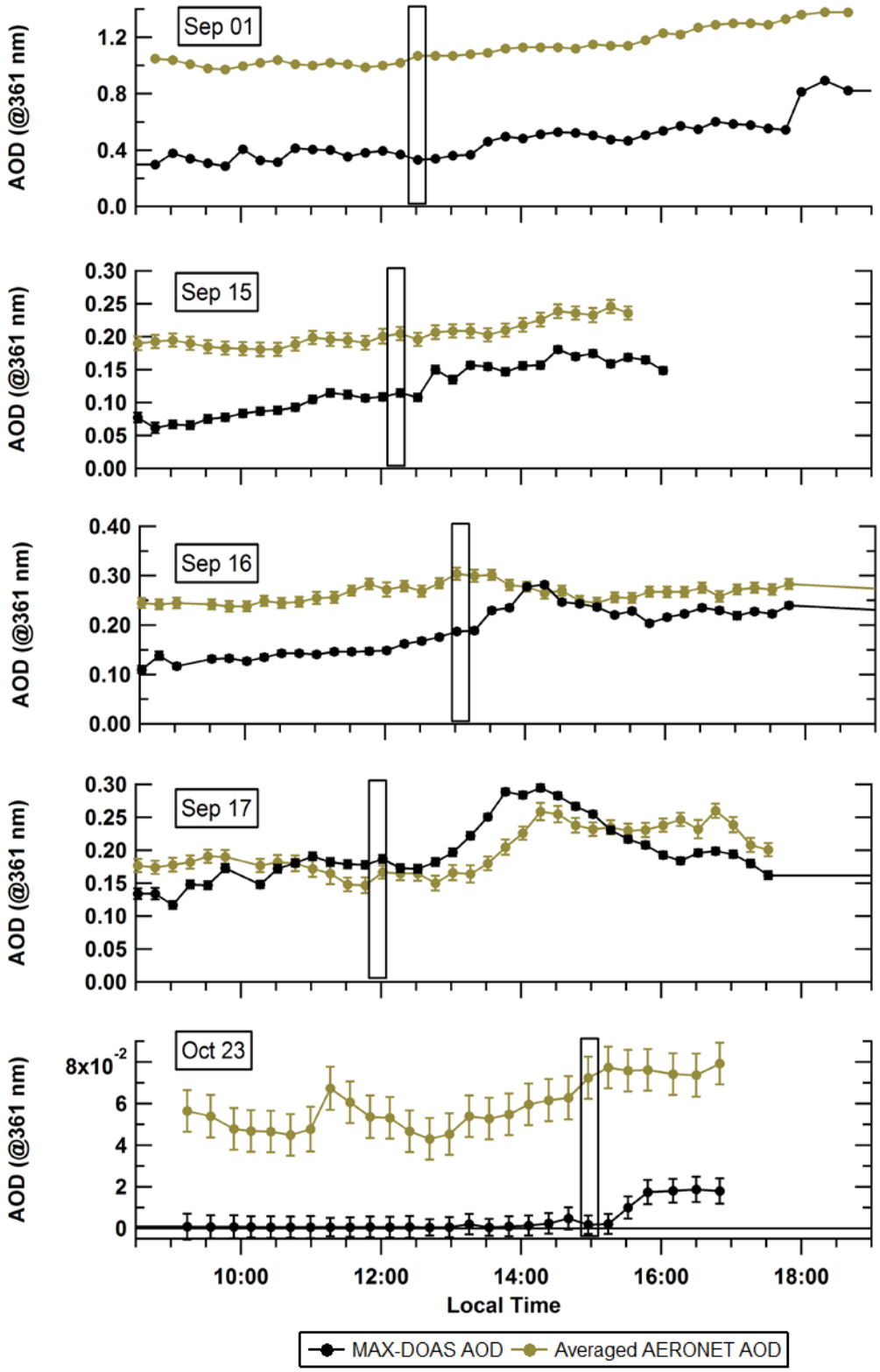

Figure C5 Diurnal trends in MAX-DOAS and AERONET AODs on lake breeze days. AERONET AODs have been averaged into the same time periods as the MAX-DOAS retrievals.

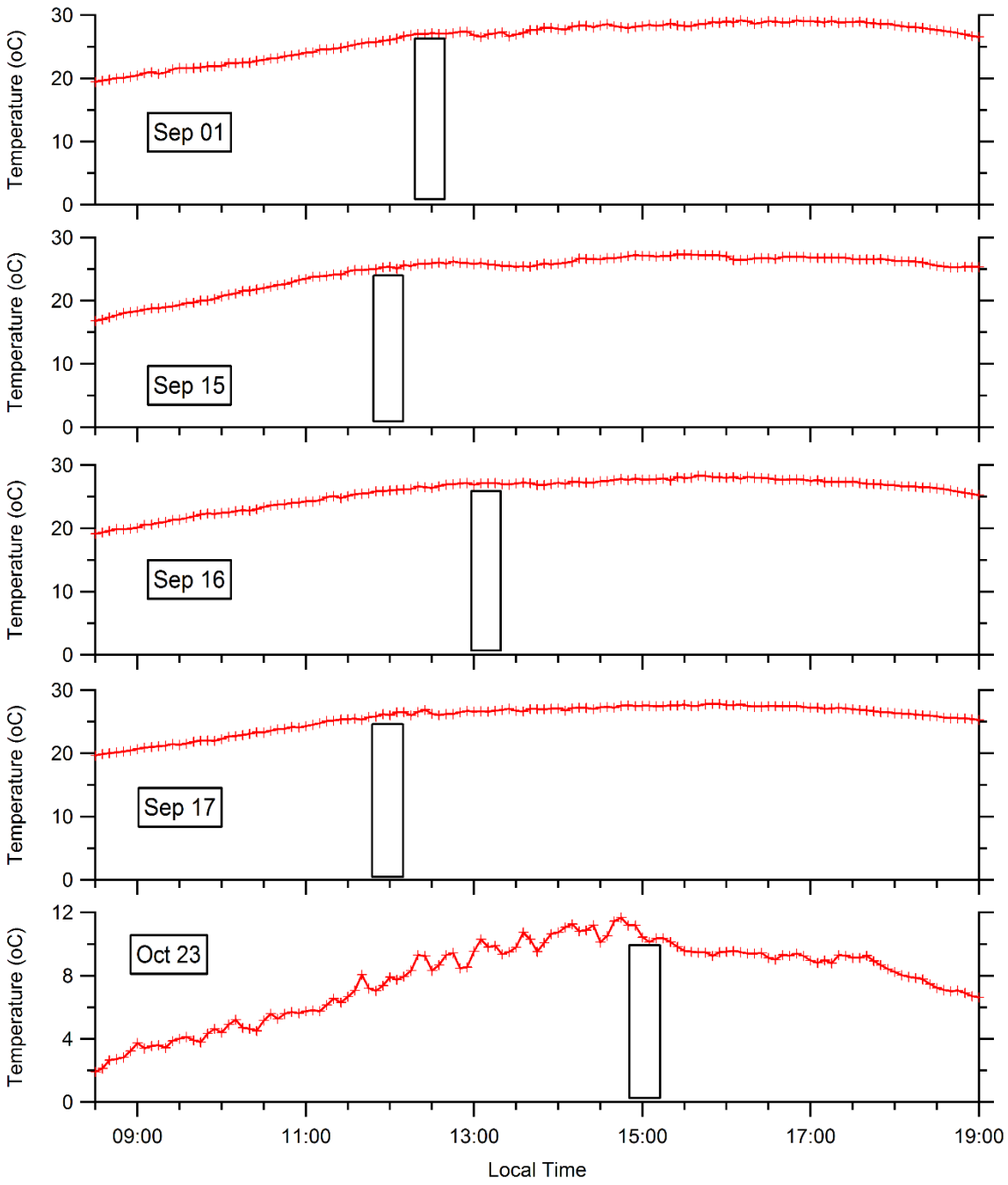

Figure C6 Near-surface temperatures from the meteorological station at the site with approximate timing of the LBFs. Note the different y-axis maximum for Oct. 23.

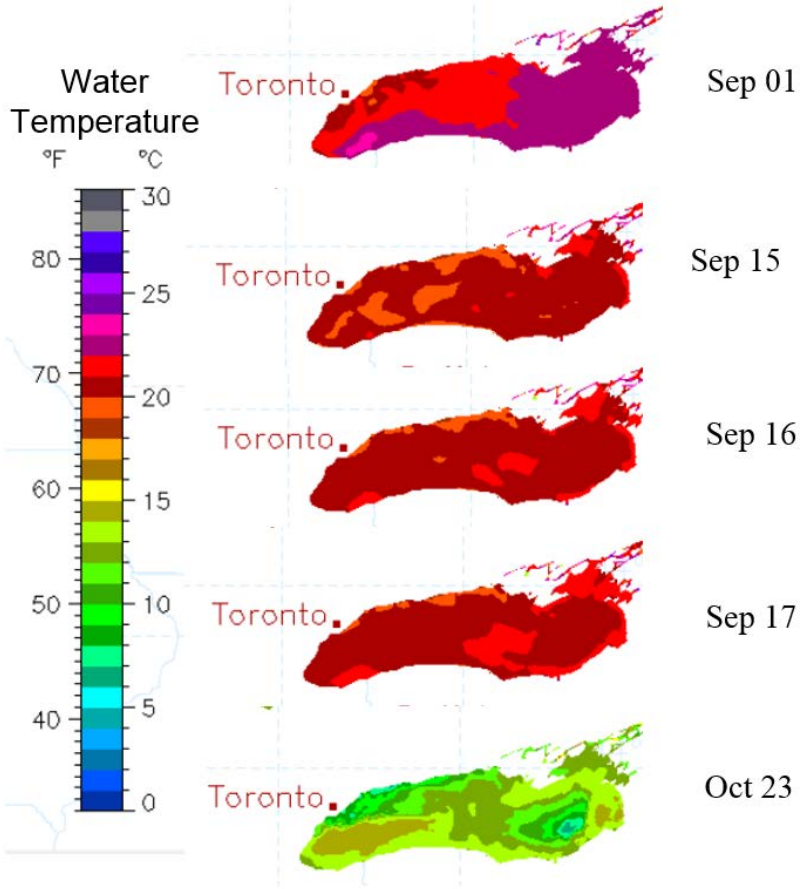

Figure C7 Lake Ontario surface temperatures on study days from Great Lakes Surface Environmental Analysis (GLSEA) (Obtained from URL: https://coastwatch.glerl.noaa.gov/glsea).

APPENDIX D: Supplement to *Estimation of NO_x and SO_2 Emissions from Sarnia, Ontario using Mobile-MAX-DOAS and a NOx-Analyzer.*

Section 1 Information on Local Meteorological Stations and Inter-comparison with Modular Station Wind Data

Table D1 Location and hourly measurement capabilities of air quality and meteorology monitoring stations in the Sarnia Region. Stations with * are operated by the Sarnia-Lambton Environmental Association (SLEA).

Name	Latitude (Degrees)	Longitude (Degrees)	NO_x	O_3	SO_2	10m-Wind	Solar Irradiance
Aamjiwnaang	42.91255	-82.4168	✓	✓	✓	✓	
*Front Street	42.9706	-82.4098	✓	✓	✓	✓	
*LaSalle Road	42.91133	-82.3799			✓	✓	
*Moore Line	42.83954	-82.4208				✓	✓
*RiverBend	42.87735	-82.4545	✓	✓	✓	✓	
Sarnia (MOECC)	42.990263	-82.395341	✓	✓	✓		
*Sombra Line	42.741413	-82.43549			✓		
*Scott Road	42.94978	-82.3972			✓	✓	

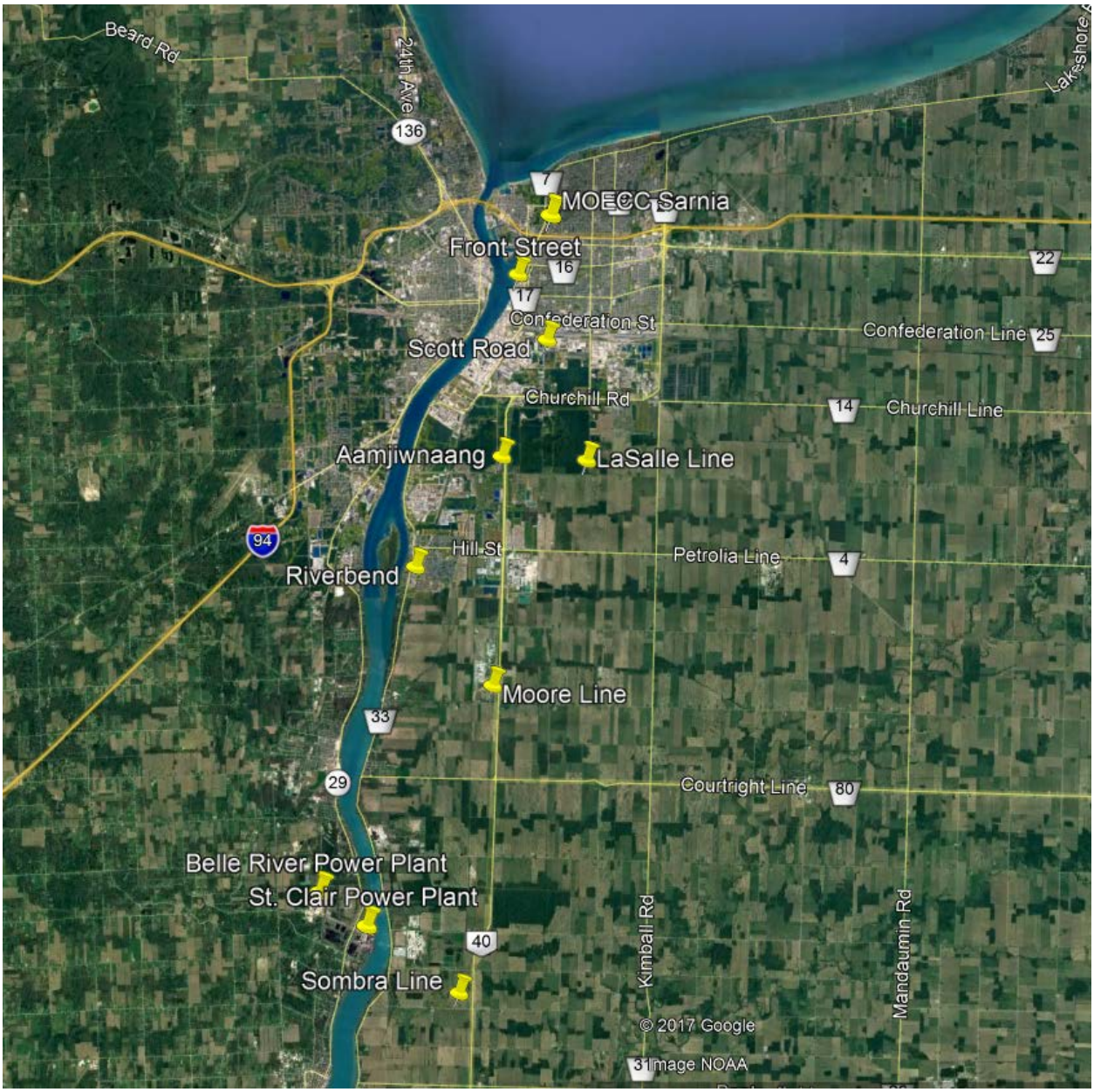

Figure D1 Locations of Air Quality and Monitoring Stations in Sarnia-Lambton Region.

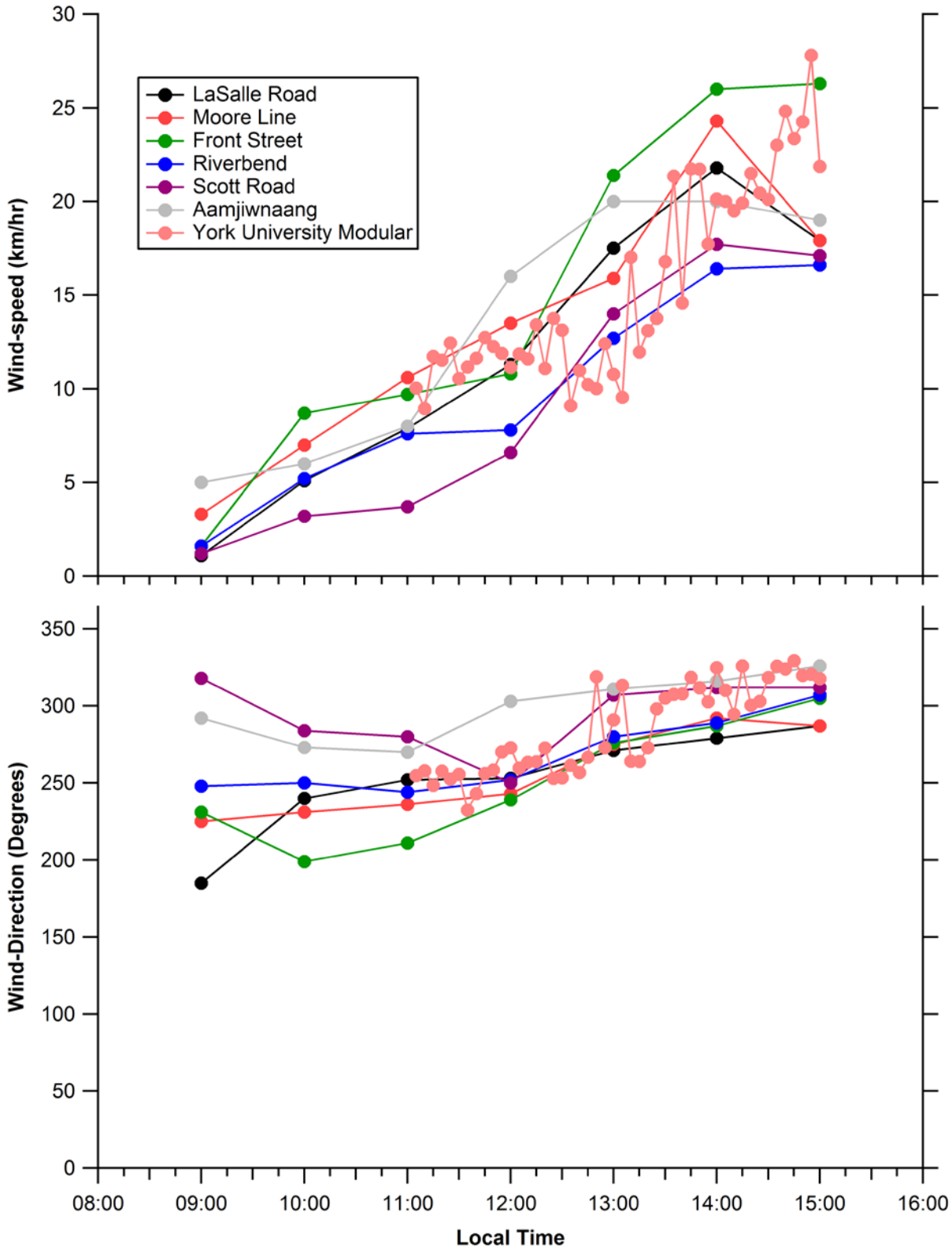

Figure D2 Day1 wind-speeds (top) and wind-directions (bottom) from permanent stations (hourly average) and 5-minute average from the modular meteorological station.

Section 2 WRF model setup and Inter-comparison of Results with Observed Winds

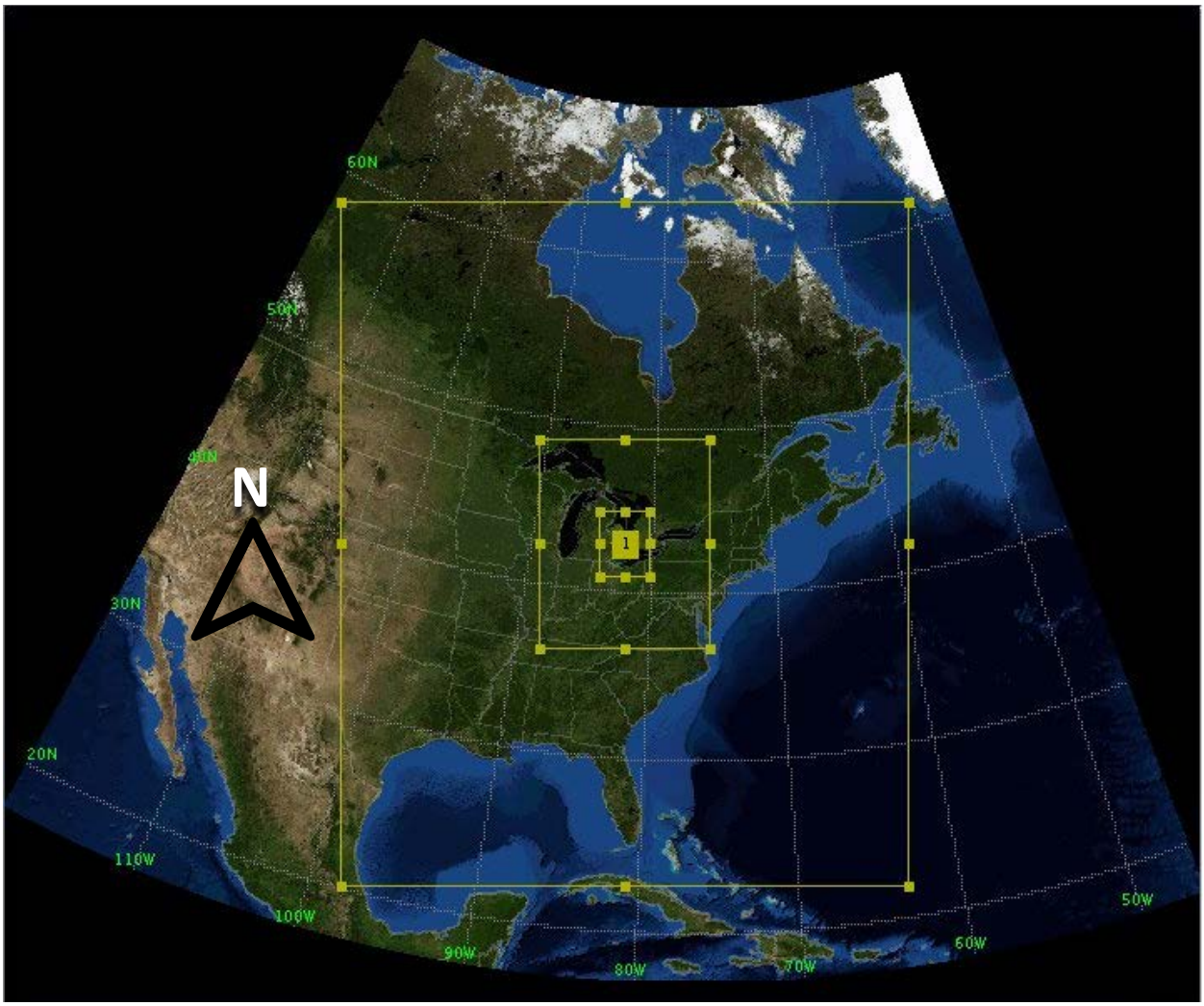

Figure D3 WRF modelled domains centred on Sarnia, Ontario.

2.1 WRF Model Setup

WRF was set up using a series of nested domains (Figure D3) centred on Sarnia, Ontario (42.9745N, 82.4066W) at 27 km, 9 km, 3 km and 1 km horizontal resolutions from the outer to innermost domains. The model had 30 vertical levels up to 100 hPa. Surface-layer physics was represented by the Monin-Obukhov scheme. Initial and lateral boundary conditions were provided using the North American Regional Reanalysis (NARR) data product, which includes assimilated meteorological observations from the North American network. Simulations were conducted using both the Yonsei University (YSU) and Mellor–Yamada–Janjic (MYJ) boundary-layer physics schemes. The YSU scheme was chosen for inter-comparison with observed winds because in literature comparisons of multiple schemes, YSU had the smallest mean bias for winds-speed and RMSE and was found to have greater consistency with observed boundary layer variables compared to local schemes such as MYJ (Banks et al., 2016; Fekih and

Mohamed, 2017). Simulations of vertical profiles of winds in similar terrain to our study (relatively flat terrain close to a water body) found that YSU performed better under unstable conditions compared to MYJ, which performed better under stable conditions (Draxl et al., 2014). YSU was used in our study because estimates of atmospheric stability conditions during our measurements suggest slightly unstable or neutral conditions (see Appendix D Section 3, Table D2). The MYJ scheme was also tested to determine whether the boundary layer scheme choice made a significant impact on the modelled wind results. The YSU and MYJ schemes produced very similar modelled wind-speed and –direction results.

2.2 Inter-comparison of Wind-Speeds and –Directions from WRF and Station Observations.

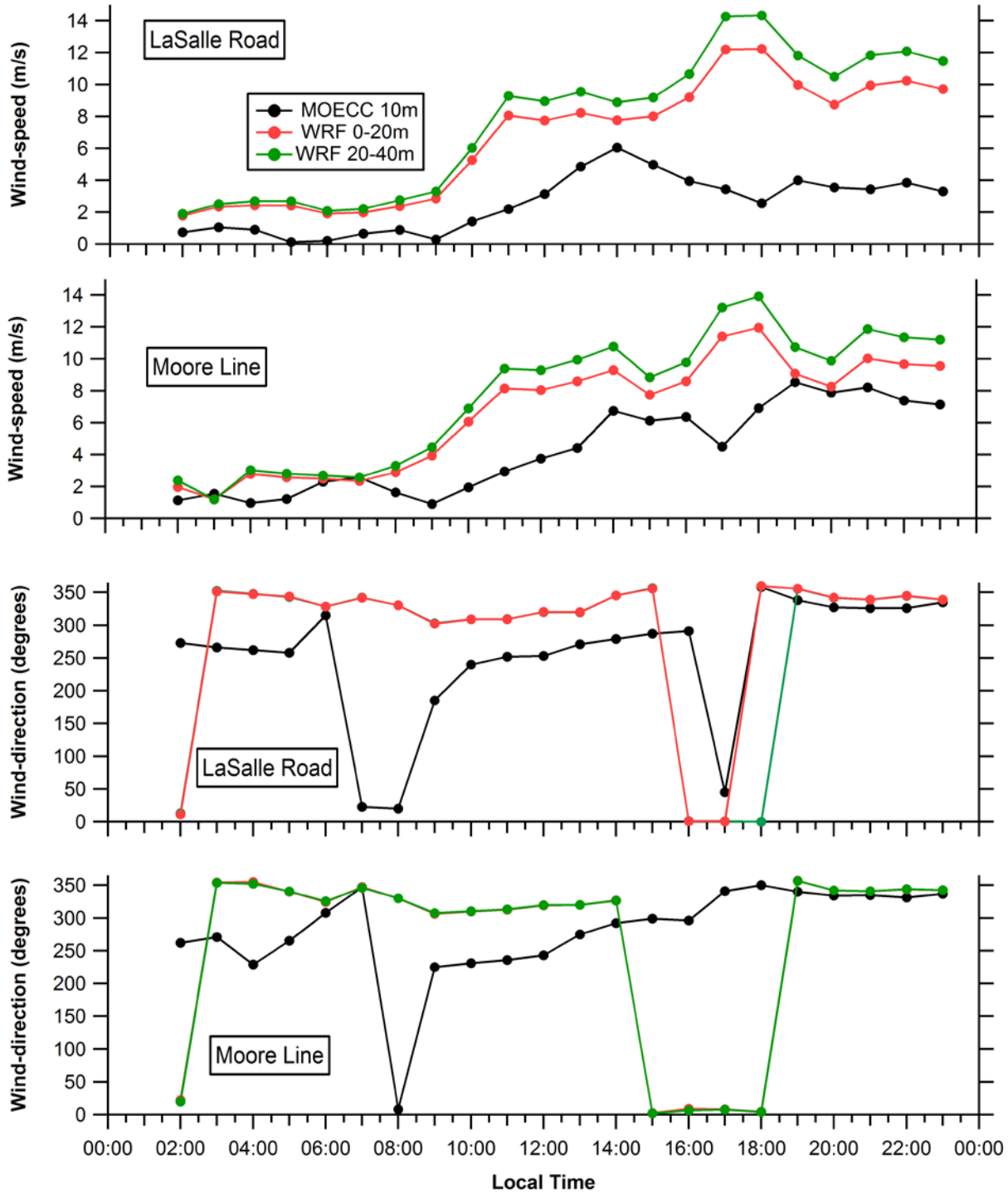

Figure D4 Day 1 comparison of hourly average wind-speeds and -directions from WRF modelling and MOECC measurements at La Salle Road and Moore Line locations.

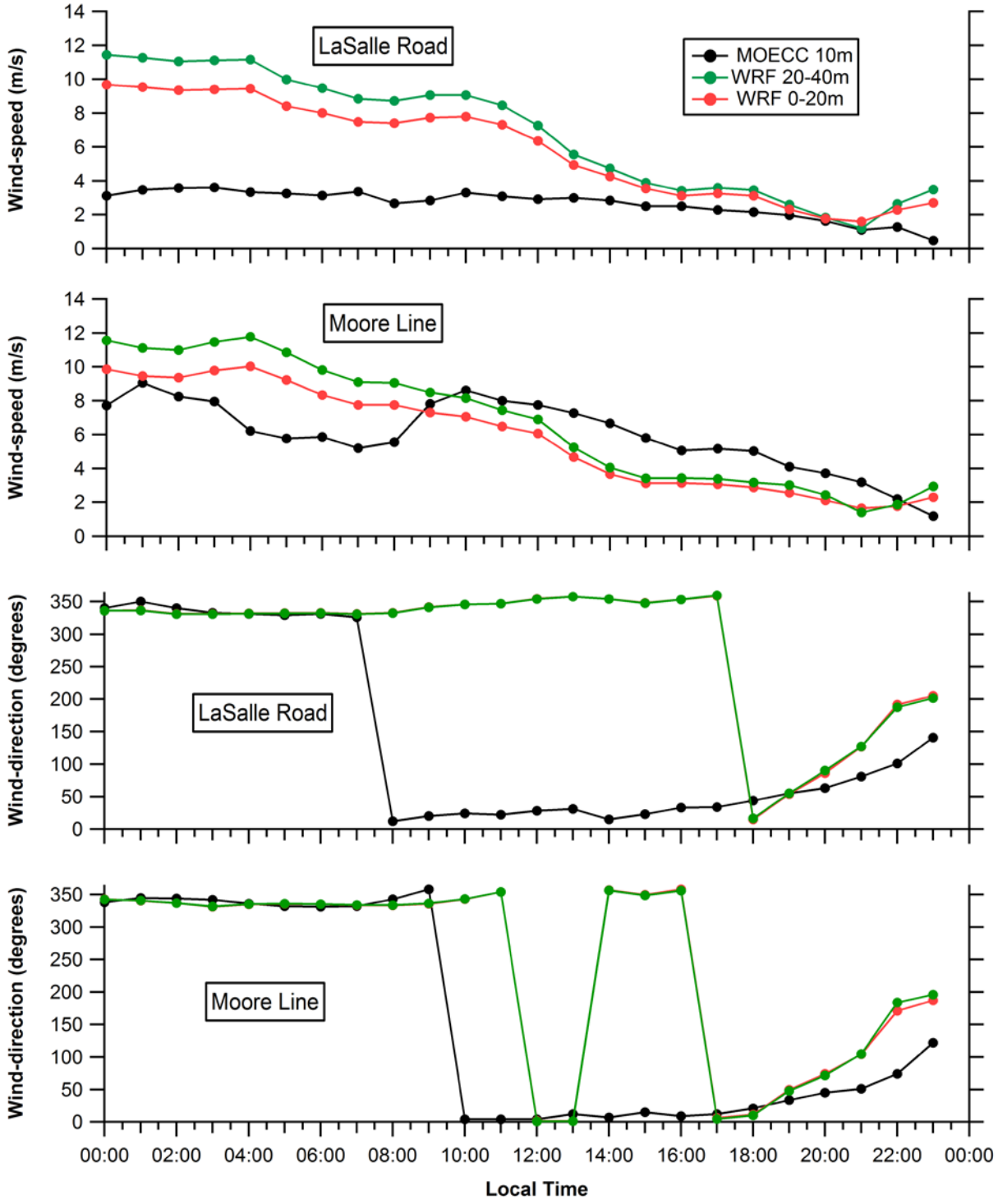

Figure D5 Day 2 comparison of hourly average wind-speeds and -directions from WRF modelling and MOECC measurements at La Salle Road and Moore Line locations.

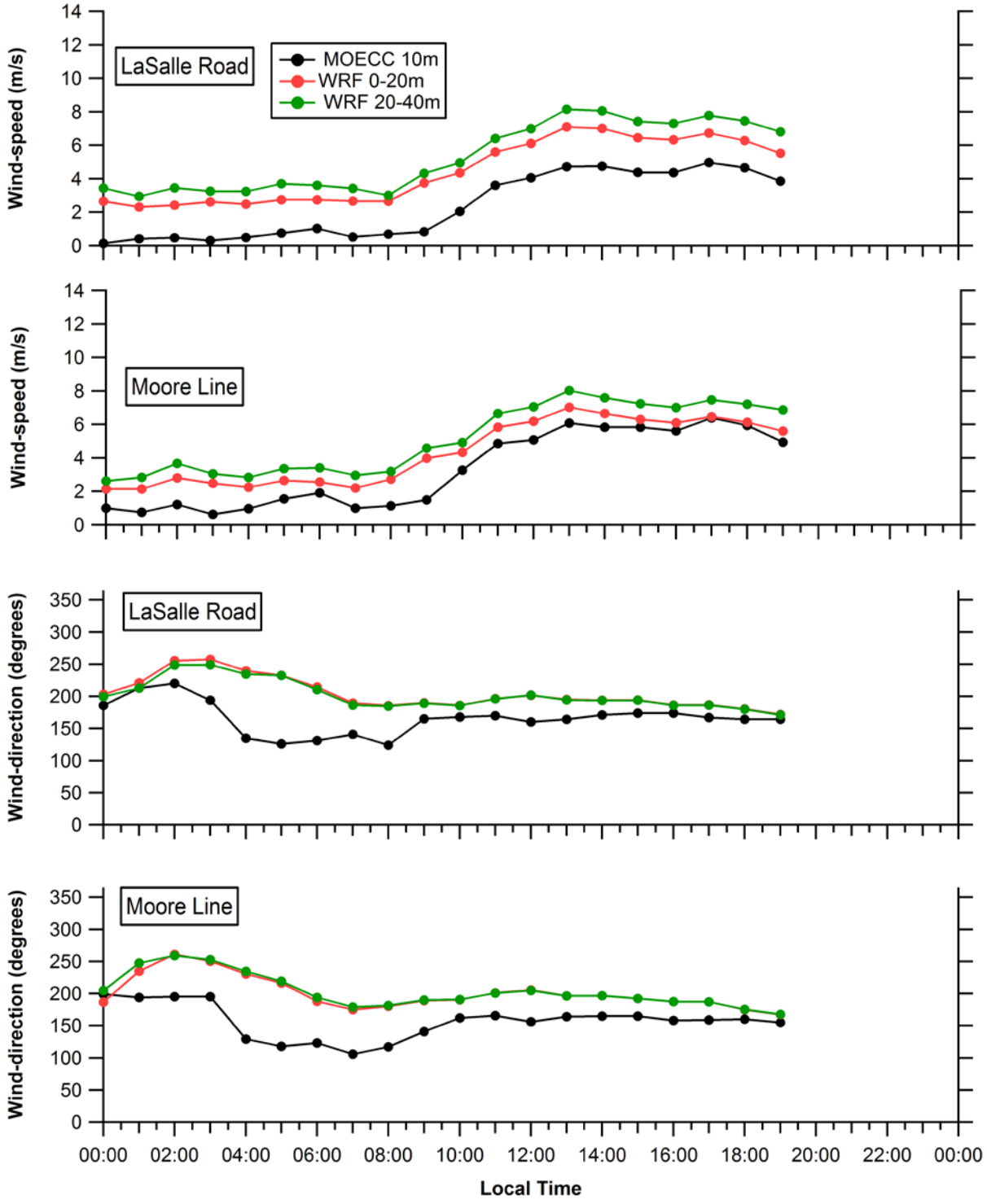

Figure D6 Day 3 comparison of hourly average wind-speeds and -directions from WRF modelling and MOECC measurements at La Salle Road and Moore Line locations.

Figures D4-D6 show inter-comparisons of hourly wind-speeds and wind-directions at La Salle Road and Moore Line station locations from MOECC observations and modelled at 1km resolution using WRF. WRF modelled wind-directions for Day 1 frequently deviated from the observed hourly values by ~75^{o} (Figure D4). WRF wind-speeds in the 0-20 m layer for Day 1 were ~2-4 times the observed 10 m winds during daylight hours (Figure D4). Overestimation of observed 10 m winds by WRF is fairly typical, but the magnitudes of the Root Mean Square Error (RMSE) for Days 1 and 2 of 4.8 m s^{-1} and 3.9 m s^{-1}, respectively, are larger than found in literature; 2-3 m s^{-1} (Banks et al., 2016; Draxl et al., 2010; Shin et al., 2012). The magnitude of the RMSE for Day 1 is greater than the wind-speeds observed while driving. Even assuming that the YSU scheme performs better during unstable conditions, which are more likely to occur during the daytime, the RMSE for daylight hours is still 4.6 m s^{-1} for Day 1. Even accounting for the typical decrease in wind-speed bias and RMSE with increasing altitude (Banks et al., 2016; Draxl et al., 2010, 2014), the WRF wind-speeds within the first 200 m are unrealistically large on Day 1 given power-law (P-L) modelled vertical profiles of wind-speeds scaled using the observed 10 m wind-speeds (Appendix D Section 3). The P-L profiles indicate that under the possible atmospheric stability conditions, wind-speeds aloft would not be as high as the modelled winds based on the measured near-surface speeds. The P-L vertical wind-speed profiles were not used to calculate emissions for reasons discussed in Appendix D Section 3.

Modelled winds for Day 2 at LaSalle Road station overestimated measured winds, which is somewhat expected based on literature, but Moore Line station modelled winds were frequently 30-40% smaller than 10 m measured winds in the 0-40 m layers, which simply suggests poor model performance (Figure D5). Day 3 wind-speeds modelled by WRF were more consistent with observed wind-speeds compared to Day 1 or 2 results, but modelled wind-directions still deviated by ~30-40^{o} during the morning (driving period) at both stations (Figure D6).

Section 3 Vertical Wind Profile Estimation using the Power Law Function

Vertical wind profiles can be estimated using a power law function.

$$\boldsymbol{U_{PL}(z) = U_n \left(\frac{z}{z_o}\right)^p} \qquad \text{(D1)}$$

Where $U_{PL}(z)$ is the wind-speed at height z, z_o is the reference height, U_n is the wind-speed at height z_o and p is the power-law index (PLI). U_n is the measured 10 m wind-speed from the local monitoring stations in this study. The PLI depends on atmospheric stability and roughness of the terrain (e.g., flat fields versus cities with many obstructions) (Kikumoto et al., 2017).

Table D2 Power-Law Exponents (PLI) for Urban and Rural Wind Profiles (EPA, 2000)

Stability Class	Definition	Urban PLI	Rural PLI
A	Very Unstable	0.15	0.07
B	Unstable	0.15	0.07
C	Slightly Unstable	0.2	0.10
D	Neutral	0.25	0.15
E	Slightly Stable	0.3	0.35
F	Stable	0.3	0.55

More stable atmospheric conditions or urban landscapes tend to produce wind-speed profiles that increase more rapidly with altitude while unstable conditions or rural landscapes tend to produce more vertically uniform profiles.

The P-L model is not used to estimate emissions because this profile was designed to model high-speed winds under neutral atmospheric stability conditions for structural engineering applications (Kikumoto et al., 2017) and is generally only applicable to <200 m while plumes may be expected at 500m+ in this study. Also, the accuracy of the P-L profile has been shown to decrease with short time intervals (e.g., < 1 hour) under low wind-speed (Kikumoto et al., 2017) such as those observed during most of the measurement periods in this study. The PLI can also depend on the height interval within <200 m (Hanafusa et al., 1986) so that different height levels may need to be modelled separately.

Table D3 P-G Stability Class from the Horizontal Standard Deviation of Wind-Direction and SRDT Method for Routes on Day 1 to Day 3.

Day	Transect	P-G Stability Class: σ_A Method	SRDT Method
1	1	N/A	C
1	2	C/D	C
1	3	C/D	B/C
2	1	D	C
3	1	D	C
3	2	D	C

In order to estimate the PLI, atmospheric stability (Pasquill-Gifford (PG) stability class) was estimated using the hourly horizontal wind-direction standard deviations σ_a measured by the modular meteorological station and adjusted for the wind-speed using hourly average LaSalle Road station data. The hourly standard deviation is computed using a pooled standard deviation from four 15-minute σ_a using the following equation (EPA, 2000).

$$\sigma_{a,1-hr} = \left[\frac{(\sigma_{a1})^2 + (\sigma_{a2})^2 + (\sigma_{a3})^2 + (\sigma_{a4})^2}{4}\right]^{1/2} \quad \text{(D2)}$$

The stability category was also estimated using the SRDT method, which is based on down-welling solar radiation and wind-speed (EPA, 2000). Hourly average solar radiation data was from the Moore Line station. The stability classes estimated using the two methods are shown in Table D3. However, based on these methods the P-G may have been either C (slightly unstable) or D (neutral) for all three days. The wind-speeds and/or horizontal wind-direction standard deviations were close to the border of the range of values for the two categories. The PLI was estimated using both C and D stability classes assuming a rural location in all cases since there were few obstructions between the measurement locations and the sources, especially for Day 3 (EPA, 2000).

Section 4 Estimation of Non-Industrial NO_x Emissions from Port Huron and Sarnia

4.1 Day 1 Port Huron Vehicular Emission Estimate

Vehicular NO_x emissions from Port Huron were estimated using traffic counts and vehicular NO_x emission factors in order to estimate NO_x influx from Port Huron and to validate the influx VCD choice. Average daily traffic counts for 2016 were obtained from the MDOT Interactive map of Port Huron (Michigan Department of Transportation, n.d.). The map provides total traffic counts and commercial traffic, allowing an estimation of the proportion of cars to trucks. This estimation is important because trucks are much more likely to have diesel engines with significantly higher NO_x emission factors. Emissions from major roads in the Port Huron area that likely impacted the measurements were included, including sections of highways 94 and 69. This estimate does not take into account the vehicular emissions that occur on small roads in Port Huron but these emissions are expected to be relatively small compared to the commercial truck emissions in this area.

The NO_x vehicular emission fluxes strongly depend on the NO_x emission factor assumed for cars and trucks. NO_x emission factors vary significantly depending on vehicle type and age with older vehicles generally emitting more NO_x per mile. Gasoline car NO_x emission factors ranged from 0.06 to 2.38 $gNO_x\ mile^{-1}$ based on measurements by Carslaw et al. (2011) and heavy-duty vehicle NO_x emission factors range from 12.4 to 26 $gNO_x\ mile^{-1}$ based on measurements in Vancouver's Cassiar Connector highway traffic tunnel (Rogak et al., 1998). The estimate assumes all non-commercial vehicles were gasoline cars and heavy-duty vehicles included semis, cube vans and dump trucks. In order to convert daily NO_x emissions to hourly NO_x emissions to compare to the Mobile-MAX-DOAS emission estimates, the vehicle emissions were assumed to occur within 12 hours of a day since less vehicular activity occurs at night. Depending on the NO_x emission factor used, the total vehicular emission estimate range was 0.03-0.25 tonnes h^{-1} The yearly contribution range is 230-1100 tonnes yr^{-1}. This range is reasonable given the 2011 emissions of NO_x from Hamilton, Ontario were estimated to be ~4000 tonnes (McMaster Institute for Transportation and Logistics, 2014) and that the population of Port Huron is ~1/20 of Hamilton's population.

4.2 Estimate of Sarnia Area Non-Industrial Emissions

2015 total Ontario NO_x emissions were 311 kilotonnes with ~82% of those emissions due to non-industrial sources (i.e., transportation, residential and utilities). Non-industrial Ontario emission may be estimated to be 255 kilotonnes in 2015. Sarnia non-industrial emission can be estimated by scaling the Ontario non-industrial emissions of 255 kilotonnes yr^{-1} by the area of Sarnia relative to the total area of all cities in Ontario, resulting in an estimate of ~1270 tonnes yr^{-1}.

Section 5 Sensitivity of Emission Estimates to VCD_{influx} Value

Table D4 Day 1 NO_x fluxes calculated with a range of influx NO_2 VCD values.

NO_2 VCD_{influx} ($x10^{15}$ molec cm^{-2})	Route 1 NO_x flux (tonnes h^{-1})	Route 2 NO_x flux (tonnes h^{-1})	Route 3 NO_x flux (tonnes h^{-1})
0.5	1.99	1.65	1.74
1	1.86	1.42	1.63
1.5	1.74	1.29	1.52
2	1.61	1.17	1.41
3	1.37	0.91	1.19
Average	1.71	1.29	1.50
Standard Deviation	0.24	0.28	0.21
Relative Standard Deviation	14%	22%	14%

Table D5 Day 2 lower limit NO_2 fluxes calculated with zero and $1x10^{15}$ molec cm^{-2} VCD_{influx} values and constant and variable NO_x/NO_2 ratios.

Conditions	NO_x (tonnes h^{-1})
VCD_{influx} = 1 $x10^{15}$ molec cm^{-2} & NO_x/NO_2 = 1.47	1.50
VCD_{influx} = 0 & NO_x/NO_2 = 1.47	1.80
VCD_{influx} = 1 $x10^{15}$ molec cm^{-2} & Variable NO_x/NO_2	2.23
Average	1.83
Standard Deviation	0.37
Relative Standard Deviation	20%

Table D6 Day 3 lower limit NO_x emissions calculated using transect averaged background VCD influx values and influx values of $0.5x10^{15}$ and $1x10^{15}$ molec cm^{-2}.

NO_2 VCD_{influx}	Route 1 NO_x (tonnes h^{-1})	Route 2 NO_x (tonnes h^{-1})
Individual Transect Averages	0.67	0.69
$0.5x10^{15}$ molec cm^{-2}	0.91	1.23
$1x10^{15}$ molec cm^{-2}	0.52	0.95
Average	0.70	0.96
Standard Deviation	0.19	0.27
Relative Standard Deviation	27%	28%

Emission estimates from Day 3 were calculating using the local average transect background VCD values and assuming constant VCD_{influx} values of 1 $x10^{15}$ and 0.5 $x10^{15}$ molec cm^{-2}. However, the emission estimates using the local average VCDs from each transect are likely the most accurate because the VCD in the background upwind of NOVA Chemicals is expected to be low and relatively constant because there are no known significant NO_x sources in that region. Also, since a local FRS was used to retrieve the DSCDs in each case, using a constant assumed background VCD for all transects likely introduces error since the NO_2 present in each FRS would vary but is negated if the average background VCD is used.

Table D7 SO_2 lower limit emissions from Day 1 route 3 with varying background VCD values.

SO_2 VCD_{influx} ($x10^{15}$ molec cm^{-2})	SO_2 (tonnes h^{-1})
0.6	3.3
1.00	2.3
1.20	1.8
Average	2.47
Standard Deviation	0.76
Relative Standard Deviation	31%

Section 6 Conversion Factor Values for Estimating NO_x Emissions from NO_2 Emissions

Table D8 Conversion Factor Values for Estimating NO_x Emissions from NO_2 Emissions. Day 2 route 1* used individual NO_x/NO_2 values rather than a route-averaged value.

Day	Route	NO_2 to NO_x Emission Estimate Conversion Factor
1	1	2.52
1	2	1.80
1	3	1.69
2	1	1.52
2	1*	2.26
3	1	1.49
3	2	1.52

Section 7 Error Estimates and Sensitivity Analysis

Table D9 Error contributions to emission estimates. * Indicates assumed value rather than from tested variability.

Gas	NO_x	NO_x	NO_x	NO_x	NO_x	NO_x	SO_2
Day	1	1	1	2	3	3	1
Route	1	2	3	1	1	2	3
DSCD	15%	15%	15%	15%	15%	15%	30%
VCD_{geo}	20%	20%	20%	20%	20%	20%	20%
NO_x/NO_2 ratio	5%	5%	5%	5%	10%	10%	N/A
Lifetime	30%	12%	12%	7%	2%	2%	N/A
Wind-Speed	N/A	N/A	N/A	N/A	N/A	N/A	N/A
Wind-Direction	22%	15%	15%	6%	12%	12%	15%
VCD_{influx}	18%	29%	19%	*25%	*20%	*20%	30%
Total Error	49%	43%	37%	37%	36%	36%	46%

Sensitivity analysis was conducted for routes by varying the NO_x/NO_2 ratio, lifetime, wind-direction, and (Day 1 only) VCD_{influx} values (Table D9). The error listed in Table D9 for each of these factors is the maximum percentage variation of the emission estimate using the standard value to the most different emission value produced using the range of values. The route respective average NO_x/NO_2 values were varied by ±1 standard deviation, the lifetime

was varied between 4 and 8 hours, the route respective wind directions were varied by ±10° and the influx VCDs for Day 1 were varied from 0.5 to $3x10^{15}$ molec cm^{-2} for NO_2 and 0.6 to $1.23x10^{15}$ molec cm^{-2} for SO_2. VCD_{influx} error on Day 2 was presumed to be similar to Day 1 on since no usable background VCD measurements were available. VCD_{influx} error for Day 3 was presumed to be the same as the VCD_{geo} error for each transect since there was little variation in the local background values. Since the emission values were calculated as lower limit estimates given 10 m wind-speed, wind-speed error was not included. SO_2 DSCD error was higher due to greater detection limit and lower sensitivity compared to NO_2.

Section 8 Relative Seasonal OH Production and Derivation of the Leighton Ratio Equation

8.1 Derivation of the Production of OH

OH is produced though reaction of $O(^1D)$, produced from photolysis of O_3, with H_2O.

$$O_3 + hv \rightarrow O_2 + O(^1D) \quad \text{(D3)}$$

$$O(^1D) + M \rightarrow O + M \quad \text{(D4)}$$

$$O(^1D) + H_2O \rightarrow 2OH + O_2 \quad \text{(D5)}$$

Given Eqs. D3-F5 the production rate of OH is:

$$P_{OH} = 2k_5[O(^1D)][H_2O] \quad \text{(D6)}$$

Where concentration is denoted by square brackets, k_5 is the rate constant for reaction (D5). Assuming $O(^1D)$ is in steady-state, the production of OH depends on the concentrations of O_3 and H_2O.

$$P_{OH} = \frac{2J_{O3}}{k_4[M] + k_5[H_2O]}[O_3][H_2O] \quad \text{(D7)}$$

Where J_{O3} is the photolysis rate constant for O_3 and k_2 is the rate constant for Reaction (S3). At typical atmospheric H_2O mixing ratios the term $k_5[H_2O]$ is small compared to the term $k_4[M]$, allowing the approximation (Seinfeld and Pandis, 2006):

$$P_{OH} \approx \frac{2J_{O3}}{k_4[M]}[O_3][H_2O] \quad \text{(D8)}$$

Therefore, P_{OH} $\alpha[O_3][H_2O]$.

Table F1 Comparison of $[H_2O]*[O_3]$ product during summer conditions and study (spring) conditions. Temperature, Relative Humidity and $[O_3]$ from SLEA Front Street Station.

Date (2017)	Local Time	Temperature (^oC)	Relative Humidity	O_3 (ppbv)	O_3 (x10^{11} molec cm^{-3})	$[H_2O]*[O_3]$ (x10^{29} $molec^2/cm^9$)	Spring/Summer
1-Jul	10:00	23	0.74	29	7.2	3.6	
1-Jul	11:00	24.1	0.68	33	8.1	4.0	
1-Jul	12:00	25	0.61	37	9.1	4.3	
21-Mar	10:00	7.8	0.53	10	2.6	0.38	10%
21-Mar	11:00	11	0.3	22	5.7	0.57	14%
21-Mar	12:00	12.3	0.29	32	8.2	0.86	20%

The product of H_2O and O_3 was calculated assuming $O(^1D)$ was in steady-state. The daytime spring-conditions products for Days 1 and 2 are approximately 10-20% of the summertime product determined from Front Street SLEA monitoring data on 01/06/2017.

8.2 Leighton Ratio Derivation

During the daytime troposphere, NO_2 is photolyzed to form NO and an $O(^3P)$ atom.

$$NO_2 + hv \rightarrow NO + O(^3P) \quad \text{(D9)}$$

The $O(^3P)$ atom reacts with molecular oxygen to form O_3 in a three-body reaction.

$$O(^3P) + O_2(+M) \rightarrow O_3(+M) \quad \text{(D10)}$$

The O_3 can then reform NO_2 from NO.

$$NO + O_3 \rightarrow NO_2 + O_2 \quad \text{(D11)}$$

When O_3 is in photostationary state, the mixing ratio of O_3 depends on the NO and NO_2 concentrations via the following equation:

$$[O_3] = (J[NO_2])/(k_{11}[NO]) \quad \text{(D12)}$$

Where J_{NO2} and k_{11} are the photolysis rate of NO_2 and the rate constant for reaction (D11), respectively.

The Leighton ratio (ϕ) is produced by dividing both sides of the equation by $[O_3]$

$$\phi = \frac{J_{NO2}[NO_2]}{k_1[NO][O_3]} \quad \text{(D13)}$$

The value of ϕ tends to be unity in regions with high NO_x levels but be greater than unity when other chemical processes convert NO to NO_2 other than the reaction of NO with O_3 (Griffin et al., 2007).

Section 9 Map of Day 1 Route 4 Mobile-MAX-DOAS VCD Measurements

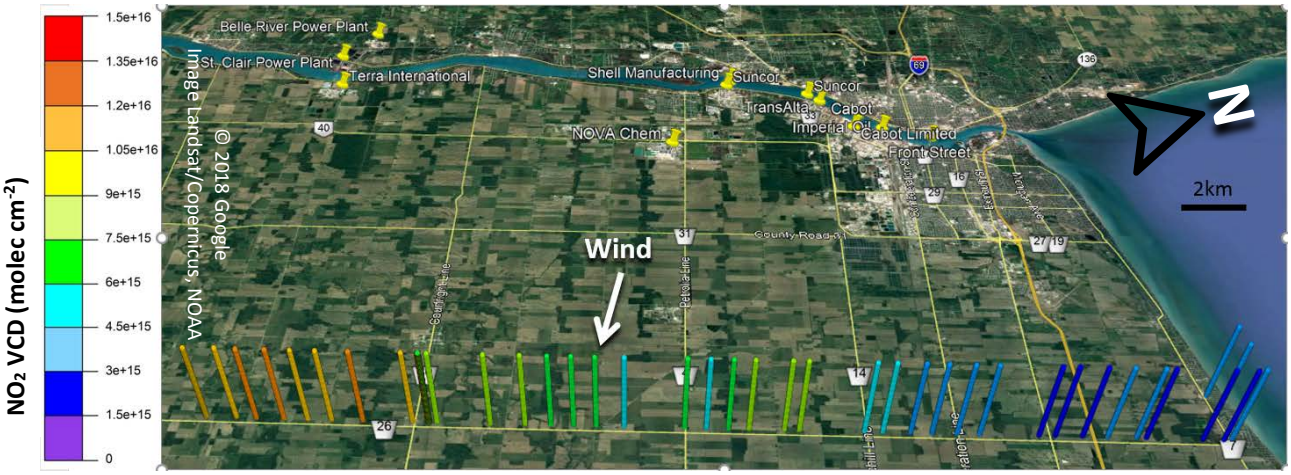

Figure D7 Day 1 Route 4 NO_2 VCDs.

References

Banks, R. F., Tiana-Alsina, J., Maria Baldasano, J., Rocadenbosch, F., Papayannis, A., Solomos, S. and Tzanis, C. G.: Sensitivity of boundary-layer variables to PBL schemes in the WRF model based on surface meteorological observations, lidar, and radiosondes during the HygrA-CD campaign, Atmospheric Res., 176, 185–201, doi:10.1016/j.atmosres.2016.02.024, 2016.

Draxl, C., Hahmann, A. N., Pena, A., Nissen, J. N. and Giebel, G.: Validation of Boundary-Layer Winds from Wrf Mesoscale Forecasts with Applications to Wind Energy Forecasting, edited by U. Betancourt and T. Ackermann, Energynautics Gmbh, Langen., 2010.

Draxl, C., Hahmann, A. N., Pena, A. and Giebel, G.: Evaluating winds and vertical wind shear from Weather Research and Forecasting model forecasts using seven planetary boundary layer schemes, Wind Energy, 17(1), 39–55, doi:10.1002/we.1555, 2014.

EPA: Meteorological Monitoring Guidance for Regulatory Modeling Applications, United States Environmental Protection Agency- Office of Air Quality Planning and Standards. [online] Available from: https://www3.epa.gov/scram001/guidance/met/mmgrma.pdf, 2000.

Fekih, A. and Mohamed, A.: Evaluation of the WRF model on simulating the vertical structure and diurnal cycle of the atmospheric boundary layer over Bordj Badji Mokhtar (southwestern Algeria), J. King Saud Univ. - Sci., doi:10.1016/j.jksus.2017.12.004, 2017.

Griffin, R. J., Beckman, P. J., Talbot, R. W., Sive, B. C. and Varner, R. K.: Deviations from ozone photostationary state during the International Consortium for Atmospheric Research on Transport and Transformation 2004 campaign: Use of measurements and photochemical modeling to assess potential causes, J. Geophys. Res. Atmospheres, 112(D10), D10S07, doi:10.1029/2006JD007604, 2007.

Hanafusa, T., Lee, C. B. and Lo, A. K.: Dependence of the exponent in power law wind profiles on stability and height interval, Atmospheric Environ. 1967, 20(10), 2059–2066, doi:10.1016/0004-6981(86)90348-3, 1986.

Kikumoto, H., Ooka, R., Sugawara, H. and Lim, J.: Observational study of power-law approximation of wind profiles within an urban boundary layer for various wind conditions, J. Wind Eng. Ind. Aerodyn., 164, 13–21, doi:10.1016/j.jweia.2017.02.003, 2017.

McMaster Institute for Transportation and Logistics: Estimating Vehicular Emissions for the Toronto and Hamilton Census Metropolitan Areas. [online] Available from: http://mitl.mcmaster.ca/reports/MITL_Emissions_Toronto_Hamilton_July.pdf, 2014.

Michigan Department of Transportation: MDOT Traffic Volumes, [online] Available from: http://mdot.maps.arcgis.com/apps/Viewer/index.html?appid=18a4b2f2ba3b4e079e935f8835862c73 (Accessed 7 October 2017), n.d.

Rogak, S. N., Pott, U., Dann, T. and Wang, D.: Gaseous emissions from vehicles in a traffic tunnel in Vancouver, British Columbia, J. Air Waste Manag. Assoc., 48(7), 604–615, doi:10.1080/10473289.1998.10463713, 1998.

Seinfeld, J. H. and Pandis, S. N.: Atmospheric Chemistry and Physics: From Air Pollution to Climate Change, John Wiley & Sons., 2006.

Shin, H. H., Hong, S.-Y. and Dudhia, J.: Impacts of the Lowest Model Level Height on the Performance of Planetary Boundary Layer Parameterizations, Mon. Weather Rev., 140(2), 664–682, doi:10.1175/MWR-D-11-00027.1, 2012.